SELF-ASSEMBLED FUNCTIONAL HYBRID MATERIALS OF CARBON ALLOTROPES AND EXTENDED π-SYSTEMS FOR VARIOUS APPLICATIONS

Thesis Submitted to AcSIR for the Award of the Degree of
DOCTOR OF PHILOSOPHY
in Chemical Sciences

By

VEDHANARAYANAN B

Registration No: 10CC11J39008

Under the Guidance of

Dr. A. AJAYAGHOSH

CSIR-NATIONAL INSTITUTE FOR INTERDISCIPLINARY SCIENCE AND TECHNOLOGY (CSIR-NIIST)
THIRUVANANTHAPURAM-695 019, KERALA, INDIA

March, 2017

Dedicated to My Beloved Parents

Loving Wife & Brother

DECLARATION

I hereby declare that the matter embodied in the thesis entitled: "**Self-Assembled Functional Hybrid Materials of Carbon Allotropes and Extended π-Systems for Various Applications**" is the result of the investigations carried out by me at the Photosciences and Photonics Section, Chemical Sciences and Technology Division, CSIR-National Institute for Interdisciplinary Science and Technology (CSIR-NIIST), Thiruvananthapuram, under the supervision of Dr. A. Ajayaghosh and the same has not been submitted elsewhere for any other degree.

In keeping with the general practice of reporting scientific observations, due acknowledgement has been made wherever the work described is based on the findings of other investigators.

Vedhanarayanan B.

Thiruvananthapuram
27-03-2017

राष्ट्रीय अंतर्विषयी विज्ञान तथा प्रौद्योगिकी संस्थान
वैज्ञानिक तथा औद्योगिक अनुसंधान परिषद्
इंडस्ट्रियल इस्टेट पी.ओ., पाप्पनकोड, तिरुवनंतपुरम, भारत-695 019
CSIR-NATIONAL INSTITUTE FOR INTERDISCIPLINARY SCIENCE & TECHNOLOGY (CSIR-NIIST)
Council of Scientific & Industrial Research
Industrial Estate P.O., Pappanamcode, Thiruvananthapuram, India-695 019
डॉ. ए. अजयघोष एफएनए, एफटीडब्ल्यूएस
निदेशक
Dr. A. Ajayaghosh FNA, FTWAS
Director

27-03-2017

CERTIFICATE

This is to certify that the work embodied in this Ph. D. thesis entitled "**Self-Assembled Functional Hybrid Materials of Carbon Allotropes and Extended π-Systems for Various Applications**" submitted by **Mr. Vedhanarayanan B.** to Academy of Scientific and Innovative Research (AcSIR), in partial fulfilment of the requirements for the award of the **Degree of Doctor of Philosophy in Chemical Sciences**, has been carried out under my supervision and guidance at the Photosciences and Photonics Section, Chemical Sciences and Technology Division of the CSIR-National Institute for Interdisciplinary Science and Technology (CSIR-NIIST), Thiruvananthapuram. I further certify that this work has not been submitted to any other University or Institution in part or full for the award of any degree or diploma.

A. Ajayaghosh
(Thesis Supervisor)

ACKNOWLEDGEMENTS

It is with great pleasure that I extend my deep sense of gratitude to Dr. A. Ajayaghosh, my thesis supervisor, for suggesting the research problem, for his valuable guidance, support and encouragement, leading to the successful completion of this work.

I would like to express my gratitude to Prof. M. V. George for being an inspiration.

I thank Dr. Suresh Das former Director and Dr. Gangan Pratap, former Acting Directors of the CSIR-National Institute for Interdisciplinary Science and Technology (CSIR-NIIST), Thiruvananthapuram, for providing the necessary facilities for carrying out this work.

My sincere thanks are also due to:

- ✓ Dr. D. Ramaiah, Dr. Narayanan Unni, Dr. Joshy Joseph, Dr. K. Yoosaf, Dr. C. Vijayakumar, Dr. B. Deb and Dr. V. Karunakaran, present and former scientists of the Photosciences and Photonics Section, Chemical Sciences and Technology Division, for their help and support.
- ✓ Dr. R. Luxmi Varma, AcSIR co-ordinator.
- ✓ Dr. K. R. Gopidas, Dr. Mangalam S. Nair, Dr. T. P. D. Rajan, who are my DAC members.
- ✓ Dr. J. D. Sudha and Dr. V. K. Praveen, for their support and fruitful discussions.
- ✓ Dr. G. Vijay Nair, Honorary Scientist, Organic Chemistry Section for his support and help.
- ✓ Dr. M. M. Shaijumon, Mr. B. Babu, and Mr. D. Damien, Indian Institute of Science Education and Research, Thiruvananthapuram, for supercapacitor studies.
- ✓ Dr. S. Srinivasan, Dr. S. Prasanthkumar, Dr. K. P. Divya, Dr. G. Anesh, Dr. K. Kartha, and Dr. P. Anees, Dr. Manoj, former members of the Photosciences and Photonics Section, for their support and advice.
- ✓ Dr. Rakhi R. B., Dr. R. K. Mishra, Dr. Manas Panda, Dr. Sreejith Sankar, Mr. R. Thirumalai, Mr. A. Sandeep, Mr. S. Vishnu, Mr. R. D. Mukhopadhyay, Ms. Divya. S. Philips, Mr. C. Sandeep, Mr. S. Ghosh, Mr. K. V. Sudheesh, Mr. A. Mal, Mr. M.

Hifsudheen, Mr. S. Das, Mr. G. Das, Dr. R. Ramakrishnan, Dr. A. Jose, Mr. Jagadeesh K., and Ms. P. Anisha, for their help and cooperation.

- ✓ Mr. J. S. Kiran for his general help and support.
- ✓ Mr. Chandrakanth C. K. for SEM analysis and Mr. Robert Philip and Mr. M. Kiran for TEM analysis.
- ✓ Ms. M. Saumini, Mr. Adarsh, Mr. P. Preethanuj, Mr. T. Arun, Mr. Saran P., and Mr. R. Gokul for NMR and Ms. S. Viji and Ms. Aathira for mass spectral analyses.
- ✓ Dr. Seetha Lakshmi K. C., my wife, for her support and motivation.
- ✓ All my teachers for their encouragement at different stages of my academic career.
- ✓ Council of Scientific and Industrial Research (CSIR), Government of India for Research fellowship.

I am deeply and forever indebted to my parents, wife and brother for their constant source of love, inspiration and blessings. Finally I would like to thank my friends and relatives for their excellent support and encouragement.

Vedhanarayanan B.

CONTENTS

CHAPTER 1

CHAPTER 2

CHAPTER 3

CHAPTER 4

List of Abbreviations

γ	Interfacial engergy
F_D	Drag force
ρ	Density
v	Velocity
V	Volume
g	Gravitational acceleration
ΔH	Enthalpy change
°C	Degree celsius
AFM	Atomic force microscopy
BET	Brunauer–Emmett–Teller
BF_4^-	Tetrafluoroborate anion
C_6H_6	Benzene
C-AFM	Conductive-atomic force microscopy
CD	Cicular dichroism
C_D	Drag coefficient
$CDCl_3$	Deuterated chloroform
CH_2Cl_2	Dichloromethane
CH_3CN	Acetonitrile
CH_3COOH	Acetic acid
CH_3OH	Methanol
$CHCl_3$	Chloroform
$Cl_2CHOC_2H_5$	α-Dichloromethylethylether
cm	Centimeter
CMC	Critical micelle concentration
CNTs	Carbon nanotubes
CoMoCAT	Cobalt-molybdenum catalyst
CTAB	Cetyltrimethylammonium bromide

CV	Cyclic voltammogram
CVD	Chemical vapour deposition
DCC	*N,N'*-dicyclohexylcarbodiimide
DCM	Dichloromethane
DEG	Diethylene glycol
DFT	Density-functional theory
DLS	Dynamic light scattering
DMAP	4-Dimethylaminopyridine
DMF	*N,N*-Dimethylformamide
DMSO	Dimethyl sulphoxide
DNA	Deoxyribonucleic acid
et al.	*Et allii/alia*
EtOH	Ethanol
F_B	Buoyant force
$FeCl_3 \cdot 6H_2O$	Ferric chloride hexahydrate
F_P	Propulsive force
FT-IR	Fourier transform infrared
g	Gram
GO	Graphene oxide
GPC	Gel permeation chromatography
H_2O	Water
H_2O_2	Hydrogen peroxide
H-bonding	Hydrogen bonding
HBr	Hydrobromic acid
HCl	Hydrochloric acid
HiPco	High pressure carbon monoxide
HOPG	Highly ordered pyrolytic graphite
HR-TEM	High resolution transmission electron microscopy
I_2	Iodine
I_{em}	Intensity of emission

IL	Ionic liquids
KBr	Potassium bromide
kg	Kilogram
KOH	Potassium hydroxide
L	Litre
l	Length
LbL	Layer-by-layer
LCST	Low critical solution temperature
LiOEt	Lithium ethoxide
LLC	Lyotropic liquid crystalline
M	Molar
m	Meter
m. p.	Melting point
MALDI-TOF	Matrix-assisted laser desorption ionization time-of-flight
MCH	Methyl cyclohexane
MD	Molecular dynamics
MHz	Mega hertz
min	Minutes
mL	Milliliter
mmol	Millimole
MnO_2	Manganese dioxide
mol	Mole
MWNT	Multi-walled carbon nanotube
N	Newton
N_2	Nitrogen
Na_2SO_4	Sodium sulphate
$NaBH_4$	Sodium borohydride
NaH	Sodium hydride
NaOH	Sodium hydroxide
NIR	Near-infrared

nm	Nanometer
Nm^{-1}	Newton per meter
NMP	*N*-Methylpyrrolidone
NMR	Nuclear magnetic resonance
ODCB	*O*-Dichlorobenzene
OPE	Oligo(*p*-phenyleneethylene)
OPM	Optical polarizing microscopy
OPV	Oligo(*p*-phenylenevinylene)
P3AT	Poly(3-alkylthiophene)
P3HT	Poly(3-hexylthiophene)
PANI	Polyaniline
PCC	Pyridinium chlorochromate
PDA	Poly(dopamine)
PDT	Photodynamic therapy
PEDOT	Poly(3,4-ethylenedioxy-thiophene)
PEI	poly(ethyleneimine)
PF	Poly(9,9-dialkylfluorene)
PF_6^-	Hexafluorophosphate anion
PFDTS	1H,1H,2H,2H-Perfluorodecyltriethoxy-silane
PFT	Poly(9,9-dialkylfluorene-*co*-3-alkylthiophene)
pH	Hydrogen ion concentration at logarithmic scale
PNIPAM	Poly(*N*-isopropylamide)
PPE	Poly(*p*-phenyleneethynylene)
PPh_3	Triphenylphosphine
ppm	Parts per million
PPV	Poly(*p*-phenylenevinylene)
PPy	Polypyrrole
PT	Polythiophene
PTT	Photothermal therapy
PVDF	Poly(vinylenedifluoride)

RBM	Radial breathing mode
R-CA/S-CA	R-Citronellic acid/S-Citronellic acid
RGO	Reduced graphene oxide
s	Seconds
SAED	Selected area electron diffraction
SDBS	Sodium dodecylbenzenesulphonate
SEM	Scanning electron microscopy
SnO_2	Tin dioxide
SPANI	Sulphonated polyaniline
SWNTs	Single-walled carbon nanotubes
t	Time
T	Temperature
TBAB	Tetrabultyl ammonium bromide
t-BuOK	Potassium *tert*-butoxide
T_e	Elongation temperature
TEA	Triethanolamine
TEM	Transmission electron microscopy
TGA	Thermal gravimetric analysis
T_{gel}	Gel melting temperature
THF	Tetrahydrofuran
$TiCl_4$	Titanium tetrachloride
T_m	Melting temperature
TMS	Tetramethylsilane
TTFV	Tetrathiafulvalene vinyl
UT	Ureidotriazine
UV	Ultra-violet
Vis	Visible
XRD	X-ray diffraction
α-CD	α-Cyclodextrin
β-CD	β-Cyclodextrin

δ	Chemical shift
$\Delta\varepsilon$	Ellipticity
ε	Molar extinction coefficient
θ	Angle
θ_{CA}	Contact angle
θ_{F}	Actual contact angle
λ_{abs}	Wavelength of absorption
λ_{em}	Wavelength of emission
λ_{ex}	Wavelength of excitation
μm	Micrometer

PREFACE

Self-assembled hybrid materials are an important class of advanced materials as they have many potential applications in various fields. The non-covalent interactions involved in the self-assembly process offer us an easy way to alter their properties. Design and development of new strategies to create hybrid materials with excellent physical, chemical and electronic properties will be helpful to create advanced technologies in the field of energy efficiency, energy storage, etc. The first chapter gives a brief summary of recent advancements in the area of self-assembled functional hybrid materials.

In the second chapter, we have shown that supramolecular self-assembly process could be used as a useful tool to exfoliate reduced graphene oxide (**RGO**), resulting in hybrid materials with improved properties. Graphene – 2D material – is known for its excellent electronic properties and numerous applications in different fields. Incorporation and homogeneous distribution of graphene in various matrices with preserved intrinsic electrical and electronic properties is a primary requirement to exploit its awesome properties. To achieve this, different strategies have been used to enhance its dispersibility, which includes chemical modifications, covalent and non-covalent functionalization. Among them, the non-covalent functionalization has been considered as a non-destructive and efficient method. By adopting the non-covalent interactions with oligo(*p*-phenylenevinylene) (**OPV**), the dispersing ability of the reduced graphene oxide (**RGO**) could be increased (1.7-1.8 mg mL^{-1}) when compared to that of the bare one. Photophysical studies revealed the aggregation behavior of hybrid in the non-polar solvent and the extent of dispersion of graphene sheets in the solution state. The detailed gelation and rheological studies explained the improved

stability of hybrid gel than the native one. Morphological studies such as SEM, OPM, AFM and TEM gave an evidence of self-assembly of π-gelator on the surface of graphene and better exfoliation of latter into bi-layer or a few-layer graphene sheets. Aggregation of π-gelator over **RGO** helped exfoliated graphene layers to remain as individual sheets with higher surface area. With the enhanced surface area and better conductivity, these hybrid materials showed excellent electrochemical performance as electrodes for supercapacitors.

In the third chapter, we have demonstrated the influence of carbon nanotubes (**CNTs**) on chirality amplification in molecular assemblies. **CNTs** facilitate amplification of molecular chirality to supramolecular helicity at a concentration much lower than that required for intermolecular interaction. UV-Vis-NIR absorption spectroscopy revealed the interaction of nanotubes with the π-gelators through π-π stacking and van der Waals interaction. The chirality amplification in molecular assemblies with **CNTs** was monitored by circular dichroism (CD) spectroscopy. A very small amount of **CNT** (0.05 mg) could influence the chirality of the molecular assemblies which is further confirmed by concentration dependent CD studies. Raman spectroscopy studies revealed the self-assembly of the molecules over the carbon nanotubes surfaces. Surprisingly, AFM analysis showed the formation of thick helical fibers of >100 nm. High-resolution TEM analysis and solid-state UV-Vis-NIR spectrum exhibited thick helical fibers which are cylindrical cables composed of individually wrapped and coaxially aligned **SWNTs**.

In the fourth chapter, we have designed and synthesized a few linear π-conjugated molecules with a polymerizable end group. The self-assembled polymer/**MWNT** hybrid materials have been prepared by polymerization to fix the molecules around the **MWNT**, thereby preventing the leaching off them from the hybrid. The better dispersing ability of

polymer/**MWNT** hybrid materials enhances the solution processing and preparation of superhydrophobic coatings. The polymer/**MWNT** hybrid materials exhibited superhydrophobic properties when coated on different substrates. The superhydrophobic coatings made from the polymer/**MWNT** hybrids showed an excellent stability with the contact angle of 169° under acidic and basic conditions. And also, these coatings reduced the frictional drag force to > 60% and improved the buoyancy of aquatic vehicles upto 1.6 fold when compared to uncoated one, thereby lowering the fuel consumption. Hence, the coatings made of hybrid materials with higher water contact angle and excellent stability have a potential role in practical applications such as self-cleaning, anti-icing, drag resistant surfaces, etc.

References

1. Formation of Coaxial Nanocables with Amplified Supramolecular Chirality through an Interaction between Carbon Nanotubes and a Chiral π-Gelator, **B. Vedhanarayanan,** Vishnu S. Nair, Vijayakumar C. Nair and A. Ajayaghosh, *Angew. Chem. Int. Ed.* **2016**, *55*, 10345–10349.
2. Exfoliation of Reduced Graphene Oxide with Self-assembled π-Gelators for Improved Electrochemical Performance, **B. Vedhanarayanan**, B. Babu, M. M. Shaijumon and A. Ajayaghosh, *ACS Appl. Mater. Interfaces* **2016**, DOI: 10.1021/acsami.6b09418.
3. Superhydrophobic Coatings of Carbon Nanotubes and Linear π-Systems with Polymerizable End Group for Various Applications. **B. Vedhanarayanan**, R. D. Mukhopadhyay, and A. Ajayaghosh **2017**. (Under preparation)

Chapter 1

Functional Hybrid Materials by Self-Assembly

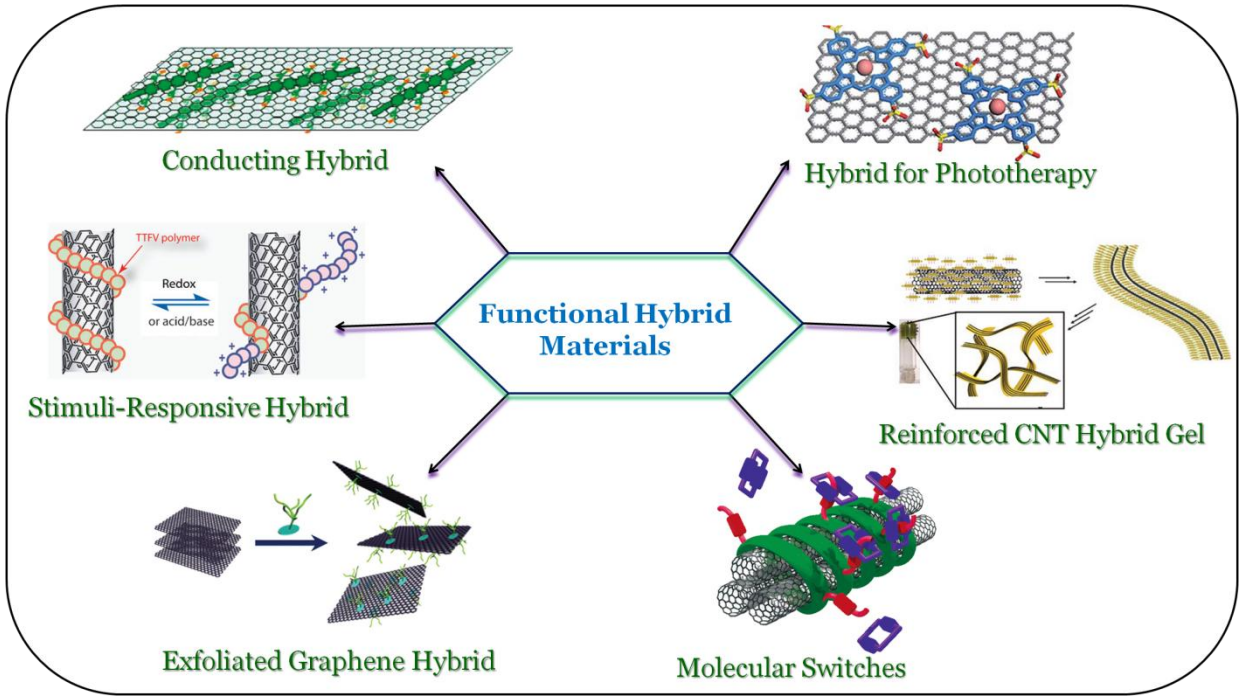

1.1. Abstract

*Self-assembled hybrid materials are an important class of advanced materials with potential applications in various fields ranging from optoelectronics to medicines. The non-covalent interactions involved in the self-assembly process offer an easy way to create hybrid materials with unique and interesting properties. In general, hybrid materials exhibit improved properties than that of their individual counterparts. In this context, carbon nanotubes (**CNTs**), graphene and graphene derivatives such as graphene oxide (**GO**) and reduced graphene oxide (**RGO**) based self-assembled hybrid materials are particularly important. These composites are solution processable and show good electrical, mechanical and chemical properties and find applications in the field of light harvesting, energy storage, optoelectronics, etc. In this chapter, a brief summary of recent developments in the area of self-assembled functional hybrid materials consisting of **CNTs**, graphene, graphene derivatives (**GO** and **RGO**), organic small molecules and polymers are described. Finally, the objectives and the approach of the investigations leading to the present thesis are presented.*

1.2. Introduction

The evolution of synthetic hybrid materials had started with the invention of an ancient dye Maya blue (mixture of indigo dye and natural clay).[1] Development in this area has been inspired by a number of functional hybrid materials found in nature such as bone (a combination of an organic component, collagen and an inorganic component, phosphate mineral), nacre (mixture of an elastic bio-polymer, chitin and carbonate

minerals), etc.[2-3] The properties of homogeneous or heterogeneous hybrid materials may be either an additive of the individual components or a new one. The major interactions among the components of hybrid materials are either non-covalent or covalent in nature. Based on these interactions, hybrid materials are classified in different ways such as organic-inorganic, bio-molecules-inorganic, polymer-inorganic, etc.[4]

Hybrid materials tailored through supramolecular self-assembly process by using non-covalent interactions such hydrogen bonding, π-π stacking, and van der Waals forces have attracted a lot of research interest due to their potential applications in various fields from materials to biology.[5-9] The reversible nature of self-assembly process provides an opportunity to fine-tune the properties of the resulting materials. Different strategies have been developed to create self-assembled hybrid materials such as template method, complementary interactions, molecular recognition, and so on.[10] Recognition properties of molecules resulting from various intermolecular interactions play a crucial role in the development of these hybrid materials. The nanoscale and mesoscale ordering of the individual building blocks in the self-assembled hybrid materials are controlled by the non-covalent interactions. The morphological features are mainly governed by these interactions, which also play an important role in deciding the properties of the resulting hybrid materials.[11-12]

Carbon nanotubes (**CNTs**) and graphene are important allotropes of carbon. Solution processing is an essential requirement in the utilization of these fascinating nanomaterials for various applications. Hybrid materials of **CNTs** and graphene

prepared by non-covalent functionalization retain the original properties of the pristine materials to a great extent with minimum structural defects.[13-14] In this chapter, we discuss about the recent advancements in the field of hybrid materials of π-gelators, aromatic molecules, and polymers with carbon nanomaterials such as graphene, graphene derivatives and carbon nanotubes (**CNTs**), prepared by the molecular assembly approach.

1.3. Graphene Based Hybrid Materials

Graphene is a two-dimensional layered structure with extended π-conjugation, which possesses unique electronic properties.[15-23] An extended honeycomb structure formed due to the covalent bonding among the sp^2 hybridized carbon atoms gives an excellent strength to weight ratio that exceeds metals and metal based hybrid materials. The zero band gap of graphene results in excellent electron mobility, making it as an alternative to the existing semiconductors in electronic devices. Graphene derivatives such as **GO** and **RGO** provide atomically thin layered structure similar to graphene.[12] But, they differ in the percentage of oxygen functionalities and sp^2 hybridized carbon atoms on their basal plane. **RGO** has minimum percentage of oxygen functionalities such as epoxide, carboxylic acid, primary and tertiary alcohols. Since it has more sp^2 hybridized carbon atoms on its basal plane, the electrical properties are superior to that of **GO**. Incorporation of graphene and its derivatives into self-assembled organic molecules led to hybrid materials with enhanced electrical and mechanical properties of the latter. Literature reports suggest that **GO** and **RGO** have been successfully incorporated into supramolecular gels, molecular assemblies of aromatic molecules

and π-conjugated polymers through non-covalent interactions and used for various applications.[24-25] Important reports on this regard are summarized in the following sections.

1.3.1. Hybrid Materials of Graphene and its Derivatives with Supramolecular Gels

Functional hybrid gels of graphene and its derivatives with aromatic molecules and polymers provide a platform to get homogenous distribution of the former in 3D architectures. These gels are mechanically stable and solution processable for optoelectronic, chemical and biosensors applications. Banerjee *et al.* have reported a stable hybrid gel of pyrene-containing peptide-based gelator with unfunctionalized and non-oxidized graphene sheets in *o*-dichlorobenzene (ODCB).[26] By introducing an oligo-peptide chain to a pyrene moiety through the *N*-terminal side, the molecule becomes a gelator that strongly interacts with graphene. Unfunctionalized graphene sheets of three to four layers were obtained by sonicating graphite powder in ODCB which can be converted to a hybrid gel by mixing with gelator molecules. The presence of graphene sheets and fibers formed by self-assembly of gelator has been confirmed by morphological studies. The improvement in the stability of hybrid gel when compared to native one was studied by rheological measurements.

In addition to pristine graphene, **GO** can also be incorporated into gel media to get mechanically stable hybrid gels. Incorporation of **GO** into conducting polymeric gels led to stable gels with better conductivity. For example, the preparation of hybrid

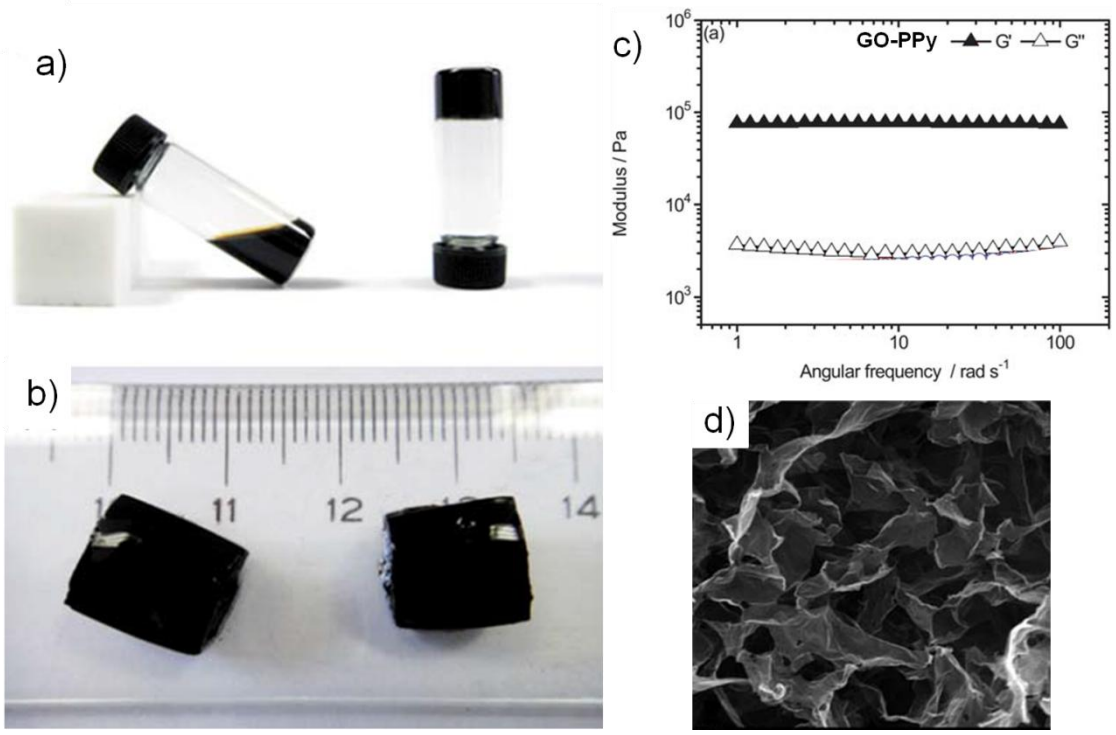

Figure 1.1. a) A photograph showing a mixture of **GO** and pyrrole, before and after in-situ polymerization. b) Photograph of free standing **GO/PPy** hybrid hydrogel. c) Rheological behavior of **GO/PPy** hybrid hydrogel. d) SEM image of dried hybrid gel.

hydrogels composed of **GO** and a conducting polymer, polypyrrole (**PPy**) was reported by Shi *et al*.[27] In-situ polymerization of monomers in the presence of an aqueous solution of **GO** with various weight ratio has been used to prepare **GO/PPy** hybrids. All **GO/PPy** hybrids showed gelation in water with the weight percentage of < 1 (Figure 1.1a and 1.1b). The hybrid gels exhibited good viscoelastic properties that were confirmed by rheological studies (Figure 1.1c). Since **GO/PPy** exhibited excellent electrical conductivity and electrochemical properties, it has been used to prepare a sensor for ammonia gas. The microstructure of dried **GO/PPy** hybrid gels as shown in Figure 1.1d, was responsible for 40% of resistance increase on exposure to

800 ppm ammonia gas for 600 s, whereas the thin film of **PPy** showed only 7% of resistance increase under similar conditions.

Han *et al.* have shown the preparation of **GO** containing hybrid hydrogel and organogel, based on amphiphilic gelators (**1a** and **1b**) consisting of carbohydrate as the polar group and pyrene moiety as the non-polar group (Figure 1.2a).[28] These gelators vary in the position of hydroxyl groups such as 1, 3 and 2, 3 carbon atoms of the six-membered carbohydrate head groups. The hybrid gels have been prepared by heating **GO** suspensions in water and DMF with the gelator to 70 °C, followed by cooling and keeping the suspension at room temperature for 30-60 minutes. The π-π stacking interaction between pyrene moieties as well as between pyrene and **GO** plays a key role in the formation of the hydrogel (Figure 1.2b). On the other hand, H-bonding among carbohydrate moieties is the major driving force in the formation of the organogel (Figure 1.2c). The rheological studies of the hybrid gels (hydrogel and organogel) showed an improvement in stability when compared to that of the native gels. The role of the position of hydroxyl groups of the carbohydrate moieties on the stability of the hybrid gels was measured by dynamic rheological studies. The hybrid gels prepared from amphiphilic gelator (**1b**) containing hydroxyl groups on carbon atoms at 2 and 3 positions of the carbohydrate unit showed poor stability due to the difference in configuration of the hydroxyl groups of the gelator. Since the hydrogel of **1a**/**GO** exhibited exfoliated **GO** sheets as shown in Figure 1.2d as well as possessed negative charges on its surface, it was used to remove the positively charged dyes from aqueous solution with a maximum percentage of dye loading. Pyrene functionalized

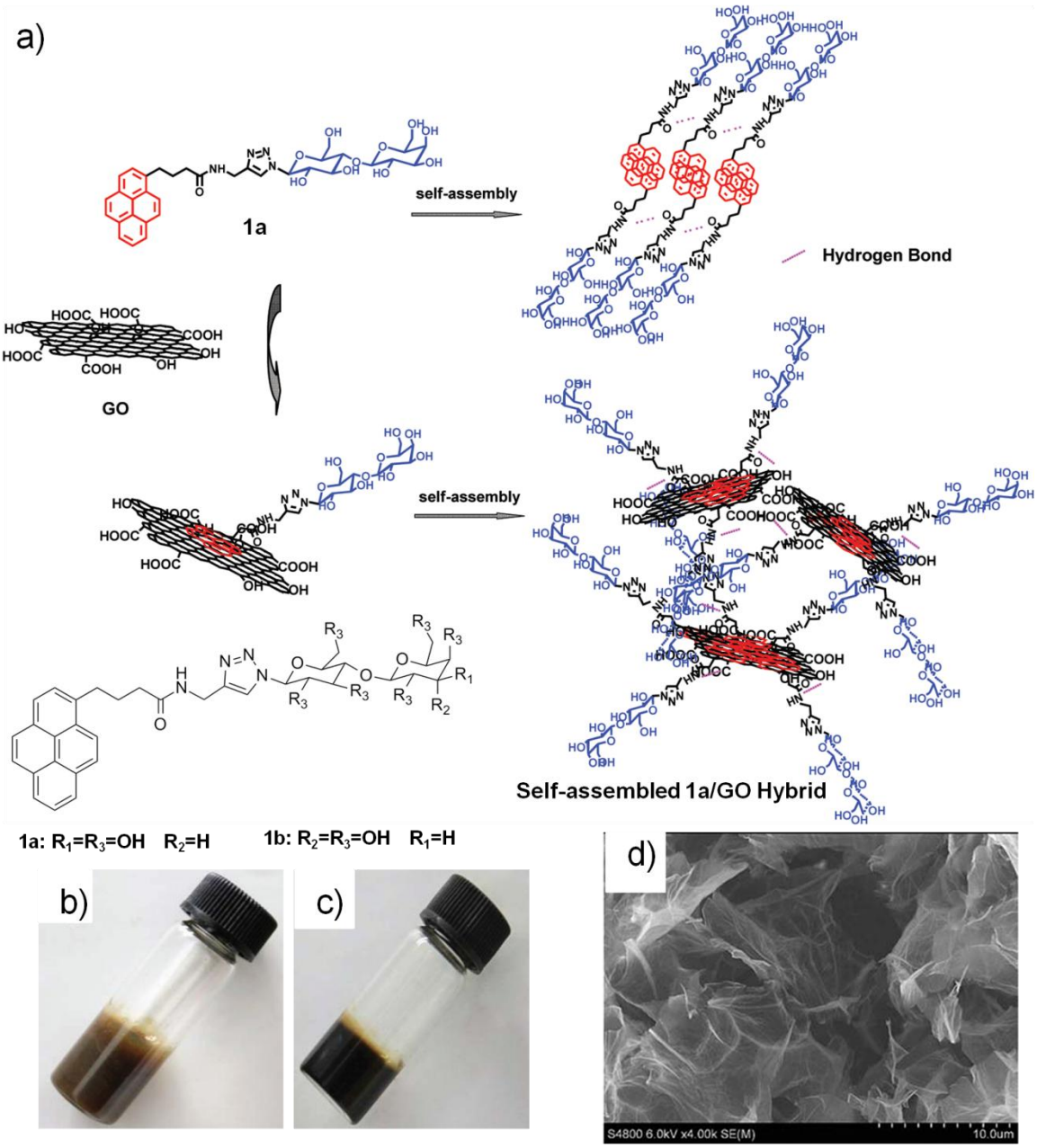

Figure 1.2. a) Schematic representation of self-assembled **1a/GO** hybrid formation. Photographs of b) hydrogel and c) organogel in DMF of **1a/GO** hybrid. d) SEM image of **1a/GO** hydrogel.

with ionic liquids (**IL**) can be used as a medium to make hybrids with **GO**. Since the ionic liquids have higher thermal stability and boiling points, they allow the thermal reduction of **GO** to **RGO**. Coskun *et al.* have reported a bi-functional strategy to

prepare hybrid gels based on ionic liquids through π-π and cation-π interactions (Figure 1.3a and 1.3b).[29] The resultant hybrid materials formed stable gels at room temperature (Figure 1.3c). The role of the pyrene moiety in the dispersion and gelation of **GO** in **ILs** has been investigated by comparing the ability of **2a** and **3a** to disperse **GO**. The **IL** without pyrene moiety exhibited no dispersion of **GO** even after a sonication for 2 h. The role of the counter ions in the formation and stability of hybrid gels also studied with two different ions such as PF_6^- and BF_4^-. Larger counter ions have lesser tendency to form hybrid gel because of weaker non-covalent interactions with thermally reduced **GO**.

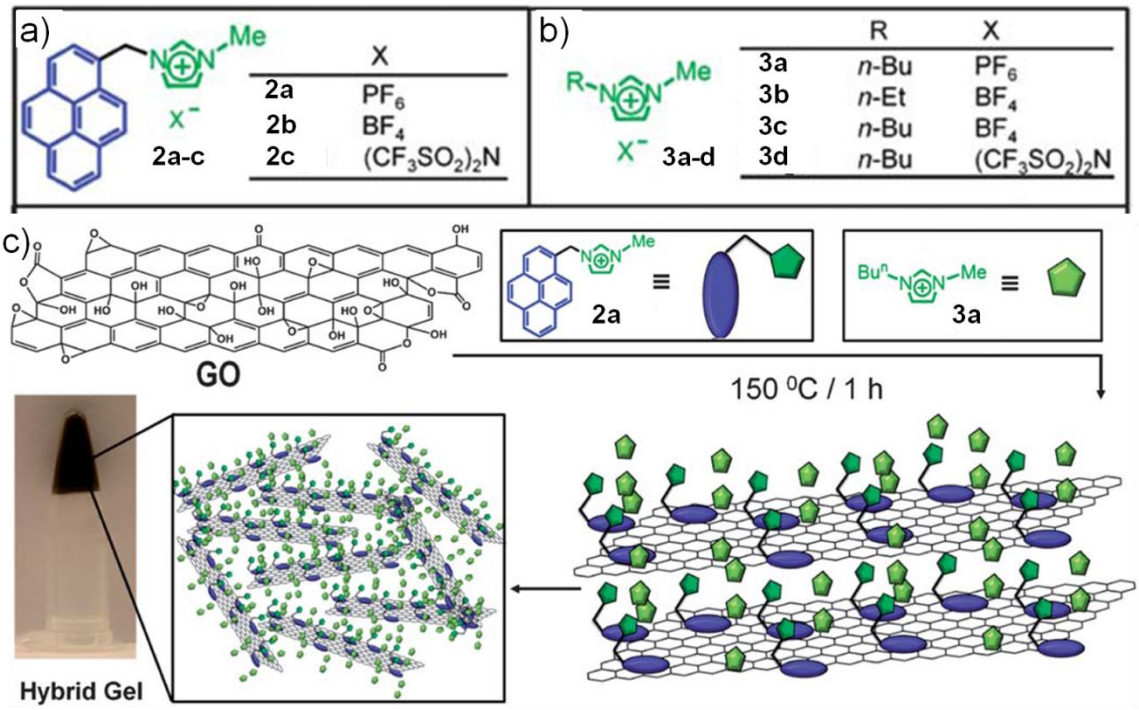

Figure 1.3. Chemical structures of a) bi-functional molecules (**2a-c**) and b) ionic liquids (**3a-d**). c) Schematic representation of hybrid gel formation from **2a**, **3a** and **GO** via thermal reduction process.

Molecular recognition has been widely used to prepare self-assembled hybrids of carbon nanomaterials through complementary host-guest interactions. Usually, the host molecules would be attached to the surface of the carbon materials by covalent or non-covalent functionalizations. The resultant hybrid materials with host molecules undergo self-assembly with appropriate guest molecules. Jiang *et al.* have reported a hybrid gel based on β-cyclodextrin (**β-CD**) functionalized **GO** (**4**/graphene hybrid) and a block copolymer of **AZO-PDMA-PNIPAM** (**5**) by using host-guest interaction (Figure 1.4a).[30] **PNIPAM** is well-known for its LCST (low critical solution temperature) property. It is soluble at room temperature (around 32 °C) due to H-bonding with water molecules, but at higher temperature, the H-bonding breaks, resulting in the phase separation from water. In this report, authors have shown that the copolymer **5** formed a gel at higher temperature with **4**/graphene hybrid. At higher temperature, sol-to-gel transformation occurred due to the cross-linked network structures resulted by the self-assembly of **PNIPAM**. On the other hand, the gel-to-sol transition occurred at 30-37 °C because of the change from cross-linked structure to collapsed state (Figure 1.4b). Rheological studies revealed the viscosity changes upon sol-gel transition and vice-versa. In addition, the hybrid hydrogel was found to be sensitive to photothermal effect.[31] The hybrid gel has been prepared by ɣ-irradiation aided polymerization of an aqueous solution of monomer and **GO**. A swelling and deswelling property of nanohybrid gel upon irradiation with NIR laser source was observed, which was attributed to the combined effect of LCST of **PNIPAM** and the

photothermal behavior of **GO**. The hybrid hydrogel has been used to regulate the liquid flow of micro-fluidic devices.

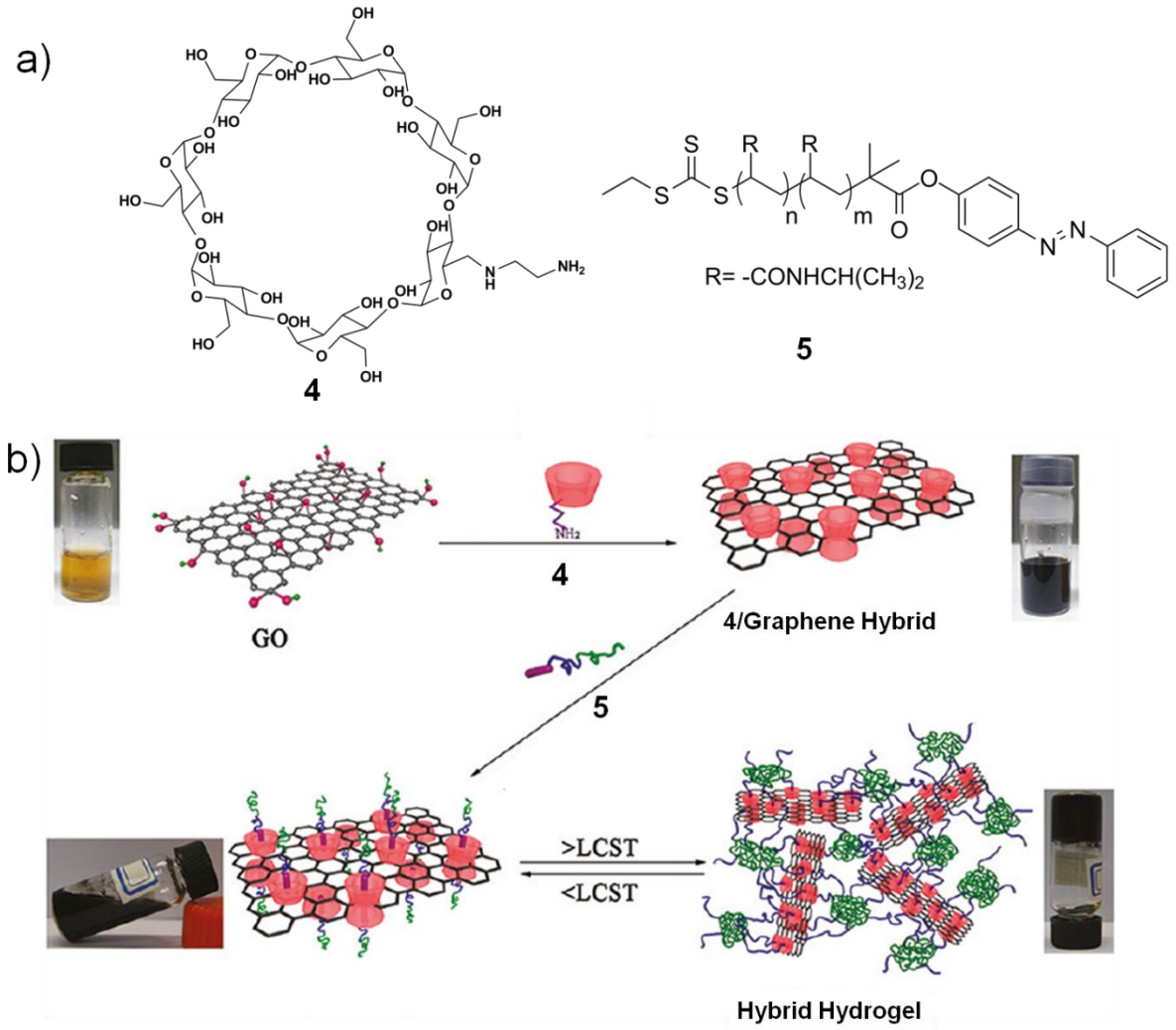

Figure 1.4. a) Chemical structures of an amino-functionalized β-cyclodextrin (**4**) and an azo-modified block copolymer (**5**). b) Schematic representation showing formation of hybrid hydrogel of **4**/graphene and **5**.

1.3.2. Hybrid Materials of Graphene and Graphene Derivatives with Aromatic Molecules

Small as well as large aromatic molecules have been used to functionalize graphene by using non-covalent interactions. Well-known aromatic molecules such as pyrene[32-34],

anthracene[35], porphyrin[36-38], perylene[39] and their derivatives have been exploited to prepare hybrid materials of graphene and reduced graphene oxide. Swastik *et al.* have reported the direct exfoliation of pristine graphene sheets from graphite using 1-pyrene carboxylic acid (**6**) in a mixture of methanol and water (Figure 1.5a).[32] The solvent mixture played a crucial role in the non-covalent interaction between pyrene moiety and graphene sheet. TEM and Raman analysis gave evidence for the presence of single, a few and multi-layered graphene sheets in the hybrid material. The functionalized graphene sheets were used as a chemical sensor as well as an ultracapacitor after depositing them on a nanoporous membrane. The chemical sensor exhibited more selectivity towards ethanol vapors when compared to water vapors, air, and carbon dioxide. On the other hand, a sheet-like aromatic amphiphile (**7**) consisting of planar pyrene units and hydrophilic dendron moiety, has been used for the selective dispersion of larger 2-D graphene sheets in water.[34] Lee *et al.* have reported that four pyrene moieties in **7** adopted a 2-D sheet-like arrangement on the surface of graphene to enhance the effective π-π interaction (Figure 1.5b). On the other hand, the oligoether moiety gave a hydrophilic environment around the hydrophobic π-surface of graphene to increase the dispersion of the latter in water. The amphiphile molecule showed an effective dispersion of graphene sheets (1.5 mg mL^{-1}) in water/methanol (7:3) mixture. In order to show the selectivity towards graphene, **7** was used to exfoliate **SWNTs**. The 2-D sheet-like conformation of amphiphile was not able to interact effectively with the curved surface of **SWNTs**. The interaction of **7** with exfoliated graphene sheets has been studied by UV-Vis absorption, and fluorescence spectroscopic

measurements. Results showed that the strong π-π interaction between **7** and graphene led to a strong hypochromic effect and fluorescence quenching. The extent of exfoliation of graphene sheets was monitored by Raman spectral and morphological studies. The presence of single and double-layered graphene sheets was confirmed by AFM and TEM measurements.

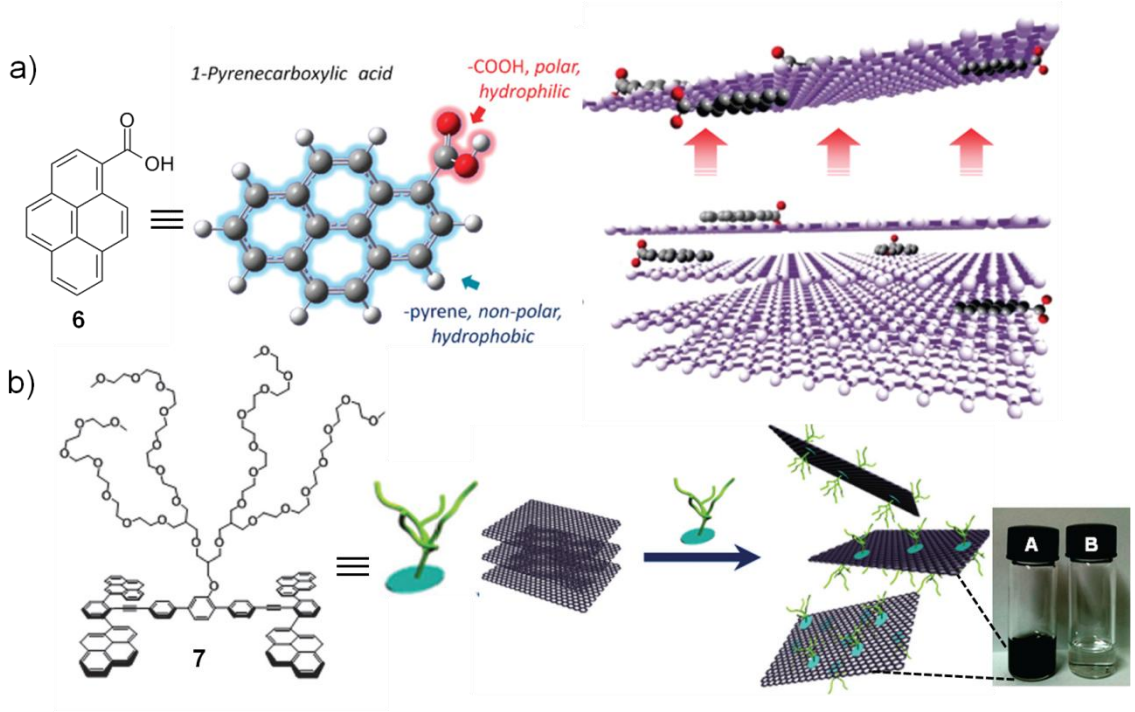

Figure 1.5. a) Chemical structure of 1-pyrene carboxylic acid (**6**) and the schematic representation of exfoliation of individual graphene sheets from bulk graphite by **6**. b) Chemical structure of pyrene amphiphile (**7**) and the schematic representation showing exfoliation of graphene sheets by **7** along with the photographs of **7**/graphene (**A**) and **7** alone (**B**) dispersions in water-methanol mixture (7:3).

Non-covalent functionalization of reduced graphene oxide with aromatic donor and acceptor molecules leads to novel hybrid materials with tunable electronic properties.[39] The sodium salt of 1-pyrene sulphonic acid (**8**, as a donor) and a disodium

salt of a bis-benzene sulphonic acid of perylene diimide (**9**, as an acceptor) were used to prepare water-soluble graphene hybrid materials (Figure 1.6a). While the aromatic molecules have strong π-π interaction with the graphene sheets, the negative charges of the molecules prevent aggregation leading to a stable dispersion of the hybrid material in the solution. The electrical conductivity of **9/RGO** was found to be 13.9 S cm^{-1}, whereas that of **8/RGO** had a value of 1.9 S cm^{-1}. The conductivity of hybrid materials was improved by thermal treatment at higher temperatures in the presence of argon and hydrogen environment. After the thermal treatment, hybrid materials with **9** and **8** exhibited the conductivity values of 1314, 1149 S cm^{-1}, whereas the pristine graphene exhibited a much lower value of 517 S cm^{-1} at similar conditions. The enhancement in the conductivity after thermal treatment is due to better graphitization and deoxygenation reaction on the basal plane of the reduced graphene oxide. These hybrid materials showed an improved power conversion efficiency in bulk heterojunction solar cells when they used as electrode materials. Rao *et al.* have reported a non-covalently functionalized graphene hybrid material with a tetra potassium salt of a coronene tetracarboxylic acid (**10**) (Figure 1.6b).[40] The charge-transfer and π-π interactions are responsible for the exfoliation of graphene sheets in solution state. The electrostatic repulsion among the negative charges of carboxylate ions of coronene derivative gives improved solution processing of reduced graphene oxide. Authors have used two different methods to prepare graphene hybrid materials, namely, thermal exfoliation of graphene oxide (**RGO-1**) and arc evaporation of graphite in the presence of hydrogen atmosphere (**RGO-2**). The molecule **10** showed

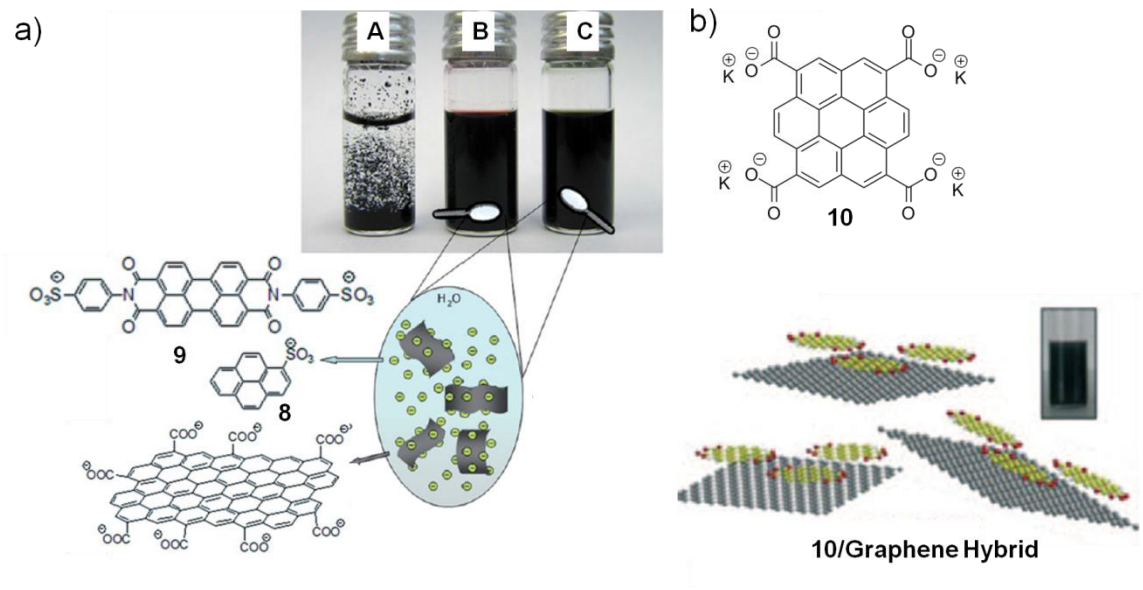

Figure 1.6. a) Chemical structures of pyrene and perylene derivatives (**8** and **9**) and a photograph of unfunctionalized **RGO** (**A**), **8/RGO** (**B**) and **9/RGO** (**C**) dispersions in water. b) Chemical structure of potassium salt of coronene tetracarboxylate (**10**) and schematic representation of individualized graphene sheets with **10.**

better interaction with **RGO-2**, resulting in more stable dispersion of graphene sheets. The amount of graphene exfoliated in water was measured as 0.15 mg mL^{-1}. The presence of single and a few-layered graphene sheets in aqueous dispersion was monitored by Raman spectral and morphological analyses.

Larger π-conjugated molecules such as porphyrin[36-37] and phthalocyanine[38] have also been used to prepare graphene-based hybrid materials. A tetra sodium salt of porphyrin tetrasulphonic acid (**11a**) and tetra(*p*-phenylsulphonate) salt of tetrakis(4-trimethylaminophenyl) porphyrin (**11b**) are also known to interact to form hybrid materials with **RGO** in water (Figure 1.7a).[37] While **11a** undergoes self-assembly on the surface of graphene through π-π interaction, the electrostatic repulsion between the

negative charges of **11a** resulted in a stable aqueous solution. Morphological studies proved the presence of single layer graphene and self-assembled **11a** molecules over the π-surface of graphene. The electrical resistance of the thin film was 5 K Ω m^{-1} with 80% of transparency. The observed low resistance was due to the improved π-conjugation achieved by chemical reduction upon hybrid preparation. Shi *et al.* have prepared a hybrid of cationic porphyrin (**12**) and negatively charged **RGO** in water.[36] The positively charged porphyrin self-assembled on the negatively charged graphene sheets via strong electrostatic attraction and π-π interaction. The non-covalent interactions leads to the flattening of porphyrin molecule by rotating the four perpendicular methyl pyridinium groups to the plane of porphyrin, which resulted in enhanced π-conjugation and electron withdrawing effect. This flattening effect has been used to detect Cd^{2+} ions selectively with rapid and sensitive responses. Phthalocyanines which are π-conjugated macrocyclic compounds and also structurally related to porphyrins have been used to prepare hybrid materials with graphene.[38] A hybrid material composed of graphene produced by direct-current arc discharge method and a tetrasodium salt of copper (II) phthalocynine-tetrasulphonic acid (**13**) has been prepared by simple sonication method in water (Figure 1.7b). In this hybrid material, graphene acts as a photosensitizer as well as a photothermal therapeutic (PTT) agent and the phthalocyanine derivative serves as a photodynamic therapeutic (PDT) agent. The hybrid material exhibited an excellent anti-cancer efficacy through the combined effect of PTT and PDT.

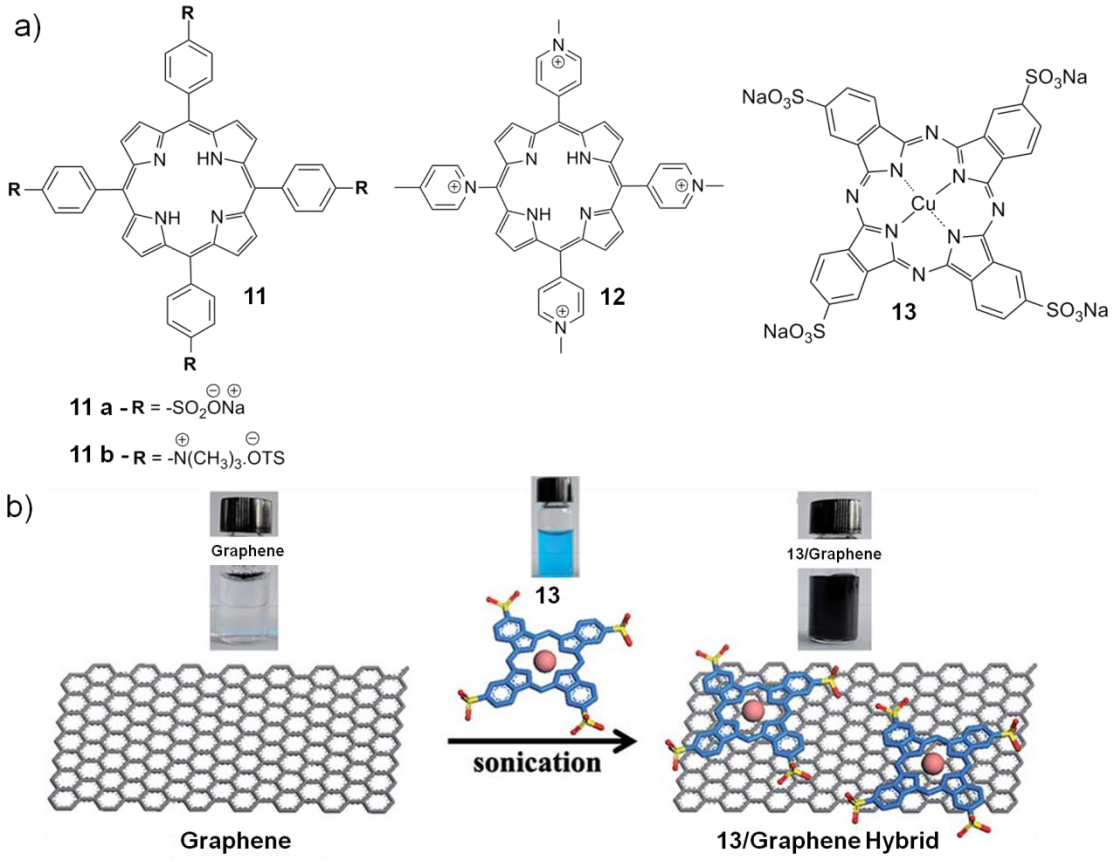

Figure 1.7. a) Chemical structures of porphyrin (**11** and **12**) and phthalocyanine (**13**) derivatives. b) Schematic representation showing preparation of **13**/graphene hybrid and photographs of graphene, **13** and **13**/graphene hybrid dispersion in water.

1.3.3. Hybrid Materials of Graphene and Graphene Derivatives with π-Conjugated Polymers

Like small aromatic molecules, π-conjugated polymers are also known to interact with graphene through non-covalent interactions. Hybrid materials of **RGO** and π-conjugated polymers such as poly(*p*-phenylenevinylene),[41] poly(*p*-phenylene-ethynylene),[42] polyaniline,[43-44] polypyrrole,[45-46] have been found applications in various optoelectronic devices such as field-effect transistors, sensors and so on.

Bardeen *et al.* have reported a hybrid material of chemically reduced graphene oxide and poly[2-methoxy-5-(2′-ethylhexyloxy)-1,4-phenylenevinylene] (**14**) and studied the time-resolved fluorescence dynamics (Figure 1.8a).[41] The fluorescence decay of **14** was monitored with various weight percentage of **RGO**. At 0% of **RGO** content, **14** showed a fluorescence lifetime of 200 ps and it decreased to 20 ps in the presence of 50% of **RGO** content. The fluorescence quenching of **14** in the presence of **RGO** followed energy transfer mechanism from polymer to graphene in the film state. Poly(*p*-phenyleneethynylene) based conjugated polyelectrolyte (**15**) was used to prepare a hybrid material with graphene (Figure 1.8b). The electrical conductivity of **15**/graphene hybrid material exhibited a low resistance of 30 K Ω m^{-1}.

Hybrid materials based on conductive polymers such as polyaniline (**PANI**), polypyrrole and polythiophene have also been reported. Wang *et al.* have prepared polyaniline (**16**)/**GO** hybrid by mild oxidation of aniline with a mixture of H_2O_2 (30%), hydrochloric acid (37%), and 0.1 mol L^{-1} $FeCl_3 \cdot 6H_2O$ in the presence of various amounts of **GO** (Figure 1.8c).[47] It has been shown that the charge storage capacity of **16** increased considerably with a minimum weight percentage of **GO**. The hybrid material showed a 50% increase in the value of capacitance than that of bare **16.** Wu *et al.* have also reported a hybrid material of **RGO**, and **16** by in-situ polymerization of aniline in the presence of **GO** followed by a reduction using hydrazine hydrate.[44] The reduced **16** during the hydrazine reduction was again reoxidized and reprotonated to get the **16/RGO** hybrid material. Morphological studies showed that the nanofibrous structures of **16** were formed on the surface of graphene

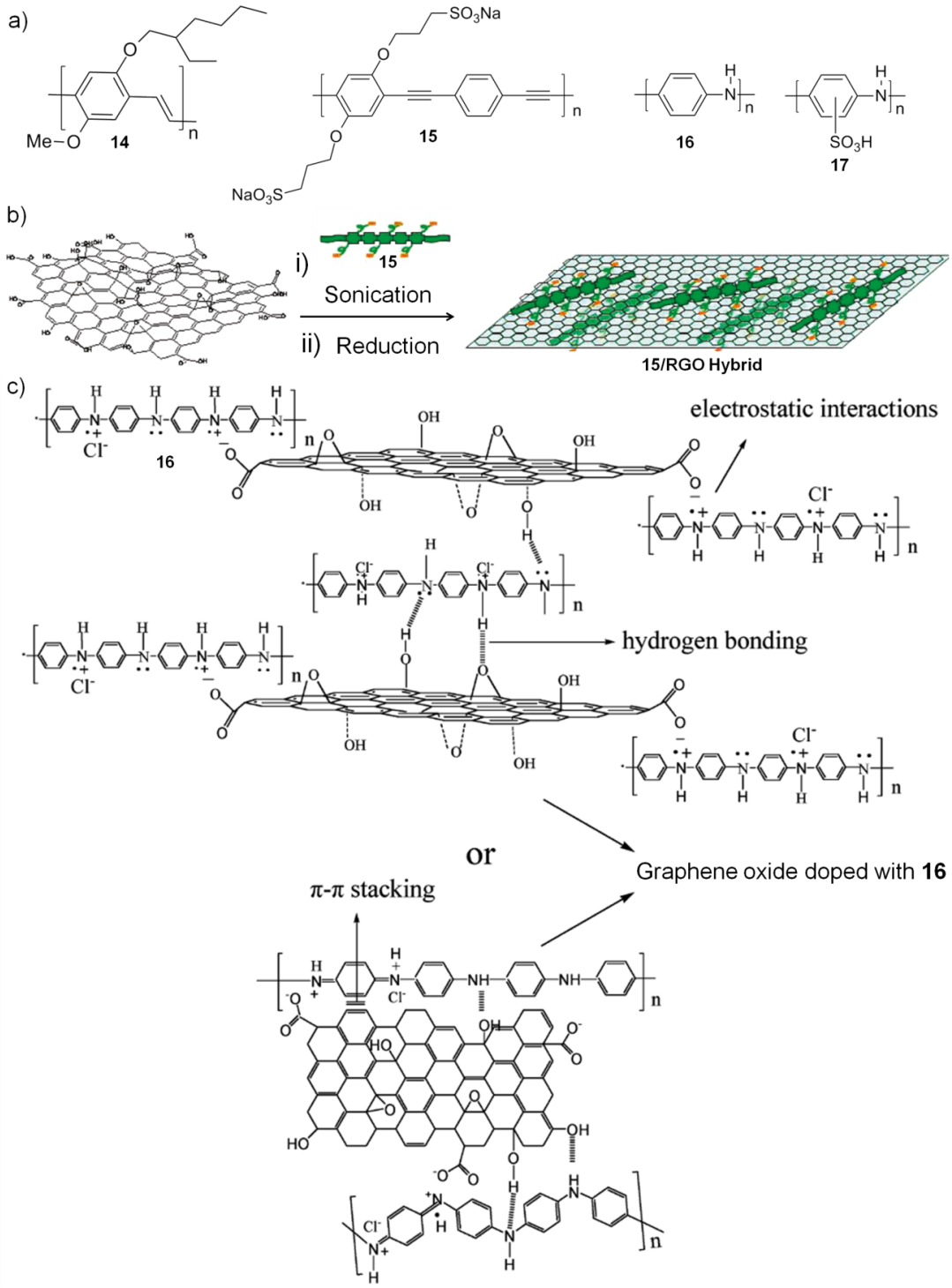

Figure 1.8. a) Chemical structures of **PPV** (**14**), **PPE** (**15**), **PANI** (**16**) and sulphonated **PANI** (**17**) polymers. b) Schematic representation of the preparation of **15/RGO** hybrid. c) Proposed various non-covalent interactions in **16/GO** hybrid.

sheets through non-covalent interactions. **RGO/16** exhibited higher conductivity as well as higher charge storage capacity when compared to that of **16**. A water soluble sulphonated polyaniline (**SPANI**) (**17**) was also employed to prepare an electroactive hybrid material of **RGO** (Figure 1.8a). The hybrid material was highly soluble in water (> 1 mg mL^{-1}) and exhibited better conductivity in the film state. The ability of hybrid in electrocatalysis was monitored by cyclic voltammetry. The hybrid material exhibited two peaks in cyclic voltammogram that correspond to two different doping states of **17** in hybrid material.[43] The water resistance stability of **17** in the hybrid was improved in acidic and neutral media when compared to that of bare **17** due to a strong π-π interaction between the polymer backbone and graphene π-surface.

Hybrid materials of polypyrrole and **GO** have been prepared by polymerization of pyrrole monomer in the presence of multi-layered graphite oxide which is an oxidized form of bulk graphite.[45-46] Polypyrrole/**GO** nanohybrid was prepared by in-situ emulsion polymerization of pyrrole in the presence of cetyltrimethylammonium bromide (**CTAB**) as an emulsifier (Figure 1.9).[46] The added **CTAB** molecules involved in micelle formation on the surface of **GO**. When the pyrrole was added to the emulsion, all pyrrole molecules entered into **CTAB** as well as **CTAB-GO** micelles and started to polymerize. After polymerization, the self-assembly of polypyrrole on the surface of the unoxidized domain of **GO** via π-π interaction led to the delamination of multi-layered graphite oxide into individual sheets in water. The electrical conductivity of polypyrrole/**GO** hybrid material was measured as 5 S cm^{-1}, whereas

bare polypyrrole and **GO** exhibited low conductivity values such as 0.9 and 1×10^{-6} S cm^{-1}, respectively.

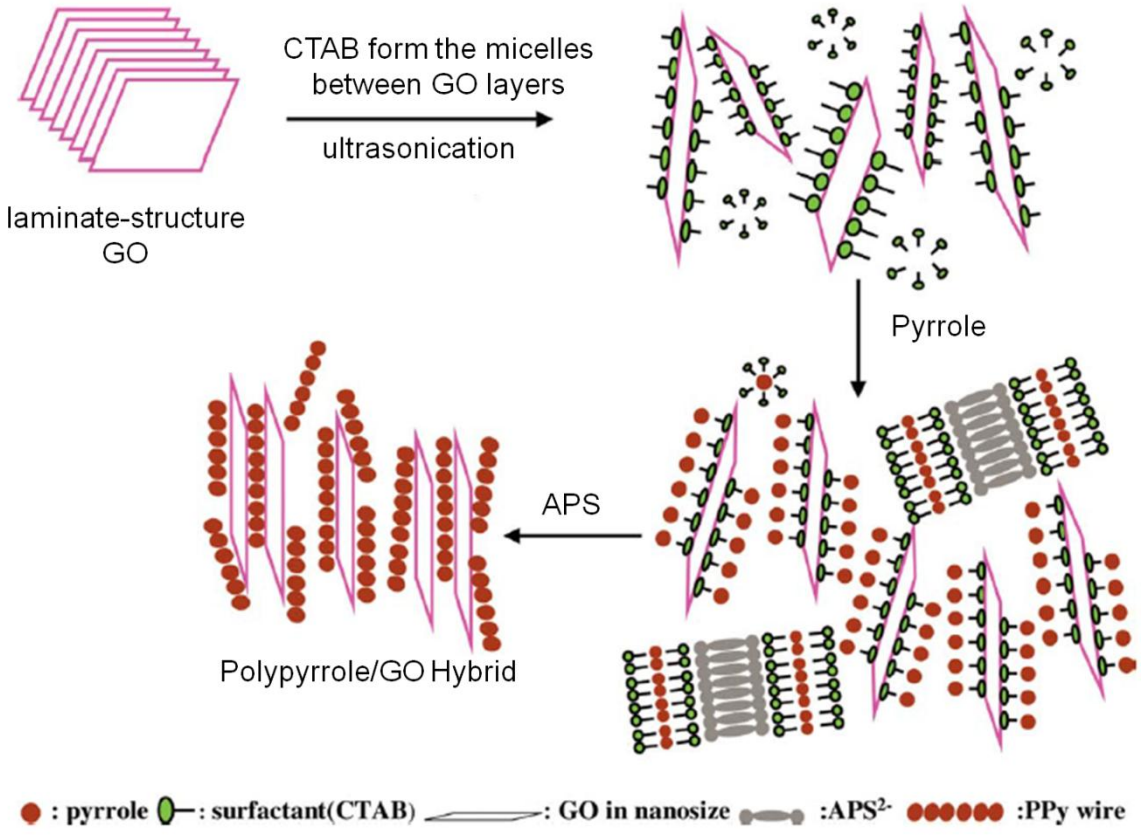

Figure 1.9. Preparation of polypyrrole/**GO** hybrid via in-situ emulsion polymerization.

In order to exploit the excellent electronic properties of graphene in bulk-heterojunction organic solar cells as an acceptor material, a few graphene hybrid materials have been prepared with well-known polymers being used in organic solar cells such as poly(3-hexylthiophene) (**P3HT**)[48-52] and poly(3,4-ethylenedioxy-thiophene) (**PEDOT**).[50-51] A hybrid material composed of **P3HT** polymer and functionalized graphene in various weight percentages (0-15%) has been reported for solar cell application.[49] A photovoltaic device fabricated with the hybrid material

exhibited a power conversion efficiency of 1.1% with an open circuit voltage of 0.72 V. In another report, Zhai *et al.* showed the supramolecular architectures of **P3HT** polymer created on the surface of exfoliated **RGO** (Figure 1.10a).[52] A mixture of anisole and *N*, *N*-dimethylformamide was used to prepare the nanofibers of **P3HT** (**18**) on the π-surface of graphene through induced crystallization by **RGO**. AFM and SEM studies proved the growth of nanofibers on the basal plane of graphene sheet, which led to the interconnection of individual graphene layers. Hybrid materials composed of **RGO** and **PEDOT** (**19**) were also prepared and used as a transparent electrode material for optoelectronic devices (Figure 1.10b).[50] The hybrid was highly transparent, conductive, thermally stable and flexible. A film of hybrid in ten-nanometer thickness exhibited an electrical conductivity of 0.2 S cm^{-1} and 88% of transmittance of light in the wavelength region of 400-1800 nm. At the same time, Seo *et al.* have also prepared a hybrid material of **RGO** with **19** as double layered graphene/**19** and triple layered graphene/**19**/graphene films with higher electrical conductivity.[51] The double and triple-layered films with the thickness of about 32 nm exhibited conductivity values of 13 and 12 S cm^{-1}, respectively. The freestanding films made up of the hybrid materials showed a transparency of 91% and 6 fold enhancements in their mechanical strength when compared to that of pristine films. The highly conductive, transparent, and freestanding films with higher mechanical strength are expected to have potential application in the area of optoelectronics, field-effect transistors, and sensors.

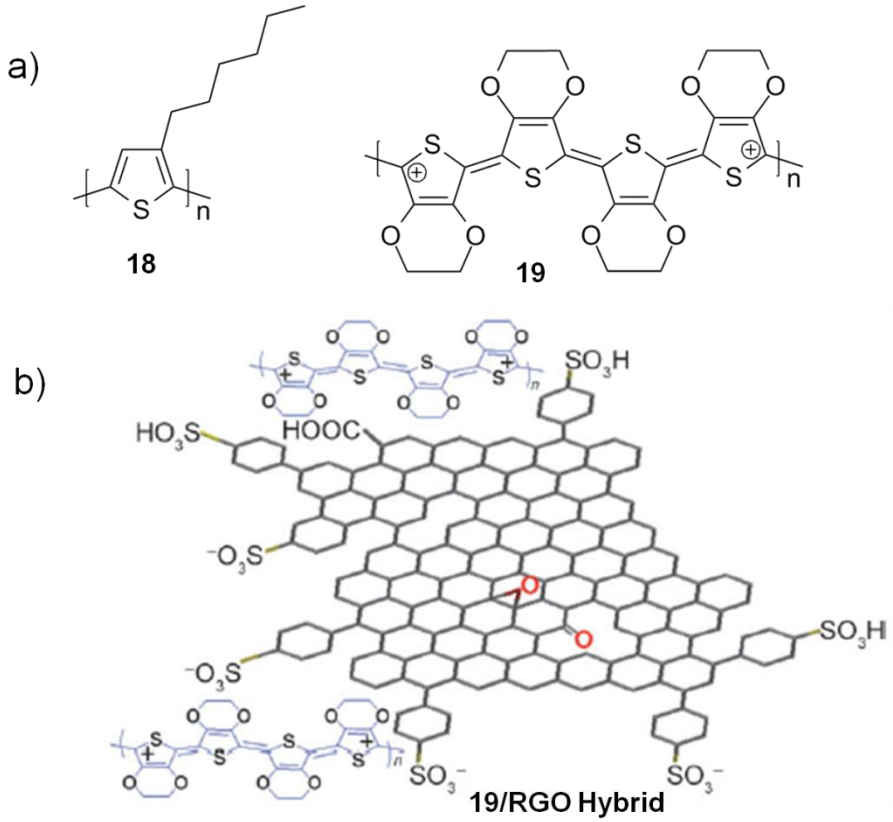

Figure 1.10. a) Chemical structures of **P3HT** (**18**) and **PEDOT** (**19**) polymers. b) Schematic representation of part of the structure of **19/RGO** hybrid.

1.4. Carbon Nanotubes Based Hybrid Materials

Carbon nanotubes (**CNTs**) are an allotrope of carbon having a one-dimensional tubular structure in nanometer size. There are many kinds of **CNTs** that include single-walled, double-walled, and multi-walled carbon nanotubes. The electrical conductivity of **CNTs** varies from metallic to semiconducting, based on the diameter and rolling angle, which also impart chirality to the tubes. **CNTs** have excellent chemical, mechanical, and electronic properties that make them an important nanomaterial for various applications. Non-covalent functionalization of carbon nanotubes (**CNTs**) with aromatic molecules and π-conjugated polymers has been investigated by several

research groups.[14,53-58] The surface modification of **CNTs** through non-covalent interactions improves their dispersion and solution processability, which make them suitable for device applications.

1.4.1. Hybrid Materials of Carbon Nanotubes and Supramolecular Gels

Solution processability of **CNTs** can be enhanced by incorporating them into supramolecular gel matrix by using various non-covalent interactions between **CNTs** and gelator molecules. Zhao *et al*. have reported the preparation of hybrid gel composed of a tetrathiafulvalene vinyl (**TTFV**)-phenylacetylene polymer, **20** and a larger diameter **HiPco-SWNTs** in toluene (Figure 1.11a and 1.11b).[59] When the concentration of **20** and **SWNT** exceeds certain level, sol-to-gel transformation was observed after ultrasonication for 30 min resulting in a coarse interconnected micro-fibrous structure (Figure 1.11c). Since the **TTF** moiety is known to show stimuli responsive behavior, a wrapping and unwrapping of **20** over the **SWNT** surface were demonstrated by external stimuli (Figure 1.11d). The process of gelation did not happen with **CoMoCAT-SWNT** because of the inability of **20** to render sufficient aggregation by adhering on the surface of smaller diameter **SWNTs**. The selective interaction of **20** with **SWNTs** was made use of enriching **SWNTs** with a particular chirality from the mixture of **SWNTs** with various chiralities. Ajayaghosh *et al*. have reported a stable hybrid π-gels of oligo(*p*-phenylenevinylene) (**OPV**) based gelators (**21a-c**) with **SWNT/MWNTs** in toluene (1.12a).[60] **21a** did not form gel at a lower concentration (1×10^{-4} M) in toluene, whereas an addition of small amount of **SWNT**/

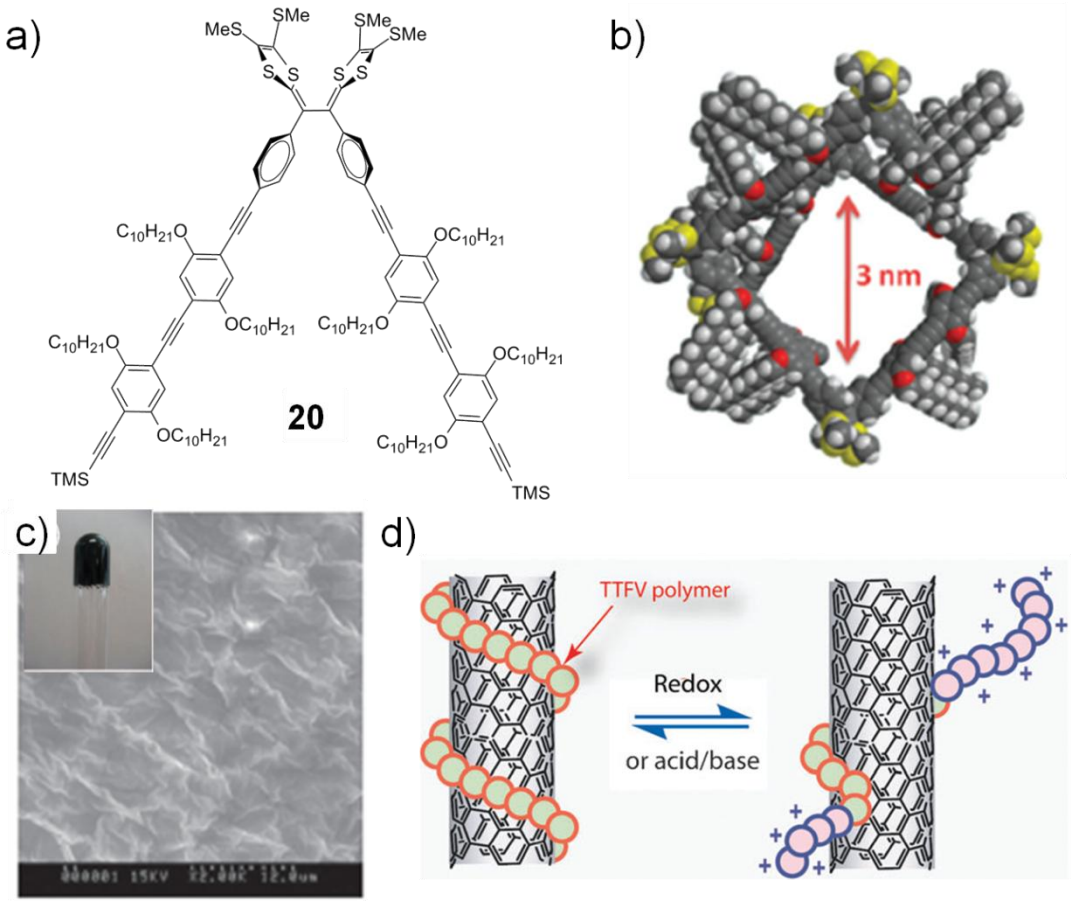

Figure 1.11. a) Chemical structure of **TTFV**-phenylaceylene polymer (**20**). b) Space-filling model of self-assembled hexamer of **20.** c) SEM image of **20/SWNT** hybrid gel (inset shows the inverted glass vial contained hybrid gel). d) Simuli-responsive wrapping and unwrapping of **20** over **SWNT** surface.

MWNT led to stable gel. The stability of the hybrid gels increased with the increasing amount of **SWNT/MWNT** which was confirmed by the gel melting temperature (T_{gel}) and rheological studies. In these hybrid gels, **OPV** helps to debundle the nanotubes in organic solvent by interacting with the π-surface. On the other hand, debundled **SWNT/MWNTs** are arranged in specific manner thereby reinforcing the supramolecular fibrous structures (Figure 1.12b and 1.12c). The hybrid gels that are made up of liner π-conjugated molecules and **CNTs** have potential application in light

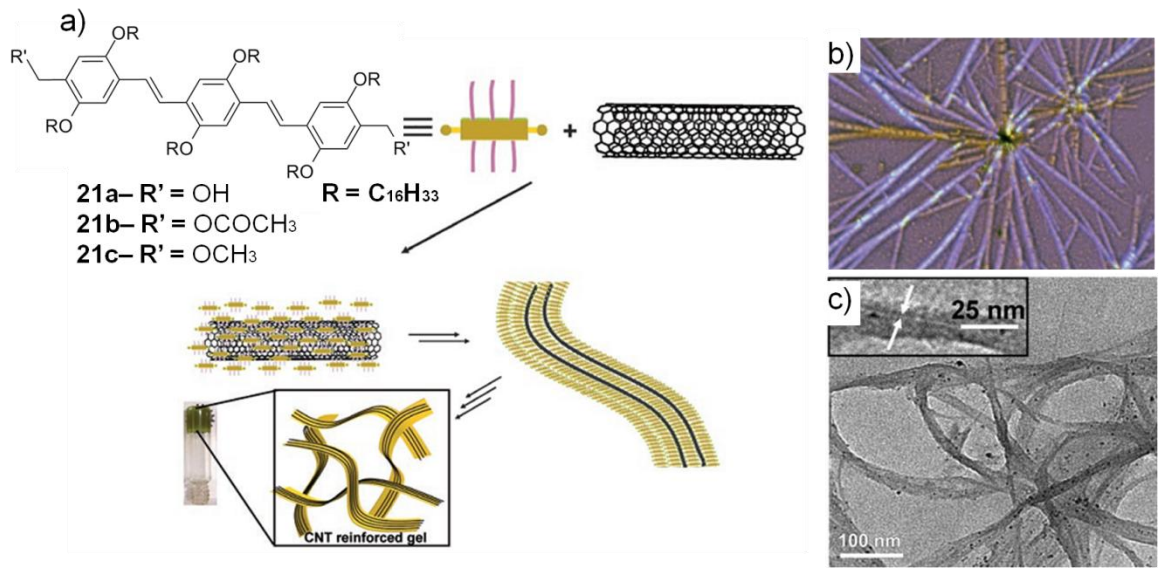

Figure 1.12. a) Chemical structures of **OPV** based π-gelators (**21a-c**) and schematic representation of **OPV/CNT** hybrid gel formation. b) OPM and c) TEM images of **21a/SWNT** hybrid (Inset of Figure 1.12c shows the presence of individualized **SWNT** in gel fiber).

harvesting and optoelectronics. In addition to π-conjugated molecules, the aromatic base pairs of the **DNA** molecules are also known to interact with **CNTs**. Liu *et al.* have reported the pH responsive and strength tunable **DNA-SWNT** hybrid hydrogel composed of linear twelve base-pair long double stranded **DNA** (duplex) and **SWNTs** (Figure 1.13a). The duplex possessed a sticky domain of eleven base long single strands with two stretches of cytosine moieties. The structure of the linear and cross-linking units are shown in Figure 1.13a as **22** and **23**, respectively.[61] When the pH of solution decreased below 6.3, **DNA-SWNT** hybrid hydrogel was formed by cross-linking of a linear **DNA** assembly structures with **SWNT** (Figure 1.13b). The formation of hydrogel is mainly due to the C---CH^+ base pair interaction between protonated and unprotonated cytosine moieties. At pH 8, the **DNA-SWNT** hybrid

hydrogel was not observed because of reduced intermolecular structure formation, confirmed by CD spectroscopy. This kind of hybrid gels would find application in bio-molecular sensing, tissue engineering, etc.

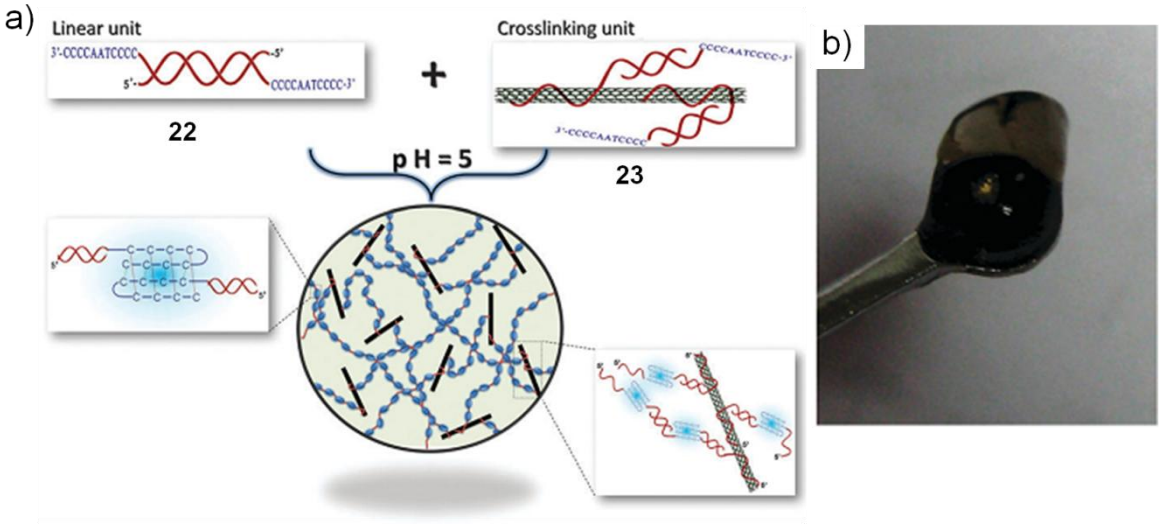

Figure 1.13. a) Schematic representation of the formation and b) a photograph of hydrogel of **DNA/SWNT** hybrid at pH 5.

Host-guest complementary interactions based on molecular recognition also have been used to prepare functional hybrid gels with **CNTs**. Harada *et al.* have successfully utilized host-guest interactions between polymers having host molecules and **Py-β-CD/SWNT** hybrid having guest molecules to form hybrid hydrogel (Figure 1.14). β-Cyclodextrin modified with pyrene moiety (**24**) has been used to disperse **SWNT** homogeneously in 1M NaOH solution. The solution of hybrid of non-covalently functionalized **SWNT** with **24** was stable for a month. The solubilization of **SWNT** and π-π interaction with pyrene moieties were confirmed by UV-Vis-NIR and fluorescence spectroscopic techniques. Poly(acrylic acid) functionalized with 2 mol %

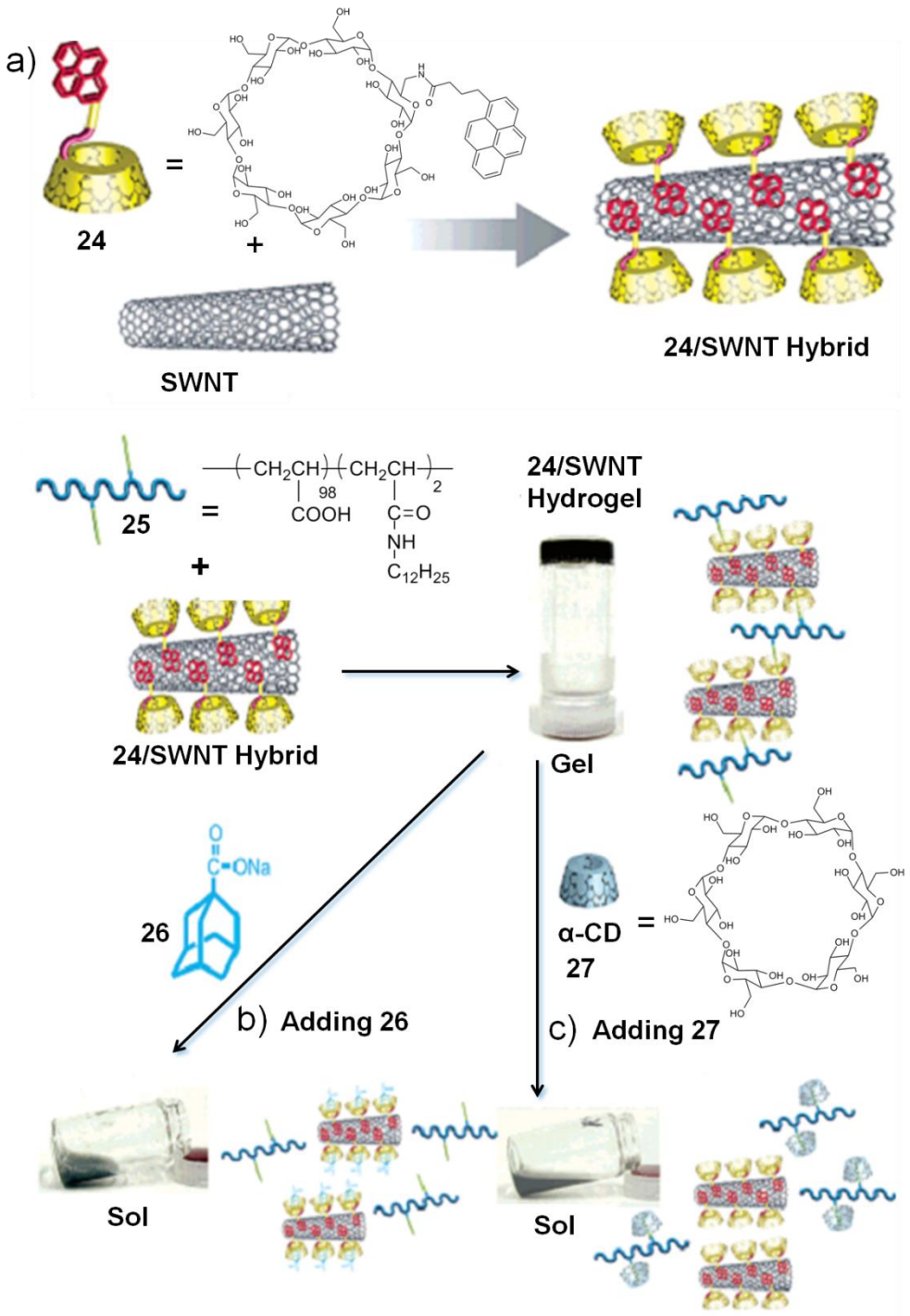

Figure 1.14. a) Schematic representation showing the formation of reversible **24/SWNT** hybrid gel. Sol-to-gel transitions while adding b) a competitive guest **26** and c) a competitive host **27**.

of dodecyl groups (**25**) was used to form a host-guest complex with a pyrene linked **β-CD** which was immobilized on **SWNT**, leading to hybrid hydrogel (Figure 1.14a). The ability of **24/SWNT** hybrid to form a hydrogel was confirmed by mixing all the components (**25** alone, a mixture of **24** and **25**, and a mixture of **SWNT** and **25**) in several possible ways in various concentrations. The chemical responsiveness of the hybrid hydrogel was studied by adding competitive guest (sodium adamantyl carboxylate, **26**) and host (α-cyclodextrin, **27**) molecules. A sol-to-gel transformation occurred after adding **26** in hybrid hydrogel since it has more affinity towards **β-CD** moieties (Figure 1.14b). Similarly, addition of **27** to hybrid hydrogel led to sol-to-gel transformation as dodecyl groups has more affinity towards **α-CD** than **β-CD** moieties (Figure 1.14c). The same research group has reported the preparation of photo-responsive supramolecular hybrid hydrogel based on α-cyclodextrin-curdlan/**SWNT** (**28/SWNT**) and azobenzene-modified poly(acrylic acid) (**29**) by utilizing host-guest interaction between α-cyclodextrin and azobenzene moiety (Figure 1.15).[62] The presence of 4 wt% of **28/SWNT** hybrid and 8.6 wt% of **29** was the minimum amount required to form the hybrid hydrogel (Figure 1.15c). The role of host-guest interaction in the formation of gel was explained by performing control experiments of mixing all components in various combinations. These mixtures did not form hybrid hydrogel due to the absence of cross-linking in multiple points to form supramolecular network structures. The effect of competitive compounds such as bare **α-CD** (**30**), sodium 1, 12-decanedicarboxylate (**31**) and tetraethylene glycol (**32**) on the stability of supramolecular hydrogel was studied by adding them in various amounts to the hybrid

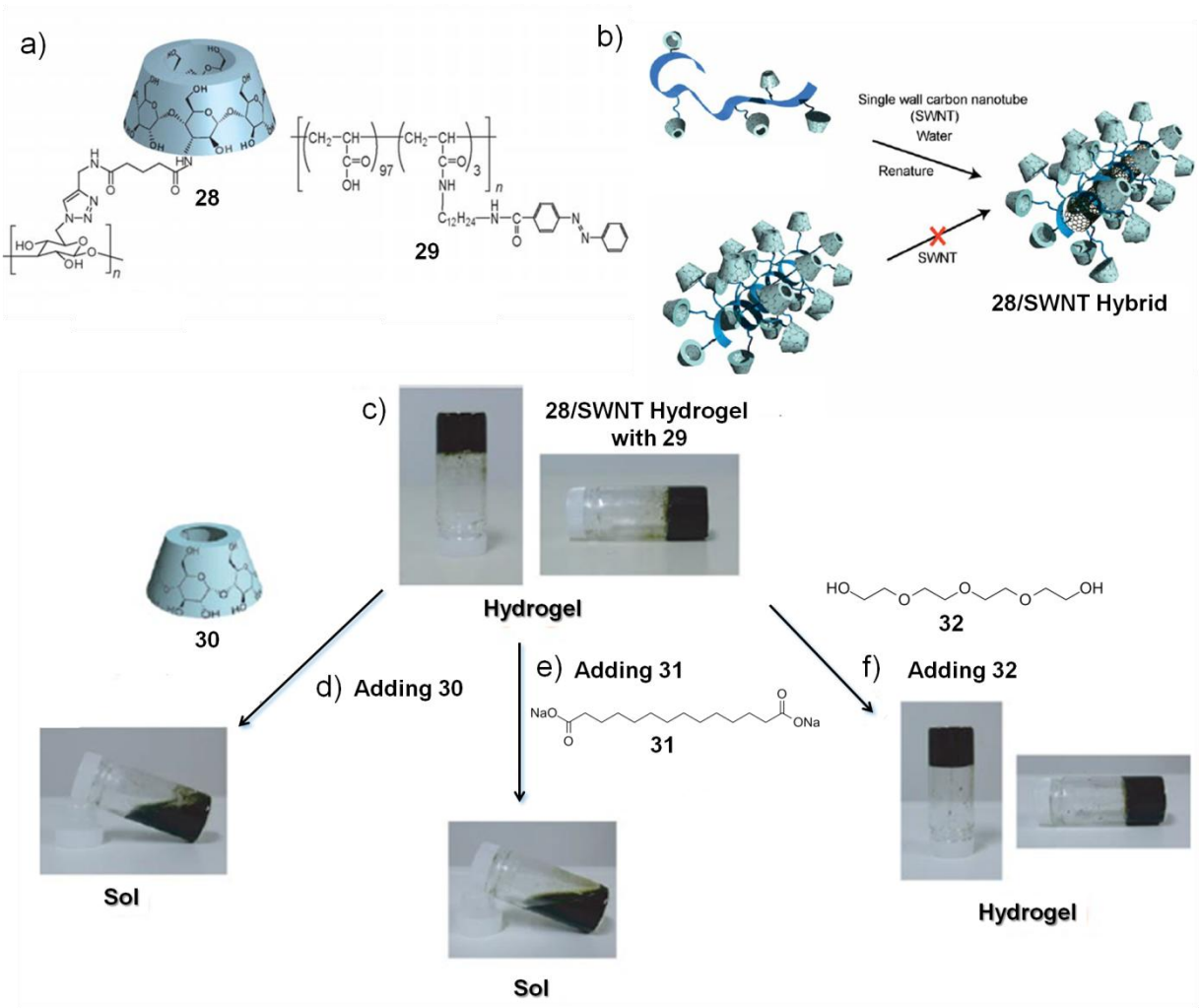

Figure 1.15. a) Chemical structures of α-cyclodextrin-modified curdlan and azobenzene-modified poly-(acrylic acid). b) Schematic representation showing the formation of **28/SWNT** hybrid. c) Photographs of hybrid hydrogel with azo-containing polymer **29**. Sol-to-gel transitions occurred while adding d) a competitive host **30** and e) competitive guest **31.** f) No sol-to-gel transition took place upon addition of **32**.

hydrogel. Addition of four equivalents of **30** to the hybrid hydrogel led to the gel-to-sol transformation by suppressing the complex formation between **α-CD** moiety of **28/SWNT** hybrid and azobenzene moiety of **29** (Figure 1.15d). A similar behavior was observed on addition of **31** into the hybrid hydrogel because of higher association

constant of the dodecyl group with **α-CD** moiety when compared to the azobenzene group (Figure 1.15e). The gel-to-sol transition was observed due to breakage of cross-links responsible for the formation of supramolecular network structures. Addition of **32** into the hybrid hydrogel did not cause a gel-to-sol transition because of the low association constant of **32** with **α-CD** of **28/SWNT** when compared to the azobenzene moieties of **29** (Figure 1.15f). The photo-responsive nature of the supramolecular hydrogel was examined by irradiating with UV as well as visible light. UV irradiation led to *trans* to *cis*-isomerization of the azobenzene moiety of **29**. Since the *cis*-isomer had less association constant with **α-CD** when compared to that of the *trans*-isomer, gel-to-sol phase transformation occurred. This phase transformation was reversed by irradiating the sol with visible light.

Water soluble bile acids which are able to form micelles have been used to make hybrid gels with **CNTs** through self-assembly process. Tan *et al.* have reported the preparation of supramolecular hybrid hydrogel composed of sodium deoxycholate (**33**) and **SWNT** (Figure 1.16a).[63] The compound **33** is known to form primary micelles with the size of 1 nm at the critical micelle concentration (CMC) of 0.05% as well as secondary micelles consisting of large rod-like self-assemblies at CMC of 0.1%, which adsorb on the surface of **SWNT** by hydrophobic interaction. A supramolecular hybrid hydrogel was prepared by the formation of complex supramolecular nanostructures initiated by **SWNT** as shown in Figure 1.16b and 1.16c. A portion of **33** from the excess amount was utilized to disperse the **SWNTs** and the remaining amount that was higher than CMC (0.05-0.1%) was involved in the

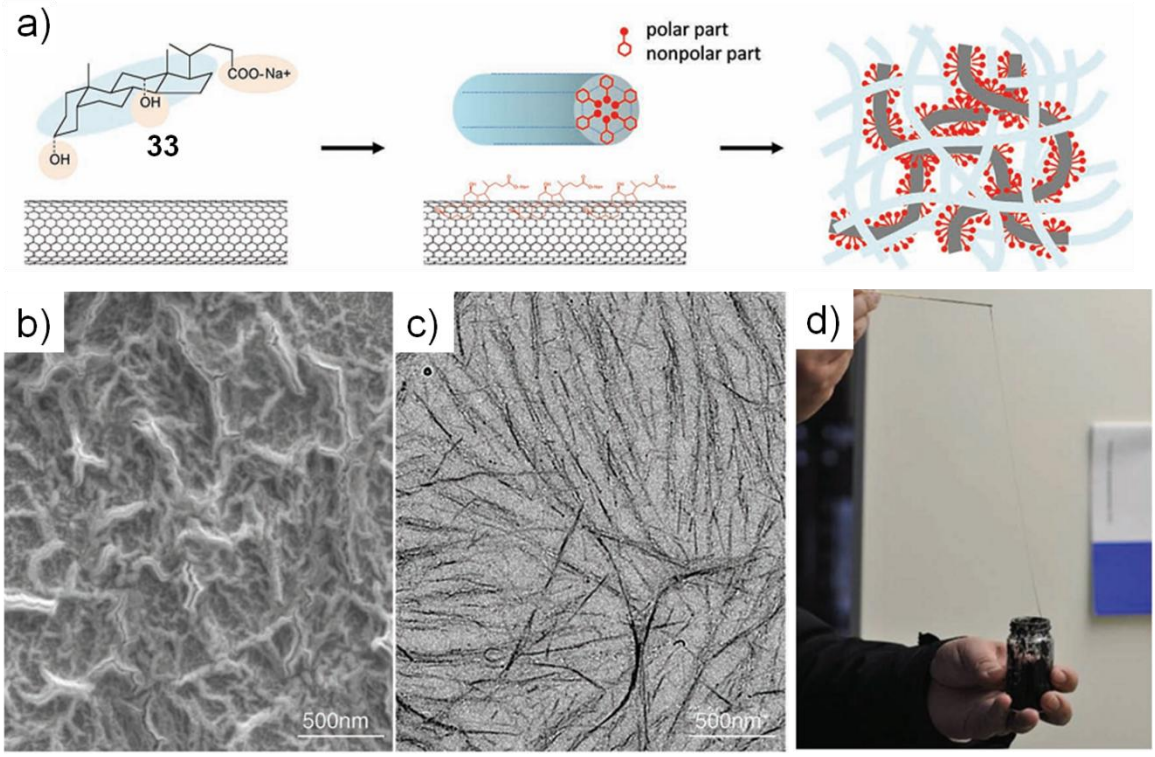

Figure 1.16. a) Schematic representation of **33/SWNT** hydrogel formation. b) SEM and c) TEM images of hybrid hydrogel of **33/SWNT**. d) A photograph showing the ability of supramolecular hydrogel of **33/SWNT** to extrude as a thread.

formation of fibrous aggregates in water. The supramolecular hydrogel showed improved mechanical strength and rheological properties. The shear modulus of hybrid hydrogel having 3% of **SWNT** showed 20 fold enhancement than that of 2% of **SWNT**. By using the supramolecular hydrogels as 'solid ink', nano patterns were made on various substrates involving solvent exchange methods and the resulting nano patterns showed excellent conducting properties. Because of higher mechanical strength and viscosity of hybrid gel, it was used to extrude thin filaments (Figure 1.16d) and they were used in stretchable and flexible electronics devices.

1.4.2. Hybrid Materials of CNTs with Aromatic Molecules

Self-assembled hybrid materials consisting of aromatic molecules and **CNTs** have been well studied in the literature. Mostly, well-known aromatic molecules such as naphthalene, anthracene, pyrene, perylene, etc. are used to prepare hybrid materials of **CNTs**.[14,64-67] Liu *et al*. have reported supramolecular **SWNT** hybrids composed of ruthenium complex tethered to β-cyclodextrin (**34**) and adamantane functionalized with pyrene (**35**) (Figure 1.17).[68] The hybrid was prepared by mixing the three components (**34, 35** and **SWNT**) in the solid state. The finely ground solid was dispersed in 0.01 M NaOH by sonication and the interaction among the components was studied by various analytical techniques. An appearance of van Hove singularities in the Vis-NIR absorption spectra indicates the dispersion of **SWNTs** in water by π-π interaction between pyrene and **SWNT** with a decrease in the fluorescence intensity of the former. Additionally, the decrease in the fluorescence intensity of the ruthenium complex explained the formation of inclusion complex between adamantyl group of **35** and **β-CD** of **34**, which was absent without **35**. Since the ruthenium complex was in close proximity to **SWNT** and pyrene after the formation of the inclusion complex, the resulted photo-induced charge transfer process could be a reason for the quenching of fluorescence intensity of the ruthenium complex. The cationic supramolecular hybrid **36** was further functionalized with **DNA**, and the resultant hybrid was used for non-viral gene delivery applications.

In addition to pyrene, other π-conjugated molecule such as perylene has been extensively used to prepare water-soluble hybrid materials. Hirsch *et al*. have used

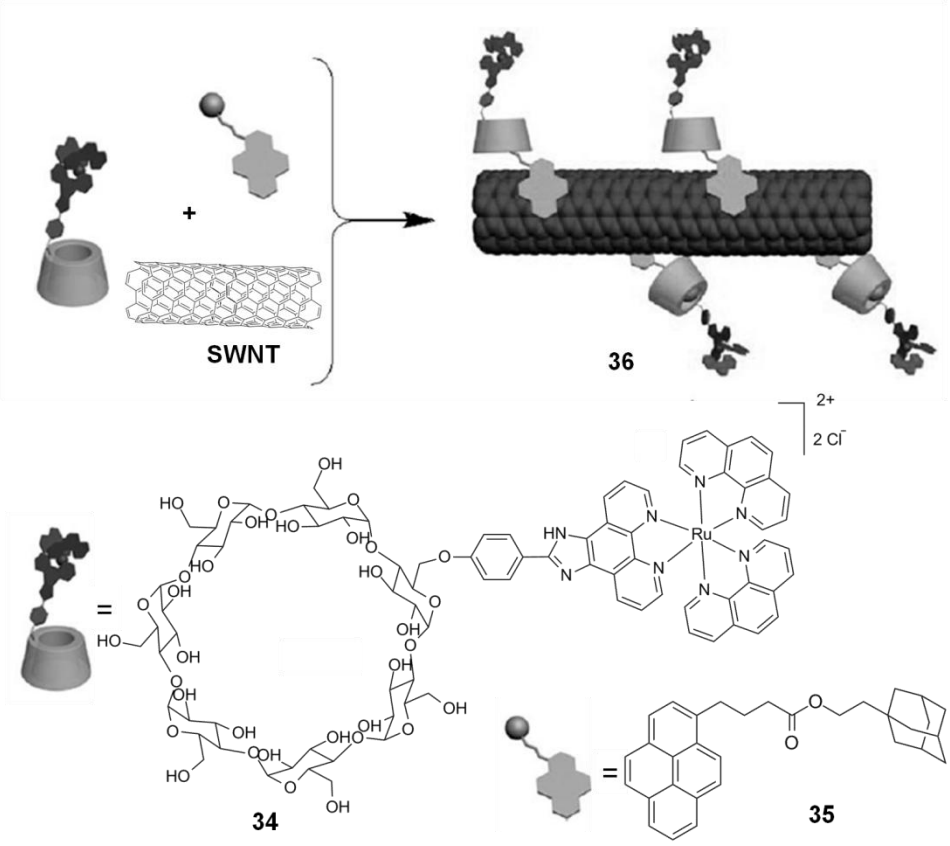

Figure 1.17. Preparation of supramolecular hybrid **36** from guest (**35**) and host (**34**) molecules functionalized with ruthenium complex and pyrene moiety, respectively.

water-soluble perylenetetracarboxy diimide molecules (**37**-**39**) functionalized with Newkome type dendritic moieties (Figure 1.18a) for dispersing **SWNT**.[69-70] The polar carboxyl groups were responsible for water solubility of these molecules and the non-polar perylene moiety facilitated the dispersion of **SWNTs**. UV-Vis-NIR absorption spectroscopy revealed that 0.01 wt % of **39** was enough to provide stable dispersion of **39/SWNT** hybrid. Morphological studies such as AFM (Figure 1.18b and 1.18c) and cryo-TEM also confirmed the presence of individual **SWNTs**. The observed fluorescence quenching of **39** in the hybrid material could be due to adsorption of **39** on the π-surface of **SWNT** resulting in photo-induced electron/energy transfer

processes. This electronic property of hybrid materials finds potential application in optoelectronic devices. Larger aromatic molecules with perylene moiety have been found to be good candidates for the separation of **SWNTs** based on their diameter.

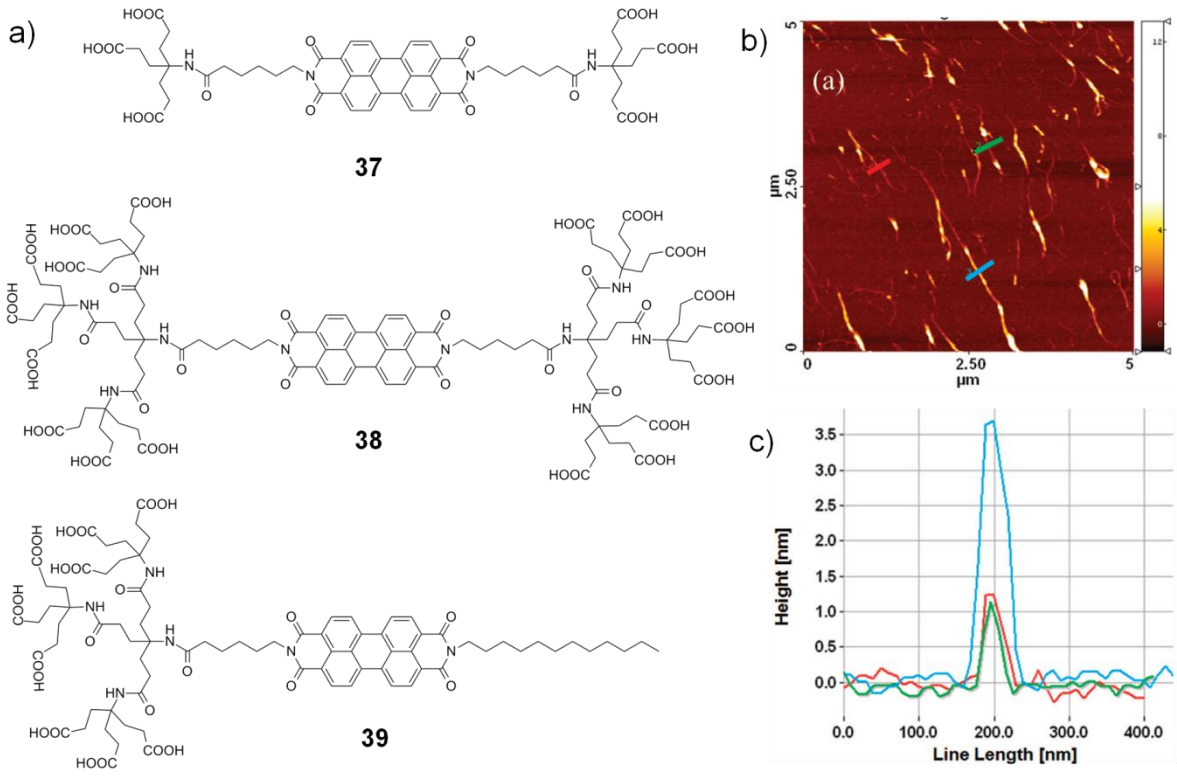

Figure 1.18. a) Chemical structures of perylene diimide based bolamphiphiles (**37** and **38**) and amphiphile (**39**). b) and c) AFM image and height profile of **39/SWNT** hybrid. (Height profiles of fibers that are marked by blue, green and red color lines in the Figure 1.18b are shown in the Figure 1.18c, respectively).

A novel tweezer-shaped molecule with two perylene units capable of sorting **SWNTs** with respect to their diameter has been reported.[71] This molecule was not only used for dispersion of **SWNTs**, but also to enrich **SWNT** with a diameter of 0.8 nm upto 70% from as-produced **HiPco-SWNT**. Guldi *et al.* have shown that perylene diimide based amphiphiles (**40** and **41**) possessed better ability to disperse **SWNTs** in

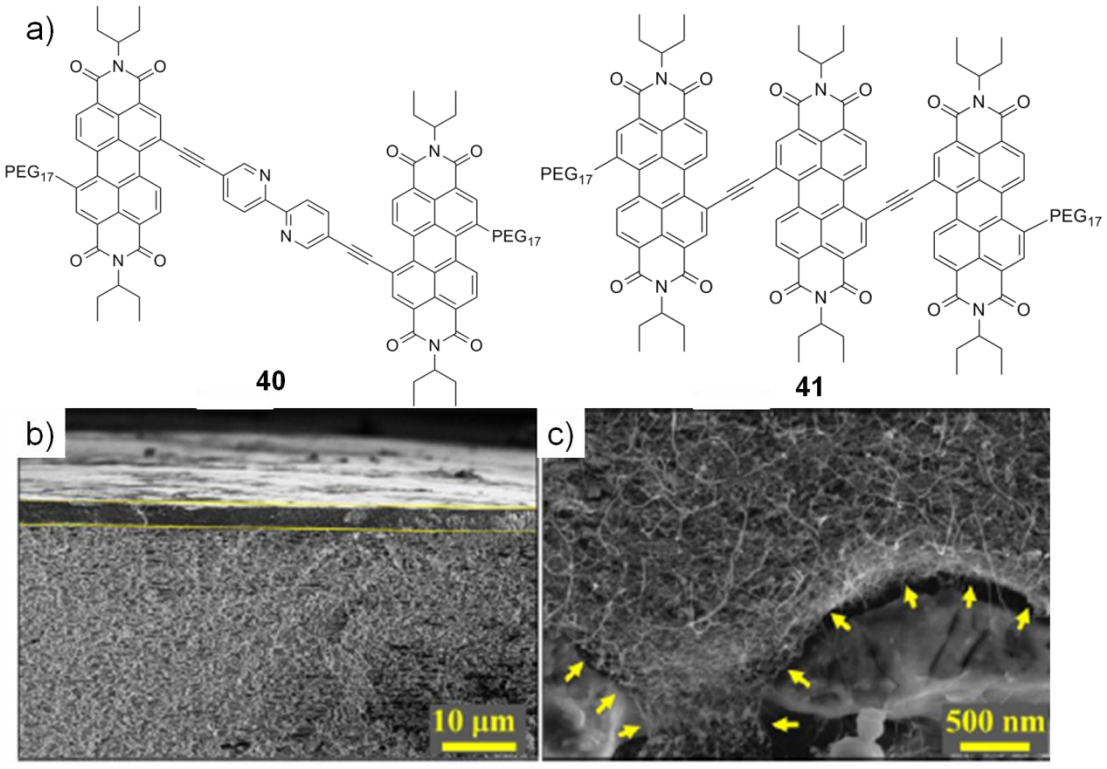

Figure 1.19. a) Chemical structures of perylene diimide based amphiphiles (**40** and **41**). b) and c) Cryo-SEM images of cross section of membrane made up of **40/SWNT** hybrid (a yellow line in Figure 1.19b and arrows in Figure 1.19c show the boundary between the membrane and cellulose acetate support).

organic and aqueous media (Figure 1.19a).[72] Cryo-TEM analysis exhibited a single layer adsorption of **40** and **41** in chloroform and a helical assembly of **40** in water on **SWNT** surface via non-covalent interactions such as hydrophobic and π-π interactions. It has been shown that the single layer of **40** is enough to give stable dispersion of **SWNT** in chloroform. A charge transfer state was formed between **40** and **SWNT** by the reorganization of the charge density in the ground state as perylene diimide moieties have electron accepting character. A rapid electron transfer from **SWNT** to **40** was observed in the excited state, which was confirmed by transient absorption

spectroscopy. A supramolecular membrane made up of **40/SWNT** from aqueous medium was used to separate gold nanoparticles with size of 2-6 nm from the wide range of particle size (Figure 1.19b and 1.19c). The porous structure of the hybrid material composed of supramolecular assemblies of **40** and **SWNT** plays a vital role in the size separation of gold nanoparticles. Similarly, hybrid material composed of **40/SWNT** in organic medium was used to prepare a bucky paper, which possessed promising electrical properties. The hybrid materials of this kind have several potential applications in the field of electronics as they are highly conductive in nature.

1.4.3. Hybrid Materials of π-Conjugated Polymers and CNTs

Similar to larger aromatic molecules, π-conjugated polymers also exhibit stronger interaction with **CNTs** because of their extended π-surface which led to more area of contact between **CNTs** and polymer backbone. The extent of interaction with **CNTs** as well as the properties of the resultant hybrid materials depends upon the electronic properties of the polymers. A large number of polymers including poly(*p*-phenylene-vinylene) (**PPV**), poly(*p-/m*-phenyleneethynylene) (**PPE**), poly(9,9-dialkylfluorene) (**PF**), poly(3-alkylthiophene) (**P3AT**), has been reported to form self-assembled stable hybrids with **CNTs**. Pang *et al.* have reported a poly[(*m*-phenyleneethynylene)-*alt*-(*p*-phenyleneethynylene)] polymer (**42**) for selective dispersion of **SWNTs** of a particular chirality (6, 5) (Figure 1.20a).[73] The rotation around carbon-carbon triple bond of the phenyleneethynylene unit of **42** played a crucial role in the helical self-assembly around the **SWNT** having a particular chirality (6, 5; Figure 1.20b). UV-Vis-NIR ab-

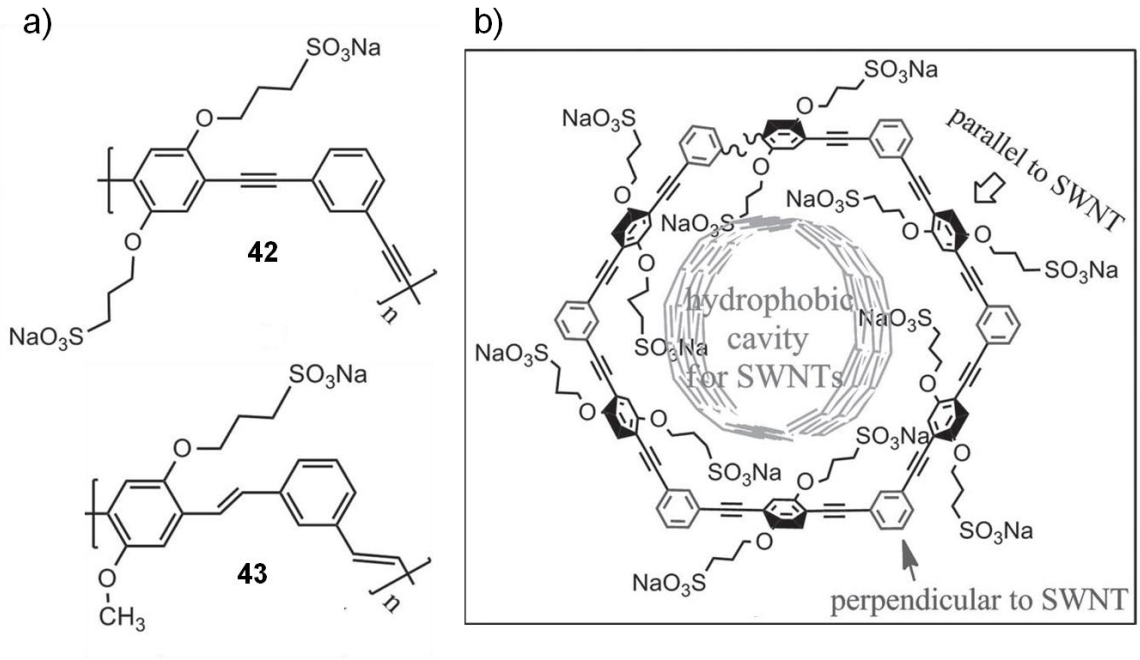

Figure 1.20. a) Chemical structures of **PPE** and **PPV** polymers (**42** and **43**). b) Schematic representation shows helically wrapped **SWNT** by **42**.

sorption and fluorescence spectroscopic studies revealed that the aqueous dispersion of **42/SWNT** possessed only the smaller diameter nanotubes such as (6, 5; d = 0.757) and (8, 3; d = 0.782), whereas the larger diameter nanotubes such as (7, 5), (8, 4), and (7, 6) (*d* = 0.829, 0.840, and 0.895 nm, respectively) were removed from the as-synthesized **SWNT** samples after centrifugation. Density-functional theory (DFT) calculations gave an additional support for the interaction of **42** with selective **SWNTs** of suitable diameter. The size of cavity formed due to the helical arrangement of **42** was more appropriate for the **SWNTs** with the diameter of 0.757 and 0.782 nm. Interestingly, the vinyl analogue **43** did not show any selectivity towards **SWNTs** of various diameter as the arrangement of **43** was not in such a way that the orbital interaction between **43** and **SWNTs** is maximized.

A polymer of poly(*m*-phenylenevinylene)-*co*-[(2,5-dioctyloxy-*p*-phenylene)-vinylene] (**44**) has been used to prepare hybrid material with **SWNTs** through helical wrapping over individual or bundles of a few nanotubes (Figure 1.21a) .[74] The amount of **44** required to disperse **SWNT** was quite high in organic solvent such as chloroform. With the help of AFM and two-photon fluorescence microscopic studies, it was proved that the fibrous network structure of the hybrid materials was formed by the wrapping of polymer **44** over the bundles of a few **SWNTs**, rather than aggregation of individually wrapped **SWNTs**. Theoretical studies explained the arrangement of **44** over the surface of the bundled **SWNTs** as a parallel orientation of the former with respect to the π-surface of the latter through strong supramolecular interactions such as π-π stacking, and van der Waals interaction. The same research group has also demonstrated the role of hetero-atom in copolymer (**45**) in the optoelectronic characteristics of the resultant hybrid materials (Figure 1.21a).[75] Addition of aqueous HCl to the chloroform solution of **45** protonated the pyridyl moieties which altered the electronic property of the hybrid as reflected in the absorption spectra. Interestingly, the concentration of H^+ needed to protonate the pyridyl functionalities, lowered in the case of **45/SWNT** hybrid and it further reduced upon increasing the content of **SWNT** in the hybrid material. The major reason for the requirement of lesser concentration of H^+ to protonate **45** in the hybrid with higher content of **SWNT** was the decreased pKa of the **45** in the presence of **SWNT**. The change in conductivities of **44** or **45/SWNT** hybrid materials was studied. Introduction of functionalities not only in the polymer backbone, but also in the alkyl chains helped to make the polymer as well as the hybrid

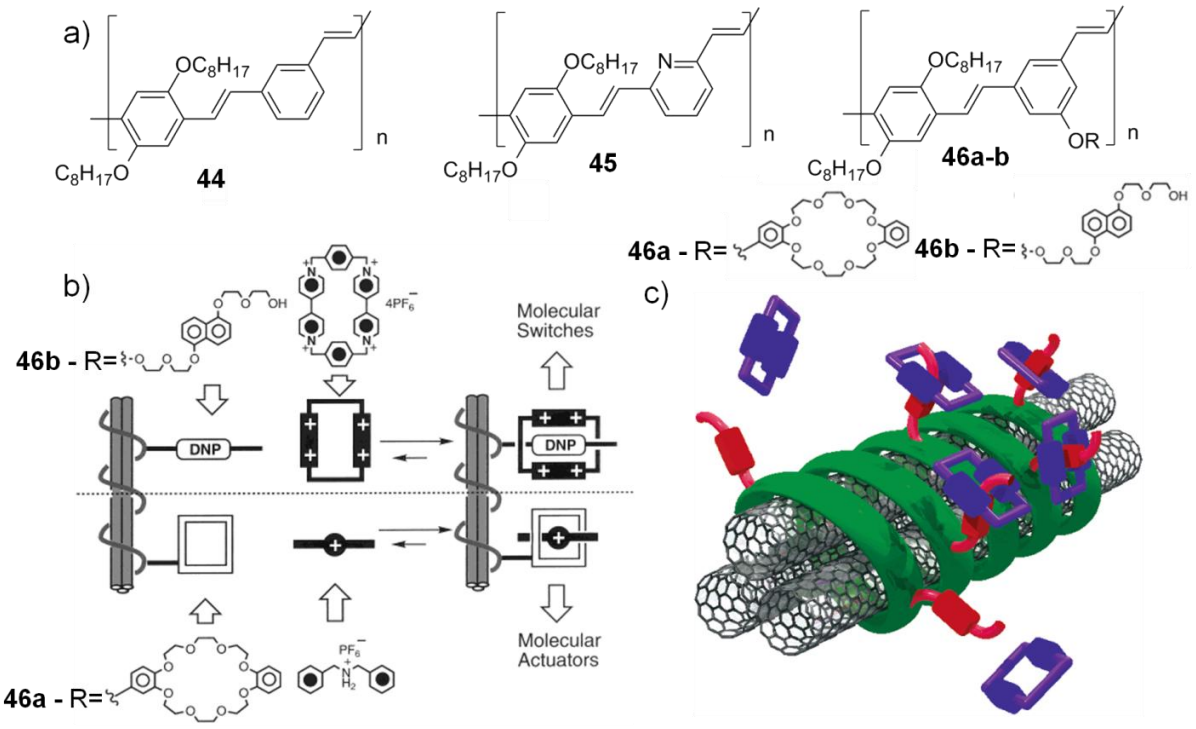

Figure 1.21. a) Chemical structures of polymers (**44, 45** and **46a-b**). b) Schematic representation of polypseudorotoxane/**SWNT** supramolecular hybrid formation from polymers **46a-b**. c) 3D representation of helical wrapping of **46b** over the bundles of few **SWNTs** and formation of polypseudorotoxanes.

materials with intriguing properties. The same authors have synthesized two polymers, one with dibenzo[24]-crown-8 macrocycles (**46a**) and other with a 1,5-dioxynaphthalene unit (**46b**) possessing polyether chain to make hybrid materials of polypseudorotaxanes with **SWNTs** (Figure 1.21b and 1.21c).[75] The formation of polypseudorotaxanes in the absence and presence of **SWNT** was studied by NMR and UV-Vis absorption spectroscopic techniques. AFM and surface potential measurements of hybrids also showed the formation of polypseudorotaxanes. These hybrid materials are expected to be helpful to make molecular actuators and switches with improved properties.

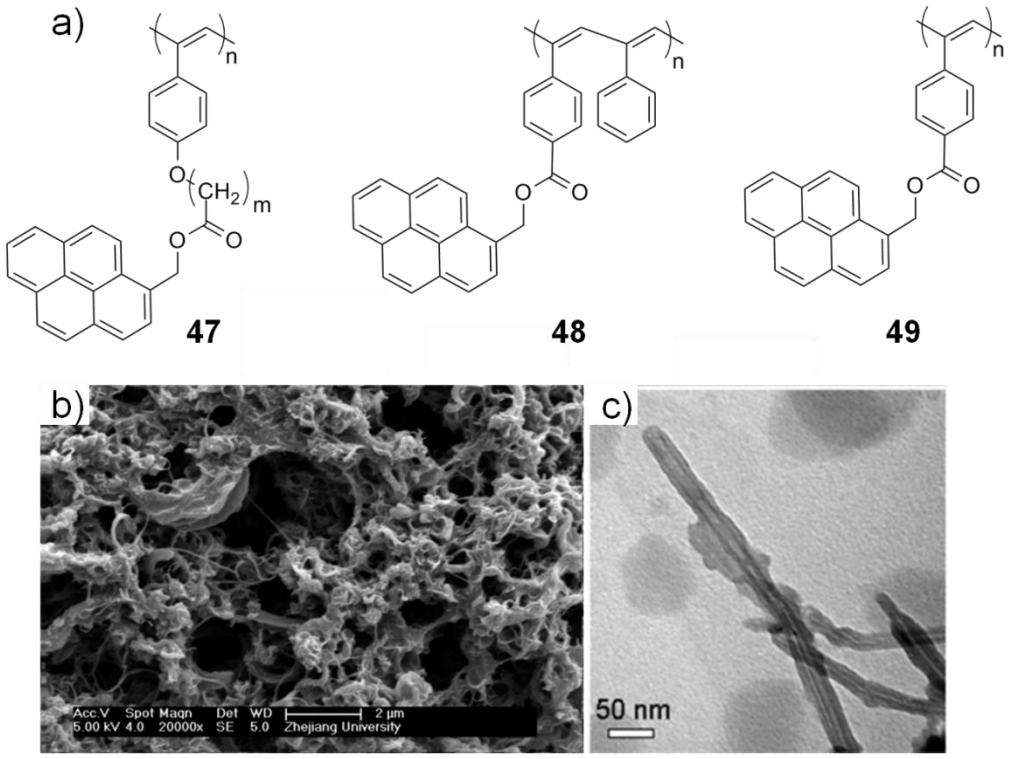

Figure 1.22. a) Chemical structures of pyrene-appended poly(phenyleneacetylene) polymers (**47, 48** and **49**). b) SEM and c) TEM images of **47** (m=10)/**MWNT** hybrid.

A few poly(phenyleneacetylene) (**47-49**) polymers tethered with pyrene groups have been used to prepare hybrid materials with **CNTs** (Figure 1.22a).[76] The hybrid materials were prepared by mixing the polymers in suitable solvent with required percentage (25%) of **MWNT**. The resultant hybrids were highly soluble in common solvents such as $CHCl_3$ and THF. The higher solubility of hybrid materials was attributed to π-π interaction of **MWNT** with π-conjugated polymer chain as well as extended π-surface of pyrene. Morphological studies such as SEM, AFM and TEM of **47/MWNT** hybrid material revealed the formation of entangled fibrous structures composed of **MWNTs** whose surfaces are fully covered with fibers of **47** (Figure

1.22b and 1.22c). The hybrid materials were thermally stable up to 338 °C with less percentage of weight loss. They showed bi-polar behavior in photovoltaic devices due to light induced charge transfer between them. The bi-polar nature of the devices could mainly be due to the uniform mixing of n-type **MWNT** and p-type polymers, whereas the individual components exhibited uni-polar behavior in fabricated devices.

Similar to **PPVs**, rigid poly(phenyleneethynylene)s (**PPEs**) have also been used in the preparation of hybrid materials with **CNTs**. Zhao *et al.* have reported a series of **PPEs** with various monomer units.[77] The structures of **PPEs** (**50-53**) are shown in Figure 1.23a. They were used to debundle as-synthesized samples of **SWNTs** in organic solvents through non-covalent interactions. The polymer **50** showed poor dispersing ability towards raw **SWNTs**, whereas polymers **51** and **52** with higher conjugation length exhibited very stable dispersion in organic solvents. The hybrid materials **51** or **52/SWNT** formed high quality films, which could be re-dispersed in organic solvents such as chloroform. Rheological measurements were carried out on the stable dispersion of hybrids, which revealed that the hybrids possess higher dynamic viscosities than bare **51** and **52**. This could be attributed to the aggregation of polymers over the **SWNT** surface via strong π-π interaction as well as the van der Waals interaction among longer alkyl chains. The dispersion of **SWNTs** using **51** and **52** were confirmed by UV-Vis-NIR absorption and fluorescence spectroscopic measurements. The appearance of van Hove singularities in the absorption spectra and the quenching of fluorescence of **51** and **52** indicate the dispersion of **SWNTs** through self-assembly process. The donor-acceptor type of interaction between polymer and

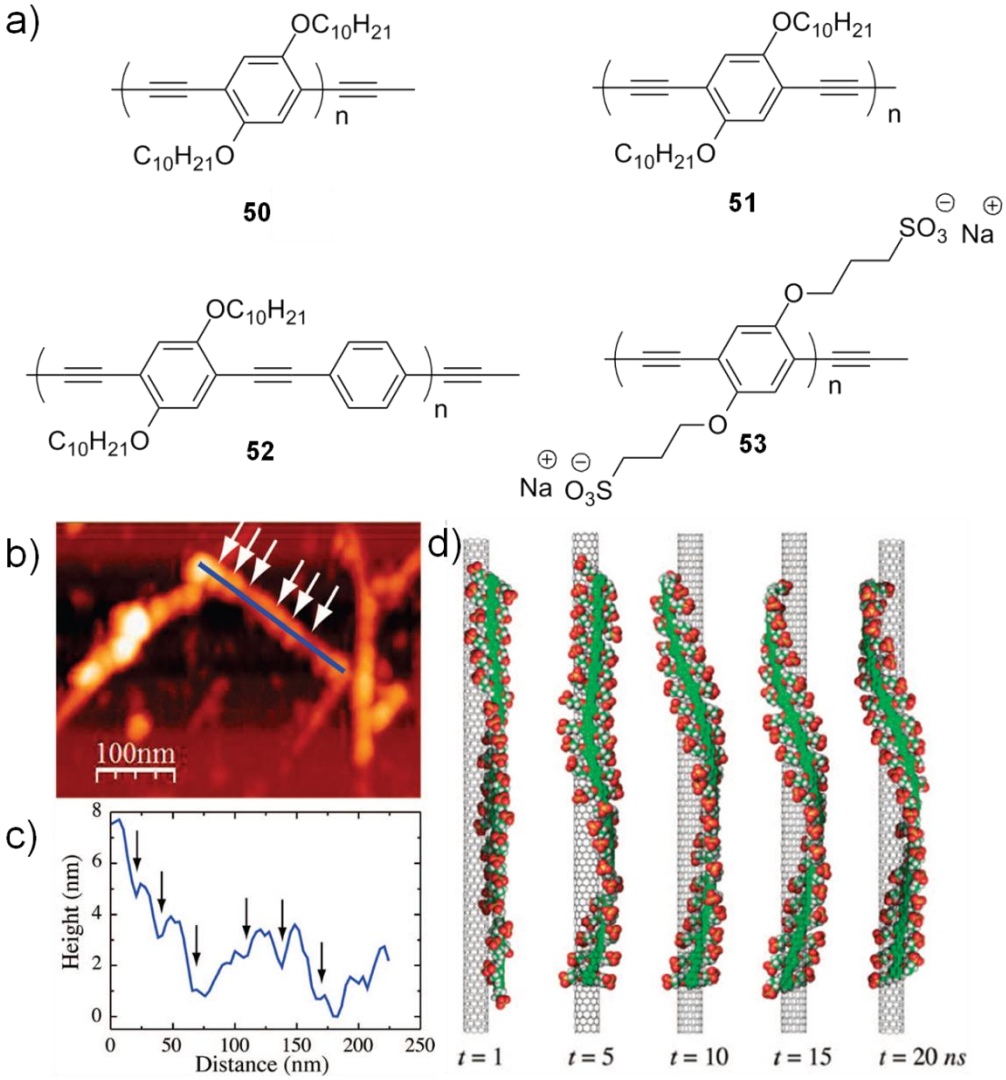

Figure 1.23. a) Chemical structures of poly(phenyleneethynylene) (**PPE**) polymers (**50, 51, 52** and **53**). b) AFM image and c) height profile of **53/SWNT** hybrid in the marked region of Figure 1.23b (helical wrapping of **53** around **SWNT** surface is shown by arrows in Figure 1.23b and corresponding helical pitch is marked in Figure 1.23c). d) Snapshots of interaction of **53** with **SWNT** with time, obtained from molecular dynamics (MD) simulation.

SWNTs is a major reason for considerable quenching of polymer fluorescence in solution state. Therien *et al.* have synthesized a water soluble polymer **53** to disperse **SWNTs** in aqueous medium (Figure 1.23a).[78] Spectroscopic technique such as UV-Vis-NIR absorption spectroscopy and microscopic techniques such as AFM and TEM

were carried out to confirm the individualization of **SWNTs** as well as the helical self-assembly of **53** over the π-surface of **SWNT**. AFM image of **53/SWNT** exhibited a helically wrapped monolayer of **53** around the nanotubes with the pitch length of 13±2 nm (Figure 1.23b and 1.23c). Molecular dynamics (MD) also proved that the helical orientation of **53** along the nanotube axis (Figure 1.23d).

Swager *et al.* have reported a light weight, transparent, and highly conductive thin film made up of poly(3-hexylthiophene) (**P3HT**) and **SWNTs**.[79] By simply adjusting the dispersion concentration of hybrid material, the thickness of film could be varied to the desired level. A transfer of thin films to any kind of substrates was easily achieved and an additional layer of **P3HT** could also be included on these conductive films by electropolymerization of the monomer of 3-hexylthiophene. Bao *et al.* have shown that dispersions of **SWNTs** in organic solvents such as chloroform, THF and ODCB could be prepared by using a regio-regular poly(3-hexylthiophene) (**54a**; Figure 1.24a).[80] Interestingly, the hybrid **54a/SWNT** exhibited nematic lyotropic liquid crystalline phase (LLC) in optical polarizing microscopic analysis, whereas the bare polymer (**54a**) and **SWNT** did not show any LLC property (Figure 1.24b-e). The appearance of birefringence in hybrid material was dependent on the concentration of **SWNT** in dispersion. It has been found that a minimum of 0.5 mg mL^{-1} of **SWNT** is necessary to exhibit birefringence. The reason for the nematic LLC phase of hybrid could be an alignment of individualized **SWNTs** with respect to each other at higher concentration.

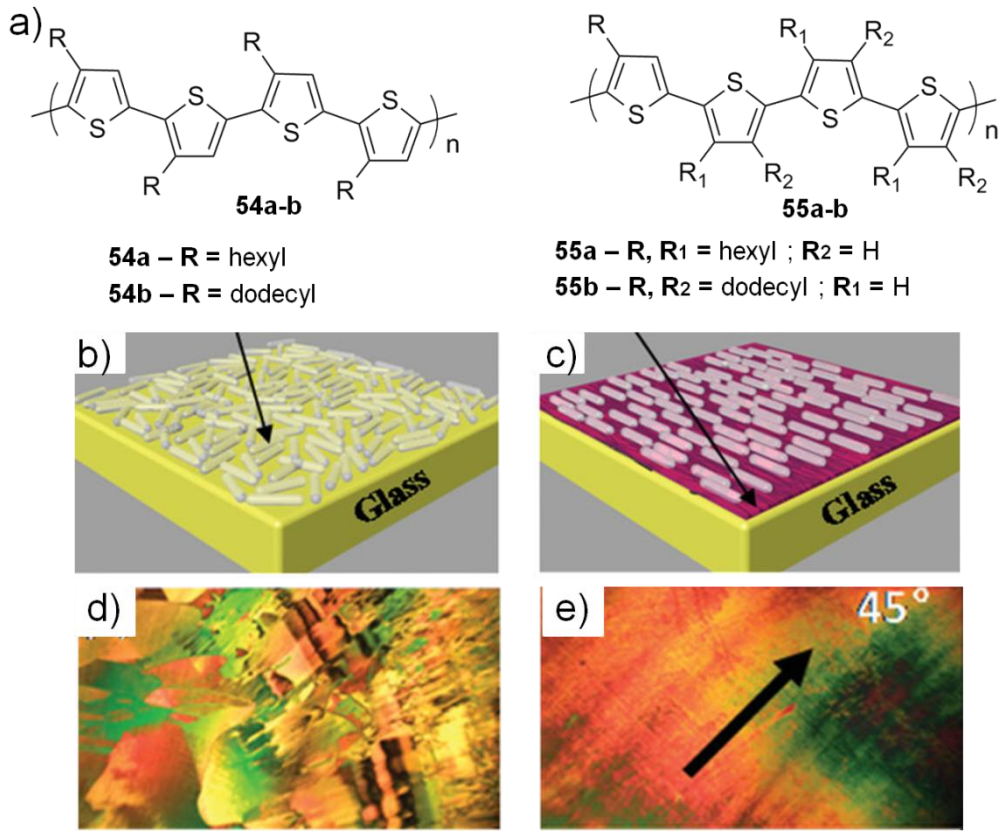

Figure 1.24. a) Chemical structures of regio-regular (**54a** and **55a**)/regio-randam(**54b** and **55b**)/ poly(3-alkylthiophene) polymers. Schematic representation of b) a random and c) shear-aligned liquid crystalline domains of **54a/SWNT** hybrid. Optical polarizing microscopic images of d) random and e) shear-aligned **54a/SWNT** hybrid on glass substrate at a direction of 45° with respect to one of the cross polarizers.

Andronov *et al.* have synthesized hybrids of **CNTs** with a few fluorene based polymers such as poly(9,9-dialkylfluorene) (**PF**) and poly(9,9-dialkylfluorene-*co*-3-alkylthiophene) (**PFT**).[81] **PF** and **PFT** showed a better dispersion of polymer/**SWNT** hybrids in organic solvents upto 40% of **SWNT**. The dispersion was stable for several weeks even after removal of free polymer from the hybrid. The conductivity of hybrid materials was comparable with pristine **SWNT**, however better than that of the bare polymers. In addition, fluorene based copolymer has been also established in the field

of chirality separation of **SWNTs** as they show difference in the interaction with a mixture of **SWNTs** of various diameter. By introducing π-conjugated molecules with particular chiral phase such as R-/S-chiral bi-naphthyl groups, even an enantiomeric pair of **SWNTs** could be separated successfully.[82]

An analysis of various reports discussed above reiterate the importance of functional hybrid materials consisting of π-conjugated organic small molecules/polymers with **CNTs**/graphene/graphene derivatives (**GO** and **RGO**) in the field of optoelectronic applications. A large number of π-conjugated systems have been exploited to the preparation of hybrid materials that show intriguing optical and electronic properties. The insights gained over the years from these studies have helped chemists to design new materials with improved properties.

1.5. Origin, Objectives and Approach to the Thesis

The origin of the present work is based on the previous reports on the interaction of a few **OPV** based π-systems with **CNTs**.[55, 60] Results of these studies encouraged us to further look into the possibilities of exploring the preparation of new hybrid materials for the detailed evaluation of their properties. The main objective of the present study was to explore the molecular self-assembly approach towards the preparation of hybrid materials based on carbon allotropes such as **CNTs** and graphene with **OPV** based gelators. Detailed investigations on the morphological features, electronic properties and superhydrophobic behavior were envisaged. We have chosen graphene and **CNTs** for our study. **OPV** and reduced graphene oxide (**RGO**) based hybrids were aimed.

We anticipated that the self-assembly behavior of **OPVs** would help to exfoliate **RGO** and thereby improving the electrochemical performance of **OPV/RGO** hybrid materials. Subsequently, we planned to make use of one dimensional nanomaterial such as **CNTs** to control the properties of molecular assemblies composed of chiral-**OPV** derivatives. Based on the strength of π-π interaction between **CNTs** and chiral-**OPVs**, we were expecting that the chiroptical properties and morphological features of the resultant hybrid materials could be tuned. Further we were interested to make superhydrophobic coatings composed of **OPV** derivatives with polymerizable end group and **CNTs** that would be highly stable and useful for various applications. Details of the approach to the above objectives are described in the present thesis.

1.6. References

(1) Gomez-Romero, P.; Sanchez, C. *New J. Chem.* **2005**, *29*, 57-58.

(2) Wegst, U. G. K.; Bai, H.; Saiz, E.; Tomsia, A. P.; Ritchie, R. O. *Nat. Mater.* **2015**, *14*, 23-36.

(3) Meyers, M. A.; Chen, P.-Y.; Lin, A. Y.-M.; Seki, Y. *Prog. Mater. Sci* **2008**, *53*, 1-206.

(4) Kickelbic, G. *Hybrid Materials. Synthesis, Characterization, and Applications*; Wiley VCH: Weinheim, Germany, **2007**.

(5) Lehn, J.-M. *Supramolecular Chemistry, Concepts and Perspectives*; VCH: Weinheim, Germany, **1995**.

(6) Lalatonne, Y.; Richardi, J.; Pileni, M. P. *Nat. Mater.* **2004**, *3*, 121-125.

(7) Nie, Z.; Petukhova, A.; Kumacheva, E. *Nat. Nanotechnol* **2010**, *5*, 15-25.

(8) Discher, D. E.; Kamien, R. D. *Nature* **2004**, *430*, 519-520.

(9) Sanchez, C.; Soler-Illia, G. J. d. A. A.; Ribot, F.; Lalot, T.; Mayer, C. R.; Cabuil, V. *Chem. Mater.* **2001**, *13*, 3061-3083.

(10) Kickelbick, G. *Hybrid Mater.* **2014**, *1*, 39-51.

(11) Sanchez, C.; Arribart, H.; Giraud Guille, M. M. *Nat. Mater.* **2005**, *4*, 277-288.

(12) Orilall, M. C.; Wiesner, U. *Chem. Soc. Rev.* **2011**, *40*, 520-535.

(13) Chen, R. J.; Bangsaruntip, S.; Drouvalakis, K. A.; Wong Shi Kam, N.; Shim, M.; Li, Y.; Kim, W.; Utz, P. J.; Dai, H. *PNAS* **2003**, *100*, 4984-4989.

(14) Zhao, Y.-L.; Stoddart, J. F. *Acc. Chem. Res.* **2009**, *42*, 1161-1171.

(15) Geim, A. K. *Science* **2009**, *324*, 1530-1534.

(16) Li, C.; Liu, M.; Pschirer, N. G.; Baumgarten, M.; Müllen, K. *Chem. Rev.* **2010**, *110*, 6817-6855.

(17) Weiss, N. O.; Zhou, H.; Liao, L.; Liu, Y.; Jiang, S.; Huang, Y.; Duan, X. *Adv. Mater.* **2012**, *24*, 5782-5825.

(18) Jariwala, D.; Sangwan, V. K.; Lauhon, L. J.; Marks, T. J.; Hersam, M. C. *Chem. Soc. Rev.* **2013**, *42*, 2824-2860.

(19) Perreault, F.; Fonseca de Faria, A.; Elimelech, M. *Chem. Soc. Rev.* **2015**, *44*, 5861-5896.

(20) Georgakilas, V.; Tiwari, J. N.; Kemp, K. C.; Perman, J. A.; Bourlinos, A. B.; Kim, K. S.; Zboril, R. *Chem. Rev.* **2016**, *116*, 5464-5519.

(21) Matsumoto, M.; Saito, Y.; Park, C.; Fukushima, T.; Aida, T. *Nat. Chem.* **2015**, *7*, 730-736.

(22) Wu, L.; Ohtani, M.; Takata, M.; Saeki, A.; Seki, S.; Ishida, Y.; Aida, T. *ACS Nano* **2014**, *8*, 4640-4649.

(23) Ji, Q.; Honma, I.; Paek, S.-M.; Akada, M.; Hill, J. P.; Vinu, A.; Ariga, K. *Angew. Chem. Int. Ed.* **2010**, *49*, 9737-9739.

(24) Li, C.; Shi, G. *Adv. Mater.* **2014**, *26*, 3992-4012.

(25) Bai, H.; Li, C.; Shi, G. *Adv. Mater.* **2011**, *23*, 1089-1115.

(26) Adhikari, B.; Nanda, J.; Banerjee, A. *Chem. Eur. J.* **2011**, *17*, 11488-11496.

(27) Bai, H.; Sheng, K.; Zhang, P.; Li, C.; Shi, G. *J. Mater. Chem.* **2011**, *21*, 18653.

(28) Cheng, Q. Y.; Zhou, D.; Gao, Y.; Chen, Q.; Zhang, Z.; Han, B. H. *Langmuir* **2012**, *28*, 3005-3010.

(29) Srinivasan, S.; Shin, W. H.; Choi, J. W.; Coskun, A. *J. Mater. Chem. A* **2013**, *1*, 43-48.

(30) Liu, J.; Chen, G.; Jiang, M. *Macromolecules* **2011**, *44*, 7682-7691.

(31) Zhu, C.-H.; Lu, Y.; Peng, J.; Chen, J.-F.; Yu, S.-H. *Adv. Funct. Mater.* **2012**, *22*, 4017-4022.

(32) An, X.; Simmons, T.; Shah, R.; Wolfe, C.; Lewis, K. M.; Washington, M.; Nayak, S. K.; Talapatra, S.; Kar, S. *Nano Lett.* **2010**, *10*, 4295-4301.

(33) Jang, J.-H.; Rangappa, D.; Kwon, Y.-U.; Honma, I. *J. Mater. Chem.* **2011**, *21*, 3462-3466.

(34) Lee, D.-W.; Kim, T.; Lee, M. *Chem. Commun.* **2011**, *47*, 8259-8261.

(35) Khanra, P.; Uddin, M. E.; Kim, N. H.; Kuila, T.; Lee, S. H.; Lee, J. H. *RSC Adv.* **2015**, *5*, 6443-6451.

(36) Xu, Y.; Zhao, L.; Bai, H.; Hong, W.; Li, C.; Shi, G. *J. Am. Chem. Soc.* **2009**, *131*, 13490-13497.

(37) Geng, J.; Jung, H.-T. *J. Phys. Chem. C* **2010**, *114*, 8227-8234.

(38) Jiang, B.-P.; Hu, L.-F.; Wang, D.-J.; Ji, S.-C.; Shen, X.-C.; Liang, H. *J. Mater. Chem. B* **2014**, *2*, 7141-7148.

(39) Su, Q.; Pang, S.; Alijani, V.; Li, C.; Feng, X.; Müllen, K. *Adv. Mater.* **2009**, *21*, 3191-3195.

(40) Ghosh, A.; Rao, K. V.; George, S. J.; Rao, C. N. R. *Chem. Eur. J.* **2010**, *16*, 2700-2704.

(41) Wang, Y.; Kurunthu, D.; Scott, G. W.; Bardeen, C. J. *J. Phys. Chem. C* **2010**, *114*, 4153-4159.

(42) Yang, H.; Zhang, Q.; Shan, C.; Li, F.; Han, D.; Niu, L. *Langmuir* **2010**, *26*, 6708-6712.

(43) Bai, H.; Xu, Y.; Zhao, L.; Li, C.; Shi, G. *Chem. Commun.* **2009**, 1667-1669.

(44) Zhang, K.; Zhang, L. L.; Zhao, X. S.; Wu, J. *Chem. Mater.* **2010**, *22*, 1392-1401.

(45) Bissessur, R.; Liu, P. K. Y.; Scully, S. F. *Synth. Met.* **2006**, *156*, 1023-1027.

(46) Gu, Z.; Li, C.; Wang, G.; Zhang, L.; Li, X.; Wang, W.; Jin, S. *J. Polym. Sci. Part B Polym. Phys.* **2010**, *48*, 1329-1335.

(47) Wang, H.; Hao, Q.; Yang, X.; Lu, L.; Wang, X. *ACS Appl. Mater. Interfaces* **2010**, *2*, 821-828.

(48) Liu, Q.; Liu, Z.; Zhang, X.; Zhang, N.; Yang, L.; Yin, S.; Chen, Y. *Appl. Phys. Lett.* **2008**, *92*, 223303.

(49) Liu, Q.; Liu, Z.; Zhang, X.; Yang, L.; Zhang, N.; Pan, G.; Yin, S.; Chen, Y.; Wei, J. *Adv. Funct. Mater.* **2009**, *19*, 894-904.

(50) Xu, Y.; Wang, Y.; Liang, J.; Huang, Y.; Ma, Y.; Wan, X.; Chen, Y. *Nano Res.* **2009**, *2*, 343-348.

(51) Choi, K. S.; Liu, F.; Choi, J. S.; Seo, T. S. *Langmuir* **2010**, *26*, 12902-12908.

(52) Chunder, A.; Liu, J.; Zhai, L. *Macromol. Rapid Commun.* **2010**, *31*, 380-384.

(53) Star, A.; Stoddart, F. J. *Macromolecules* **2002**, *35*, 7516-7520.

(54) Llanes-Pallas, A.; Yoosaf, K.; Traboulsi, H.; Mohanraj, J.; Seldrum, T.; Dumont, J.; Minoia, A.; Lazzaroni, R.; Armaroli, N.; Bonifazi, D. *J. Am. Chem. Soc.* **2011**, *133*, 15412-15424.

(55) Srinivasan, S.; Praveen, V. K.; Philip, R.; Ajayaghosh, A. *Angew. Chem. Int. Ed.* **2008**, *47*, 5750-5754.

(56) Babu, S. S.; Praveen, V. K.; Ajayaghosh, A. *Chem. Rev.* **2014**, *114*, 1973-2129.

(57) Roy, S.; Banerjee, A. *RSC Adv.* **2012**, *2*, 2105-2111.

(58) Roy, S.; Baral, A.; Banerjee, A. *Chem. Eur. J.* **2013**, *19*, 14950-14957.

(59) Liang, S.; Chen, G.; Peddle, J.; Zhao, Y. *Chem. Commun* **2012**, *48*, 3100-3102.

(60) Srinivasan, S.; Babu, S. S.; Praveen, V. K.; Ajayaghosh, A. *Angew. Chem. Int. Ed.* **2008**, *47*, 5746-5749.

(61) Cheng, E.; Li, Y.; Yang, Z.; Deng, Z.; Liu, D. *Chem. Commun* **2011**, *47*, 5545-5547.

(62) Tamesue, S.; Takashima, Y.; Yamaguchi, H.; Shinkai, S.; Harada, A. *Eur. J. Org. Chem.* **2011**, *2011*, 2801-2806.

(63) Tan, Z.; Ohara, S.; Naito, M.; Abe, H. *Adv. Mater.* **2011**, *23*, 4053-4057.

(64) Guldi, D. M.; Rahman, G. M. A.; Jux, N.; Balbinot, D.; Hartnagel, U.; Tagmatarchis, N.; Prato, M. *J. Am. Chem. Soc.* **2005**, *127*, 9830-9838.

(65) Guldi, D. M.; Rahman, G. M. A.; Prato, M.; Jux, N.; Qin, S.; Ford, W. *Angew. Chem. Int. Ed.* **2005**, *44*, 2015-2018.

(66) Guldi, D. M.; Rahman, G. M. A.; Zerbetto, F.; Prato, M. *Acc. Chem. Res.* **2005**, *38*, 871-878.

(67) Paloniemi, H.; Ääritalo, T.; Laiho, T.; Liuke, H.; Kocharova, N.; Haapakka, K.; Terzi, F.; Seeber, R.; Lukkari, J. *J. Phy. Chem. B* **2005**, *109*, 8634-8642.

(68) Yu, M.; Zu, S. Z.; Chen, Y.; Liu, Y. P.; Han, B. H.; Liu, Y. *Chemistry* **2010**, *16*, 1168-1174.

(69) Backes, C.; Schmidt, C. D.; Hauke, F.; Böttcher, C.; Hirsch, A. *J. Am. Chem. Soc.* **2009**, *131*, 2172-2184.

(70) Backes, C.; Schmidt, C. D.; Rosenlehner, K.; Hauke, F.; Coleman, J. N.; Hirsch, A. *Adv. Mater.* **2010**, *22*, 788-802.

(71) Backes, C.; Schmidt, C. D.; Hauke, F.; Hirsch, A. *Chem. Asian J.* **2011**, *6*, 438-444.

(72) Tsarfati, Y.; Strauss, V.; Kuhri, S.; Krieg, E.; Weissman, H.; Shimoni, E.; Baram, J.; Guldi, D. M.; Rybtchinski, B. *J. Am. Chem. Soc.* **2015**, *137*, 7429-7440.

(73) Chen, Y.; Xu, Y.; Wang, Q.; Gunasinghe, R. N.; Wang, X. Q.; Pang, Y. *Small* **2013**, *9*, 870-875.

(74) Steuerman, D. W.; Star, A.; Narizzano, R.; Choi, H.; Ries, R. S.; Nicolini, C.; Stoddart, F. J.; Heath, J. R. *J. Phy. Chem. B* **2002**, *106*, 3124-3130.

(75) Star, A.; Liu, Y.; Grant, K.; Ridvan, L.; Stoddart, F. J.; Steuerman, D. W.; Diehl, M. R.; Boukai, A.; Heath, J. R. *Macromolecules* **2003**, *36*, 553-560.

(76) Yuan, W.; Sun, J.; Dong, Y.; Häussler, M.; Yang, F.; Xu, H.; Qin, A.; Lam, J. W. Y.; Zheng, Q.; Tang, B. *Macromolecules* **2006**, *39*, 8011-8020.

(77) Rice, N. A.; Soper, K.; Zhou, N.; Merschrod, E.; Zhao, Y. *Chem. Commun* **2006**, 4937.

(78) Kang, Y. K.; Lee, O.-S. S.; Deria, P.; Kim, S. H.; Park, T.-H. H.; Bonnell, D. A.; Saven, J. G.; Therien, M. J. *Nano Lett.* **2009**, *9*, 1414-1418.

(79) Gu, H.; Swager, T. M. *Adv. Mater.* **2008**, *20*, 4433-4437.

(80) Lee, H.; You, W.; Barman, S.; Hellstrom, S.; LeMieux, M. C.; Oh, J.; Liu, S.; Fujiwara, T.; Wang, W.; Chen, B.; Jin, Y.; Kim, J.; Bao, Z. *Small* **2009**, *5*, 1019-1024.

(81) Cheng, F.; Imin, P.; Maunders, C.; Botton, G.; Adronov, A. *Macromolecules* **2008**, *41*, 2304-2308.

(82) Akazaki, K.; Toshimitsu, F.; Ozawa, H.; Fujigaya, T.; Nakashima, N. *J. Am. Chem. Soc.* **2012**, *134*, 12700-12707.

Chapter 2

Self-Assembled Hybrids of Oligo(*p*-phenylenevinylene) Based Gelators and Reduced Graphene Oxide for Energy Storage Devices

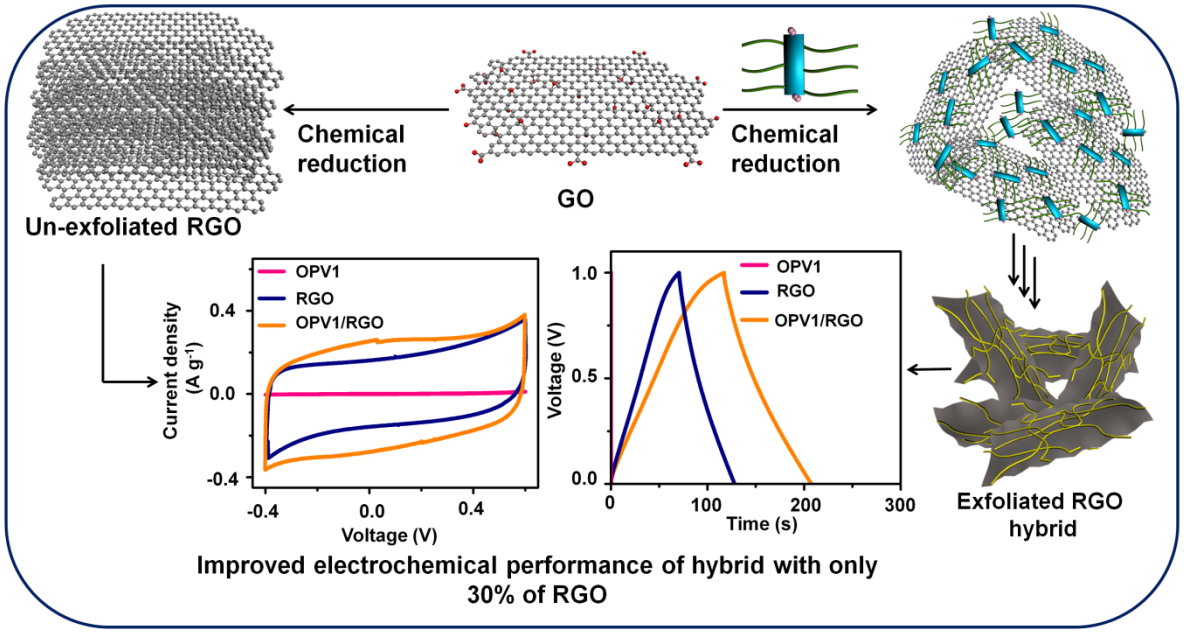

2.1. Abstract

*Among several methodologies to improve the solution processing of graphene based materials, non-covalent functionalization has been considered as a non-destructive and efficient method. In this work, it has been shown that supramolecular self-assembly process can be used as a useful tool to exfoliate reduced graphene oxide (**RGO**), resulting in hybrid materials with improved properties. The dispersing ability of non-covalently functionalized reduced graphene oxide is increased when compared to the bare one. Aggregation of the π-gelator over **RGO** aided the exfoliation of graphene layers to remain as individual sheets with higher surface area. With the enhanced surface area and better conductivity, these hybrid materials showed excellent electrochemical performance as electrodes for supercapacitors.*

2.2. Introduction

Graphene -one dimensional graphite- is known for its excellent electronic properties and applications in different fields.[1-9] Incorporation and homogeneous distribution of graphene in various matrices with preserved intrinsic electrical properties is a primary requirement for their use in electronic devices. Among the various routes reported to achieve mono/few-layer graphene, by micromechanical, chemical vapour deposition (CVD), etc., the chemical reduction of exfoliated graphene oxide (**GO**) has been shown as an easiest and scalable method.[10-14] During the process of chemical reduction, the functional groups (carboxyl, hydroxyl, and epoxide) responsible for the complete dispersion of **GO** in the polar solvents (water, methanol, tetrahydrofuran

(THF), dimethyl formamide, etc.) would be removed.[15-17] The hydrophilic surface of **GO** becomes hydrophobic as all sp^3 hybridized carbon change to sp^2 hybridized one upon chemical reduction. Due to strong π-π interaction, the one atom thick sheets of reduced graphene oxide (**RGO**) undergo extensive re-stacking into thick micrometer-sized graphite-like structures, making it rather difficult to exploit the unusual properties of single layer graphene. Diverse strategies have been used to avoid such re-stacking of reduced graphene oxide, which include covalent and non-covalent functionalizations.[18] Among these methods, non-covalent functionalization offers the most useful and non-destructive method to alter the material properties without changing much the chemical structure of graphene.[19-25]

Aromatic polycyclic hydrocarbons are widely used for the exfoliation of graphitic materials. Oligo(*p*-phenylenevinylene) (**OPV**) based π-gelators are one such class of molecules. They are widely used in the fields of organic electronics, photovoltaic devices, field-effect transistors, sensing, imaging, etc., because of their excellent solution processing and significant physical and chemical properties.[26] They can be used as a matrix to incorporate graphene since gelation process involves specific intermolecular non-covalent interactions, admitting hydrogen bonding, π-π stacking, van der Waals forces, etc. **OPV** based gelators have recently been exploited to make hybrid gels by incorporating **SWNT**.[27] It has been found that **CNT** accelerates the self-assembly of **OPV** and stabilizes the resultant hybrid gels by acting as a reinforcing agent. The ratio of storage modulus (*G'*) and loss modulus (*G"*) of the composite is greater than that of **OPV** gels which indicate enhanced stability and

elastic response of the former. The physical reinforcement of the self-assembled **OPV** tapes is considered responsible for the improved rheological properties.

π-Gelators may also interact with graphene through non-covalent interactions.[28-29] Pyrene-containing peptide-based organogelator has been reported as a host for the incorporation of graphene to prepare fluorescent hybrid organogel system, which showed more rigidity than the native gel.[28] Graphene nanosheets can be introduced into the nanofibrillar network structure within the hybrid system resulting in improved properties. For example, measurements of strorage modulus (*G'*) and loss modulus (*G"*) of hybrid gel showed that graphene containing hybrid organogel was seven times more rigid than that of native organogel.

Graphene and graphene based hybrid materials have been studied as electrode materials for energy storage devices such as supercapacitors.[30-43] However, to achieve high performance of such double layer supercapacitors, effective electrode surface area has a critical role. **RGO** tends to aggregate, leading to poor electrolyte wetting, thus resulting in reduced capacitance. Several methods have been explored to spatially separate the graphene sheets,[44-47] which were shown to improve the electrochemical performance of the electrode. Li *et al*. have demonstrated that water can be used as an effective spacer for **RGO** to prevent the restacking of individual sheets into graphite-like structure. A vaccum filtration technique was used to prepare self-assembled, and solvated graphene (SSG) film from the colloidal suspension of **RGO** (Figure 2.1a). The water content of the graphene film was found to be 92 wt% and the highly swollen film exhibited the resistivity of 1086 Ω square^{-1} with the **RGO** content of 0.045 mg

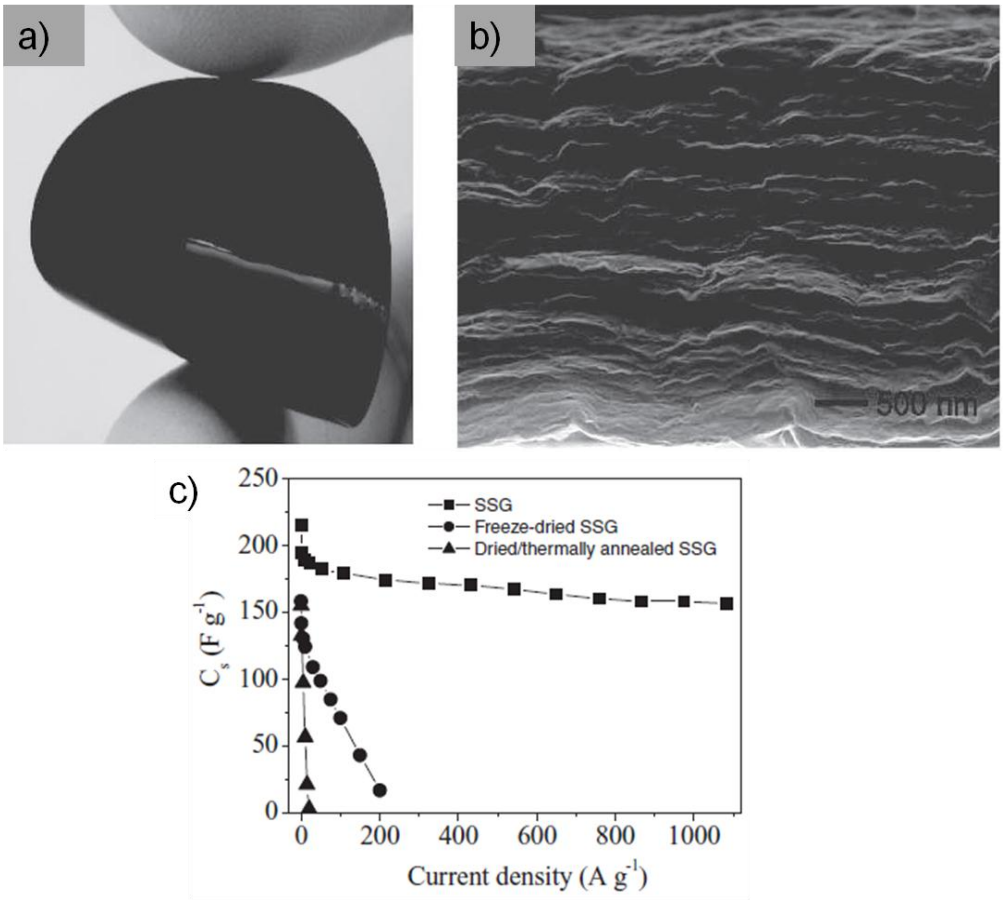

Figure 2.1. a) A photograph of SSG film. b) SEM image of the cross-section of a freeze-dried SSG film. c) Specific capacitances measured at various current densities.

cm^{-2}. The colloidal interactions among the **RGO** sheets were responsible for the formation of self-assembled graphene film. During the filtration process, the intersheet electrostatic repulsive forces developed by the negatively charged carboxylic groups on the surface of **RGO** prevented the re-stacking of graphene sheets (Figure 2.1b). And also, the hydration forces due to the tight absorption of water molecules with the hydrophilic groups present on the **RGO** surface gave an additional repulsive force to prevent the re-stacking of individual **RGO** sheets. The SSG film showed better electrochemical performance when compared to that of the freeze-dried and thermally

dried graphene films (Figure 2.1c). The specific capacitance of SSG film was calculated as 215 F g^{-1} in 1 M aqueous H_2SO_4 electrolyte.

A few organic molecules also have been used as the spacer to prevent the re-stacking of individual **RGO** sheets. Diethylene glycol (**DEG**) was used as a spacer, and a mild-reducing agent for **GO** to give **DEG** grafted **RGO** hybrid material (Figure 2.2a). **DEG/RGO** was prepared by heating the suspension of **DEG** and **GO** (0.3 mg mL^{-1}) to 150 °C in a Teflon-lined autoclave for 10 h. During the reduction, **DEG** molecules were covalently bonded with the functional groups present on the surface of **GO**. The freeze-dried **DEG/RGO** hybrid was highly dispersible in water and alcohol. **DEG/RGO** exhibited a specific capacitance of 237 F g^{-1} at a current density of 0.1 A g^{-1} in 6 M KOH as an electrolyte (Figure 2.2 b). Similarly, a triethanolamine (**TEA**)/ **RGO** hybrid was prepared by using **TEA** as a spacer molecule to prevent re-stacking of **RGO** sheets. A homogenous aqueous suspension of **TEA** and **GO** (30 mg) was heated in Teflon-lined autoclave at 105 °C for 5 h followed by 180 °C for 10 h (Figure 2.2c). The dried **TEA/RGO** hybrid showed an increased interlayer spacing as the covalently attached **TEA** molecules on the surface of **RGO** sheets behaved as a spacer. **TEA/RGO** exhibited a specific capacitance of 211 F g^{-1} in 1 M aqueous H_2SO_4 electrolyte.

In addition to organic molecules, electrochemically active carbon nanomaterials such as carbon nanotubes also have been used as a spacer to increase the inter-layer spacing among individual **RGO** sheets (Figure 2.3). **RGO/CNT** hybrid materials were prepared by heating a series of **GO** and **CNT** (pre-prepared aqueous solution of sodi-

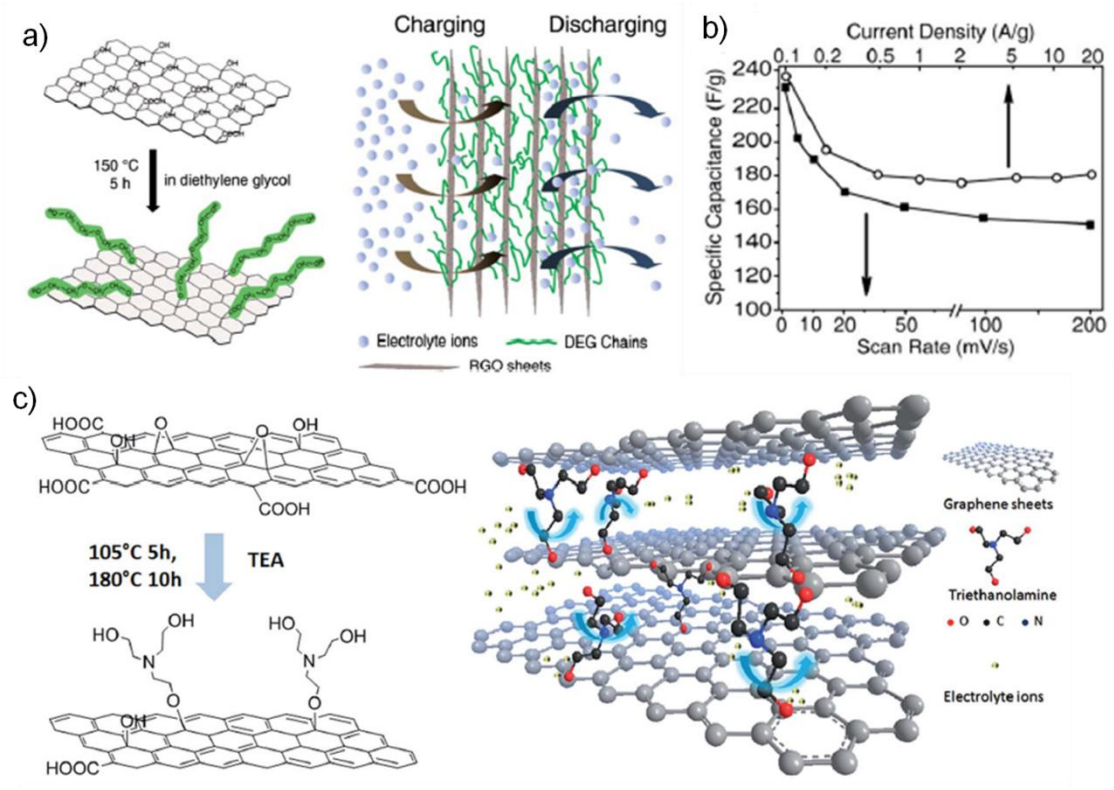

Figure 2.2. a) Schematic representation showing preparation of **DEG/RGO** hybrid and the grafted **DEG** chains on the surface of **RGO** as spacers to introduce suitable porosity into the multilayered graphene structure. b) Specific capacitances of **DEG/RGO** at various current densities and scan rates. c) Schematic representation of the preparation of **TEA/RGO** hybrid and as-prepared 3D **TEA/RGO** nanostructure with charge transfer characteristics.

um dodecylbenzenesulphonate (**SDBS**)) solutions with different weight percentages of **GO** and **CNT** to 180 °C for 18 h in a Teflon-lined autoclave. After hydrothermal reaction, **RGO/CNT** hybrids were obtained as hydrogels and the excess surfactant (**SDBS**) removed by washing with water. **RGO/CNT** hybrid with 1:1 weight ratio of **RGO** and **CNT** exhibited the specific capacitance of 318 F g^{-1} in 30 wt% aqueous KOH as an electrolyte (Figure 2.3e).

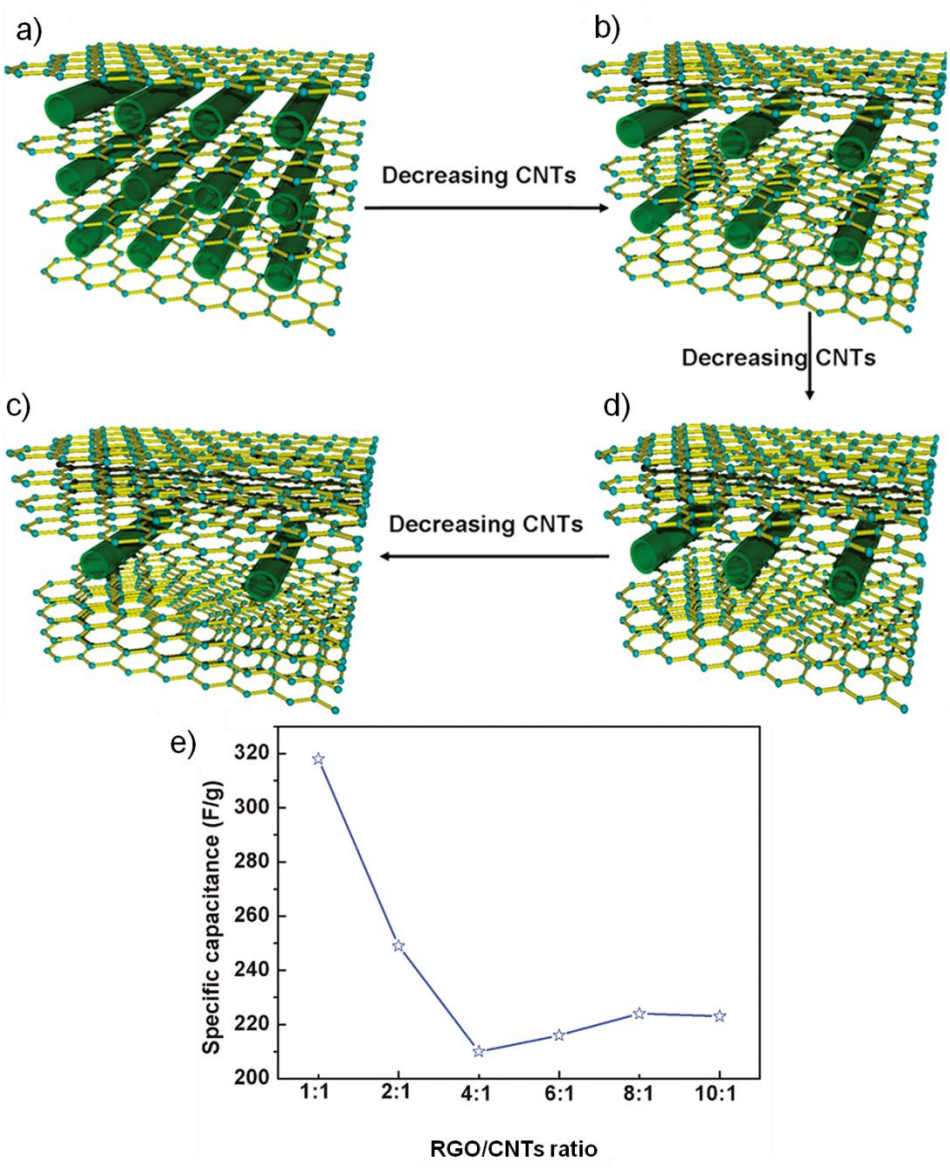

Figure 2.3. a-d) Schematic representation of 3D hybrid structure engineering with decreasing spacer **CNT** loading. e) Specific capacitance of **RGO/CNT** hybrids with different weight ratio of **RGO** to **CNTs**.

Even several molecules have been used to prevent re-stacking of **RGO**, π-gelators are less exploited in the exfoliation of **RGO** thereby increasing its electrochemical performance in energy storage devices.[48] In this work, we have shown the preparation of hybrid materials of **RGO** and **OPVs** with varying **RGO** content by

exploiting the supramolecular self-assembly process. It has also been shown that such self-assembled π-gelator acts as an excellent spacer to avoid re-stacking of individual graphene layers. The electrochemical performance of these hybrid materials as electrodes for supercapacitors has been studied.

2.3. Results and Discussion

2.3.1. Synthesis of OPV Derivatives

The **OPV** based π-gelator **OPV1** derivative was synthesized by reducing the bisaldehyde (**8**), according to a known procedure as shown in Scheme 2.1.[49-52] The 1,4-hydroquinone (**1**) on reaction with 1-bromohexadecane in DMF in the presence of NaOH readily afforded 1,4-(hexadecyloxy)benzene (**2**) in a 63% yield. Subsequent bromomethylation of **2**, as per a general bromomethylation procedure with paraform-aldehyde and HBr in acetic acid provided the bisbromomethyl derivative **3** in a 90% yield. Compound **3** on acetylation with potassium acetate afforded the compound **4** in a 88% yield which upon hydrolysis with KOH, resulted in the bisalcohol **5** in a 90% yield**.** Oxidation of the bisalcohol with pyridinium chlorochromate (PCC) gave the corresponding bisaldehyde **6** in a 92% yield.

The Wittig reaction of **6** with bisphosphonium salt **7**, which was prepared *in-situ* by the reaction of the bisbromo derivative **3** with PPh_3, yielded a mixture of *trans*- and *cis*-vinylene isomers of the conjugated bisaldehyde **8**. These isomeric mixtures

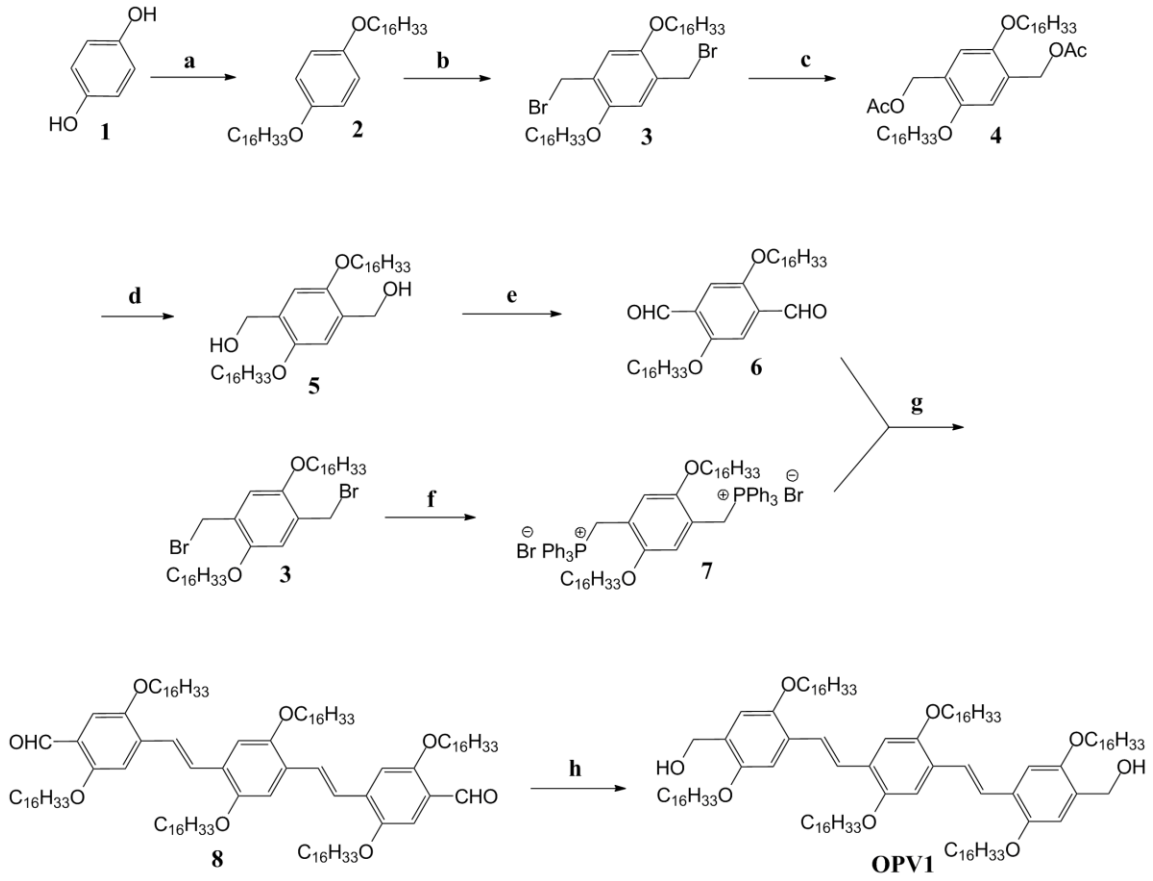

Scheme 2.1. Reagents and conditions for the synthesis of **OPV1**: a) 1-Bromohexadecane, NaOH, DMF, 100 °C, 24 h (63%). b) Paraformaldehyde, 33% HBr in CH_3COOH, glacial CH_3COOH, 70 °C, 4 h (90%). c) KOAc, TBAB, $CH_3CN/CHCl_3$, reflux, 12 h (88%). d) KOH (5N)/CH_3OH, distilled THF, reflux, 4 h (90%). e) PCC, CH_2Cl_2, 27 °C, 3 h (92%). f) PPh_3, dry C_6H_6, reflux, 4 h. g) i) LiOEt, dry CH_2Cl_2, 27 °C, 15 min; ii) I_2, CH_2Cl_2, 27 °C, 12 h (in dark) (71 %). h) $NaBH_4$, CH_3OH, CH_2Cl_2, 27 °C, 30 min (90 %).

were converted to the all-*trans* derivative by treating with iodine in dichloromethane at room temperature, in a 71% yield. The high efficiency of these synthetic transformations ensures the ease of isolation and purification of the products at each step. The bisalcohol functionalized **OPV** was synthesized by reduction of **8** with $NaBH_4$ in dichloromethane (Scheme 2.1).

Synthesis of **OPV2**, was accomplished by the Wittig-Horner reaction[50] of the bisphosphonate (**10)** with the monoaldehyde (**9**) using NaH in a 67% yield (Scheme 2.2). The monoaldehyde (**9**) was prepared by Vilsmeier formylation of 1,4-(hexadecyloxy)benzene (**2**) with α,α-dichloromethylethylether in a 78% yield. The corresponding bisphosphonate derivative (**10**) was prepared by the reaction of bisbromomethyl derivative (**3**) with triethyl phosphite.

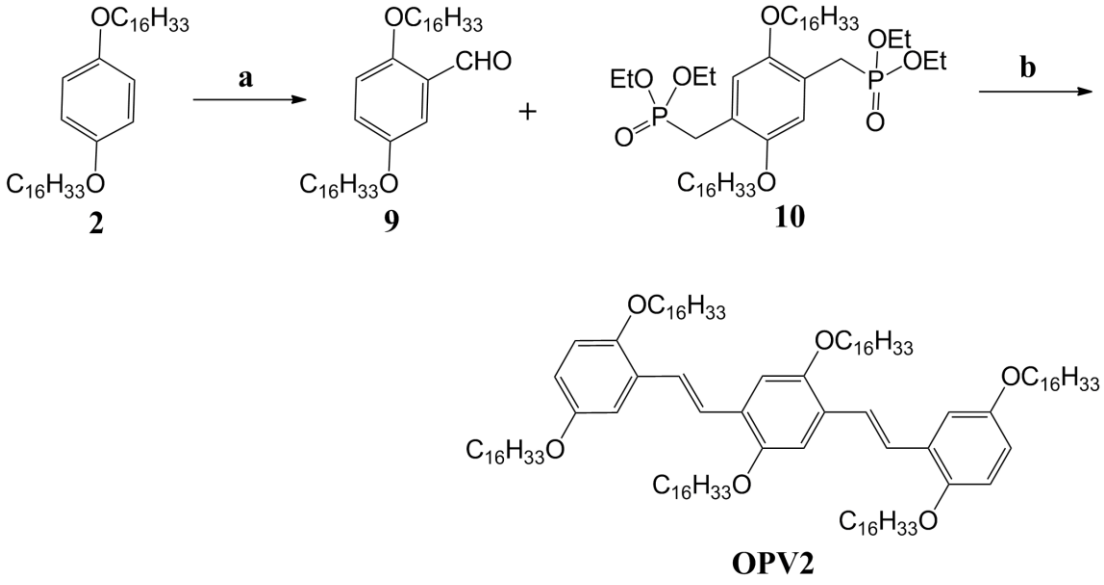

Scheme 2.2. Reagents and conditions for the synthesis of **OPV2**: a) $TiCl_4$, $Cl_2CHOC_2H_5$,CH_2Cl_2, 0 °C. b) NaH, THF, 70 °C, 10 h (67 %).

2.3.2. Preparation and Characterization of OPV1-2/RGO Hybrids

The **OPV/RGO** hybrid materials were prepared by chemical reduction ($NaBH_4$) of **GO** in the presence of the **OPV** based π-gelators (**OPV1-2**) in different ratios (Figure 2.4a). The resultant hybrid materials composed of **OPV1-2** and **RGO** were redispersed in THF to get the exfoliated **RGO** sheets. The exfoliated **OPV/RGO** hybrid materials

were obtained after removing the solvent by evaporation. The dried samples were used for further studies.

The ability of the prepared hybrids to disperse in organic solvents was monitored by sonicating them in various solvents for a few min. **OPV1/RGO** hybrid was well dispersible in most of the non-polar and polar aprotic solvents. The resultant solutions were found stable for a week without the settling of larger graphene particles (Figure 2.4b). The dispersion test of **OPV1/RGO** was carried out in various solvents that include *n*-hexane, *n*-decane, cyclohexane, chloroform ($CHCl_3$), dichloromethane, toluene, ODCB and THF. Although the hybrid materials showed better dispersion in all of the above solvents, the amount of hybrid material dispersed was higher in a few solvents such as toluene, ODCB and THF. The amount of **RGO** dispersed in the solvents has been calculated by conventional gravimetric method.[23] Photophysical studies of the hybrid materials were performed to understand the interaction between **OPV1** molecules and **RGO**. The absorption and emission spectra of **OPV1** in the presence and absence of **RGO** are shown in Figures 2.5a and 2.5b, respectively. The absorption spectrum of **OPV1** (1×10^{-4} M) in toluene in the absence of **RGO** showed a maximum at 410 nm with no aggregation band (Figure 2.5a). **OPV1/RGO** hybrid (0.5 mg of **OPV1/RGO** with 2 wt% of **RGO** in 1 mL of toluene, concentration of **OPV1** = 8×10^{-5} M) exhibited a blue shifted absorption maximum at 398 nm with decreased absorbance and a broad absorption around 470 nm. The decrease in the intensity of absorption with the broadening of the peak around 470 nm indicates the assembly of **OPV1** molecules on the surface of **RGO**. The effect of temperature on the

aggregation behavior of **OPV1** in the hybrid material was studied by heating the above toluene solution of **OPV1/RGO** from 20-40 °C (inset of Figure 2.5a). The blue shifted absorption peak at 398 nm slowly changed to 409 nm with an increase in the absorb-

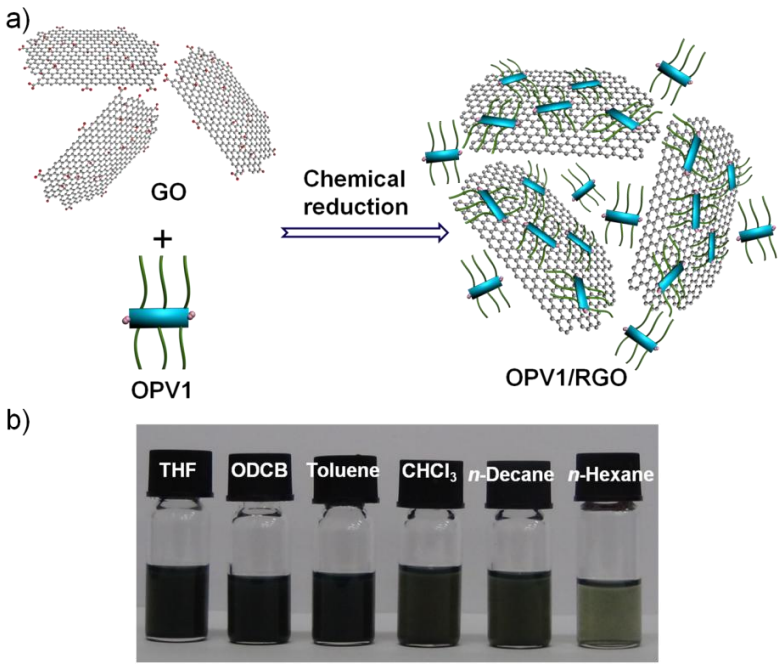

Figure 2.4. a) Schematic representation showing preparation of **OPV1/RGO** hybrids from graphene oxide (**GO**) via chemical reduction ($NaBH_4$ in THF/MeOH (10:1). b) Photograph showing dispersion of **OPV1/RGO** hybrid in various solvents (6 mg of **OPV1/RGO** with 30% of **RGO** in 1 mL of solvent).

ance. Further, the intensity of the broad absorption band at 470 nm corresponding to the aggregation of **OPV1** is gradually decreased and vanished at 40 °C. This observation indicates that the **OPV1** molecules are self-assembled on the surface of **RGO** leading to the exfoliation of the latter. The small decrease in the absorbance of **OPV1/RGO** at 660 nm upon heating to 40 °C can be attributed to the re-stacking and settling of the dispersed **RGO** sheets as the π-π interaction between **OPV1** and **RGO** as well as the hydrogen bonding (H-bonding) interaction among **OPV1** molecules

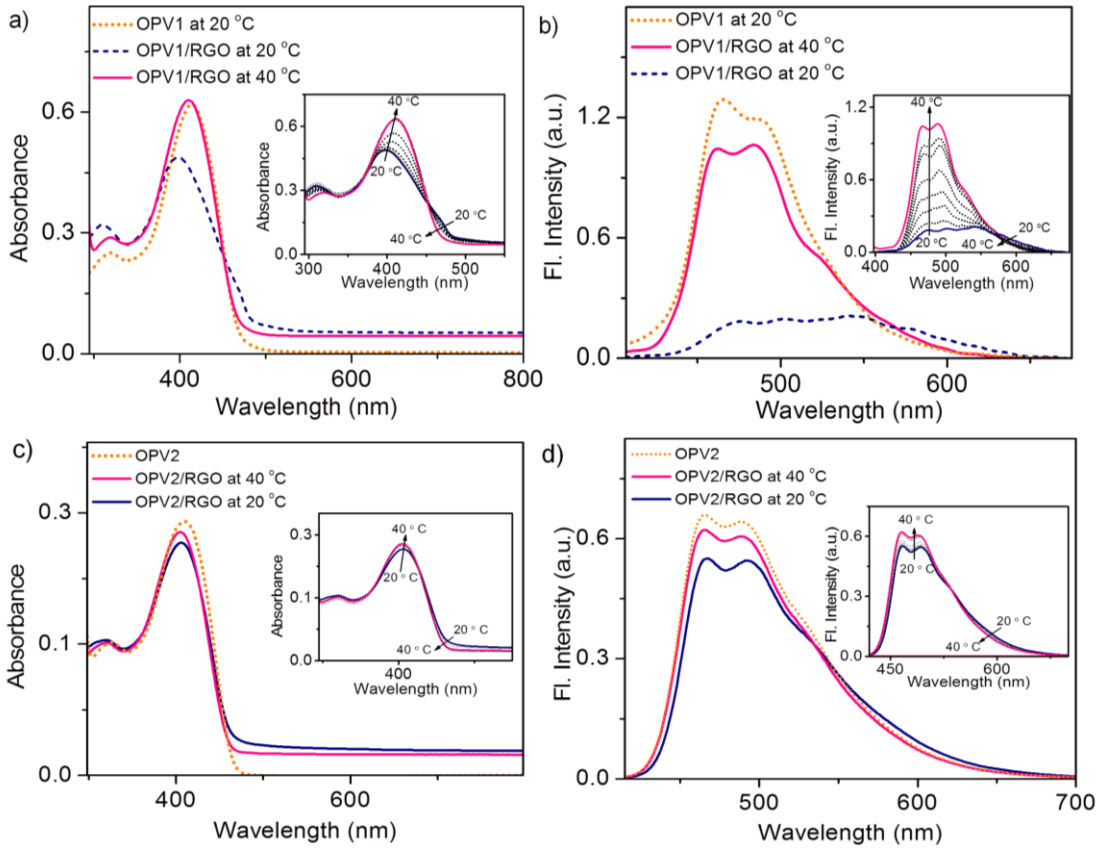

Figure 2.5. a), c) Absorption and b), d) fluorescence spectra of **OPV1** and **OPV2** (c = 1 × 10^{-4} M) and their hybrids (0.5 mg with 2 wt% of **RGO** in 1 mL) in toluene (l = 1 mm, λ_{ex} = 380 nm). Insets show the variable temperature absorption and fluorescence spectra, respectively.

diminished at higher temperatures. The settled **RGO** particles can be redispersed by cooling to 20 °C followed by sonication. This observation reveals that the interaction of **OPV1** plays a key role in the exfoliation of **RGO** in solution phase. The emission spectrum of **OPV1** exhibited two peaks at 465 and 496 nm, whereas **OPV1/RGO** showed a broad peak with less intensity from 450 to 600 nm at 20 °C in toluene (Figure 2.5b). On heating the toluene solution of **OPV1/RGO**, the broad emission peak slowly changed to the monomer emission of **OPV1** indicating the disaggregation of **OPV1** from the surface of **RGO** (inset of Figure 2.5b). Since **OPV2** has a weak

aggregation tendency when compared to **OPV1**, it exhibited very small changes in the absorption and fluorescence spectra as shown in the Figures 2.5c and 2.5d.

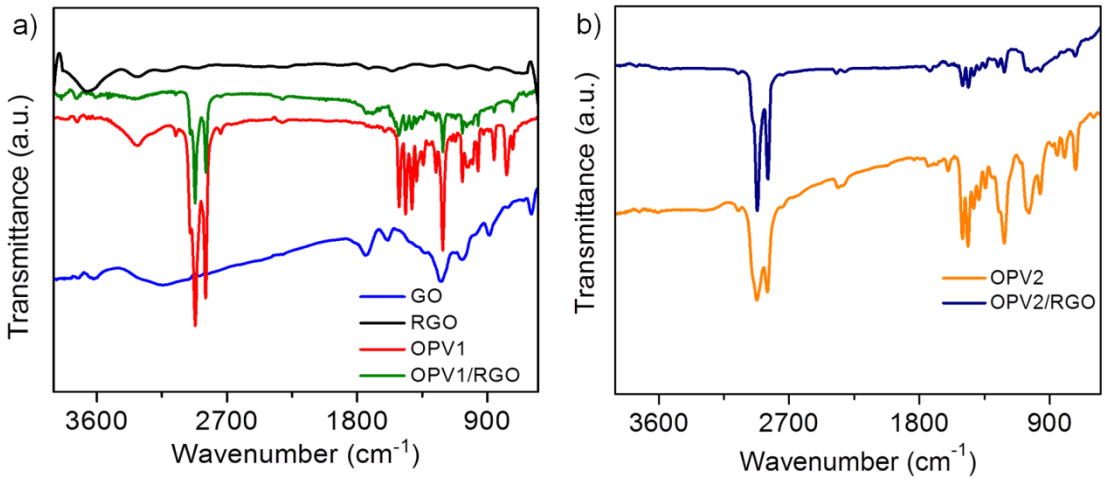

Figure 2.6. FT-IR spectra of a) **GO**, **RGO**, **OPV1** and **OPV1/RGO** and b) **OPV2** and **OPV2/RGO**.

In addition to the photophysical experiments, other spectroscopic techniques such as infrared and Raman spectroscopy were used to characterize the **OPV1-2/RGO** hybrid materials. Fourier transform infrared (FT-IR) spectrum of the **GO** showed peaks corresponding to -O-H (3619 cm^{-1}), COOH (1595 cm^{-1}), epoxide C-O-C (1222 cm^{-1}) and C=O (1739 cm^{-1}) (Figure 2.6a). These peaks became less intense in the FT-IR spectra of **RGO** and **OPV1/RGO** due to the removal of most of the functional groups from the surface of **GO** upon chemical reduction. The characteristic peaks of the **OPV1** at 3320 cm^{-1} (-OH), 2922 and 2848 cm^{-1} (aromatic C-H stretching mode) and 700-900 cm^{-1} (aromatic C-H out of plane bending mode) indicate the absence of any structural changes of **OPV1** during the process of chemical reduction. The aromatic C-H bending mode around 700-900 cm^{-1} had almost diminished in the case of **OPV1/RGO** hybrid. This observation indicates that there is a strong π-π interaction

between **OPV1** and **RGO**. **OPV2/RGO** exhibited broad peaks in the region of 700-900 cm^{-1} (aromatic C-H out of plane bending vibration) due to π-π interaction between **OPV2** and **RGO** sheets (Figure 2.6b).

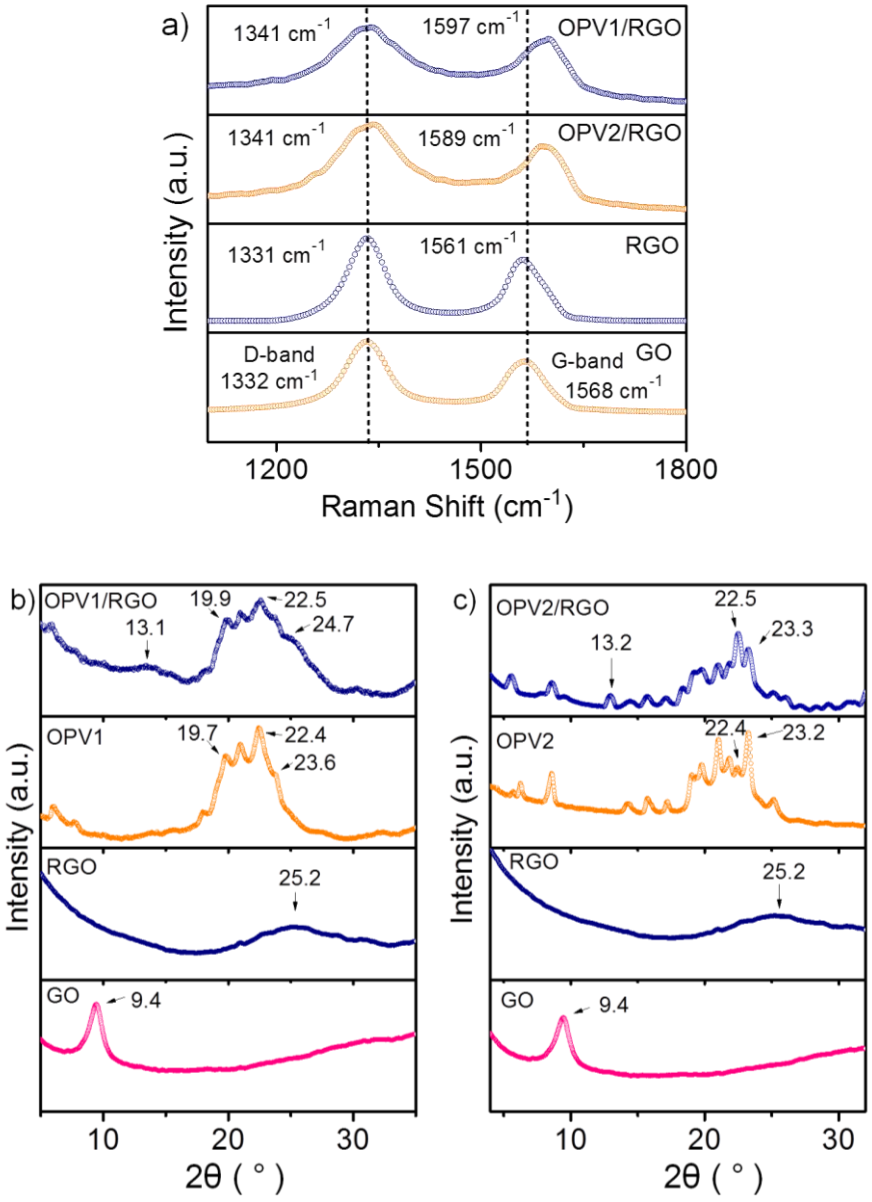

Figure 2.7. a) Raman spectra of **GO**, **RGO**, **OPV1/RGO** and **OPV2/RGO**. b) and c) XRD profiles of **GO**, **RGO**, **OPV1**, **OPV2** and their hybrids.

Raman spectroscopic studies gave evidence of exfoliation of **RGO** by **OPV1**. Raman spectrum of **GO** exhibited the D-band and the G-band at 1332, 1568 cm^{-1}, respectively (Figure 2.7a). **RGO** showed D-band with a slight shift to 1331 cm^{-1} and G-band to 1561 cm^{-1} with considerable downshift of 7 cm^{-1}. The downshift of G-band is an indication of the re-stacked and un-exfoliated **RGO** sheets. In the case of **OPV1/RGO** hybrid, the D-band at 1341 cm^{-1} became broad, and the G-band appeared at 1597 cm^{-1} with upshift of 36 cm^{-1} when compared to that of **RGO**. The larger upshift of G-band is an evidence of the exfoliation of **RGO** sheets into a few layers in the presence of **OPV1** through π-π interaction.[53-54] The ratio of the intensities of D- and G-bands (I_D/I_G) gave the information about the defect sites in the **RGO** and **OPV1/RGO** hybrid material. The value of (I_D/I_G) of **GO** was 1.2, whereas it became 1.1 and 1.08 in the case of **RGO**, **OPV1/RGO** respectively. This observation indicates that the amount of defects present in the **RGO** and **OPV1/RGO** are less when compared to that of **GO**. **OPV2/RGO** showed D-band at 1341 cm^{-1} and G-band at 1589 cm^{-1} with the upshift of 28 cm^{-1} when compared to that of **RGO**. The value of (I_D/I_G) of **OPV2/RGO** was 1.09 which indicated the defects present in the graphene sheets. X-ray diffraction (XRD) studies were used to understand the interlayer spacing in the hybrid material. The XRD of **GO** exhibited a peak at 9.4° (2θ) corresponding to a d-spacing of 0.94 nm (Figure 2.7b). The larger d-spacing of **GO** is due to the functional groups present on the basal plane of **GO**. In the case of **RGO**, a broad peak appeared around 25.2° (2θ) corresponding to the interlayer d-spacing of 0.35 nm. The smaller d-spacing (0.35 nm) of **RGO** reveals that the individual sheets are closely

stacked in the case of **RGO** when compared to that of **GO**. In contrast, a broad peak around 13.1° (2θ, d-spacing = 0.67 nm) was observed for **OPV1/RGO** hybrid, indicating a larger interlayer distance arising from the exfoliated **RGO** sheets, mediated by **OPV1** due to π-π interaction between them. The XRD peaks corresponding to **OPV1** persisted with less shifted 2θ values in **OPV1/RGO** hybrid, indicating that **OPV1** follows similar self-assembly process in both native and hybrid materials. **OPV2/RGO** also showed the similar changes in the XRD studies as **OPV1/RGO** (Figure 2.7c).

When the amount of **OPV1/RGO** hybrid is increased up to a certain concentration (5.4 mg of **OPV1/RGO** with 2 wt% of **RGO** in 1 mL of solvent) in non-polar solvents such as toluene, the resultant solution became non-flowing solid mass (gel). A photograph of the hybrid gels of **OPV1/RGO** with varying **RGO** contents is shown in Figure 2.8a. The gel melting temperature (T_{gel}) of the hybrid gels as well as the native gel were measured and plotted against the percentage of **RGO** (Figure 2.8b). The gradual increase in the T_{gel} of the hybrid gels from 42-53 °C with an increasing percentage of **RGO** (0 – 10 wt %), shows the improved stability of the hybrid gels with increased content of **RGO**. The viscoelastic properties of the native and the hybrid gels were studied by rheological measurement (Figure 2.8c). In this measurement, storage modulus (*G'*) and loss modulus (*G"*) of the hybrid gels showed the characteristic solid and liquid-like behavior of a viscoelastic material. *G'* and *G"* of the native and the hybrid gels exhibited a plateau over a range of angular frequency from 0.01 to 100 rad s^{-1}. Since the difference between the *G'* and *G"* was almost one

order of magnitude, the native and hybrid gels can be considered as viscoelastic materials.[27] The storage modulus (*G'*) of the hybrid gel was higher than that of the native **OPV1** gel. This observation reveals that the stability of the former has been improved significantly than that of the latter as the exfoliated **RGO** sheets gave an additional physical strength to the hybrid gel.

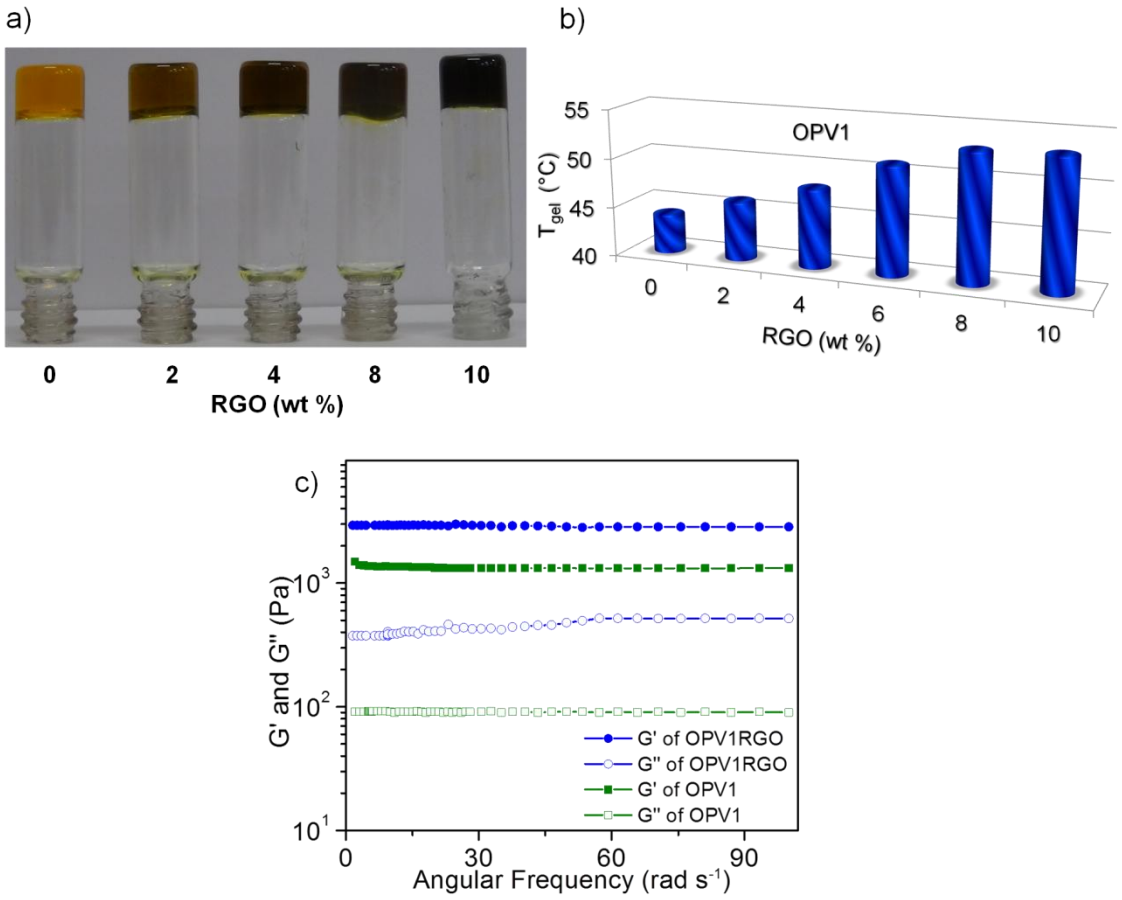

Figure 2.8. a) A Photograph of **OPV1** gels in toluene with various **RGO** contents (6 mg of **OPV1** in 1 mL of toluene for native gel and 5.4 mg of **OPV1/RGO** with 2-10 wt% of **RGO** in 1 mL of toluene for hybrid gels). b) Plot showing gel melting temperature (T_{gel}) of **OPV1** and **OPV1/RGO** gels with various amounts of **RGO** (2-10 wt %). c) Rheological behavior of **OPV1** and **OPV1/RGO** gels.

Morphological studies were carried out to explain the exfoliation of **RGO** by self-assembled **OPV1** molecules. Scanning electron microscope (SEM) investigation of **OPV1** gel exhibited entangled fibrous network structure (Figure 2.9a), whereas **RGO** drop cast from toluene showed micrometer-sized flakes as shown in Figure 2.9c. In the case of **OPV1/RGO** hybrid gel, the **OPV1** molecules self-assemble over the basal plane of the reduced graphene oxide sheets, resulting in one-dimensional network structures (Figure 2.9b). **OPV2/RGO** hybrid exhibited the self-assembled fibers of **OPV2** molecules on the surface of graphene (Figure 2.9d). These fibrous structures are responsible for the exfoliation of **RGO** sheets in the hybrid material. The native and the hybrid gels were drop cast on glass plates and analyzed by optical polarizing microscope (OPM). The dried **OPV1** gel showed rigid fiber like texture (Figure 2.10a), whereas hybrid gel exhibited entangled short fibers (Figure 2.10b) when cooled from their isotropic melt. Similarly, **OPV2** exhibited straight fiber-like textures, whereas **OPV2/RGO** showed short fiber-like textures (Figure 2.10c and 2.10d). The presence of exfoliated **RGO** sheets is responsible for the change in the refractive index of the hybrid gel, which led to a different kind of texture when compared to the native one. Transmission electron microscope (TEM) images of **OPV1**, **RGO** and **OPV1/RGO**, are showed in Figures 2.11. TEM image of **RGO** exhibited thick flakes of a few micrometer in size with several number of layers (Figure 2.11b), whereas in the case of **OPV1**, an entangled network structure of one-dimensional nanofibers having width of 100-200 nm were observed (Figure 2.11a). Self-assembled nanofibers of **OPV1** molecules were clearly seen on the surface of

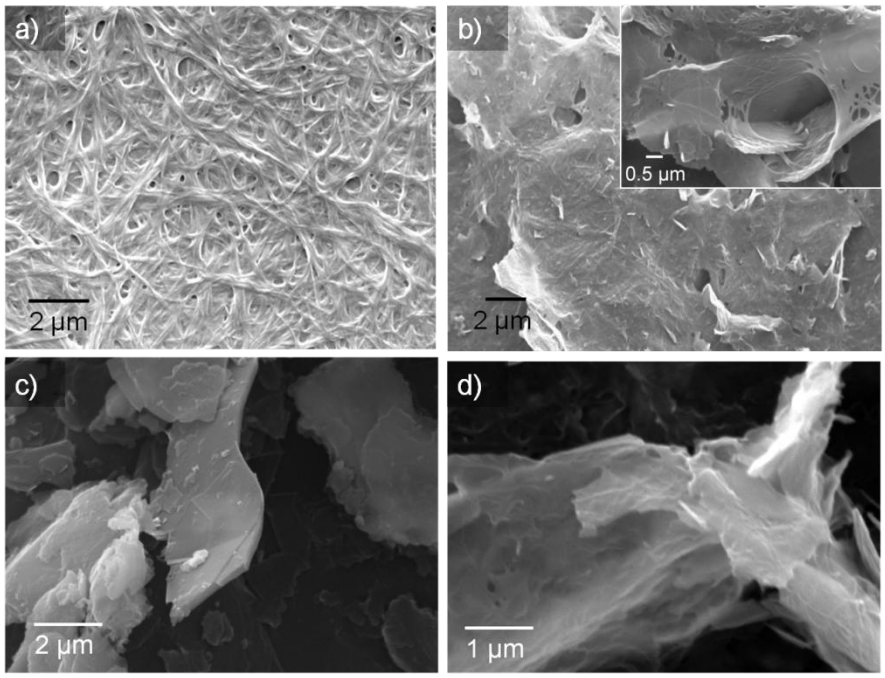

Figure 2.9. SEM images of a) **OPV1**, b) **OPV1/RGO**, c) **RGO**, and d) **OPV2/RGO** (Inset of (b) shows the 3D macroscopic structure of exfoliated **RGO** sheets with **OPV1** fibrous network structure).

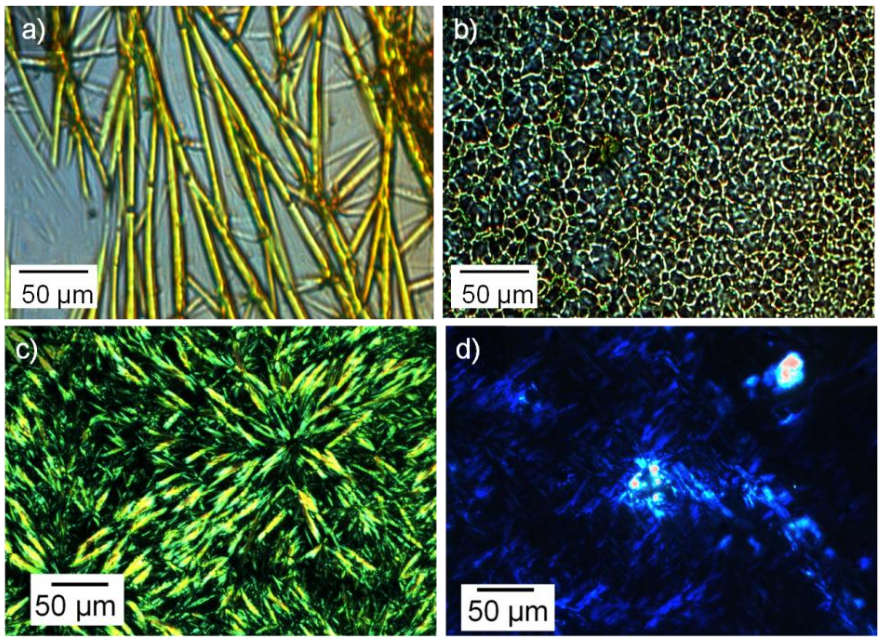

Figure 2.10. OPM images of a) **OPV1**, b) **OPV1/RGO**, c) **OPV2**, and d) **OPV2/RGO** hybrids.

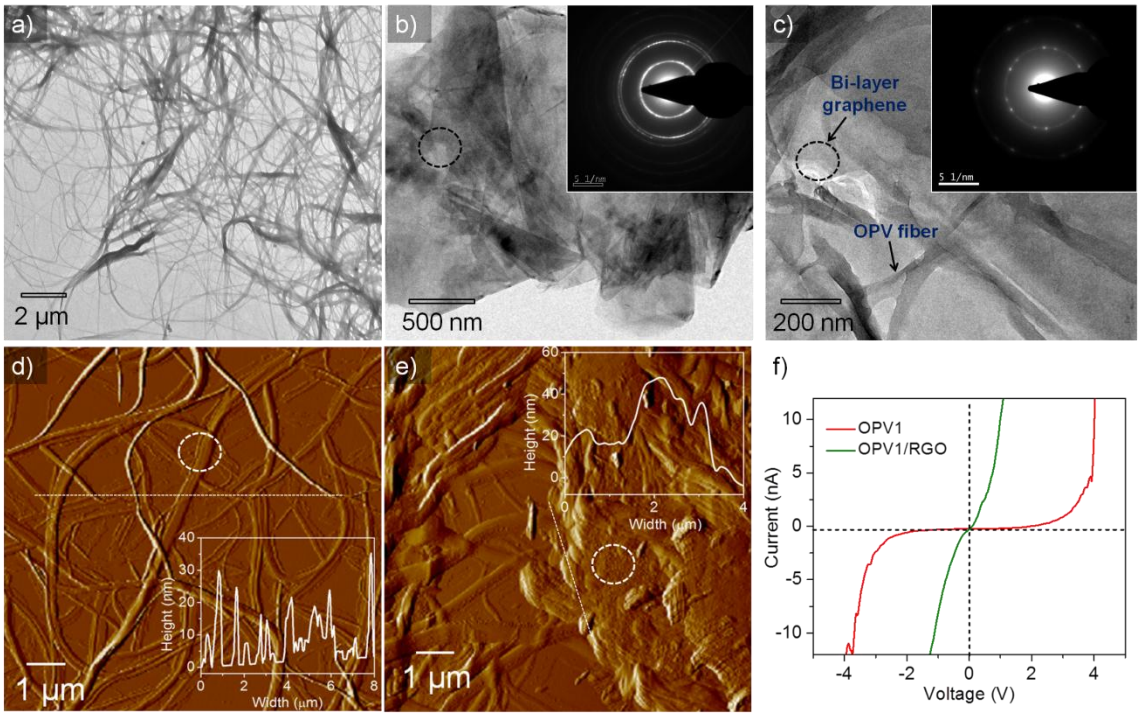

Figure 2.11. TEM images of a) **OPV1**, b) **RGO**, and c) **OPV1/RGO**, drop cast from toluene solution (insets of Figure 2.11b and 2.11c show SAED patterns in the marked regions respectively). AFM images of d) **OPV1** and e) **OPV1/RGO**, drop cast on freshly cleaved HOPG from toluene solution (insets of Figure 2.11d and 2.11e show height profiles corresponding to the marked regions). f) *I-V* responses of **OPV1** and **OPV1/RGO**, measured by C-AFM at encircled regions of Figure 2.11d and 2.11e, respectively.

RGO sheets in the case of **OPV1/RGO** hybrid (Figure 2.11c). The number of layers in a graphene flake was confirmed by selected area electron diffraction (SAED) experiment. The SAED patterns obtained from **OPV1/RGO** sample exhibited the characteristic spots corresponding to bi-layer of exfoliated graphene sheets (inset of Figure 2.11c), whereas in the case of **RGO**, SAED exhibited a ring-like pattern due to the disordered arrangement of several number of **RGO** sheets in bulk sample (inset of Figure 2.11b). Atomic force microscope (AFM) analysis of **OPV1** showed nanometer-

sized entangled fibers with height of 10-30 nm and width of 100-250 nm (Figure 2.11d), whereas **OPV1/RGO** showed fibrous network structure over the exfoliated **RGO** sheets with height of 20-50 nm (Figure 2.11e). Even though the height of the reduced bi-layer graphene oxide sheets is expected to be in the range of 2 nm, the increased height of the exfoliated sheets in the **OPV1/RGO** is attributed to the presence of several nanometer-sized self-assembled fibers on the surface of the **RGO** sheets.

The *I-V* response of **OPV1** by conductive AFM (C-AFM) measurements revealed an insulator-like behavior with a conductivity of 5.7×10^{-6} S m^{-1} (Figure 2.11f), whereas in the case of **OPV1/RGO**, conductor-like *I-V* characteristic was observed with a measured conductivity of 4.1 S m^{-1}. The bulk conductivity of these materials was also calculated by four-probe measurement. **OPV1/RGO** showed better

Table 2.1. Four-probe (electrical) conductivity measurements of **RGO**, **OPV1**, **OPV2** and their hybrids.

Sample	RGO	OPV1	OPV2	OPV1/RGO	OPV2/RGO
Bulk Conductivity (S m^{-1})	5.2	1.2×10^{-6}	3.5×10^{-7}	3.7	1.8

conductivity than **OPV1** and their values are listed in Table 2.1. The lower conductivity of **OPV1/RGO**, when compared to that of **RGO**, can be attributed to the increased contact resistance when the **OPV1** molecules self-assembled on the surface of the exfoliated graphene sheets. We measured the surface area of the **OPV1/RGO**

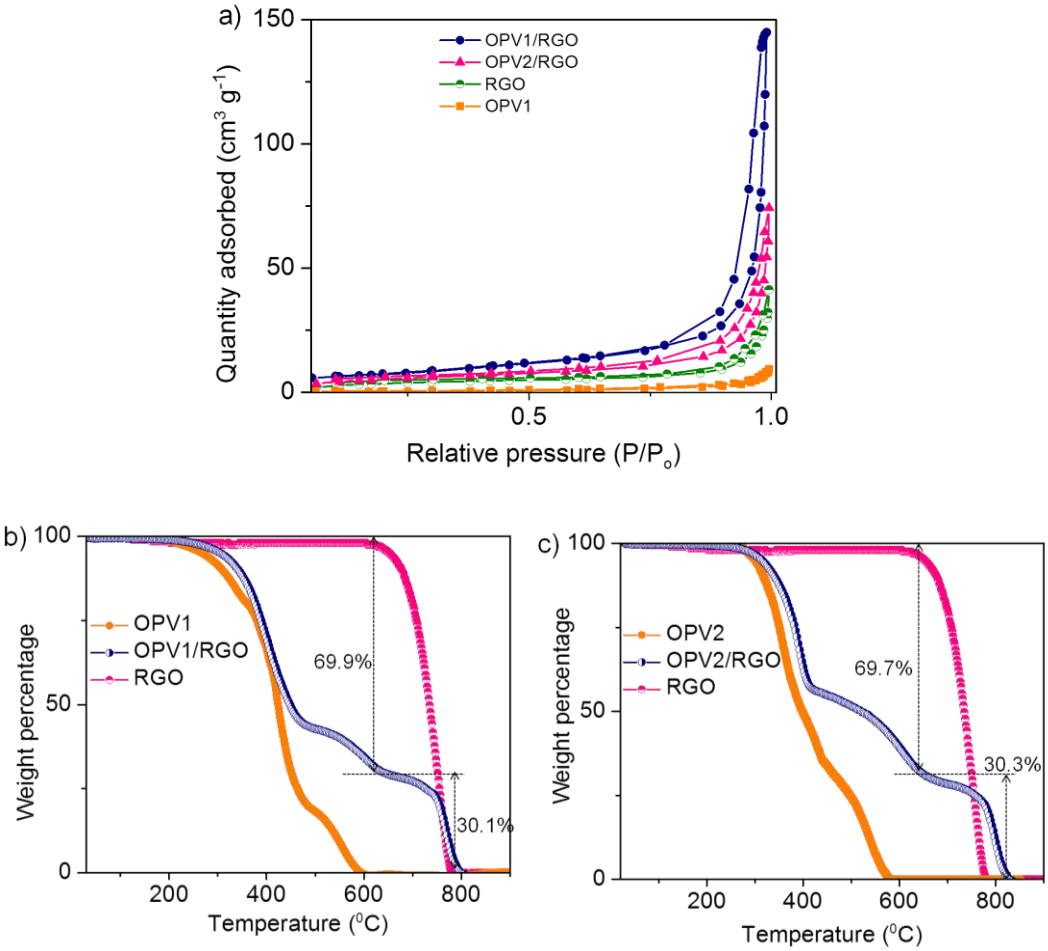

Figure 2.12. a) BET surface area analyses of **OPV1**, **RGO**, **OPV1/RGO**, and **OPV2/RGO**. TGA curves of c) **OPV1/RGO** and d) **OPV2/RGO** with the **RGO** content of 30%. The measurements were carried out under nitrogen atmosphere with the heating rate of 10 °C min^{-1}.

hybrid (30% of **RGO**) as it exhibited more exfoliated graphene sheets, evident from the dispersion test and the morphological studies. Brunauer–Emmett–Teller (BET) surface area measurement revealed that **OPV1/RGO** had a surface area of ~250 m^2 g^{-1}, whereas **RGO** and **OPV1** showed ~120 m^2 g^{-1}, ~40 m^2 g^{-1}, respectively (Figure 2.12a). The N_2 adsorption behavior of all materials exhibited type-III adsorption isotherm with

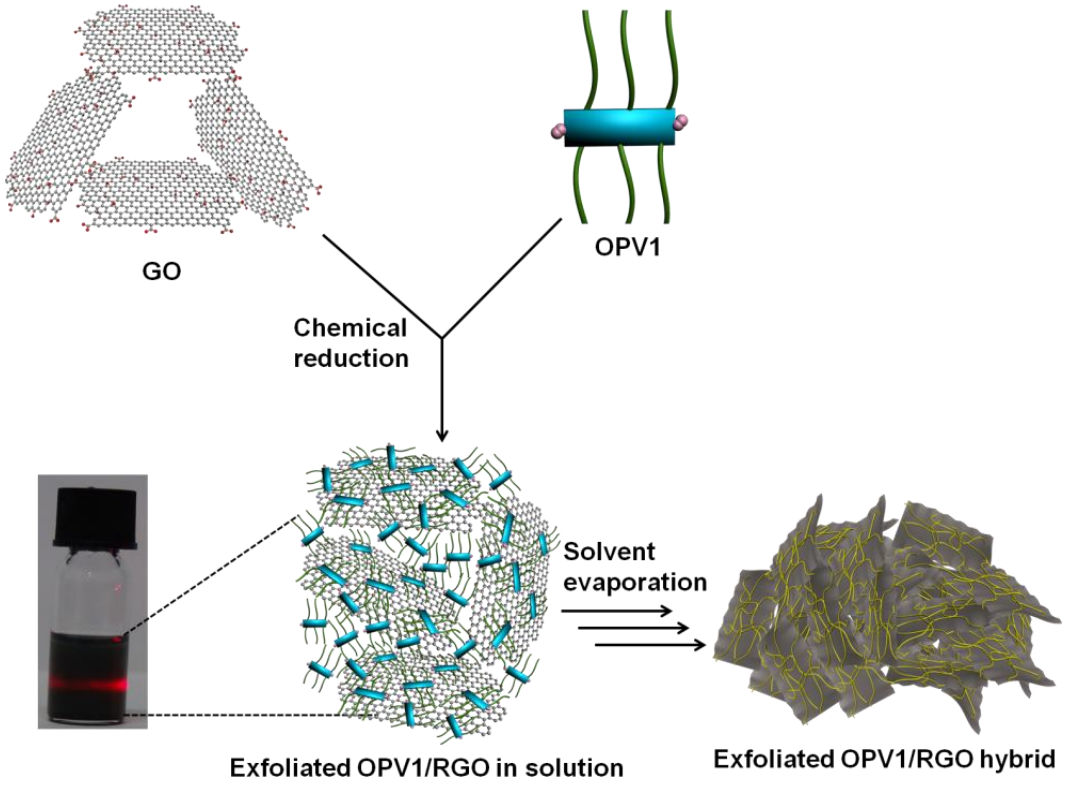

Scheme 2.3. Schematic representation of the formation of exfoliated **OPV1/RGO** hybrid through a self-assembly process (laser illumination exhibits Tyndall effect from dispersed graphene sheets in toluene).

respect to the IUPAC standards. The type-III adsorption isotherm is an indication of macroscopic porosity of the hybrid material. The gas adsorption and desorption processes followed almost similar path with slight deviation. The increased surface area of the hybrid materials can be attributed to the self-assembly of **OPV1** on the surface of the individual **RGO** sheets that prevent re-stacking into graphite-like structure. The formation of exfoliated **RGO** sheets with self-assembled **OPV1** molecules on their surface is shown in Scheme 2.3. These results prompted us to explore the electrochemical performance of the hybrid materials since it exhibited improved surface area and conductivity required for an electrode material for energy

storage devices such as supercapacitors.[41,55-57] For this purpose, we used **OPV1/RGO** hybrid with 30% of **RGO** content. The contents of **RGO** in **OPV1/RGO** and **OPV2/RGO** hybrids were confirmed by thermal gravimetric analysis (TGA) (Figure 2.12b and 2.12c).

2.3.3. Supercapacitor Studies of OPV1-2/RGO Hybrids

Two-electrode configuration closely mimics the physical configuration of a real capacitor and is the best way of assessing the performance of a supercapacitor. Hence, electrochemical energy storage property of **OPV1/RGO** hybrid was evaluated in symmetric two-electrode configuration. Cyclic voltammograms (CVs) for symmetric supercapacitors based on **RGO** and **OPV1/RGO** at different scan rates ranging from 1-100 mV s^{-1} are shown in Figure 2.13a and 2.13c, respectively. Both the samples retained nearly rectangular CV loops, indicating ideal capacitive behavior and low contact resistance. The galvanostatic charge-discharge curves of **RGO** and **OPV1/RGO** at different constant current densities ranging from 1-20 A g^{-1} (Figure 2.13b and 2.13d, respectively) maintained triangular shape with a very low ohmic drop, characteristic of excellent capacitive behavior. The CV loops of **OPV1**, **RGO**, and **OPV1/RGO** at a scan rate of 5 mV s^{-1} are shown in Figure 2.13e. The difference in the areas of the CV loops for these samples indicate different levels of stored charges in them. It is also evident that the capacitive performance of **OPV1** based symmetric capacitor is negligibly small. Figure 2.13f shows the comparison of the galvanostatic charge-discharge curves for these supercapacitors at a constant current

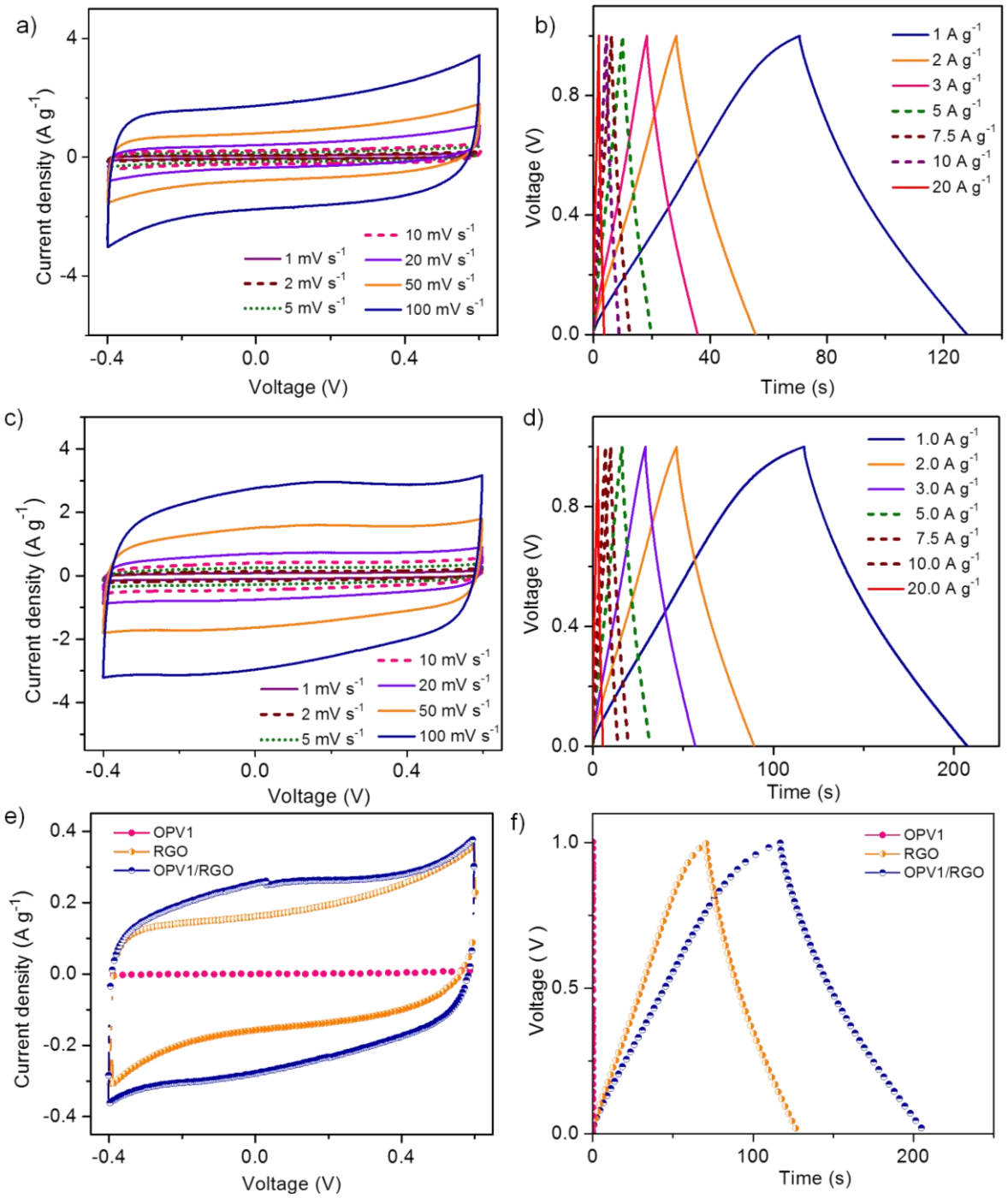

Figure 2.13. a) and c) CV curves at various scan rates, b) and d) galvanostatic charge-discharge curves at various current densities of **RGO** and **OPV1/RGO** (30 wt% of **RGO**), respectively. e) CV curves at a scan rate of 5 mV s^{-1}, and f) galvanostatic charge-discharge curves at a current density of 1 A g^{-1} of **OPV1**, **RGO**, and **OPV1/RGO**.

density of 1 A g^{-1}. The constant current charge-discharge curves of devices are nearly triangular, with reduced internal resistance at the beginning of the discharge curve. The specific capacitance values for the symmetric supercapacitors based on **OPV1**, **RGO**, and **OPV1/RGO** samples are < 1, 114 and 181 F g^{-1} respectively. The excellent electrochemical performance exhibited by **OPV1/RGO**, with only 30% of **RGO** content, could be due to its higher electroactive accessible surface area when compared to **RGO**, though **RGO** showed better electrical conductivity than **OPV1/RGO**.

Variations in specific capacitance of **RGO** and **OPV1/RGO** with increasing current densities are shown in Figure 2.14a. In general, at lower current densities (from 1–5 A g^{-1}), the specific capacitance decreases with the increase in discharge current density, due to the internal resistance of the electrode. The accessibility of electrolyte ions to the inner part of the electrode at lower current density values provides a maximum coverage of all available pores of the electrode material. In contrast, at higher current densities, only the outer surface of electrode material is available to the electrolyte ions, which leads to the lower specific capacitance values. At current densities above 5 A g^{-1}, specific capacitance tends to get stabilized. **OPV1/RGO** hybrid exhibited more than 60% of its capacitance (181 F g^{-1} at a current density of 1 A g^{-1}) even at a higher current density of 20 A g^{-1}, indicating the relatively good high-rate capability. **RGO** based symmetric capacitor is also able to retain ~57% of its capacitance at the high current density of 20 A g^{-1}. The cycle life is another important factor for evaluating the performance of supercapacitors. Cyclic stability curves for

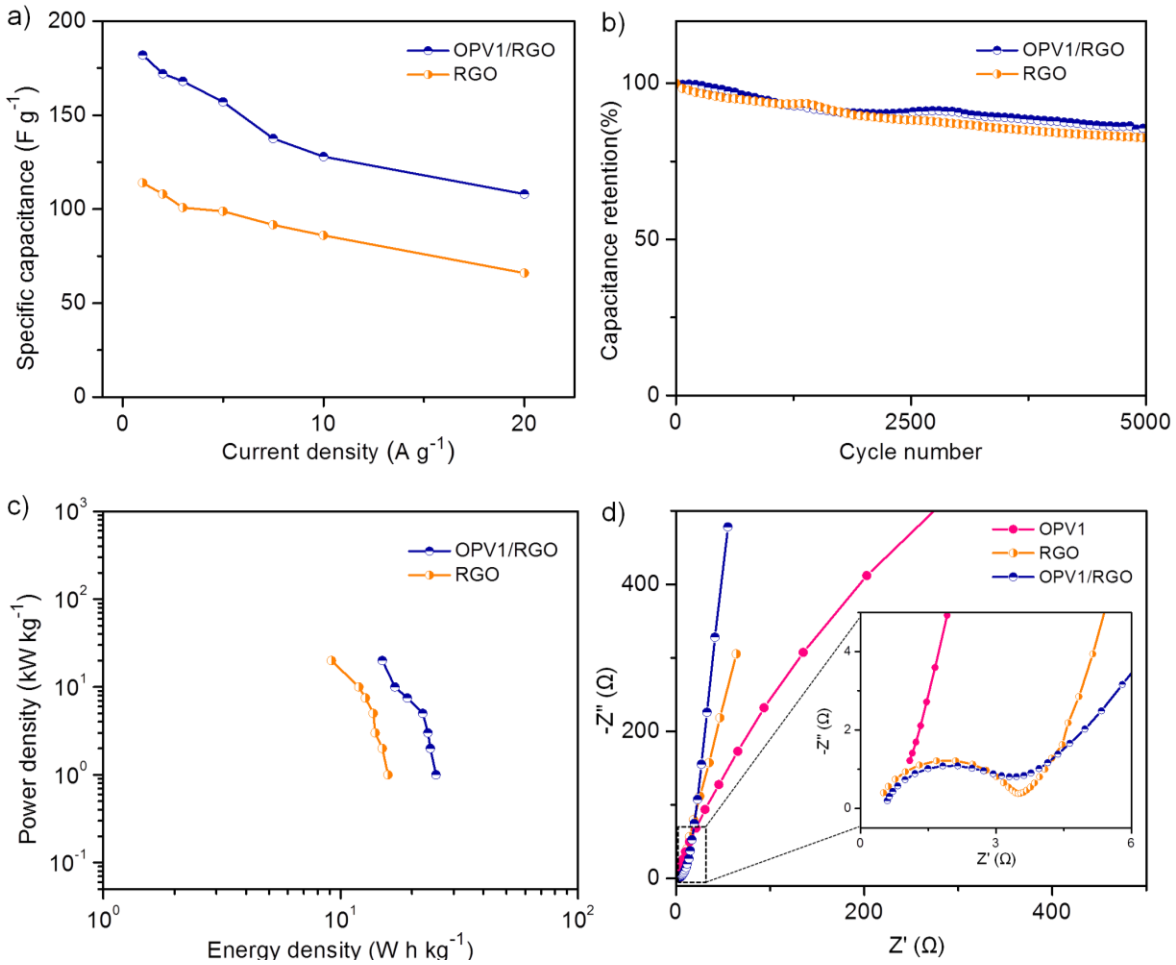

Figure 2.14. a) Specific capacitance *vs.* current density and b) capacitance retention *vs.* cycle number plots of **OPV1/RGO** (30 wt% of **RGO**) and **RGO**. c) Ragone and d) Nyquist plots of **OPV1**, **RGO** and **OPV1/RGO** (30 wt% of **RGO**).

symmetric supercapacitors at a constant current density of 1 A g^{-1} are illustrated in Figure 2.14b. The specific capacitance values for both **RGO** and **OPV1/RGO** based symmetric capacitors gradually decrease with increasing cycles. At the end of 5000 cycles, supercapacitors based on **RGO** and **OPV1/RGO** samples retain respectively ~84% and ~88% of their maximum capacitance. Improved stability exhibited by **OPV1/RGO** could be due to the presence of the self-assembled π-gelator on the

surface of the exfoliated **RGO** sheets, which is absent in the case of bare **RGO**. Figure 2.14c shows the Ragone plot (power density *vs*. energy density) of the symmetric supercapacitors based on **RGO** and **OPV1/RGO**. By using the charge-discharge curves at various current densities, energy (E) and power densities (P) of **RGO** and **OPV1/RGO** were calculated based on the equations (1 and 2).

$$E = \frac{1}{2} C_{sp} \Delta V^2 \qquad \text{(Eq. 1)}$$

where 'ΔV' is a voltage difference during the discharge process and C_{sp} is the calculated specific capacitance.

$$P = \frac{E}{\Delta t} \qquad \text{(Eq. 2)}$$

where 'Δt' is the discharge time.

RGO and **OPV1/RGO** showed the energy densities of 9 and 15 W h kg^{-1} at a power density of 20 kW kg^{-1}. At the same time, the calculated energy densities of **RGO** and **OPV1/RGO** were as high as 16 and 26 W h kg^{-1} at a power density of 0.2 kW kg^{-1}. From the analysis of Ragone plot, it is evident that **OPV1/RGO** works as a very promising electrode material for high-performance supercapacitors. The experimental impedance spectra (Nyquist plots) for symmetric capacitors based on **OPV1**, **RGO**, and **OPV1/RGO** are shown in Figure 2.14d. A straight line followed by a semicircle arc in low- and high-frequency regions respectively, are the characteristics of a Nyquist plot. The resistance (R_s) corresponding to the bulk electrolyte solution can be measured from an intercept of the real axis at high frequency. The diameter of the semicircle in the high-frequency range gives the value of charge transfer resistance

Table 2.2. Comparison of specific capacitance values of a few reported **RGO** hybrids with **OPV1/RGO**.

S. No.	Material	Specific Capacitance ($F\ g^{-1}$)	Reference
1.	Chemical activation of exfoliated graphene oxide (EGO)	166	*Science*, **2011,** *332*, 1537-1541
2.	Chemically modified graphene	135	*J. Phys. Chem. C*, **2011**, *115*, 12367-12374
3.	Graphene/ionic liquid	154.1	*Nano Lett.*, **2010**, *10*, 4863-4868
4.	RGO/polymer multilayer	394 μF/*cm2*	*Nano Lett.*, **2011**, *11*, 1423-1427
5.	RGO by solvothermal method	276	*J. Phys. Chem. C*, **2011**, *115*, 7120-7125
6.	RGO/MnO2 (~50% of RGO)	188	*J. Phys. Chem. C*, **2011**, *115*, 6448-6454
7.	RGO/propylene carbonate (~55% of RGO)	140	*Phys. Chem. Chem. Phys.*, **2011**, *13*, 17249-17254
8.	Graphene sheet	122.6	*Carbon* **2010**, *48*, 1731-1737
9.	Graphene based	99-134	*Nano lett.*, **2008**, *8*, 3498-3502
10.	Graphene /SnO_2 (~45% of RGO)	43.4	*Nanotechnology*, **2009**, *20*, 455602-455607
11.	**π-Gelator/RGO hybrid (OPV1/RGO)** (30% of RGO)	**181**	**Present work**

(R_{ct}), which can be related to the electrical conductivity and electroactive surface area of the electrode material. If the electroactive surface area is larger, the R_{ct} would be lower. The line at the low-frequency region makes an angle of 45° with the real axis. This line is called the Warburg line, and it depends on the ionic diffusion of electrolyte into the interface of the electrode materials. **OPV1/RGO**, **RGO**, and **OPV1** exhibited

low values of R_s in the range of 0.5-0.9 Ω, indicating uniform contact at the interface of substrates and active materials. **OPV1** showed huge impedance at higher frequency region due to its poor conductivity and very low surface area, exhibiting very poor electrochemical performance. **OPV1/RGO** exhibited the R_{ct} value of 2.5 Ω in comparison with **RGO** (3.0 Ω), which indicates the better electroactive surface area of the hybrid. Exfoliated **GOs**, prepared by chemical activation[58] and microwave exfoliation method[59], have been reported to exhibit the specific capacitances of 166 and 191 F g^{-1} respectively. **RGO** based hybrid materials with MnO_2,[60] SnO_2,[61] and propylene carbonate[48] showed specific capacitance values of 188, 43, 140 F g^{-1} respectively (Table 2.2). In the present work, we have achieved the specific capacitance value of 181 F g^{-1} at current density of 1 A g^{-1} for exfoliated π-gelator/**RGO** (**OPV1/RGO**) hybrid material having just 30% of **RGO**, thus maximizing the accessible surface area, resulting in much higher specific capacitance.

In order to find out the role of aggregation of molecules in the electrochemical properties as well as in the exfoliation of **RGO**, electrochemical performance studies were conducted for **OPV2** and **OPV2/RGO**. From the photophysical studies, it has been shown that **OPV2** has less aggregation tendency when compared to that of **OPV1** under similar conditions. Results showed that the extent of exfoliation of **RGO** sheets by **OPV2** was less when compared to that of **OPV1**, which in turn led to comparatively low performance in electrochemical behavior (Figure 2.15). This observation highlights the fact that the aggregation behavior of π-conjugated molecules has a strong influence on the extent of exfoliation and the electrochemical

performance. More precisely, it can be stated that the π-π, H-bonding, and van der Waals interactions are responsible for stronger aggregation of **OPV1** while, only π-π and van der Waals interactions led to lesser aggregation behavior of **OPV2**.

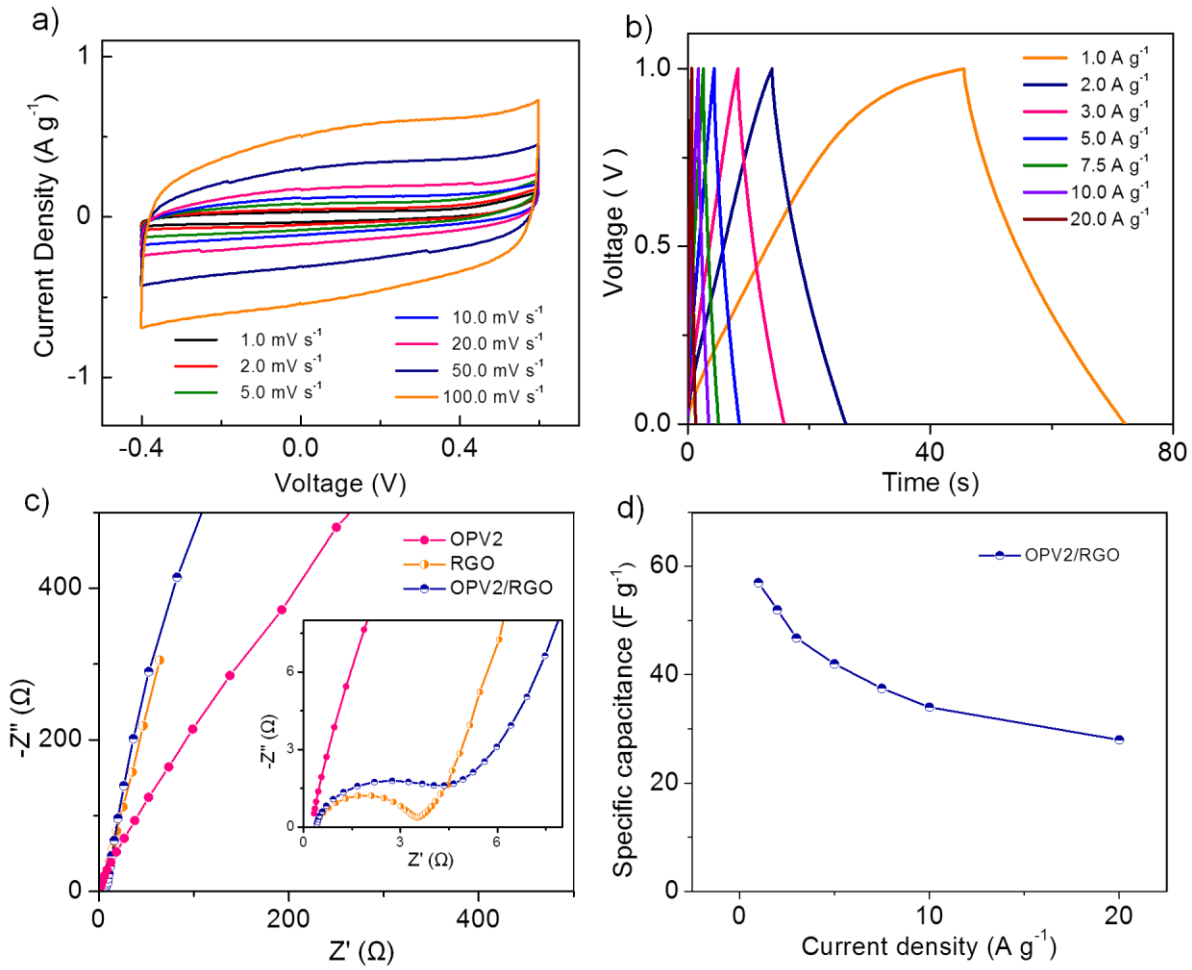

Figure 2.15. a) Cyclic voltammograms at various scan rates, b) galvanostatic charge-discharge curves at various current densities of **OPV2/RGO**. c) Nyquist plot of **OPV2**, **RGO** and **OPV2/RGO**. d) Specific capacitance *vs.* current density plot of **OPV2/RGO**.

2.4. Conclusions

In summary, we have demonstrated the influence of π-gelators on the exfoliation of reduced graphene oxide sheets that resulted in an improved electrochemical

performance of the resulted hybrid material with lesser graphene content. Photophysical studies showed the aggregation behavior of the gelator and the extent of dispersion of graphene sheets in the solution state. The detailed gelation and rheological studies revealed the improved stability of the hybrid gel when compared to that of the native gel. Morphological studies using SEM, OPM, AFM and TEM indicated that the self-assembly of the π-gelator on the surface of graphene sheets facilitates the exfoliation of the latter into a bi-layer/few-layer graphene sheets. Superior electrochemical performance was obtained for the hybrid materials with lesser **RGO** content, which has the potential as supercapacitors for energy storage application.

2.5. Experimental Section

2.5.1. General

Graphite powder (particle size < 20μm) was purchased from Aldrich. **OPVs** were synthesized and characterized according to the literature method.[27,62,48-51] ^{1}H and ^{13}C NMR spectra were recorded on a 500 MHz Bruker Advance DPX spectrometer using TMS as internal standard. FT-IR spectra were recorded on a Shimadzu IR Prestige-21 Fourier Transform Infrared Spectrophotometer. High-resolution mass spectra were measured on a JEOL JM AX 505 HA mass spectrometer. Matrix-assisted laser desorption ionization time-of-flight (MALDI-TOF) mass spectra were obtained on a Shimadzu AXIMA-CFR PLUS spectrometer by using α-cyano-4-hydroxycinnamic acid as a matrix.

2.5.2. Synthesis and Characterization of OPVs

OPV1-2 were prepared according to the literature method[27,62,49-52] and unambiguously characterized.

Preparation of OPV1. The bisaldehyde **8** (356 mg, 0.2 mmol) was dissolved in a mixture of methanol (25 mL) and dichloromethane (175 mL). To this solution, $NaBH_4$ (0.4 mmol) was added and stirred at room temperature for 30 minutes. The reaction mixture was poured into water and extracted with dichloromethane. The organic layer was dried over anhydrous Na_2SO_4 and the solvent was removed to give the corresponding bisalcohol derivative **OPV1** as a yellow solid. The crude product was then purified by column chromatography (100-200 mesh) using 1:1 $CHCl_3$-hexane mixture as an eluent.

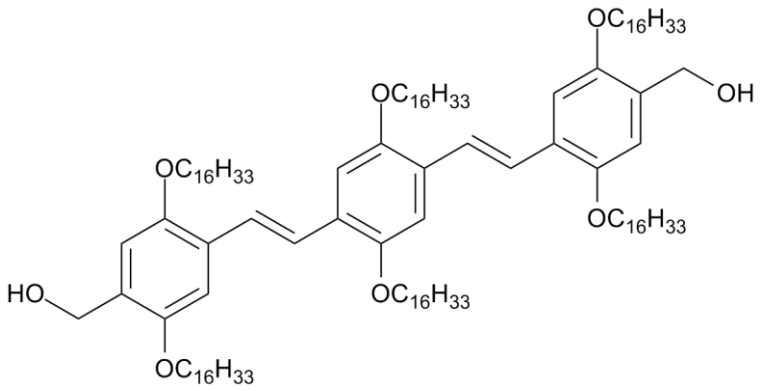

OPV1

Yield: 92%; **m. p.**: 113-114 ºC; **FT-IR** (KBr) ν_{max}: 3381, 2918, 2845, 1511, 1460, 1418, 1388, 1341, 1259, 1202, 1068, 1011, 965, 851 cm^{-1}. **^{1}H NMR** (300 MHz, $CDCl_3$) δ: 7.46 (s, 4H, phenyl-*H*), 7.13 (d, 4H, vinyl-*H*), 6.86 (s, 2H, phenyl-*H*), 4.68

(s, 4H, –CH_2OH), 3.97-4.04 (m, 12H, –OCH_2–), 2.30 (br, 2H, –O*H*), 1.25-1.83 (m, 168H, –CH_2–), 0.85-0.88 (m, 18H, –CH_3) ppm; **^{13}C NMR** (75 MHz, $CDCl_3$) δ: 151.0, 150.6, 129.2, 127.3, 127.2, 123.3, 122.6, 114.0, 110.7, 109.1, 69.7, 69.4, 68.5, 62.3, 31.9, 29.7, 29.5, 29.4, 29.3, 28.9, 28.7, 26.3, 26.2, 22.6, 14.1 ppm; **MALDI-TOF-MS**: calculated *m/z* for $C_{120}H_{214}O_8$: 1783.63, found: 1783.55.

Preparation of OPV2. Synthesis of **OPV2**, was accomplished by the Wittig-Horner reaction of the bisphosphonate (**10**) with monoaldehyde (**9**) using NaH in a 65% yield.[50]

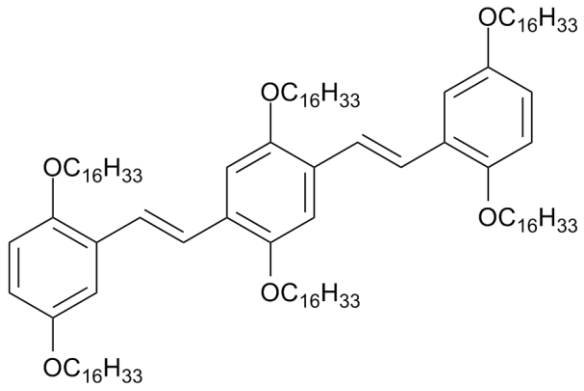

OPV2

Yield: 67%; **m. p.:** 111-112 ºC; **FT-IR** (KBr) ν_{max}: 2923, 2840, 1506, 1465, 1429, 1398, 1347, 1254, 1223, 1074, 965, 847, 790, 720 cm^{-1}. **^{1}H NMR** (300 MHz, $CDCl_3$) δ : 7.34-7.42 (m, 4H, vinyl-*H*), 7.06-7.18 (m, 4H, phenyl-*H*), 6.71-6.87 (m, 4H, phenyl-*H*), 3.94-4.04 (m, 12H, –OCH_2–), 1.26-1.85 (m, 168H, –CH_2–), 0.86-0.89 (m, 18H, –CH_3) ppm; **^{13}C NMR** (75 MHz, $CDCl_3$) δ: 153.3, 151.5, 150.9, 129.2, 128.3, 127.4, 114.0, 113.4, 112.2, 110.7, 69.5, 68.6, 31.9, 29.7, 29.6, 29.58, 29.4, 29.3, 26.2, 26.2,

26.1, 22.6, 14.0 ppm; **MALDI-TOF-MS**: calculated *m/z* for $C_{118}H_{210}O_6$: 1723.61, found: 1723.58.

2.5.3. Description on Experimental Techniques

Measurements

Absorption and emission spectra were measured on a Shimadzu UV-3101 PC NIR scanning spectrophotometer and SPEX-Fluorolog F112X spectrofluorimeter. Variable temperature studies were performed in a 1 mm quartz cuvette with a thermistor which is attached to the cuvette holder wall. Raman spectra were recorded using a HR800 LabRAM confocal Raman spectrometer operating at 20 mW laser power (He-Ne laser source with 633 nm excitation wavelength) using a peltier cooled CCD detector. Samples for the SEM imaging were prepared by drop casting a toluene solution of the **OPV1-2/RGO** hybrids on aluminium grid. SEM imaging was performed on a Zeiss EVO 18 Cryo Special Edition with variable pressure detector working at 20-30 kV. OPM studies were performed using a Leica DFC 490 microscope with heating and cooling stage connected to a temperature programmer (Mettler Toledo FP82HT). TEM was performed on a JEOL-JEM0310 microscope with an accelerating voltage of 300 kV. Samples were prepared by drop casting the toluene solution of the **OPV1-2/RGO** hybrids on carbon coated TEM grids. NTEGRA (NT-MDT) atomic force microscope (AFM) operating in tapping mode regime was used to record the AFM images under ambient conditions and the offline mode was used to do AFM section analysis. Samples for AFM analysis were prepared by drop casting the toluene solution on freshly cleaved mica surface followed by drying at ambient conditions. The

rheological properties of the **OPV1** and the hybrid gels with **RGO** were measured using a Physical Modular Compact (MCR 150) rheometer from Anton Paar. The gap of 0.14 mm was fixed between the cone and the plate. Angular frequency-sweep (ω) measurements were carried out in the of 0.01 to 100 rad s^{-1} with a constant strain amplitude (γ) of 1% at 25 °C. The gel melting temperatures (T_{gel}) of the gels were measured by the dropping ball method (weight of steel ball = 100 mg).[27] Thermogravimetric analysis (TGA) was performed on a Shimadzu Thermal Analyser at a heating rate of 10 °C per min in nitrogen atmosphere.

Preparation of OPV1-2/RGO Hybrids

A typical procedure for the preparation of the **OPV1-2/RGO** hybrids with varying weight percentages of **RGO** is as follows: Graphene oxide (prepared by modified Hummer's method)[63] (0.5-9.5 mg) and **OPV1-2** (9.5-0.5 mg) were sonicated in 50 mL of dry THF for 1 h. To this suspension, a mixture of 200 mg of $NaBH_4$ and 5 mL of methanol was immediately added and the resultant suspension was subsequently heated to 80 °C for 2 h. After cooling to room temperature, the solvent was removed under vacuum and the hybrid material was washed with water to remove excess salts. The resultant hybrid materials were redispersed in THF to get exfoliated **RGO** sheets. The exfoliated **OPV/RGO** hybrid materials were obtained after removing the solvent by evaporation. The dried samples were used for further studies.

General Procedure for Gelation

The hybrid gels were prepared by heating **OPV1/RGO** (5.4 mg) with various **RGO** contents (2-10 wt %) to 40 °C in toluene (1 mL) and then sonicating for 1-2 min.

The resultant dispersion was cooled to room temperature and the non-flowing solid-like mass while inverting the glass vial upside down confirmed the formation of gels. The dried gel samples were prepared by slow evaporation of solvent under ambient condition.

Electrochemical studies

The electrodes for the electrochemical studies were prepared by mixing active material (60%) with acetylene black (30%) and PVDF (10%) in NMP solvent. The slurry was coated on stainless steel plate and dried at 120 °C in vacuum for at least 5 h. Two-electrode configuration was used for all the measurements in presence of 6 M KOH as electrolyte in a multichannel work station (Biologic VMP3).

2.6. References

(1) Geim, A. K. *Science* **2009**, *324*, 1530-1534.

(2) Li, C.; Liu, M.; Pschirer, N. G.; Baumgarten, M.; Müllen, K. *Chem. Rev.* **2010**, *110*, 6817-6855.

(3) Weiss, N. O.; Zhou, H.; Liao, L.; Liu, Y.; Jiang, S.; Huang, Y.; Duan, X. *Adv. Mater.* **2012**, *24*, 5782-5825.

(4) Jariwala, D.; Sangwan, V. K.; Lauhon, L. J.; Marks, T. J.; Hersam, M. C. *Chem. Soc. Rev.* **2013**, *42*, 2824-2860.

(5) Perreault, F.; Fonseca de Faria, A.; Elimelech, M. *Chem. Soc. Rev.* **2015**, *44*, 5861-5896.

(6) Georgakilas, V.; Tiwari, J. N.; Kemp, K. C.; Perman, J. A.; Bourlinos, A. B.; Kim, K. S.; Zboril, R. *Chem. Rev.* **2016**, *116*, 5464-5519.

(7) Ji, Q.; Honma, I.; Paek, S.-M.; Akada, M.; Hill, J. P.; Vinu, A.; Ariga, K. *Angew. Chem. Int. Ed.* **2010**, *49*, 9737-9739.

(8) Wu, L.; Ohtani, M.; Takata, M.; Saeki, A.; Seki, S.; Ishida, Y.; Aida, T. *ACS Nano* **2014**, *8*, 4640-4649.

(9) Matsumoto, M.; Saito, Y.; Park, C.; Fukushima, T.; Aida, T. *Nat. Chem.* **2015**, *7*, 730-736.

(10) Wang, J.; Manga, K.; Bao, Q.; Loh, K. *J. Am. Chem. Soc.* **2011**, *133*, 8888-8891.

(11) Weiss, N. O.; Zhou, H.; Liao, L.; Liu, Y.; Jiang, S.; Huang, Y.; Duan, X. *Adv. Mater.* **2012**, *24*, 5782-5825.

(12) Chang, H.; Wu, H. *Adv. Funct. Mat.* **2013**, *23*, 1984-1997.

(13) Hirsch, A.; Englert, J. M.; Hauke, F. *Acc. Chem. Res.* **2013**, *46*, 87-96.

(14) Gao, W.; Alemany, L. B.; Ci, L.; Ajayan, P. M. *Nat. Chem.* **2009**, *1*, 403-408.

(15) Paredes, J. I.; Villar-Rodil, S.; Martínez-Alonso, A.; Tascón, J. M. D. *Langmuir* **2008**, *24*, 10560-10564.

(16) Dreyer, D. R.; Park, S.; Bielawski, C. W.; Ruoff, R. S. *Chem. Soc. Rev.* **2009**, *39*, 228-240.

(17) Chua, C. K.; Pumera, M. *Chem. Soc. Rev.* **2014**, *43*, 291-312.

(18) Chua, C. K.; Pumera, M. *Chem. Soc. Rev.* **2013**, *42*, 3222-3233.

(19) An, X.; Simmons, T.; Shah, R.; Wolfe, C.; Lewis, K. M.; Washington, M.; Nayak, S. K.; Talapatra, S.; Kar, S. *Nano Lett.* **2010**, *10*, 4295-4301.

(20) Hao, R.; Qian, W.; Zhang, L.; Hou, Y. *Chem. Commun.* **2008**, *0*, 6576-6578.

(21) Jo, K.; Lee, T.; Choi, H.; Park, J.; Lee, D.; Lee, D.; Kim, B.-S. *Langmuir* **2011**, *27*, 2014-2018.

(22) Lee, D. W.; Kim, T.; Lee, M. *Chem. Commun.* **2011**, *47*, 8259-8261.

(23) Qi, X.; Pu, K. Y.; Li, H.; Zhou, X.; Wu, S.; Fan, Q. L.; Liu, B.; Boey, F.; Huang, W.; Zhang, H. *Angew. Chem. Int. Edn.* **2010**, *49*, 9426-9429.

(24) Stankovich, S.; Dikin, D. A.; Dommett, G. H. B.; Kohlhaas, K. M.; Zimney, E. J.; Stach, E. A.; Piner, R. D.; Nguyen, S. T.; Ruoff, R. S. *Nature* **2006**, *442*, 282-286.

(25) Su, Q.; Pang, S.; Alijani, V.; Li, C.; Feng, X.; Müllen, K. *Adv. Mater.* **2009**, *21*, 3191-3195.

(26) Babu, S. S.; Praveen, V. K.; Ajayaghosh, A. *Chem. Rev.* **2014**, *114*, 1973-2129.

(27) Srinivasan, S.; Babu, S. S.; Praveen, V. K.; Ajayaghosh, A. *Angew. Chem. Int. Ed.* **2008**, *47*, 5746-5749.

(28) Adhikari, B.; Nanda, J.; Banerjee, A. *Chem. Eur. J.* **2011**, *17*, 11488-11496.

(29) Samanta, S. K.; Subrahmanyam, K. S.; Bhattacharya, S.; Rao, C. N. R. *Chem. Eur. J.* **2012**, *18*, 2890-2901.

(30) Vivekchand, S. R. C.; Rout, C. S.; Subrahmanyam, K. S.; Govindaraj, A.; Rao, C. N. R. *J. Chem. Sci.* **2008**, *120*, 9-13.

(31) Fan, Z.; Yan, J.; Wei, T.; Zhi, L.; Ning, G.; Li, T.; Wei, F. *Adv. Funct. Mater.* **2011**, *21*, 2366-2375.

(32) Mishra, A. K.; Ramaprabhu, S. *J. Phys. Chem. C* **2011**, *115*, 14006-14013.

(33) Pumera, M. *Energy Environ. Sci.* **2011**, *4*, 668-674.

(34) Choi, B. G.; Yang, M.; Hong, W. H.; Choi, J. W.; Huh, Y. S. *ACS Nano* **2012**, *6*, 4020-4028.

(35) Ghosh, S.; An, X.; Shah, R.; Rawat, D.; Dave, B.; Kar, S.; Talapatra, S. *J. Phys. Chem. C* **2012**, *116*, 20688-20693.

(36) Huang, Y.; Liang, J.; Chen, Y. *Small* **2012**, *8*, 1805-1834.

(37) Lee, J. H.; Shin, W. H.; Ryou, M. H.; Jin, J. K.; Kim, J.; Choi, J. W. *ChemSusChem* **2012**, *5*, 2328-2333.

(38) Reddy, A. L. M.; Gowda, S. R.; Shaijumon, M. M.; Ajayan, P. M. *Adv. Mater.* **2012**, *24*, 5045-5064.

(39) Kuila, T.; Mishra, A. K.; Khanra, P.; Kim, N. H.; Lee, J. H. *Nanoscale* **2013**, *5*, 52-71.

(40) Lee, J. H.; Park, N.; Kim, B. G.; Jung, D. S.; Im, K.; Hur, J.; Choi, J. W. *ACS Nano* **2013**, *7*, 9366-9374.

(41) Shao, Y.; El-Kady, M. F.; Wang, L. J.; Zhang, Q.; Li, Y.; Wang, H.; Mousavi, M. F.; Kaner, R. B. *Chem. Soc. Rev.* **2015**, *44*, 3639-3665.

(42) Wu, Z.-S.; Liu, Z.; Parvez, K.; Feng, X.; Müllen, K. *Adv. Mater.* **2015**, *27*, 3669-3675.

(43) Kundu, S.; Ragupathy, P.; Pillai, V. K. *J. Electrochem. Soc.* **2016**, *163*, A1112-A1119.

(44) Wang, Y.; Wu, Y.; Huang, Y.; Zhang, F.; Yang, X.; Ma, Y.; Chen, Y. *J. Phys. Chem. C* **2011**, *115*, 23192-23197.

(45) Yang, X.; Zhu, J.; Qiu, L.; Li, D. *Adv. Mater.* **2011**, *23*, 2833-2838.

(46) Yu, Y.; Sun, Y.; Cao, C.; Yang, S.; Liu, H.; Li, P.; Huang, P.; Song, W. *J. Mater. Chem. A* **2014**, *2*, 7706-7710.

(47) Song, B.; Sizemore, C.; Li, L.; Huang, X.; Lin, Z.; Moon, K.-s.; Wong, C.-P. *J. Mater. Chem. A* **2015**, *3*, 21789-21796.

(48) Sun, Y.; Wu, Q.; Shi, G. *Phys.Chem.Chem.Phys.* **2011**, *13*, 17249-17254.

(49) Ajayaghosh, A.; George, S. J. *J. Am. Chem. Soc.* **2001**, *123*, 5148-5149.

(50) George, S. J.; Ajayaghosh, A. *Chem. Eur. J.* **2005**, *11*, 3217-3227.

(51) Ajayaghosh, A.; Praveen, V. K. *Acc. Chem. Res.* **2007**, *40*, 644-656.

(52) Ajayaghosh, A.; Praveen, V. K.; Srinivasan, S.; Varghese, R. *Adv. Mater.* **2007**, *19*, 411-415.

(53) Gupta, A.; Chen, G.; Joshi, P.; Tadigadapa, S.; Eklund, P. C. *Nano Lett.* **2006**, *6*, 2667-2673.

(54) Ferrari, A. C. *Solid State Commun.* **2007**, *143*, 47-57.

(55) Armaroli, N.; Balzani, V. *Energy Environ. Sci.* **2011**, *4*, 3193-3222.

(56) Chen, D.; Feng, H.; Li, J. *Chem. Rev.* **2012**, *112*, 6027-6053.

(57) Damien, D.; Babu, B.; Narayanan, T. N.; Reddy, L. A.; Ajayan, P. M.; Shaijumon, M. M. *Graphene* **2013**, *1*, 37.

(58) Zhu, Y.; Murali, S.; Stoller, M. D.; Ganesh, K. J.; Cai, W.; Ferreira, P. J.; Pirkle, A.; Wallace, R. M.; Cychosz, K. A.; Thommes, M.; Su, D.; Stach, E. A.; Ruoff, R. S. *Science* **2011**, *332*, 1537-1541.

(59) Zhu, Y.; Murali, S.; Stoller, M. D.; Velamakanni, A.; Piner, R. D.; Ruoff, R. S. *Carbon* **2010**, *48*, 2118-2122.

(60) Zhang, J.; Jiang, J.; Zhao, X. S. *J. Phys. Chem. C* **2011**, *115*, 6448-6454.

(61) Fenghua, L.; Jiangfeng, S.; Huafeng, Y.; Shiyu, G.; Qixian, Z.; Dongxue, H.; Ari, I.; Li, N. *Nanotechnology* **2009**, *20*, 455602.

(62) Srinivasan, S.; Praveen, V. K.; Philip, R.; Ajayaghosh, A. *Angew. Chem. Int. Ed.* **2008**, *47*, 5750-5754.

(63) Hummers, W. S.; Offeman, R. E. *J. Am. Chem. Soc.* **1958**, *80*, 1339-1339.

Chapter 3

A Study on the Interaction of Chiral π-Gelators with Carbon Nanotubes

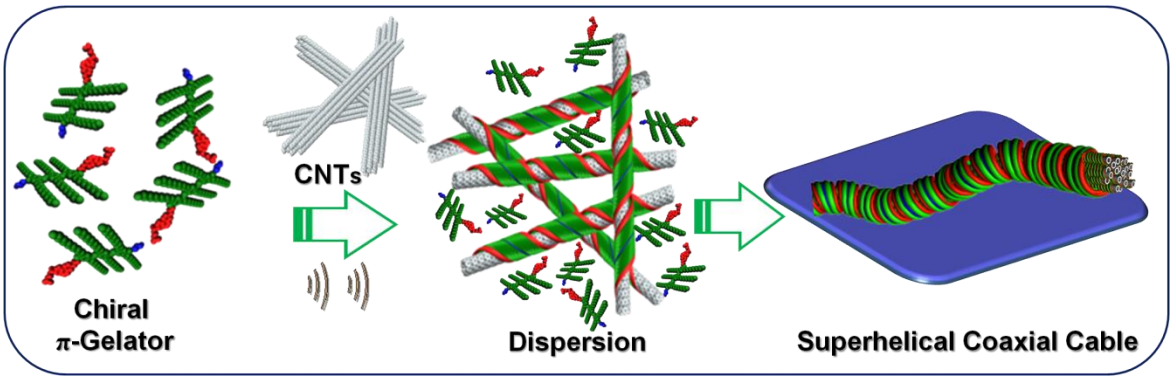

3.1. Abstract

*In an attempt to gather experimental evidence for the influence of carbon allotropes on supramolecular chirality, we studied the interaction of carbon nanotubes (**CNTs**) with **OPV** based chiral π-gelators. It has been found that **CNTs** facilitate the amplification of molecular chirality of the π-gelator, **MC-OPV** at a concentration much lower than that required for intermolecular interaction. For example, at a concentration 1.8 × 10^{-4} M, **MC-OPV** did not exhibit CD signal, however, addition of 0-0.6 mg of **SWNT** resulted in amplified chirality as evident from the CD spectrum. AFM analysis of the hybrid material revealed the formation of thick helical fibers of >100 nm. From the high resolution TEM analysis and solid-state UV-Vis-NIR spectrum, it was established that the thick helical fibers are cylindrical cables composed of individually wrapped and coaxially aligned **SWNTs**. Such a magnificent effect of **CNTs** on supramolecular chirality and cylindrical cable formation has not been reported previously.*

3.2. Introduction

Nature creates several helical and multiple helical architectures; from simple α-helix of polypeptides and double helix of nucleic acids to more complex helical proteins, microtubules and collagen triple helix structures.[1-5] These architectures are formed through specific pathways in which molecular building blocks are fixed in appropriate positions.[6-10] It is important to understand the pathways developed and utilized by nature to construct such functional helical structures. This knowledge will not only help to understand life, but also enable the design and construction of new functional helical architectures.[11-14] Formation of these structures are

controlled by various factors which include molecular size, shape, morphology, etc. Most of these helical structures use non-covalent interactions such as H-bonding, π-π stacking, van der Waals interactions, to arrive supramolecular architectures. It is well known that the chiral character of building blocks in helical polymers decides their chiroptical properties. Polymers made from homochiral monomers, will show net optical activity, that could be measured by circular dichroism spectroscopy. In case of copolymers, the net optical activity depends on the fraction of homochiral building blocks present in that polymer, even though a large amount achiral monomers are present. This phenomenon is called 'chirality amplification', also refered to as "sergeants-soldiers effect". If helical copolymers are comprised of both enantiomers of a chiral monomer, then the copolymer structure is controlled by "majority rule". [15-18] Both covalently bound and supramolecular polymers have been studied theoretically and experimentally to explain the "sergeants-soldiers" principle and the "majority rule".

Meijer *et al.* have reported the occurance of chirality amplification in supramolecular aggregates of π-systems through "sergeants-soldiers effect".[19] The compound **1a** exhibited a cooperative model of self-assembly to form highly ordered chiral columns, in diluted alkane solutions (10^{-4} – 10^{-6} mol L^{-1}; Figure 3.1a). The CD spectrum of disc shaped molecule **1a** was negative and strong in dodecane at room temperature, however no CD response was seen in chloroform (Figure 3.1b). In presence of chiral solvent, the derivative **1b** showed more negative Cotton effect than that of **1a** in dodecane. A strong Cotton effect was observed when 2.5 mol % of the chiral **1a** was added to the achiral **1b** in hexane.

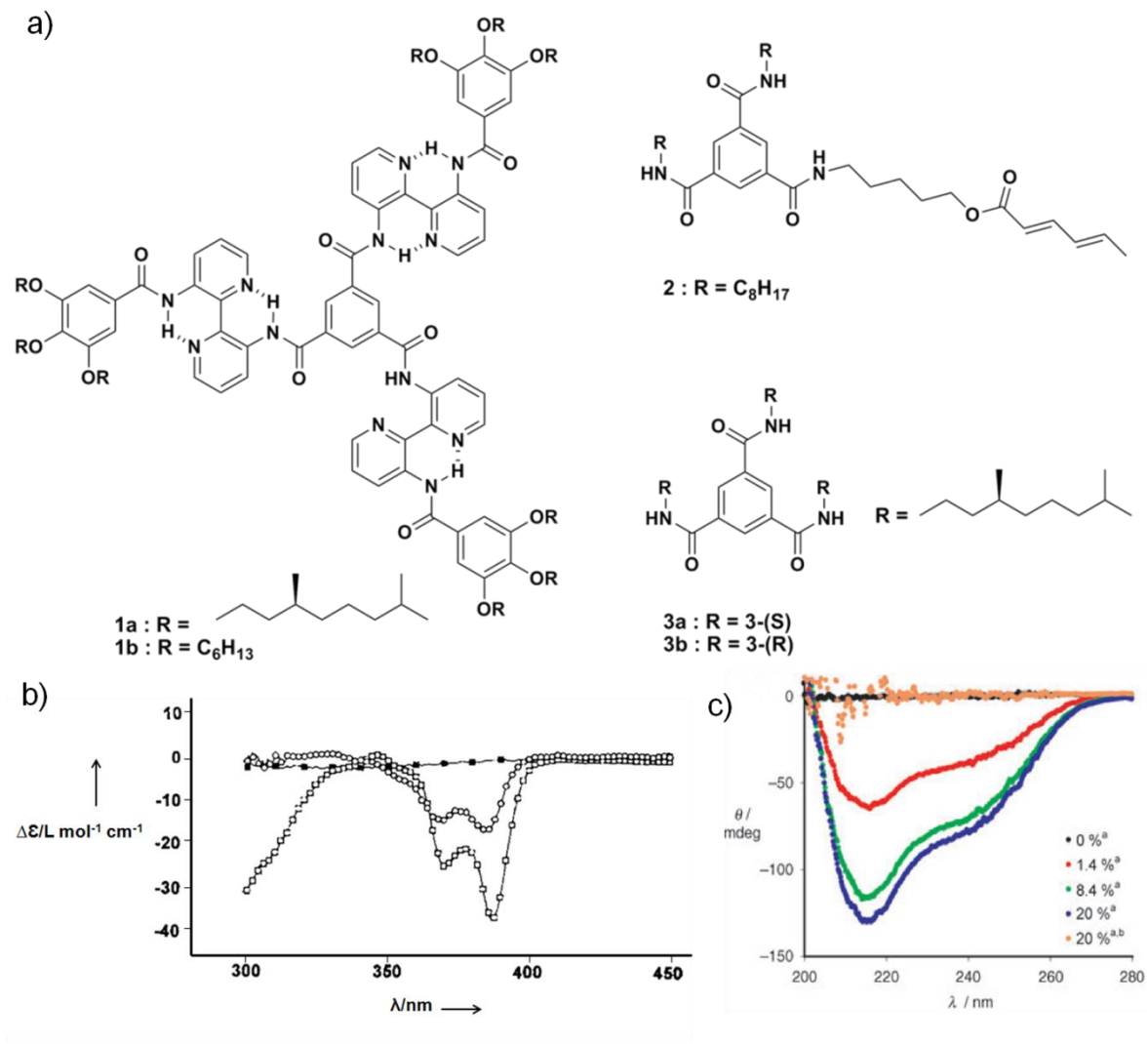

Figure 3.1. a) Chemical structures of disc-shaped molecules (**1-3**). b) CD spectra of **1a** and **1b** in $CHCl_3$ (▪), dodecane (○) and (S)-(-)-2, 6-dimethylocatane (◦). c) CD spectra of monomer **2** in the presence of different amount of sergeant, **3a** in cyclohexane (c =8.1 x 10^{-4} M, l = 0.1 cm).

The curve of anisotropic factor '*g*' as a function of the amount of **1a** added, explained very well the "sergeants-soldiers" principle in a dynamic supramolecular systems. The strong cooperative response of molecules **1a** and **1b** was due to tilted bipyridine units with respect to C_3-symmetry core. This could be explained by steric factors which controlled the interactions between molecules.

Folding of polymer into preferred handedness, even after removal of structure directing agent, is mainly governed by various supramolecular

interactions.[5,20-23] For example, CD spectra of the monomer **2** having polymerizable group (sorbyl) with the different fraction of sergeant **3a** explain the supramolecular "sergeants-soldiers effect" (Figure 3.1c).[24-25] Increasing the amount of chiral monomer led to a strong negative Cotton effect in the CD spectrum. The negative Cotton effect showed by the polymer constructed using **2** and **3a**, explains that the self-assembly process is purely intramolecular in nature within the molecularly dissolved polymer. These experiments show that non-covalent interactions can be used to amplify and store chiral information as structurally robust architectures.[26-33] C_3-symmetric trisamide based on oligo(*p*-phenyleneethylene) (**OPE**) molecules **4a** and **4d** exhibited helical columnar aggregates via π-π stacking of the aromatic core and α-helical type intermolecular amide hydrogen bonding (Figure 3.2).[34] Even at very dilute conditions, a mixture of achiral **4a** and chiral **4d** trisamide molecules formed helical aggregates resulted in strong Cotton effects. At the same time, the **OPE** attached with chiral side chains through ether linkage failed to form ordered aggregates with preferred helicity. The trisamide (**4b**) with three amide groups and one stereogenic centre exhibited less tendency to amplify the chirality of the racemic mixture of **4a**. Absence of CD response of C_3-symmetric molecule with complete ether linkage explains the importance of the amide functionality in helical self-assembly process. The mixture of achiral trisamide **1a** and the chiral non-helical bisamide **5c** gave helical structures with a preferred chirality in a co-operative fashion. The morphology of the mixture of **4a** and **5c** was confirmed as right handed helical fibrils. The thickness of these fibrils was in the range of 3.2 - 5.2 nm.

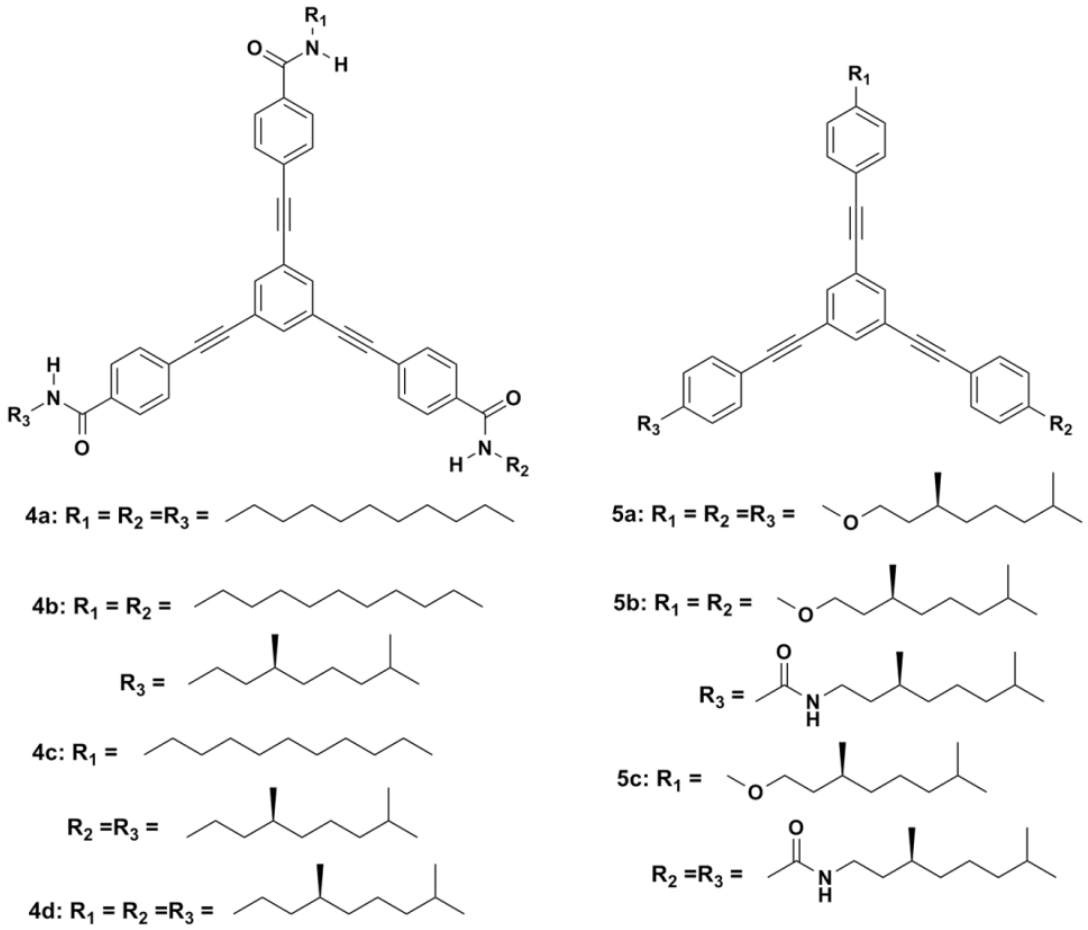

Figure 3.2. Chemical structures of C_3-**OPE** (**4** and **5**) molecules.

Co-assembly of an achiral **OPV** (**6a**) and a chiral **OPV** (**6b**) has been reported to form oppositely handed chiral structures when compared to the chiral analogue **6b** (Figure 3.3a).[35] Left-handed helical structures were formed by **6b** in dodecane solution at dilute conditions with an exciton-coupled bisignate CD signal (Figure 3.3b). A CD signal with positive Cotton effect was observed for the mixture of **6b** and **6a** containing 1.67 mol % of the former, and the signal intensity was increased when the composition of **6b** reached upto 22 mol %. Interestingly, further increase in the mol % of **6b** led to a decrease in the CD intensity and attained negative Cotton effect at 100 mol % of **6b**.[36-39] The mixture of **6a** with 20 mol % of **6b** exihibited the presence of non-helical stacks and P-helices. Co-

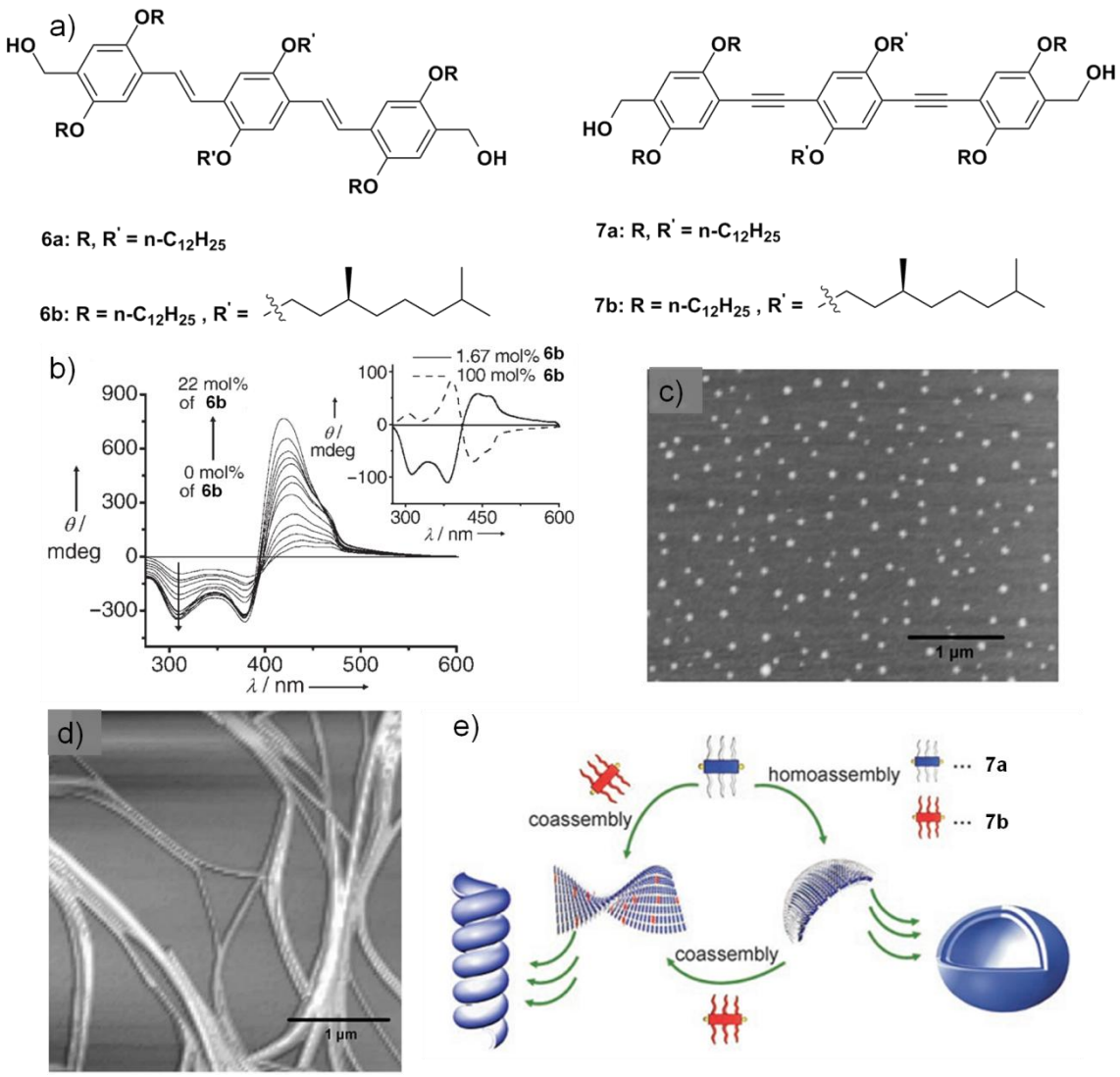

Figure 3.3. a) Chemical structures of **OPV** (**6a-b**) and **OPE** (**7a-b**) derivatives. b) Change in the CD spectrum during the co-assembly of **6a** and **6b** in dodecane (7.5×10^{-4} M) at different compositions of **6b** (0 – 22 mol %); the inset shows the mirror-image relationship of the CD spectra of **6b** and the **6a-6b** co-assembly at 1.67 mol % of **6b**. Tapping-mode AFM image of c) **7a** and d) **7a-7b** co-assembly. e) Schematic representation showing formation of vesicles and helical tubes on homo- and co-assemblies of **7a** and **7b**.

assembly of the **OPEs** (**7a** and **7b**) which showed a structural transformation from vesicles to helical nanotubes.[40] Chiral **7b** exihibited a different behavior when compared to **6b** due to the difference in π-π interaction. The mixture of 70 mol % of **7a** and 30 mol % of **7b** showed a maximum induced CD signal (ICD). Further

increase in the composition of **7b** upto 50 mol % resulted in the disappearance of ICD signal due to the destabilization of the co-assembly. Dynamic Light Scattering (DLS) experiment and morphological analysis (AFM and TEM) explained the structure of aggregates formed by **7a**, as vesicles or spherical aggregates. In the case of the co-assembly of **7a** with 8 mol % of **7b**, both spherical aggregates and helical structures were observed (Figure 3.3c). A complete transformation of vesicles to helical structures was observed at 25 mol % of **7b** (Figure 3.3d and 3.3e). The width and the height of the helical fibres were in the range of 90 nm and 6-25 nm respectively. The tubular nature of the helical structures was confirmed by TEM analysis and the diameter of tubes was in the range of 55-90 nm.

Chirality amplification in self-assembly of achiral **OPV** (**A-OPVUT**) molecules functionalized with mono-ureidotriazine (**UT**) moiety through self-complementary quadrapole H-bonding interactions using homochiral citronellic acid (**R-CA** or **S-CA**) has been reported by Meijer *et al.* (Figure 3.4a).[41] Self-assembly of **A-OPVUT** (**8)** in methyl cyclohexane (MCH) led to the formation of supramolecular helical stacks (Figure 3.4b). Host-guest complexation of the helical stacks with **R-** or **S-CA** resulted in the formation of 1:1 adduct of **8** and **R-CA/S-CA** via orthogonal two-point H-bonding interactions between acid and uridotriazine moiety. Chirality induction in the self-assembly of **8** with **R-CA/S-CA** under thermodynamic conditions showed strong mirror image Cotton effects. CD titration experiments of **8** with varying amount of both R-and S-enantiomers of citronellic acid showed a gradual increase in the CD signal via isodichroic point at the zero crossing. The mechanism of the self-assembly process was found to ob-

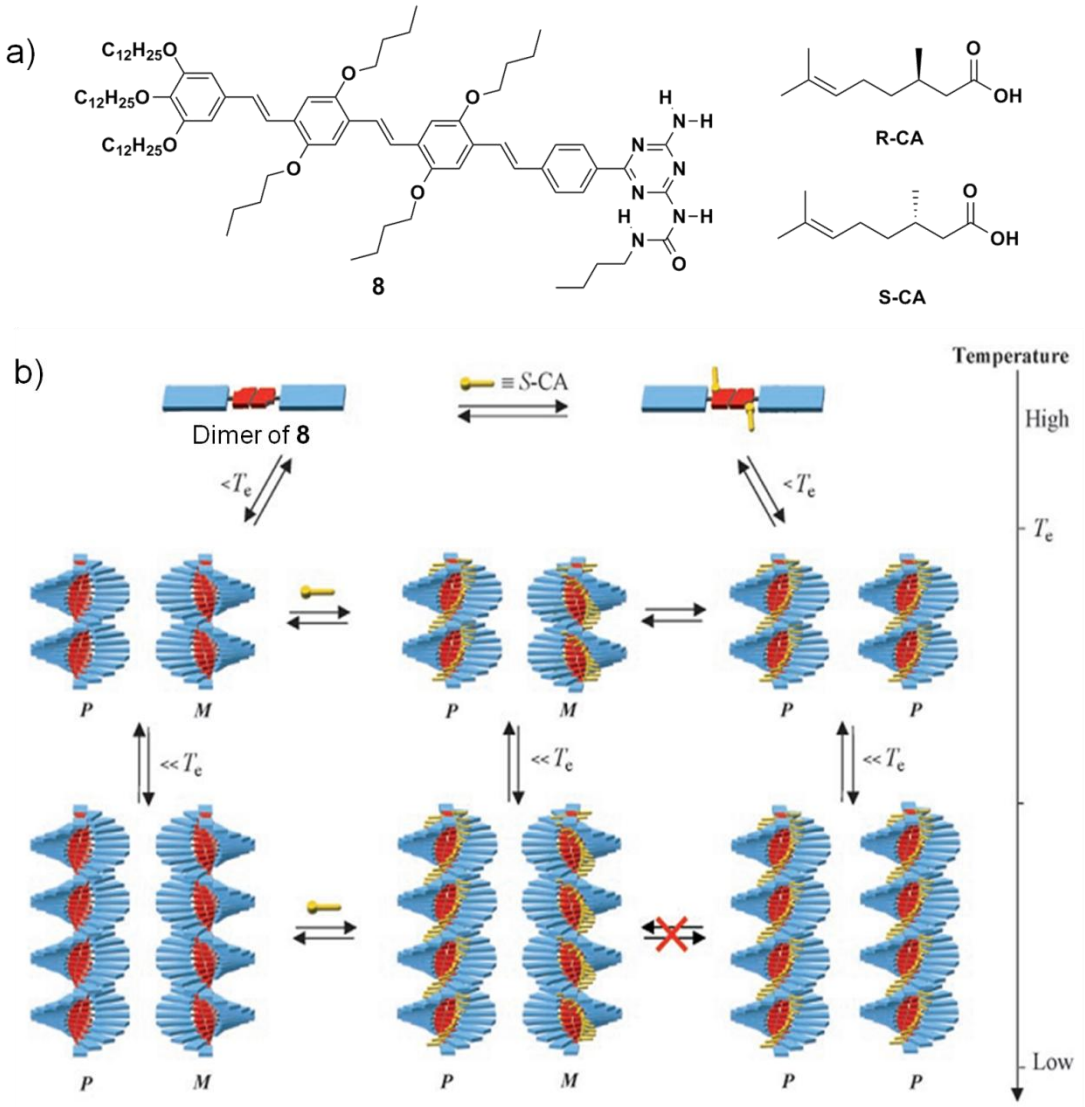

Figure 3.4. a) Chemical structures of **A-OPVUT** (**8**) and R- or S-citronellic acid (**R-CA** or **S-CA**). b) Schematic representation of chiral induction in **8** with chiral acid guest (**S-CA**).

ey the nucleation-growth model and fitting of the CD titration cooling curve led to constant elongation temperature, T_e and constant enthalpy, H_e for both individual and host-guest assemblies. AFM analysis did not show any remarkable change in morphologies of the homo- and the co-assemblies of **8** with **R-CA/S-CA** enantiomers. The chirality amplification in self-assembly of the achiral **8** was

achieved by transferring the chiral information from the supramolecular chiral regulators to the achiral stacks.[42]

Carbon nanotubes (**CNTs**) are an excellent class of nanostructures with unique properties that facilitate applications ranging from materials to medicines.[43-47] In particular, they are useful for the development of functional hybrid materials of π-conjugated molecules, polymers and DNA.[48-52] Some of the π-conjugated molecules and **CNTs** based hybrids play crucial role in optoelectronic devices.[53-56] Selective interaction of polymers or DNA with **CNTs** is employed to separate **CNT** of particular electronic properties from a mixture of **CNTs**. Polycyclic aroma-

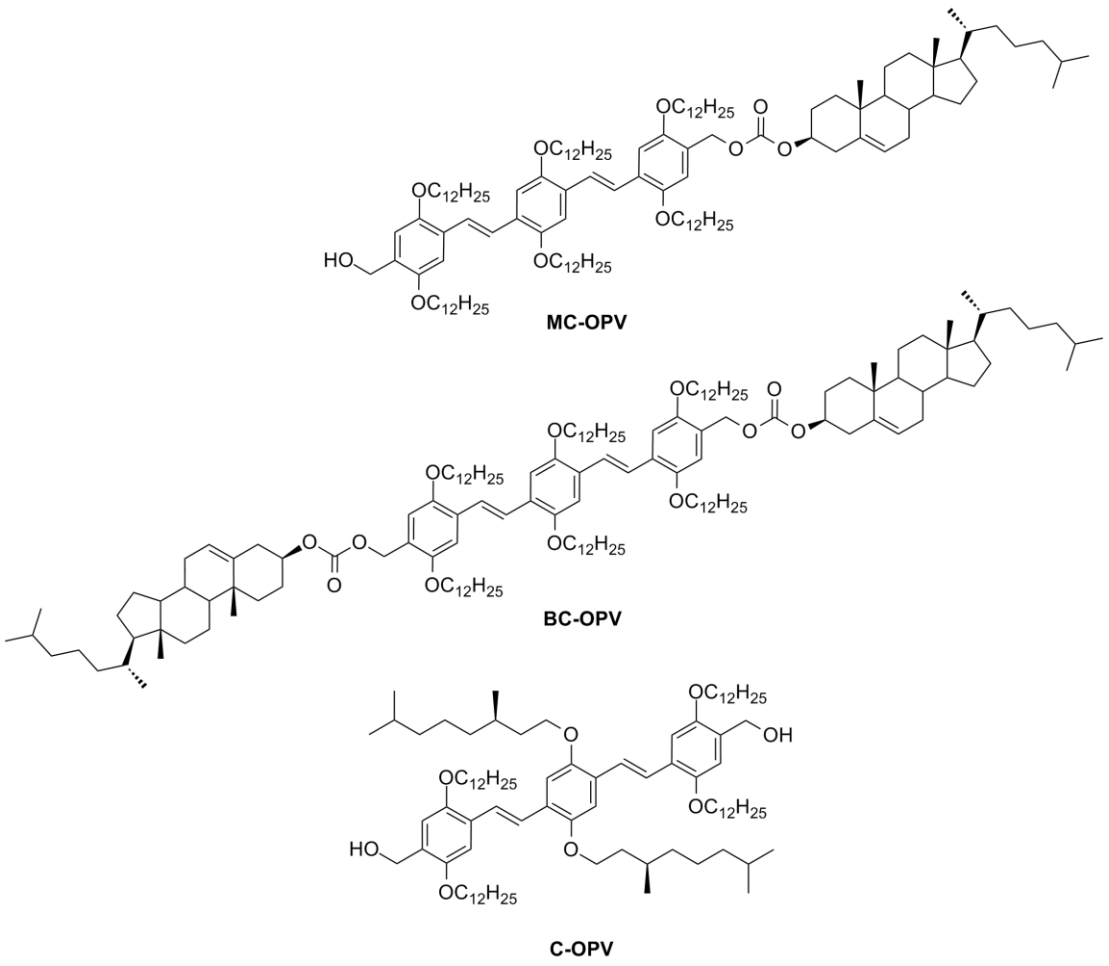

Figure 3.5. Chemical structures of **OPV** derivatives.

tic hydrocarbons are known to interact with **CNTs** leading to their dispersion in organic solvents.[57-58] It has been reported that **OPV** derived π-gelators strongly interact with **CNTs** to form strong gels with improved physical properties.[59] These results prompted us to study the effect of **CNTs** on the self-assembly of chiral π-gelators. For this purpose we have chosen an **OPV** based π-gelator having appended cholesterol moieties.[60] These molecules are known to self-assemble to form helical strutures of different morphology. In the present study, we used a monocholesterol-appended **OPV** molecule (**MC-OPV**) and the results were compared with the bischolesterol-appended **OPV** molecule (**BC-OPV**) and also with a chiral **OPV** alcohol (**C-OPV**) (Figure 3.5).

3.3. Results and Discussion

3.3.1. Synthesis of OPV Derivatives

MC-OPV, **BC-OPV** and **C-OPV** were prepared as described in the literature.[60-62] The cholesterol-appended derivatives (**MC-OPV** and **BC-OPV)** were synthesised by refluxing the corresponding **OPV** alcohol (**OPV3**) with cholesteryl chloroformate in benzene in the presence of pyridine as catalyst (Scheme 3.1). **OPV3** and **C-OPV** were synthesized by following a reported procedure.[61-62] All the compounds were characterized by IR, ^{1}H NMR, ^{13}C NMR, and MALDI-TOF mass spectrometry.

3.3.2. Photophysical Studies

MC-OPV solution in *n*-decane at a concentration of 1.8×10^{-4} M was selected for the studies. At this concentration, **MC-OPV** does not aggregate as evident from the absorption spectrum which showed the presence of the monomer species only (λ_{max}

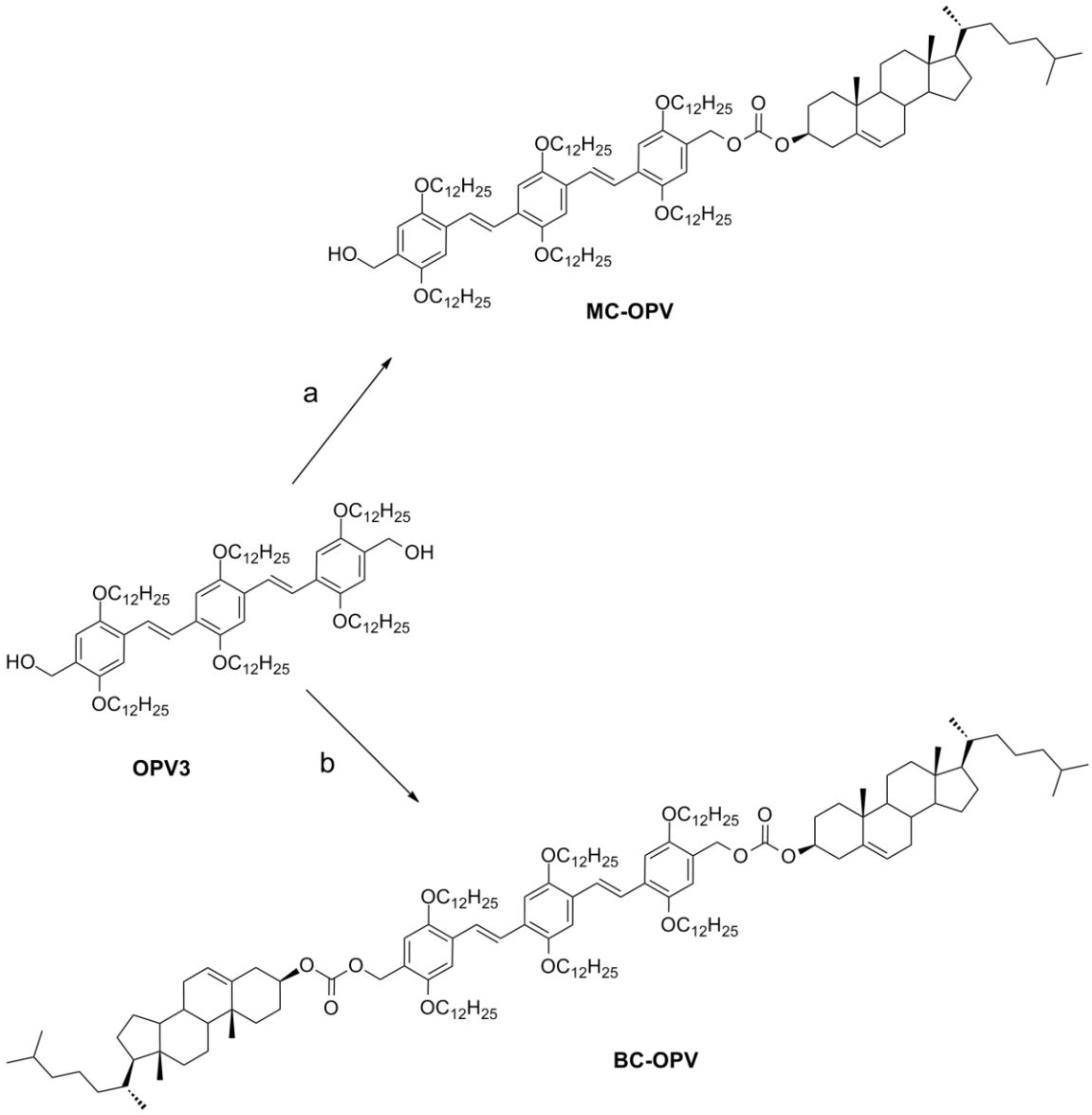

Scheme 3.1. Synthesis of **MC-OPV** and **BC-OPV**. Reagents and conditions: a) cholesteryl chloroformate (1.2 equiv.), pyridine (dry), benzene (dry), reflux, 8 h; b) cholesteryl chloroformate (2.2 equiv.), pyridine (dry), benzene (dry), reflux, 12 h.

= 402 nm; Figure 3.6.a). Further evidence for this observation was obtained from the CD spectrum which did not show any signal at this concentration. Interestingly, when a small amount of **SWNT** (0.05 mg) was added to this solution and sonicated for 1-2 minutes, a blue shift of the absorption maximum (λ_{max} = 397 nm) with a shoulder band around 450 nm was observed indicating the aggregation of **MC-**

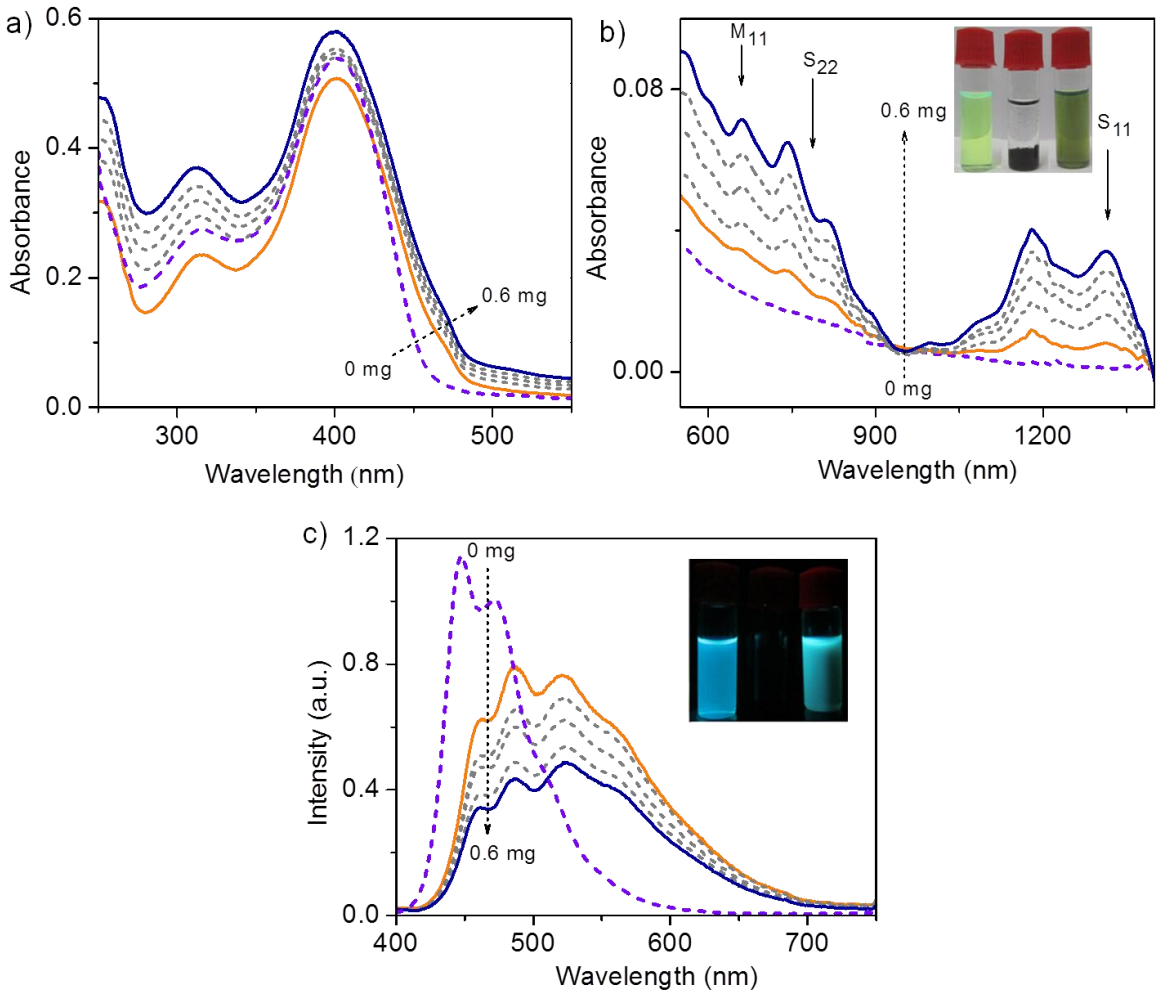

Figure 3.6. a) UV-Vis absorption spectra, b) fluorescence spectra and c) Vis-NIR absorption spectra (550 – 1400 nm) of **MC-OPV** (c = 1.8 × 10^{-4} M, l = 1 mm, λ_{ex} = 380 nm) in the absence (dotted line) and presence (solid lines) of **SWNT**. (Inset: Photographs of **MC-OPV**, **SWNT** and **MC-OPV/SWNT** hybrid in *n*-decane (left to right) (3.6b) under ambient light) and (3.6c) under UV light.

OPV. In addition, the appearance of van Hove singularities in the wavelength region of 550-1400 nm was observed due to the unbundling and dispersion of **SWNTs** (Figure 3.6b).[59,63] The baseline shift in the absorption spectra of **MC-OPV** after addition of **CNTs** was due to the Rayleigh scattering of debundled **CNTs** in *n*-decane solution. Visual evidence for the dispersion of the **SWNTs** in **MC-OPV** solution was obtained from the photograph of the hybrid in *n*-decane (inset of Figure 3.6a). Fluorescence spectra of the hybrid solutions were also measured and

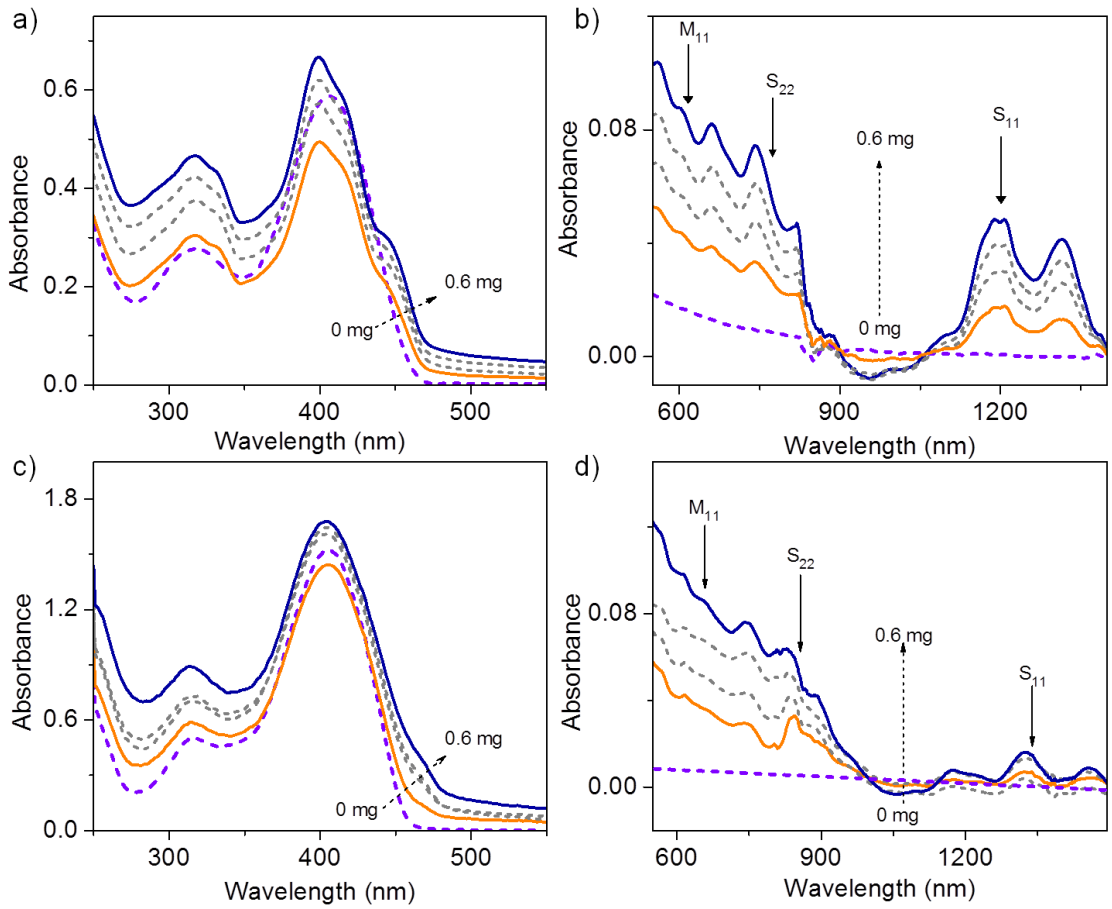

Figure 3.7. UV-Vis and Vis-NIR absorption spectra (550 – 1400 nm) of a), b) **BC-OPV** (c = 2.1 × 10^{-4} M) and c), d) **C-OPV** (c = 4.5 x 10^{-4} M) in *n*-decane, respectively, in the absence (dotted line) and presence (solid lines) of **SWNT** (l = 1 mm, λ_{ex} = 380 nm).

compared with that of **MC-OPV**. The emission bands of **MC-OPV** at 460 and 495 nm (corresponding to the monomer emission) decreased, whereas a broad emission band (corresponding to the aggregate emission) appeared around 550 nm on addition of **CNT** (Figure 3.6c). As a result, the cyan emission of the solution turned into greenish-cyan in presence of **CNT** (inset of Figure 3.6c). These optical studies revealed that **MC-OPV** molecules undergo self-assembly on the surface of **SWNTs**. **BC-OPV** and **C-OPV** also showed similar changes in the absorption and emission spectra (Figure 3.7). **BC-OPV** (c = 2.1 × 10^{-4} M) exhibited an absorption

maximum at 404 nm in *n*-decane for monomer species (Figure 3.7a). The absorption band of **BC-OPV** were shifted to lower wavelength of 398 nm with the appearance of two shoulder bands around 412 and 441 nm while adding various amounts of **CNTs** (0 – 0.6 mg) due to the aggregation of molecules by interacting with the surface of **CNTs**. Debundling of **CNTs** resulted from the interaction between molecules and **CNT** surface as confirmed by van Hove singularities in the wavelength region of 550-1400 nm (Figure 3.7b). **C-OPV** exhibited an absorption band at 406 nm, which showed a blue shift to 403 nm after the addition of **CNTs** (0 – 0.6 mg) in *n*-decane (Figure 3.7c). The unbundling of **CNTs** was confirmed by the van Hove singularities in the region of 550-1400 nm (Figure 3.7d).

In order to understand whether the aggregates formed on the **CNT** surface is helical in nature, chiroptical studies were carried out using circular dichroism (CD) spectroscopy. No CD signal was observed for **MC-OPV** at 1.8×10^{-4} M concentration in *n*-decane as this concentration was not enough to induce aggregation and helical organization of the chromophores. Interestingly, on addition of 0.05 mg of **SWNT**, a CD signal with good intensity (6 M^{-1} cm^{-1}; dissymmetry factor, $g = 1.24 \times 10^{-4}$) with a maximum at 396 nm was observed (Figure 3.8a). This observation implies that the aggregate formed upon the addition of **SWNT** is helical in nature. Similarly, **BC-OPV** and **C-OPV** did not show any CD signal at the concentration of 2.1×10^{-4} M and 4.5×10^{-4} M, respectively (Figure 3.8b and 3.8c). After addition of 0.05 mg of **SWNT**, **BC-OPV** exhibited a CD signal with two negative peaks with a maximum at 420 nm and two positive peaks with a maximum at 386 nm (Figure 3.8b). **C-OPV** showed a CD signal with

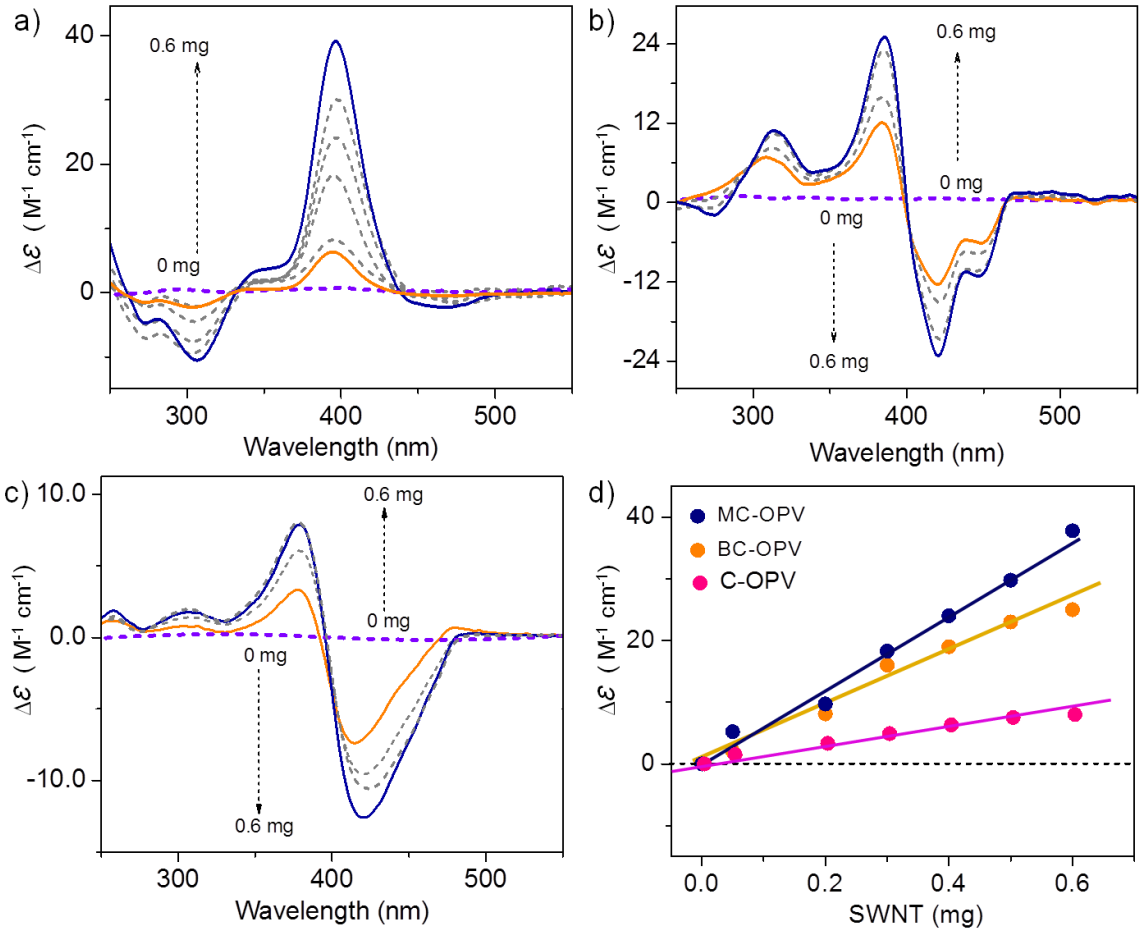

Figure 3.8. CD spectra of a) **MC-OPV** (c = 1.8 × 10^{-4} M), b) **BC-OPV** (c = 2.1 × 10^{-4} M), and c) **C-OPV** (c = 4.5 x 10^{-4} M) in *n*-decane with various amount of **SWNT** (0 - 0.6 mg). d) Plot showing changes in CD intensities of **MC-OPV**, **BC-OPV**, and **C-OPV** with respect to the amount of **SWNT** added.

a negative peak at 420 nm and a positive peak at 378 nm after addition of 0.05 mg of **SWNT** (Figure 3.8c). The amounts of the added **SWNTs** have significant influence on the intensities of CD signals of the **MC-OPV**, **BC-OPV**, and **C-OPV** (Figure 3.8d). For example, addition of 0 – 0.6 mg of **SWNT** to the solutions of **MC-OPV** (concentration kept constant at 1.8 × 10^{-4} M), **BC-OPV** (c = 2.1 × 10^{-4} M), and **C-OPV** (c = 4.5 x 10^{-4} M) showed significant increase in their CD intensities. The maximum CD of 38, 25, and 10 M^{-1} cm^{-1} were obtained in the presence of 0.6 mg **SWNT** respectively. No further enhancements were seen when

the **SWNT** concentrations were above 0.6 mg. Further, a detailed concentration dependent study was performed to find out the minimum concentrations of **MC-OPV**, **BC-OPV** and **C-OPV** required to give a CD signal in the presence and absence of **SWNT** (amount of **SWNT** was kept constant at 0.2 mg; Figure 3.9). It was found that at least 2.2×10^{-4} M concentration was needed to give a considerable CD signal for **MC-OPV** in the absence of **SWNT**. On the other hand, a concentration of 1.8×10^{-4} M of **MC-OPV** was good enough to give CD signal in the presence of **SWNT** (Figure 3.9a). In the case of **BC-OPV** and **C-OPV**, concentrations of 2.4×10^{-4} M and 6.0×10^{-4} M, respectivley were needed to give a considerable CD signal in the absence of **SWNT**. Conversely, the concentrations of 2.1×10^{-4} M (**BC-OPV**) and 4.5×10^{-4} M (**C-OPV**) were enough to give CD signals in the presence of **SWNT** (Figure 3.9b and 3.9c).

Comparison of the plots of CD intensity of **OPV**s at varying amounts of **SWNT** and **MWNT** is shown in Figure 3.10a and 3.10b, respectively. When the intensities of CD signals of **OPVs** were compared after the addition of 0.2 mg of **SWNT**, **MC-OPV** showed better chirality amplification than **BC-OPV** and **C-OPV**. Similarly, it exhibited better amplification with 0.3, 0.4, 0.5, 0.6 mg of **SWNT** than that of the other two derivatives (Figure 3.10a). The difference in the chirality amplification between the different **OPV** derivatives is due to the different aggregation behavior under similar experimental conditions. It was found that **MC-OPV** having hydrogen bonding moiety (hydroxyl) showed aggregation at a lower concentration (1.8×10^{-4} M) in the presence of **SWNT**. In the case of **BC-OPV**, it has two cholesteryl moieties (no H-bonding moiety) and showed relatively less

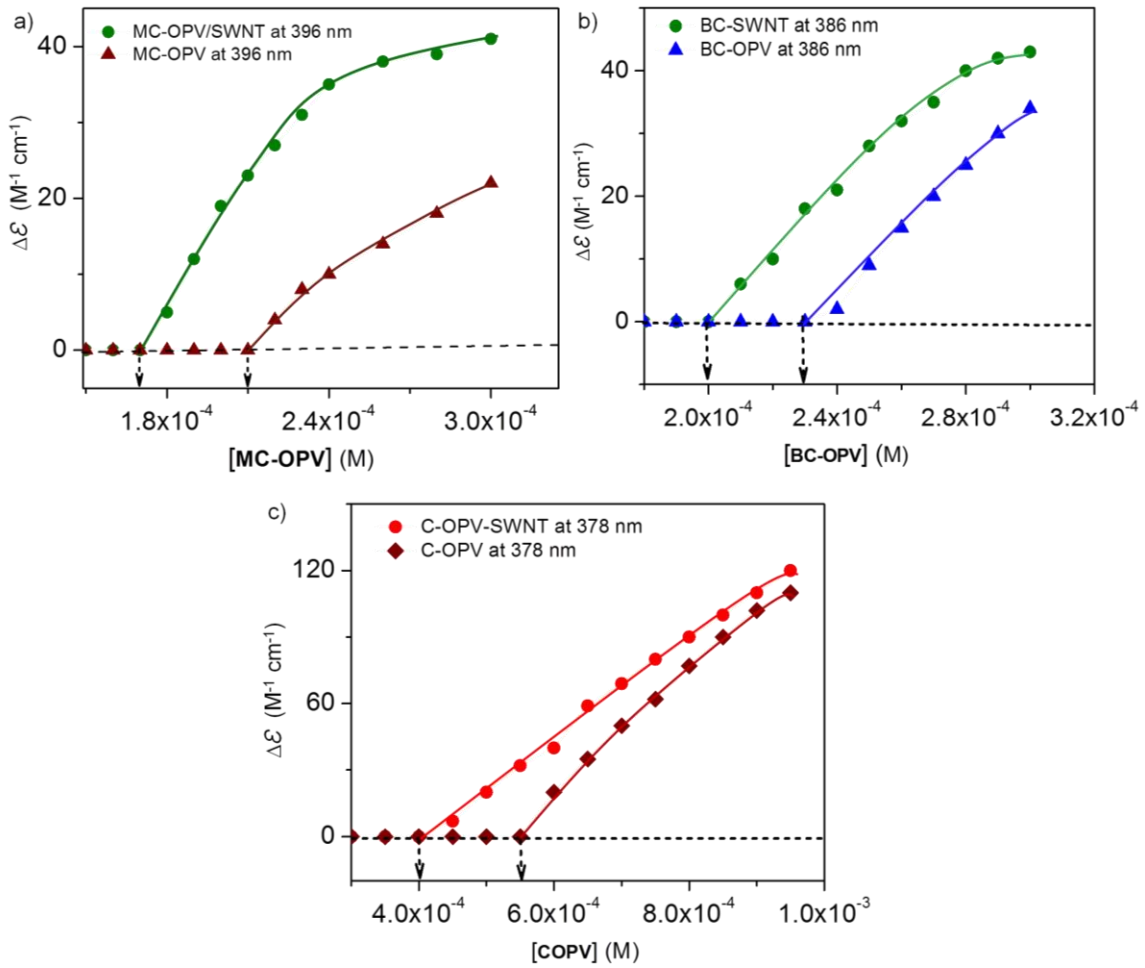

Figure 3.9. Changes in CD intensities with increasing concentration of a) **MC-OPV** (c = 1.8 × 10^{-4} M), b) **BC-OPV** (c = 2.1 × 10^{-4} M), and c) **C-OPV** (c = 4.5 x 10^{-4} M) in the presence of 0.2 mg of **SWNT** in *n*-decane.

aggregation tendency than **MC-OPV**. Even though **C-OPV** has two hydrogen bonding moieties, it showed relatively lesser aggregation behavior in the presence of **SWNT** because of two branched chiral chains present in it. The branched chains are known to increase the solubility and decrease the aggregation. The π-π stacking interaction between the molecules and **CNTs** plays a crucial role in the observed phenomenon. It was found that the strength of the π-stacking interaction was directly proportional to the aggregation ability of the molecules that follows the order **MC-OPV** > **BC-OPV** > **C-OPV**. **C-OPV** and **BC-OPV** exhibited relatively

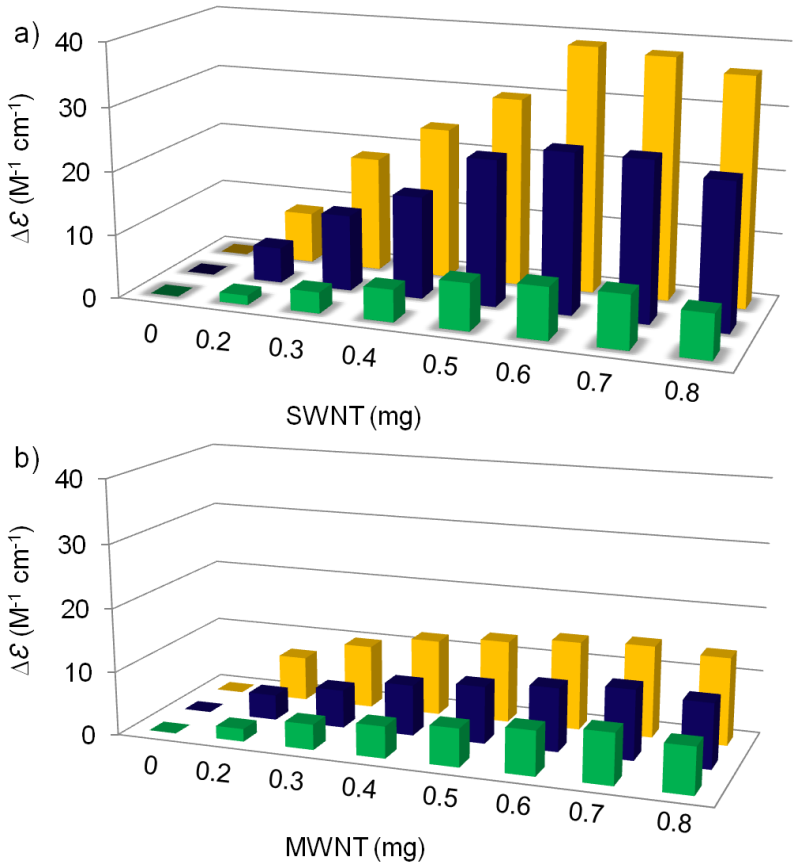

Figure 3.10. 3D plot showing ellipticity ($\Delta\mathcal{E}$) of **MC-OPV**, **BC-OPV**, and **C-OPV** with increasing amount of a) **SWNT** and b) **MWNT**.

weaker interaction with **SWNT** probably due to their high solubility. On the other hand, **MC-OPV** has relatively better aggregation ability and hence it showed good chirality amplification in the presence of **CNTs**. It must be noted that all **OPV** derivatives, in general, showed comparatively less chirality amplification in the presence of **MWNT** (Figure 3.10b). This could be explained as follows; one **MWNT** consists of several **SWNTs** of different diameters stacked together (concentric tubes). This feature of the **MWNT** reduces the overall surface area available for interacting with **OPVs** when compared to that of the similar quantity of **SWNTs**.

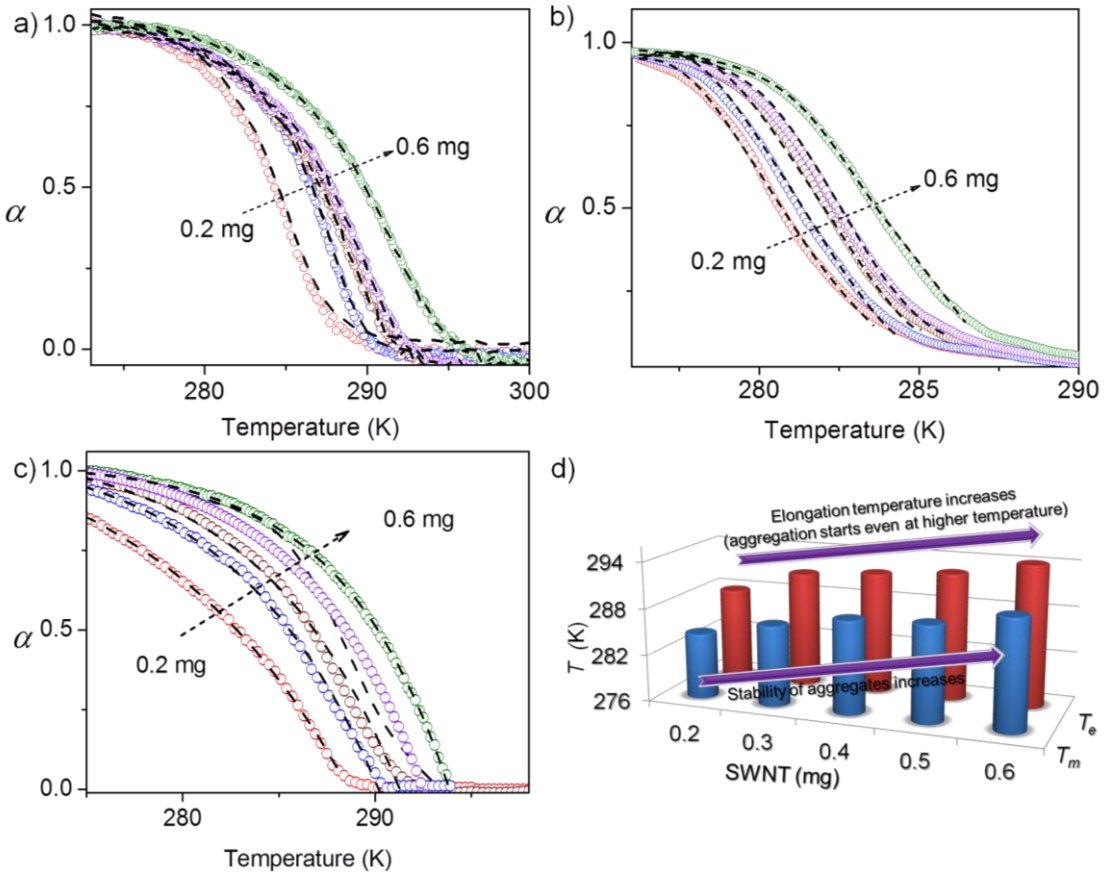

Figure 3.11. Degree of aggregation (α) of a) **MC-OPV/SWNT** (c = 1.8 × 10^{-4} M), b) **BC-OPV/SWNT** (c = 2.1 × 10^{-4} M), and c) **C-OPV** (c = 4.5 x 10^{-4} M) with varying amount of **SWNT** (0 – 0.6 mg) in *n*-decane (obtained from variable temperature CD data). d) 3D plot showing the melting (T_m) and elongation (T_e) temperature of **MC-OPV/SWNT** with increasing amount of **SWNT**.

Fitting of variable temperature CD spectra of the hybrids revealed that the self-assembly process follows a cooperative mechanism (Figure 3.11).[64] Thermodynamic parameters such as elongation temperature (T_e), melting temperature (T_m) and enthalpy change (ΔH) of the self-assembly of **MC-OPV/SWNT**, **BC-OPV/SWNT**, **C-OPV/SWNT** hybrids were calculated by fitting the curves obtained from variable temperature CD studies (Figure 3.11). The elongation temperature of supramolecular aggregates of **MC-OPV** was 288 K in the presence of 0.2 mg of **SWNT**, whereas it increased up to 294 K in the presence of 0.6 mg of **SWNT**. Similarly, the elongation temperature of **BC-OPV** and **C-**

Table 3.1. Thermodynamic parameters accounting the self-assembly of **MC-OPV/SWNT** (c = 1.8 ×10^{-4} M), **BC-OPV/SWNT** (c = 2.1 × 10^{-4} M), and **C-OPV/SWNT** (c = 4.5 x 10^{-4} M) in *n*-decane with increasing amount of **SWNT**.

	Wt. of SWNT	ΔH kJ mol^{-1}	T_e (K)	T_m (K)
MC-OPV/SWNT	0.2	-120	288.0	284.5
	0.3	-121	290.9	286.4
	0.4	-124	291.6	287.9
	0.5	-120	292.4	288.3
	0.6	-122	294.2	290.1
BC-OPV/SWNT	0.2	-116	283.7	280.6
	0.3	-118	284.6	281.3
	0.4	-116	285.9	282.2
	0.5	-112	286.5	282.9
	0.6	-115	287.3	283.8
C-OPV/SWNT	0.2	-110	288.2	282.7
	0.3	-112	290.1	285.5
	0.4	-115	291.0	286.7
	0.5	-109	292.3	288.3
	0.6	-105	293.7	289.0

OPV increased from 283 to 287 K and 288 to 293 K in the presence of 0.2 – 0.6 mg of **SWNT** (Figure 3.11d). The increase in the elongation temperature implies that the self-assembly process starts even at higher temperatures in the presence of **SWNTs**. Similarly, the melting temperatures of the aggregates were found to be increased with increasing amounts of **SWNT** (Table 3.1). The higher melting temperature indicates that **SWNTs** are not only able to amplify the supramolecular

chirality but also enhances the stability of the aggregates. The thermodynamic properties of **BC-OPV/SWNT** and **C-OPV/SWNT** were listed in the Table 3.1.

3.3.3. Raman Spectral Studies

Raman spectral changes of **SWNT** and the hybrid materials are shown in Figure 3.12. They reveal that strong interaction is present between **OPVs** and **SWNT**. The radial breathing mode (RBM) region of the pristine **SWNT** showed four peaks at 194 cm^{-1}, 216 cm^{-1}, 242 cm^{-1} and 257 cm^{-1}. In case of **MC-OPV/SWNT**, the peak at 194 cm^{-1} was shifted to the higher wavenumber of 198 cm^{-1} (Figure 3.12a). Similarly, the peaks at 216 cm^{-1}, 242 cm^{-1} and 257 cm^{-1} were shifted to 220 cm^{-1}, 245 cm^{-1} and 261 cm^{-1} with an upshift of 4 cm^{-1}, 3 cm^{-1} and 4 cm^{-1}, respectively. **BC-OPV/SWNT** exhibited the upshift peaks at 196, 220, 245 and 259 cm^{-1} when compared to the peaks of **SWNT** in RBM region. **C-OPV/SWNT** also showed the upshift peaks at 195, 217, 243 and 258 cm^{-1}. The G-band of **SWNT** at 1584 cm^{-1} shifted to 1593cm^{-1} in case of **MC-OPV/SWNT** (Figure 3.12b). **BC-OPV/SWNT** and **C-OPV/SWNT** exhibited the upshift of G-band at 1589 and 1586 cm^{-1}, respectively. The upshift of peaks of the hybrids could be attributed to the unbundling of **SWNTs** by **OPV** molecules as well as the pressure excreted by the helically wrapped **OPV** molecules around the **SWNT** surface.[65-67] Among **OPV** derivatives, **MC-OPV** showed the higher upshift of peaks when compared to that of **BC-OPV** and **C-OPV** as it has stronger interaction with the π-surface of **SWNTs** than the other derivatives.

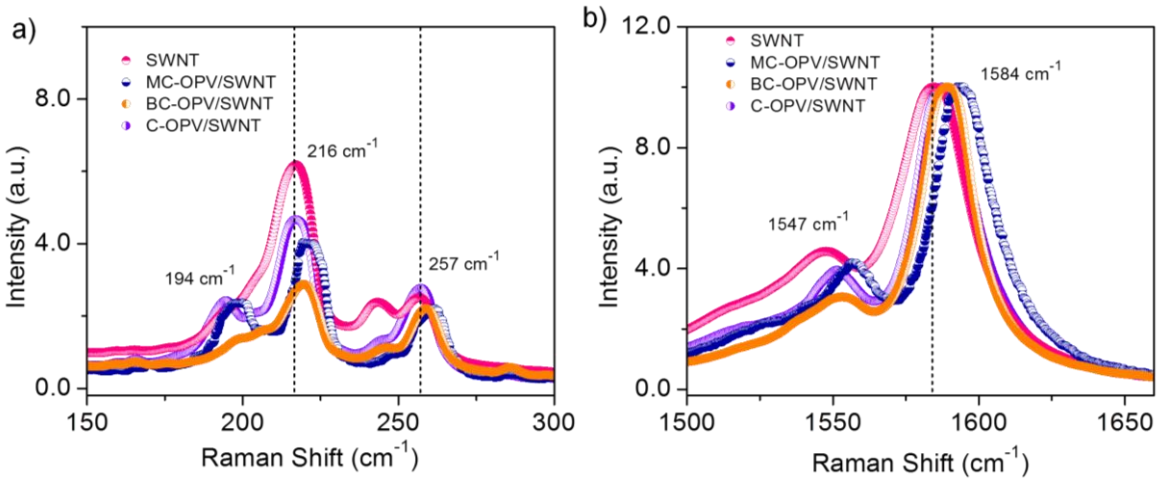

Figure 3.12. Raman spectra of **SWNT**, **MC-OPV/SWNT**, **BC-OPV/SWNT**, and **C-OPV/SWNT** at a) RBM region and b) G-band region.

3.3.4. Morphological Studies

Morphology of the chiral aggregates of the hybrid materials was studied by AFM and TEM analyses. AFM images of **MC-OPV** indicate the formation of helical fibers of 50-150 nm in width having a helical pitch of 50-80 nm (Figure 3.13a and 3.13b). However, the heights of the fibers were in the range of 4-6 nm indicating that they are very thin. On the other hand, the **MC-OPV/SWCNT** mixture showed densely aggregated thin fibers (width of 20–100 nm) that are bundled to form superstructures of **SWNTs** helically wrapped with **MC-OPV** (more than 100 nm width; Figure 3.13c and 3.13d). The hybrid fibers showed right handed helical pitch (100–200 nm) in most cases. Since the UV-Vis-NIR absorption spectrum showed dispersion of **CNTs** upon interaction with **MC-OPV** indicating the debundling of the former, the observation of superfibers of more than 100 nm width was a surprise. The inset in Figure 3.13d shows an isolated helical superstructure having a width of 90 nm. Interestingly, the section analysis of the superfiber showed a height of 60 nm, which is nearly 10 times more than that of the **MC-OPV** fibers, indica-

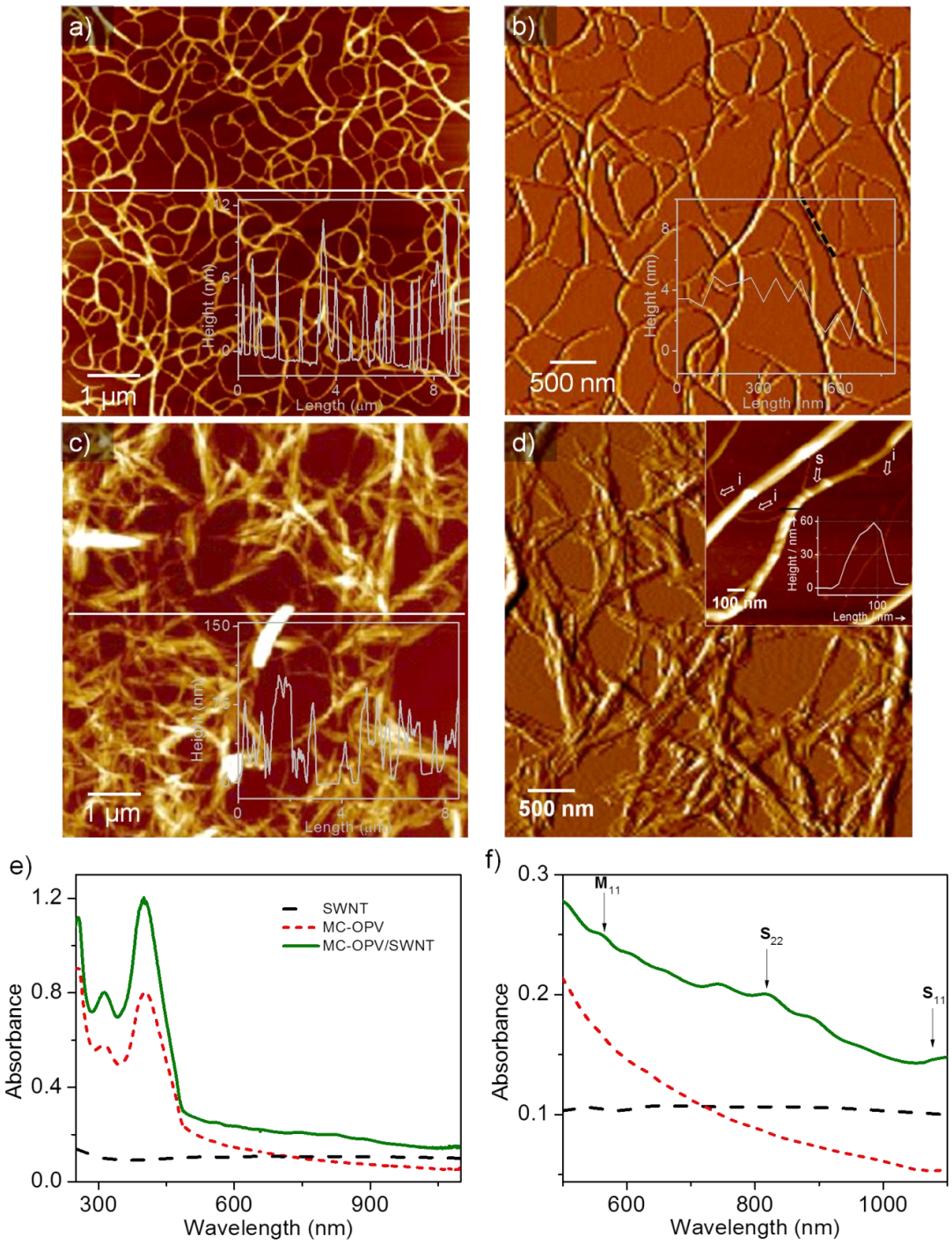

Figure 3.13. a), c) AFM height and b), d) magnitude images of **MC-OPV** and **MC-OPV/SWNT,** respectively, drop cast on freshly cleaved mica surface from *n*-decane solution (c = 1.8 x 10^{-4} M). Inset of Figure 3.13d shows the AFM height image of indvidually wrapped (marked by symbol 'i') and supercoiled fibers (marked by symbol 's') of the hybrid along with the height profile of a supercoiled fiber at the marked region (black line). Height profiles of marked regions of Figures 3.13a-c are shown as inset. d) Solid-state (film) UV-Vis-NIR absorption spectra of **SWNT**, **MC-OPV** and **MC-OPV/SWNT**. Figure 3.13f shows the zoomed area in the range of 550 – 1200 nm.

ting a cylindrical morphology for the hybrid assembly. Since the size of each **SWNT** is approximately 1 nm, the formation of such large cylindrical fibers can be explained in two different ways; wrapping of **MC-OPV** on to the bundled **CNTs** or the rebundling of the individual **CNTs** wrapped by **MC-OPV**, which are subsequently wrapped by **MC-OPV** upon evaporation on mica substrate. If the superstructures are formed through the former route, one should not see the van Hove singularity of the individual **CNTs**. Contrarily, if the superstructures are formed through the latter route; the UV-Vis-NIR absorption spectrum of the hybrid material should show the van Hove fine structures of **SWNTs**. In order to establish this hypothesis, we measured the solid-state UV-Vis-NIR absorption spectrum of **MC-OPV/SWNT** hybrid film, which exhibited the van Hove singularity (Figure 3.13e and 3.13f). This observation supports the formation of superstructures by the latter route in which each **CNTs** are separated one another by the helically wrapped **MC-OPV** which is further established by TEM analysis of **MC-OPV/SWNT** (Figure 3.14 and 3.15). The high resolution TEM images of a large (~25 nm) and a small (~10 nm) cylindrical cable indicate the presence of aligned **SWNT** in the supercoiled fibers. In addition, we also observed the aggregated superhelical fibers of >100 nm width (Figure 3.14c and 3.14d) which are coincident with the AFM images (Figure 3.13c and 3.13d). The intensity histograms of the HR-TEM images reveal that the individual **CNTs** are closely bound in the pristine **SWNT** with an average intertubular distance of 0.66 ± 0.05 nm (Figure 3.13d), whereas when they are individually wrapped by **MC-OPV** and aligned in the supercoiled fibers of

MC-OPV/SWNT, the average intertubular distance is increased to 0.8-0.9 ± 0.05 nm (Inset of Figure 3.15a and 3.15b).

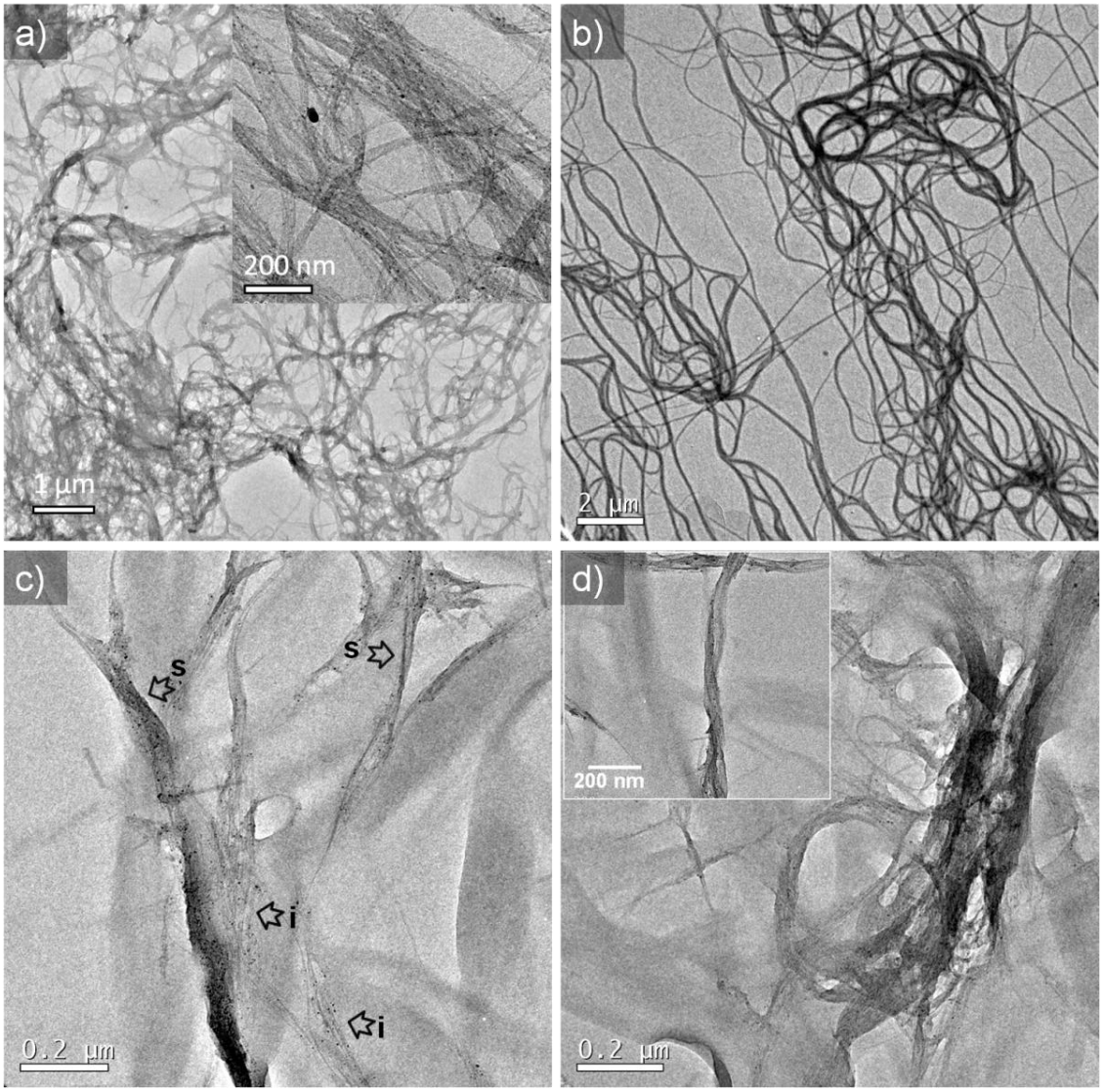

Figure 3.14. HR-TEM images of a) **SWNT**, b) **MC-OPV** and c), d) **MC-OPV/SWNT**, drop cast from *n*-decane solution (c = 1.8 x 10^{-4} M). Inset (Figure 3.14a) shows the zoomed image of bundled **SWNT**. The individually wrapped (marked by symbol 'i') and supercoiled (marked by symbol 's') single fibers of the hybrids are shown in Figure 3.14c. Inset (Figure 3.14d) shows the HR-TEM image of a supercoiled **MC-OPV/SWNT** fiber).

Based on the above experimental data, the formation of coaxial cylindrical cables of **SWNTs** can be explained as shown in Scheme 3.2. In solution, **SWNTs** interact with **MC-OPV** to form helically wrapped individual nanotubes. Drop cas-

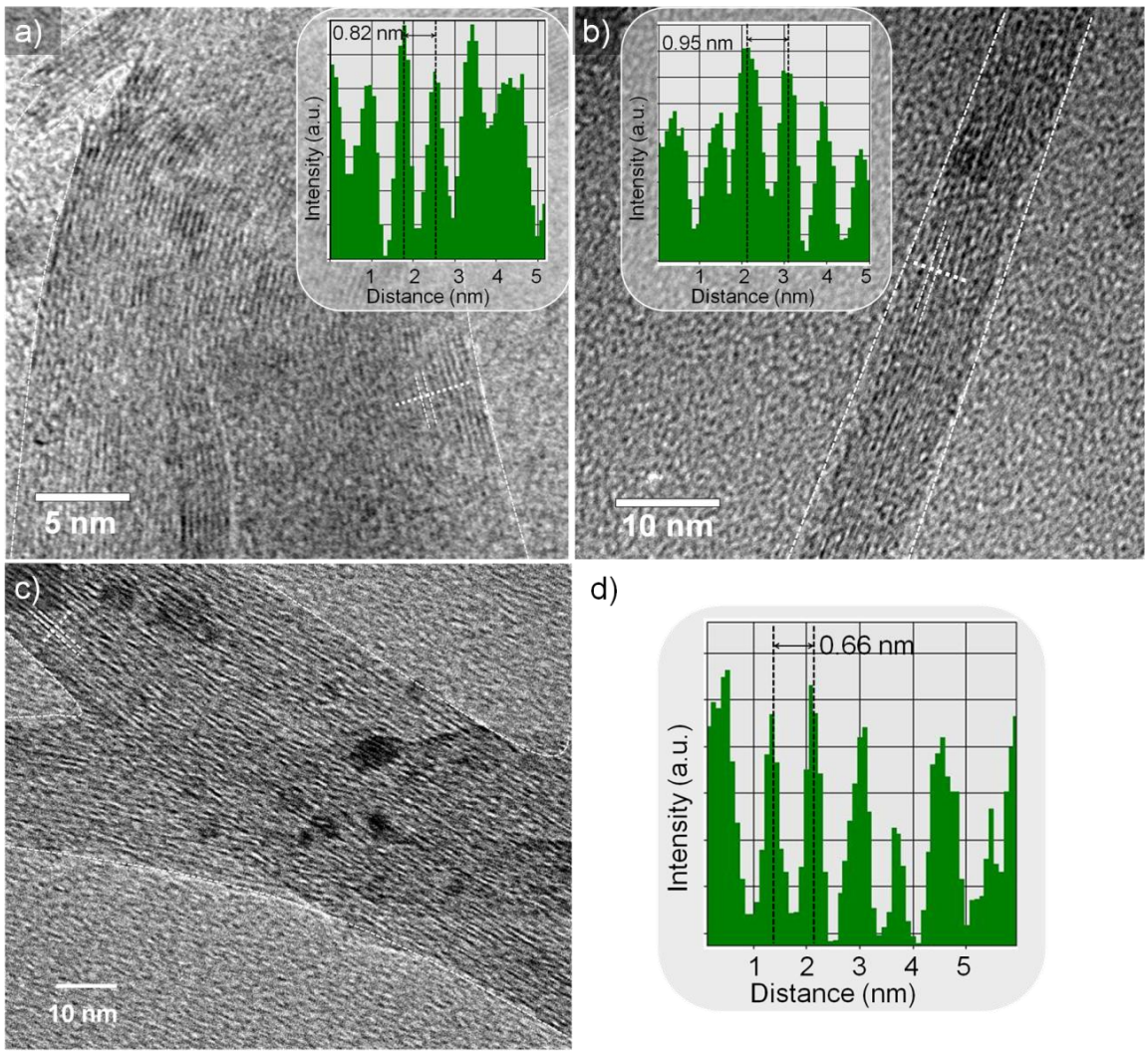

Figure 3.15. a) and b) HR-TEM images of the cylindrical cables of **MC-OPV/SWNT**, drop cast from *n*-decane solution (c = 1.8 × 10^{-4} M). Insets (Figure 3.15a and 3.15b) show intensity histograms of the marked regions. c) HR-TEM image of **SWNT**, drop cast from *n*-decane solution recorded for the purpose of comparing the tube diameter with the **MC-OPV/SWNT** hybrid. d) Intensity histogram of the marked region in Figure 3.15c.

ting of the wrapped nanotubes on substrates followed by evaporation of the solvent results in rebundling of the individually wrapped **CNTs**, which are further wrapped with **MC-OPV**s to form >100 nm cylindrical cables having aligned **CNTs.**

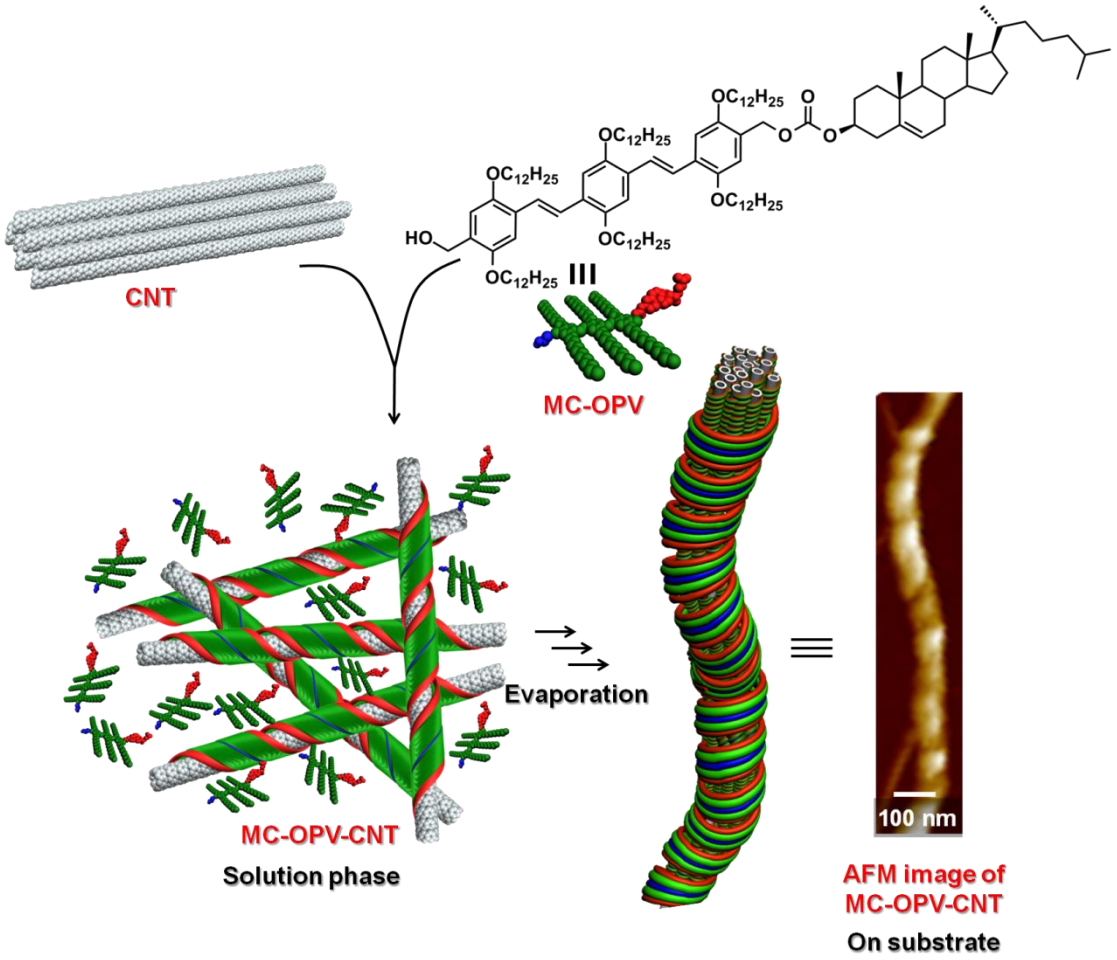

Scheme 3.2. Schematic representation of the formation of coaxial cylindrical nanocables of **CNTs** by helically wrapped π-gelators leading to chirality amplification.

3.4. Conclusions

In summary, presented here is the experimental evidence for the influence of **CNTs** on the chirality amplification in molecular assemblies as illustrated with chiral π-gelators. The extent of chirality amplification depends upon the strength of interaction of the gelator with **CNTs** as well as the strength of the gelator aggregation. **MWNTs** exhibited relatively weak chirality amplification when compared to that of **SWNT**, due to the less average surface area of the former, available for the gelator interaction. Detailed UV-Vis-NIR, AFM and TEM analyses of the hybrid revealed an interesting morphological feature in which each

nanotube is site isolated to form coaxially aligned cylindrical cables. Such alignment of nanotubes without any external force is a unique example of nanotube self-alignment and can be exploited for making hybrids with intriguing physical properties.

3.5. Experimental Section

3.5.1. General

SWNTs (HiPco) were obtained from Carbon Nanotechnologies Inc. and **MWNTs** were purchased from Aldrich. The solvents used were purified and dried by standard methods prior to use. **OPVs** were synthesized according to the literature method and characterized.[60-62] NMR spectra were recorded on a 500 MHz Bruker Advance DPX spectrometer using TMS as internal standard. Matrix-assisted laser desorption ionization time-of-flight (MALDI-TOF) mass spectra were obtained on a AXIMA-CFR PLUS (SHIMADZU) MALDI-TOF mass spectrometer.

3.5.2. Synthesis and Characterization

General Procedure for the Synthesis of Cholesterol-OPV Derivatives

The bisalcohol derivative (**OPV3**) (1 mmol) was dissolved in dry benzene (15 mL) by stirring. To this solution, cholesteryl chloroformate (1.2 mmol for **MC-OPV** or 2.2 mmol for **BC-OPV**) and catalytic amount of pyridine (0.1 mmol) were added and refluxed for 8 h under argon atmosphere. The solvent was evaporated and the residue was dissolved in chloroform followed by precipitation with methanol. The crude mixture was filtered and the product was then purified by eluting through a silica column using chloroform-hexane (1:2) mixture. After purification, the monocholesterol derivative was obtained as the major product (70%). The yield of

the bischolesterol derivative was improved by using 2.2 mmol of cholesteryl chloroformate followed by refluxing for 12 h under similar reaction conditions (90%).

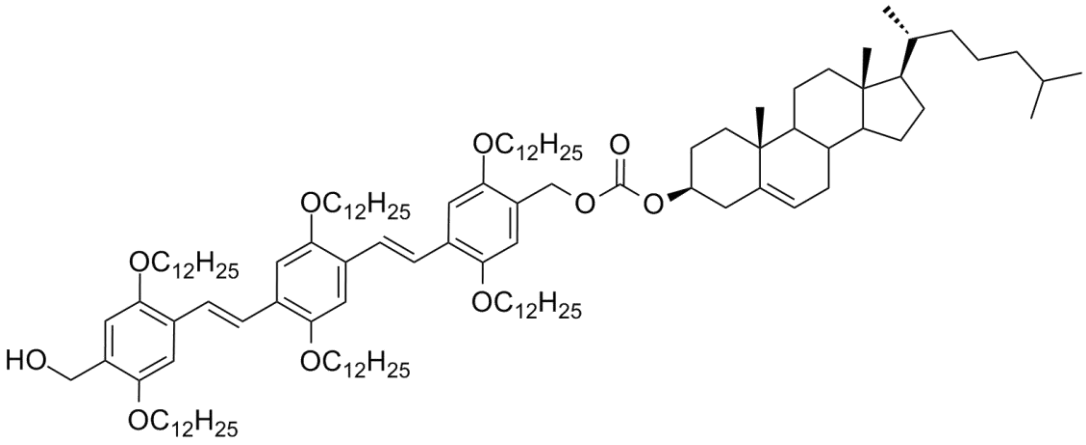

Yield: 70%; **m. p.:** 141-143 °C; **FT-IR** (KBr) ν_{max}: 3327, 2921, 1740, 2850, 1508, 1466, 1458, 1423, 1388, 1345, 1255, 1208, 1073, 1012, 722, 806, 853, 965, 694 cm^{-1}; **^{1}H NMR** (500 MHz, $CDCl_3$) δ : 7.42-7.45 (d, 4H, phenyl-*H*), 7.09-7.11 (d, 4H, vinyl-*H*), 6.84-6.89 (s, 2H, phenyl-*H*), 5.40 (s, 1H, C=C*H*–), 5.20 (s, 2H, –CH_2–OCO–), 4.68 (s, 2H, –CH_2OH), 4.49-4.51 (m, 1H, –OC*H*–), 4.02-4.04 (m, 12H, –OCH_2–), 0.93-2.43 (m, 160H, –CH_2– and –CH_3), 0.87 (m, 18H, –CH_3), 0.68 (s, 3H, –CH_3) ppm; **^{13}C NMR** (300 MHz, CDCl3) δ : 155.3, 155.1, 152.8, 151.6, 142.7, 142.4, 139.9, 135.2, 128,6, 128.4, 128.2, 127.0, 126.8, 123.4, 116.1, 115.8, 114.3, 108.7, 108.5, 76.4, 69.5, 68.2, 63.7, 60.7, 56.9, 56.6, 49.7, 42.5, 40.1, 39.8, 37.9, 37.5, 37.0, 36.7, 36.1, 32.2, 31.7, 29.8, 29.6, 29.6, 29.5, 29.4, 28.9, 28.7, 28.5, 28.3, 27.7, 25.5, 24.6, 24.3, 22.9, 22.6, 21.5, 19.6, 19.0, 14.0,12.1 ppm; **MALDI-TOF-MS**: calculated *m/z* for $C_{124}H_{210}O_{10}$: 1859.59, found: 1860.05.

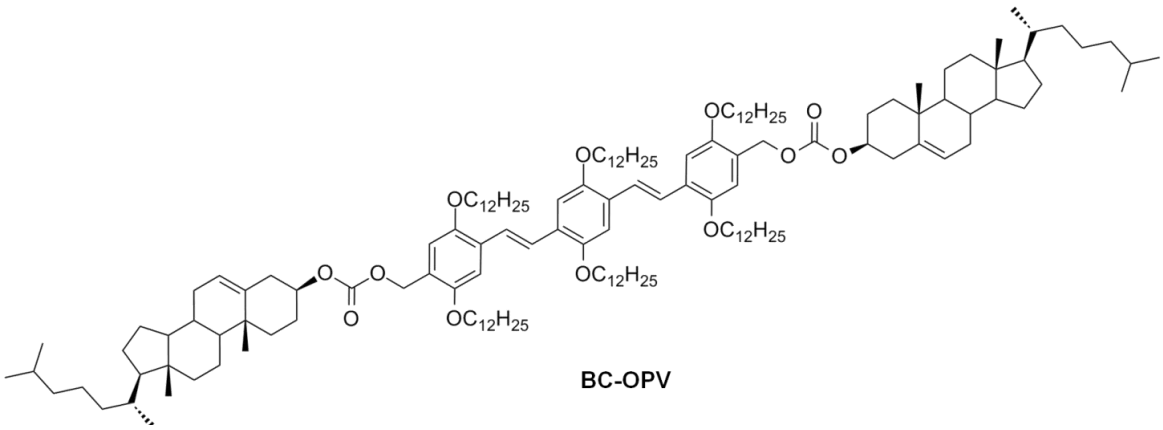

BC-OPV

Yield: 90%; **m. p.:** 110-112 °C; **FT-IR** (KBr) $\nu_{\max}$: 2924, 2851, 1740, 1508, 1465, 1426, 1384, 1349, 1267, 1206, 1071, 1030, 1007, 968, 947, 856, 793, 723, 695 cm^{-1}; **^{1}H NMR** (500 MHz, CDCl$_3$) δ: 7.43-7.46 (d, 4H, phenyl-*H*), 7.11-7.14 (d, 4H, vinyl-*H*), 6.88-6.92 (s, 2H, phenyl-*H*), 5.41 (s, 2H, C=C*H*–), 5.21 (s, 4H, –C*H$_2$*–OCO–), 4.49-4.53 (m, 2H, –OC*H*–), 3.98-4.05 (m, 12H, –OC*H$_2$*–), 0.92-2.43 (m, 200H, –C*H$_2$*– and –C*H$_3$*), 0.90 (m, 18H, –C*H$_3$*), 0.68 (s, 6H, –C*H$_3$*) ppm; **^{13}C NMR** (300 MHz, CDCl3) δ: 155.3, 152.8, 151.6, 142.7, 139.9, 135.2, 128.2, 127.0, 126.8, 123.4, 116.1, 114.3, 108.7, 76.4, 69.5, 68.2, 63.7, 56.9, 56.6, 49.7, 42.6, 40.1, 39.9, 37.9, 37.5, 37.0, 36.7, 36.0, 32.2, 32.0, 31.7, 29.8, 29.6, 29.6, 29.5, 29.3, 28.9, 28.7, 28.5, 28.2, 27.7, 25.5, 24.6, 24.3, 22.9, 22.6, 21.5, 19.6, 19.0, 14.0, 12.1 ppm; **MALDI-TOF-MS**: calculated *m/z* for $C_{152}H_{254}O_{12}$: 2271.93, found: 2271.72.

C-OPV was prepared according to the literature method [61-62] and unambiguously characterized.

Yield: 95%; **m. p.:** 83-84 °C; **FT-IR** (KBr): $\nu_{\max}$: 3348, 2924, 2846, 1506, 1465, 1424, 1387, 1258, 1206, 1046, 968, 865 cm^{-1}; **^{1}H NMR** (500 MHz, CDCl3, TMS) δ :7.42-7.47 (d, 4H, phenyl-*H*), 7.05-7.15 (d, 4H, vinyl-*H*), 6.82-6.94 (s, 2H,

phenyl-*H*), 4.72- 4.74 (d, 4H, –CH_2OH), 4.02-4.16 (m, 12H, –OCH_2–), 0.75-1.8 (m, 118H, –CH_2– and –CH_3) ppm; **^{13}C NMR** (300 MHz, CDCl3) δ : 151.0, 150.6, 129.4, 127.7, 127.2, 126.7, 123.5, 114.1, 110.5, 69.5, 69.1, 68.2, 62.4, 31.6, 29.8, 29.1, 29.3, 28.9, 28.7, 27.6, 25.6, 24.4, 19.2, 14.0 ppm; **MALDI-TOF-MS**: calculated *m/z* for $C_{92}H_{158}O_8$: 1391.20, found: 1391.10.

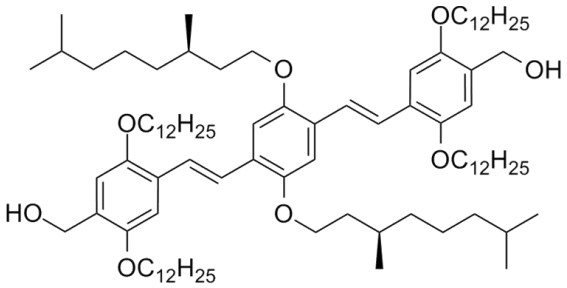

C-OPV

3.5.3. Description on Experimental Techniques

Measurements

The details of UV-Vis absorption spectrophotometer, spectrofluorimeter, Raman spectrometer, atomic force microscope and transmission electron microscope are described in the section 2.5.3 of Chapter 2. Temperature dependent studies were carried out in a 1 mm quartz cuvette with a thermistor directly attached to the wall of the cuvette holder. CD experiments were performed on JASCO 810 spectrometer using a quartz cuvette of 1 mm path length, equipped with peltier thermostatic cell holders, at various temperatures. CD spectra were recorded as θ in millidegrees, and converted into $\Delta\varepsilon$ using the equation $\Delta\varepsilon = \theta/ (33982\ c\ l)$, where $\Delta\varepsilon$ is the difference in the molar absorptivity for oppositely polarized light in $M^{-1}cm^{-1}$, c is the concentration in M and l is the path length in cm. The dissymmetry factor g_{abs} was calculated using the equation $g_{abs} = \Delta\varepsilon/\varepsilon$ where ε is the molar absorptivity at a particular wavelength.

n-Decane solution of **SWNT**, **MC-OPV** and **MC-OPV/SWNT** were drop cast on cleaned glass substrates and dried. The dried samples were subjected to Raman measurements. Samples for the AFM/TEM analysis were prepared by drop casting a *n*-decane solution on freshly cleaved mica substrate/carbon coated TEM grids and the samples were dried at ambient conditions.

General procedure for preparation of OPV/CNT hybrids

Solutions were prepared by dissolving **MC-OPV** (1-2 mg) in 2 mL of *n*-decane by heating to 50 °C followed by adding **SWNT** (0.1-0.6 mg) or **MWNT** (0.1-0.6 mg). The solution was sonicated in a low power ultrasonic bath for a few minutes. The resultant mixture was cooled to room temperature to get **MC-OPV/CNT** hybrid, which was used for further studies. **BC-OPV/C-OPV/CNT** hybrids were also prepared in the same manner with the appropriate amounts of **BC-OPV** and **C-OPV** derivatives for required concentrations in *n*-decane.

3.6. References

(1) Lehn, J.-M. *Angew. Chem. Int. Ed.* **1990**, *29*, 1304-1319.

(2) Rowan, A. E.; Nolte, R. J. M. *Angew. Chem. Int. Ed.* **1998**, *37*, 63-68.

(3) Lawrence, D. S.; Jiang, T.; Levett, M. *Chem. Rev.* **1995**, *95*, 2229-2260.

(4) Green, M. M.; Jha, S. K. *Chirality* **1997**, *9*, 424-427.

(5) Soai, K.; Shibata, T.; Morioka, H.; Choji, K. *Nature* **1995**, *378*, 767-768.

(6) Green, M. M.; Cheon, K.-S.; Yang, S.-Y.; Park, J.-W.; Swansburg, S.; Liu, W. *Acc. Chem. Res.* **2001**, *34*, 672-680.

(7) Schmuck, C. *Angew. Chem. Int. Ed.* **2003**, *42*, 2448-2452.

(8) Brunsveld, L.; Lohmeijer, B. G. G.; Vekemans, J. A. J. M.; Meijer, E. W. *Chem. Commun.* **2000**, *0*, 2305-2306.

(9) Cornelissen, J. J. L. M.; Rowan, A. E.; Nolte, R. J. M.; Sommerdijk, N. A. J. M. *Chem. Rev.* **2001**, *101*, 4039-4070.

(10) Teramoto, A. *Prog. Polym. Sci.* **2001**, *26*, 667-720.

(11) Yashima, E.; Maeda, K.; Nishimura, T. *Chem. Eur. J.* **2004**, *10*, 42-51.

(12) Mateos-Timoneda, M. A.; Crego-Calama, M.; Reinhoudt, D. N. *Chem. Soc. Rev.* **2004**, *33*, 363-372.

(13) Serrano, J. L.; Sierra, T. *Coord. Chem. Rev.* **2003**, *242*, 73-85.

(14) Brizard, A.; Oda, R.; Huc, I. *Low Molecular Mass Gelator*; Springer: Berlin, Germany, 2005.

(15) Luisi, P. L. *The Emergence of Life*; Cambridge University Press, 2006.

(16) Eelkema, R.; Feringa, B. L. *Org. Bio. Chem.* **2006**, *4*, 3729-3745.

(17) Weissbuch, I.; Leiserowitz, L.; Lahav, M. In *Prebiotic Chemistry*; Springer: Berlin,Germany, 2005.

(18) Maeda, K.; Yashima, E. *Supramolecular Chirality*; Springer: Berlin, Germany, 2006.

(19) Palmans, A. R. A.; Vekemans, J. A. J. M.; Havinga, E. E.; Meijer, E. W. *Angew. Chem. Int. Ed.* **1997**, *36*, 2648-2651.

(20) Wulff, G.; Dhal, P. K. *Macromolecules* **1990**, *23*, 4525-4527.

(21) Philp, D.; Stoddart, J. F. *Angew. Chem. Int. Ed.* **1996**, *35*, 1155-1196.

(22) Yashima, E.; Matsushima, T.; Okamoto, Y. *J. Am. Chem. Soc.* **1997**, *119*, 6345-6359.

(23) Cornelissen, J.; Fischer, M.; Sommerdijk, N.; Nolte, R. J. M. *Science* **1998**, *280*, 1427-1430.

(24) Wilson, A. J.; Masuda, M.; Sijbesma, R. P.; Meijer, E. W. *Angew. Chem. Int. Ed.* **2005**, *44*, 2275-2279.

(25) Masuda, M.; Jonkheijm, P.; Sijbesma, R. P.; Meijer, E. W. *J. Am. Chem. Soc.* **2003**, *125*, 15935-15940.

(26) Prins, L. J.; De Jong, F.; Timmerman, P.; Reinhoudt, D. N. *Nature* **2000**, *408*, 181-184.

(27) Cornelissen, J.; Donners, J.; de Gelder, R.; Graswinckel, W. S.; Metselaar, G. A.; Rowan, A. E.; Sommerdijk, N.; Nolte, R. J. M. *Science* **2001**, *293*, 676-680.

(28) Brunsveld, L.; Vekemans, J.; Hirschberg, J.; Sijbesma, R. P.; Meijer, E. W. *PNAS* **2002**, *99*, 4977-4982.

(29) Lehn, J. M. *Science* **2002**, *295*, 2400-2403.

(30) Reinhoudt, D. N.; Crego-Calama, M. *Science* **2002**, *295*, 2403-2407.

(31) Whitesides, G. M.; Grzybowski, B. *Science* **2002**, *295*, 2418-2421.

(32) Mislow, K. *Collect. Czech. Chem. Commun.* **2003**, *68*, 849-864.

(33) de Jong, J. J. D.; Lucas, L. N.; Kellogg, R. M.; van Esch, J. H.; Feringa, B. L. *Science* **2004**, *304*, 278-281.

(34) García, F.; Sánchez, L. *J. Am. Chem. Soc.* **2011**, *134*, 734-742.

(35) Ajayaghosh, A.; Varghese, R.; George, S. J.; Vijayakumar, C. *Angew. Chem. Int. Ed.* **2006**, *45*, 1141-1144.

(36) Prince, R. B.; Moore, J. S.; Brunsveld, L.; Meijer, E. W. *Chem. Eur. J.* **2001**, *7*, 4150-4154.

(37) Prins, L. J.; Timmerman, P.; Reinhoudt, D. N. *J. Am. Chem. Soc.* **2001**, *123*, 10153-10163.

(38) Schenning, A. P. H. J.; Kilbinger, A. F. M.; Biscarini, F.; Cavallini, M.; Cooper, H. J.; Derrick, P. J.; Feast, W. J.; Lazzaroni, R.; Leclère, P.; McDonell, L. A.; Meijer, E. W.; Meskers, S. C. J. *J. Am. Chem. Soc.* **2002**, *124*, 1269-1275.

(39) Prins, L. J.; Huskens, J.; de Jong, F.; Timmerman, P.; Reinhoudt, D. N. *Nature* **1999**, *398*, 498-502.

(40) Ajayaghosh, A.; Varghese, R.; Mahesh, S.; Praveen, V. K. *Angew. Chem. Int. Ed.* **2006**, *45*, 7729-7732.

(41) George, S. J.; Tomović, Ž.; Smulders, M. M. J.; de Greef, T. F. A.; Leclère, P. E. L. G.; Meijer, E. W.; Schenning, A. P. H. J. *Angew. Chem. Int. Ed.* **2007**, *46*, 8206-8211.

(42) George, S. J.; de Bruijn, R.; Tomović, Ž.; Van Averbeke, B.; Beljonne, D.; Lazzaroni, R.; Schenning, A. P. H. J.; Meijer, E. W. *J. Am. Chem. Soc.* **2012**, *134*, 17789-17796.

(43) Iijima, S. *Nature* **1991**, *354*, 56-58.

(44) Ajayan, P. M. *Chem. Rev.* **1999**, *99*, 1787-1799.

(45) Simmons, T. J.; Rivet, C. J.; Singh, G.; Beaudet, J.; Sterner, E.; Guzman, D.; Hashim, D. P.; Lee, S. H.; Qian, G. G.; Lewis, K. M.; Karande, P.; Ajayan,

P. M.; Gilbert, R. J.; Dordick, J. S.; Linhardt, R. J. *ACS Sym. Ser.* **2012**, *1119*, 155-174.

(46) Heister, E.; Brunner, E. W.; Dieckmann, G. R.; Jurewicz, I.; Dalton, A. B. *ACS. Appl. Mater. Interfaces* **2013**, *5*, 1870-1891.

(47) De Volder, M. F. L.; Tawfick, S. H.; Baughman, R. H.; Hart, A. J. *Science* **2013**, *339*, 535-539.

(48) Dyke, C. A.; Tour, J. M. *Chem. Eur. J.* **2004**, *10*, 813-817.

(49) Guldi, D. M.; Rahman, G. M. A.; Zerbetto, F.; Prato, M. *Acc. Chem. Res.* **2005**, *38*, 871-878.

(50) Münzer, A. M.; Michael, Z. P.; Star, A. *ACS Nano* **2013**, *7*, 7448-7453.

(51) Babu, S. S.; Praveen, V. K.; Ajayaghosh, A. *Chem. Rev.* **2014**, *114*, 1973-2129.

(52) Bilalis, P.; Katsigiannopoulos, D.; Avgeropoulos, A.; Sakellariou, G. *RSC. Adv.* **2014**, *4*, 2911-2934.

(53) Tans, S. J.; Devoret, M. H.; Dai, H. J.; Thess, A.; Smalley, R. E.; Geerligs, L. J.; Dekker, C. *Nature* **1997**, *386*, 474-477.

(54) Opatkiewicz, J.; LeMieux, M. C.; Bao, Z. *ACS Nano* **2010**, *4*, 2975-2978.

(55) Maligaspe, E.; Sandanayaka, A. S. D.; Hasobe, T.; Ito, O.; D'Souza, F. *J. Am. Chem. Soc.* **2010**, *132*, 8158-8164.

(56) D'Souza, F.; Das, S. K.; Zandler, M. E.; Sandanayaka, A. S. D.; Ito, O. *J. Am. Chem. Soc.* **2011**, *133*, 19922-19930.

(57) Guldi, D. M.; Rahman, G. M. A.; Zerbetto, F.; Prato, M. *Acc. Chem. Res.* **2005**, *38*, 871-878.

(58) Zhao, Y.-L.; Stoddart, J. F. *Acc. Chem. Res.* **2009**, *42*, 1161-1171.

(59) Srinivasan, S.; Babu, S. S.; Praveen, V. K.; Ajayaghosh, A. *Angew. Chem. Int. Ed.* **2008**, *47*, 5746-5749.

(60) Ajayaghosh, A.; Vijayakumar, C.; Varghese, R.; George, S. J. *Angew. Chem. Int. Ed.* **2006**, *45*, 456-460.

(61) George, S. J.; Ajayaghosh, A.; Jonkheijm, P.; Schenning, A. P. H. J.; Meijer, E. W. *Angew. Chem. Int. Ed.* **2004**, *43*, 3422-3425.

(62) George, S. J.; Ajayaghosh, A. *Chem. Eur. J.* **2005**, *11*, 3217-3227.

(63) Srinivasan, S.; Babu, S. S.; Praveen, V. K.; Ajayaghosh, A. *Angew. Chem.* **2008**, *120*, 5830-5833.

(64) Smulders, M. M. J.; Nieuwenhuizen, M. M. L.; de Greef, T. F. A.; van der Schoot, P.; Schenning, A. P. H. J.; Meijer, E. W. *Chem. Eur. J.* **2010**, *16*, 362-367.

(65) Stéphan, C.; Nguyen, T. P.; de la Chapelle, M. L.; Lefrant, S.; Journet, C.; Bernier, P. *Synt. Met.* **2000**, *108*, 139-149.

(66) Zhao, Q.; Wagner, H. D. *Phil. Trans. R. Soc. Lon. A* **2004**, *362*, 2407-2424.

(67) Utsumi, S.; Kanamaru, M.; Honda, H.; Kanoh, H.; Tanaka, H.; Ohkubo, T.; Sakai, H.; Abe, M.; Kaneko, K. *J. Colloid Interface Sci.* **2007**, *308*, 276-284.

Chapter 4

Superhydrophobic Coatings of Carbon Nanotubes and Polymerizable Linear π-Systems

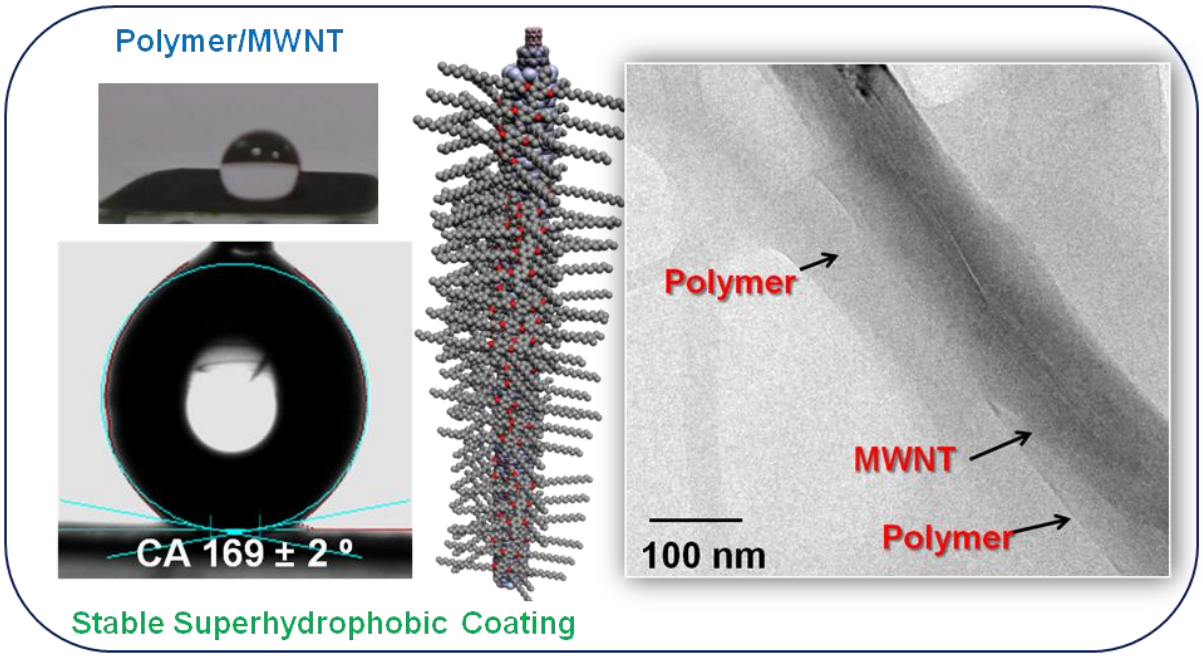

4.1. Abstract

*A few linear π-conjugated molecules with polymerizable end groups have been designed and synthesized. The corresponding self-assembled polymer/**MWNT** hybrids were prepared via π-stacking and polymerization of these molecules around the **MWNTs**. The better dispersion of these polymer/**MWNT** hybrid materials in organic solvents offer easy solution processing and hence the effective preparation of their coatings. The formulation obtained from these polymer/**MWNT** hybrid materials exhibited superhydrophobic properties when coated on different substrates. These superhydrophobic coatings exhibited significantly high water contact angle and have excellent stability even under acidic and basic conditions. For instance, the formulation obtained from **poly-S-OPV1/MWNT** resulted in surfaces with water contact angles of 169 ± 2°. When the hull of a water moving vehicle (a model boat with a mass of 36 g) was coated with the formulation of **poly-V-OPV/MWNT**, the drag coefficient (C_D = 0.19) was reduced by >60%, when compared to that of the uncoated one (C_D = 0.50). Remarkably, the boat with a coated hull experienced a 1.6 fold increase in buoyant force and this enhancement in buoyancy allowed to carry an additional 25% of cargo on board. Hence, such superhydrophobic coatings with superior water contact angle and low drag coefficients are promising candidates for applications such as self-cleaning, anti-icing, and drag resistant surfaces.*

4.2. Introduction

Wettability and anti-wettability are important properties of any surface, which play significant role in the overall utility of materials for specific applications. Hydrophobicity is one such property. The first superhydrophobic surface was made by

coating carbon soot on rough crystals of arsenic trioxide.[1] The phenomenon of "lotus effect" explained by Brathloot *et al.*[2] has attracted the attention of scientists in search of artificial self-cleaning materials. Similarly, the sticky superhydrophobicity of rose petals has been of interest to scientists.[3] Water contact angle and contact angle hysteresis (the difference between the advancing and receding contact angles) are important parameters determining the properties of a superhydrophobic surface. While both lotus leaves and rose petals have high contact angles, low contact angle hysteresis is observed for the former and high contact angle hysteresis for the later. The nano- and microscopic architectures along with an epicuticular wax coating are responsible for the superhydrophobic behavior as well as self-cleaning properties of lotus leaves. This phenomenon is also known in other biological surfaces such as plant leaves of triticum, rice leaves, duck's feather, back of desert beetle, spider silks, water slider's leg, etc.[4-8] Deeper understanding of the mechanism of natural superhydrophobic surfaces helped scientists to design and develop several artificial superhydrophobic surfaces for practical applications.[9-10]

In order to explain the wetting properties of a surface, two theoretical models have been proposed, Wenzel model and Cassie-Baxter model.[11-12] If a sessile droplet of water is placed on a flat surface, it normally adopts a spherical shape (Figure 4.1). The angle between the solid surface and the interface of liquid-vapor is called the contact angle (θ_{CA}) that depends on the interfacial energies between liquid-vapor (γ_{LV}), solid-vapor (γ_{SV}), and solid-liquid (γ_{SL}) interfaces (Equation 1). If the θ_{CA} is less than

90°, the surface is said to be hydrophilic; if the θ_{CA} is greater than 90°, then the surface is considered as hydrophobic, and if the θ_{CA} is > 150°, the surface is considered as superhydrophobic.

$$\cos \theta_{CA} = \gamma_{SV} - \gamma_{SL} / \gamma_{LV} \qquad \text{(Eq.1)}$$

Figure 4.1. Schematic representation of a droplet placed on a) a flat and b), c) rough substrates. The hydrophobicity is described using Wenzel or Cassie-Baxter model depending on the roughness of the surface.

Depending on the roughness of the surface, a droplet is considered in either Wenzel model or Cassie-Baxter model. In Wenzel model, θ_{CA} is described as a function of actual contact angle θ_F and the ratio of apparent area of the rough surface to the actual surface area (R; Equation 2; Figure 4.1b). In the case of Cassie-Baxter model, the rough surface is considered to be made up of small textures with protrusions (Figure 4.1c). Because of trapped air underneath the droplet, the liquid cannot wet the textures. Here, θ_{CA} is described as a function of the fraction of the surface in contact with the liquid (Equation 3).

$$\cos \theta_{CA} = R \cos \theta_F = R\, \gamma_{SV} - \gamma_{SL} / \gamma_{LV} \qquad \text{(Eq. 2)}$$

$$\cos \theta_{CA} = -1 + \emptyset_S (1+ \gamma_{SV} - \gamma_{SL} / \gamma_{LV}) \quad \text{(Eq. 3)}$$

A combination of right surface chemistry and appropriate surface roughness plays the crucial role in the preparation of superhydrophobic surfaces.[13] There are two major steps involved in the generation of superhydrophobic surfaces: (i) the fabrication of nanoscale rough surfaces and (ii) the functionalization with materials of low surface energy (mostly fluorinated molecules or macromolecules). Several methods have been used to prepare superhydrophobic surfaces including lithography, plasma techniques, electrochemical methods, chemical vapor deposition, sol-gel techniques, etc.[14-19] Among various superhydrophobic materials developed,[9-10,13,20] carbon allotropes such as carbon nanotubes[21-22], graphene[23] and fullerenes[15] based hybrid materials have attracted a lot of interest due to easy solution processability and excellent physical and mechanical properties. Carbon nanotubes-based superhydrophobic hybrid materials have been well studied for different applications such as water-repellent, self-cleaning and anti-icing surfaces, oil-water separation, etc.[24-30] Jiang *et al.* have demonstrated the large area fabrication of vertically grown **CNTs** by pyrolysis of phthalocyanine.[31] The honeycomb-like microstructures were shown to be responsible for the water-repellent properties of the prepared films, with a lower sliding angle (Figure 4.2a and 4.2b). The length of the aligned carbon nanotubes was ~10 μm and was tuned by altering the reaction time. In order to improve the water repellency of the vertically aligned **CNTs**, the percentage of oxygen functionalities should be minimal and was achieved by expo-

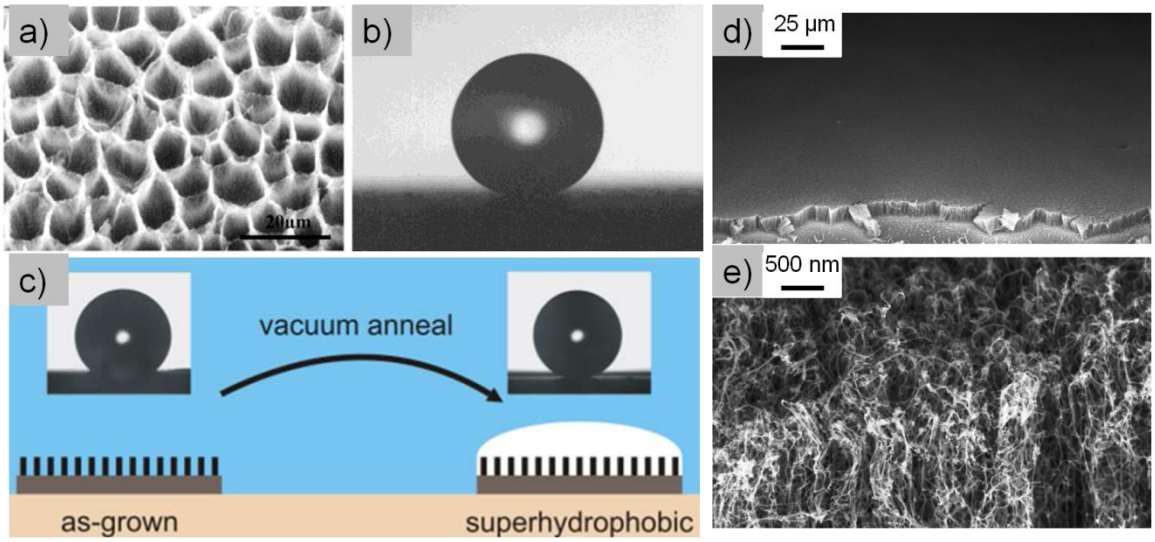

Figure 4.2. a) SEM images of honeycomb-like aligned **CNT** arrays. b) Photograph of a water droplet on the superhydrophobic **CNT** arrays. c) Schematic representation showing process of vacuum annealing to transform as-grown **CNT** arrays into a superhydrophobic surface at a moderate temperature. d) and e) SEM images of as-grown **CNT** arrays.

sing the **CNT** arrays to a vacuum annealing process at a moderate temperature (Figure 4.2c).[32] For the successful manifestation of superhydrophobicity, **CNTs** arrays have been grown uniformly across the substrate, without any large-scale irregularities and surface defects (Figure 4.2d and 4.2e). The stability of these superhydrophobic **CNT** arrays was studied by dispersing them in solutions of varying pH, however, good stability was observed only at neutral pH. Instead of vacuum annealing, the superhydrophobic properties were enhanced by chemical vapor deposition (CVD) of silicone over aligned **CNT** arrays. Kim *et al.* have demonstrated the fabrication of **CNT** arrays with nanoscale roughness by a simple contact transfer technique and subsequent silicone coating (Figure 4.3a).[33] Well-aligned **CNT** arrays have been

prepared with a spacing of 45-160 µm and a width of 65 µm (Figure 4.3b and 4.3c). During the CVD process, silicone was deposited over the individual **CNTs** as well as the top surface of **CNT** arrays, thereby reducing the surface energy.

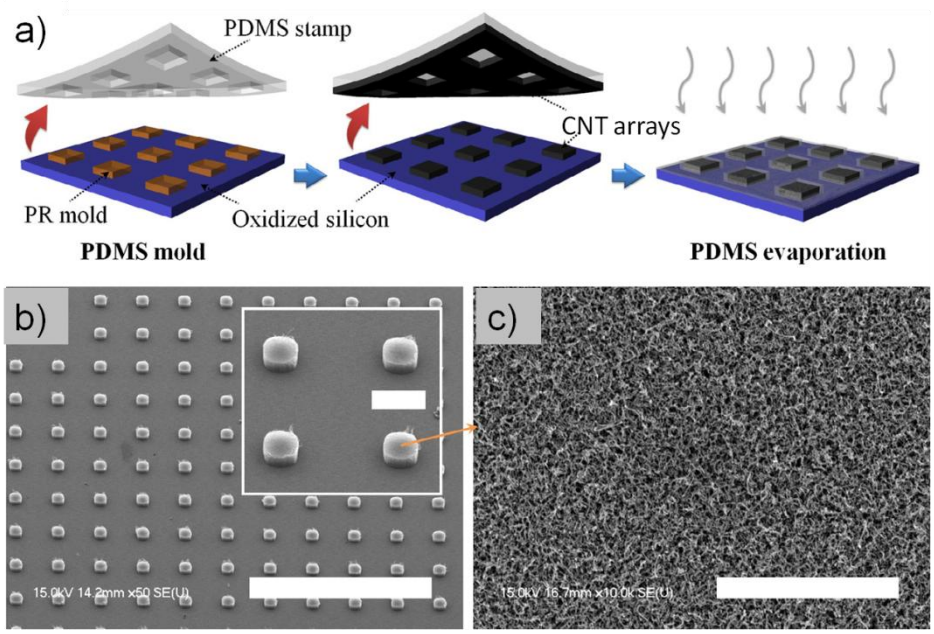

Figure 4.3. a) Schematic representation showing fabrication of vertically aligned hierarchical **CNT** surfaces. b) and c) SEM images of the fabricated **CNT** arrays.

Unlike as-grown aligned **CNT** arrays, **CNT**-based hybrid materials prepared by covalent and non-covalent functionalization have been established for their easy preparation methods and better superhydrophobic properties.[27,34-37] Zheng *et al*. have reported a superhydrophobic film composed of **CNTs**, covalently modified with acetone molecules.[37] The **CNTs** were covalently connected to acetone molecules through surface defects, forming C(acetone)-O-C(nanotube) linkage. The spray coated acetone functionalized **CNT** hybrid on a glass substrate showed good

superhydrophobic properties when compared to that of unfunctionalized **CNTs**. A **CNT**-based hybrid material obtained via covalent functionalization with poly(dopamine) (PDA) and poly(ethyleneimine) (PEI) are also shown to form a platform for creating superhydrophobic films.[27] The **CNTs** were first covalently functionalized with poly(dopamine) via in-situ polymerization under basic conditions, followed by a layer-by-layer (LbL) self-assembly of the hybrid material using with PEI (Figure 4.4a). Finally, superhydrophobic properties were introduced by CVD of

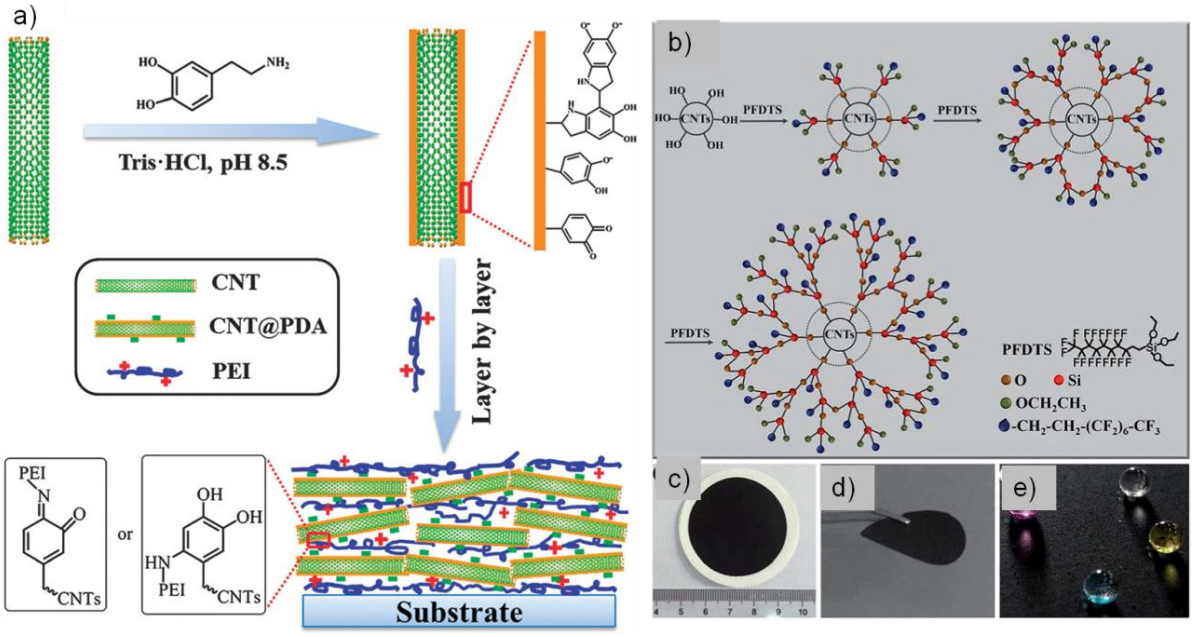

Figure 4.4. Schematic representations of a) the preparation of **CNT**/poly(dopamine)/ poly(ethyleneimine) hybrid film by layer-by-layer self-assembly method, and b) the fabrication of superhydrophobic **PFDTS/CNT** hybrid. Photographs of c) **PFDTS/CNT** flim prepared on **PVDF** membrane via filteration process, d) a free-standing **PFDTS/CNT** film peeled off from the membrane and e) colored water droplets on the free-standing superhydrophobic film.

fluoroalkyl silane over the LbL self-assembled hybrid material. A robust **CNT**-based superhydrophobic material was also prepared by attaching a fluorine-containing organosilane (1H,1H,2H,2H-perfluorodecyltriethoxy-silane, **PFDTS**) to the surface hydroxy groups of the **CNTs** (Figure 4.4b).[36] A **PVDF** membrane coated with the hybrid material exhibited better superhydrophobic properties, and also the resulting membrane was used for the separation of surfactant stabilized oil-water mixture, with high separation efficiency (Figure 4.4c-e).

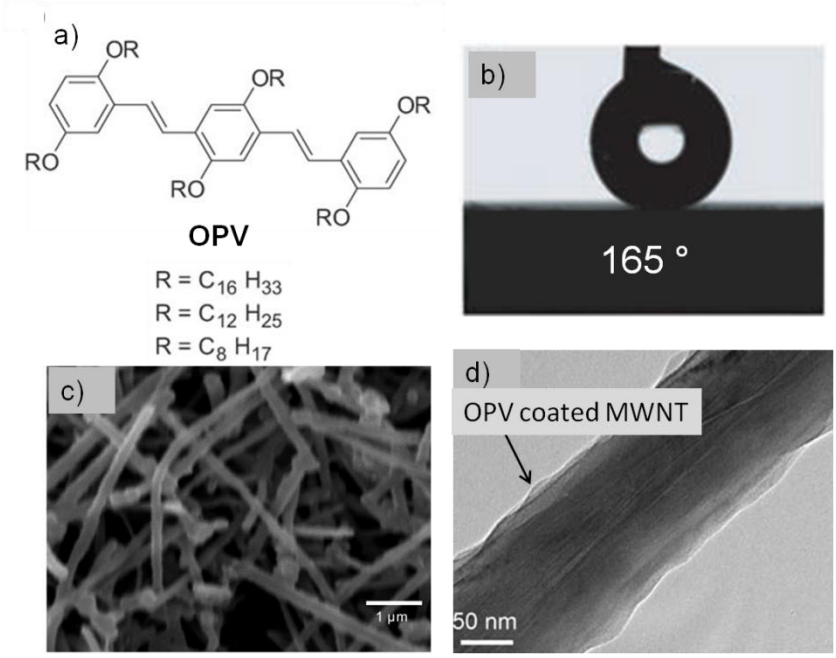

Figure 4.5. a) Chemical structures of the **OPV** derivatives. b) Photograph of a water droplet on **OPV/MWNT** coated superhydrophobic glass substrate, with a water contact angle of 165°. c) SEM and d) TEM images of **OPV/MWNT** hybrid.

Non-covalently functionalized **CNT**-based hybrid materials are found to be superior to the covalently functionalized one as the electronic properties of **CNTs** are

preserved in the former.[38-39] But the preservation of the inherent properties of **CNTs** may be achieved at the expense of the stability of the hybrid material in the absence of strong covalent functionalization. Self-assembled hybrid materials of **CNTs** with π-conjugated molecules are more suitable for making superhydrophobic surfaces, as tuning of their nano- as well as microscopic morphologies is easy and efficient. Ajayaghosh *et al.* have demonstrated a superhydrophobic coating based on **CNTs** and linear π-conjugated molecules such as oligo(*p*-phenylenevinylene)s (**OPV**) through a bottom-up self-assembly approach (Figure 4.5).[35] The self-assembled hybrid materials were prepared by utilizing strong π-π interactions between **CNTs** and **OPVs** in organic solvents. **OPVs** underwent self-assembly over the π-surface of the **CNTs**, leading to a wax-like coating around them. The nano- and microscopic morphologies of the hybrids were responsible for the excellent superhydrophobic properties (Figure 4.5b-d).

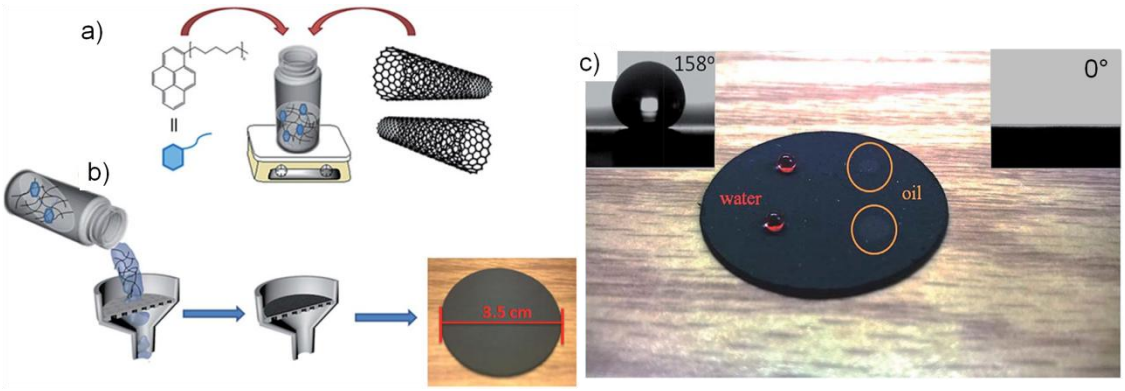

Figure 4.6. Schematic representations of a) the preparation of alkyl pyrene and **MWNT** hybrid and b) the vacuum filteration process to make the free-standing hybrid film. c) Photograph of water and oil droplets on the free-standing superhydrophobic film (Insets show the film with a water contact angle of 158° and an oil contact angle of 0°, respectively).

These superhydrophobic coatings exhibited better stability at highly acidic and basic conditions. A self-assembled hybrid material of alkyl pyrene and **CNT** was also prepared by non-covalent functionalization in an organic solvent (Figure 4.6).[34] The strong π-π interactions between the pyrene moiety and the **CNT** led to the adsorption of alkyl pyrene molecules onto the **CNT** surface. A free-standing film was prepared by filtering the dispersion of hybrid in NMP. The resultant film exhibited excellent superhydrophobic as well as superoleophilic properties (Figure 4.6b and 4.6c).

Surfaces with hierarchical roughness and low surface energy are highly significant for multifarious applications. Several attempts including chemical vapor deposition, fabrication of aligned polymer nano-pillars by templating, and sol-gel methods have been made to create hierarchical micro- and nanostructures with excellent wetting and anti-wetting properties. However, these methods involve rigorous experimental conditions, and tedious fabrication procedures. The work described in this chapter is aimed at developing easily processable superhydrophobic coatings derived from **CNTs** and **OPV** derived π-systems using the principle of molecular self-assembly. The potential application of this coating in achieving energy efficiency is also described.

4.3. Results and Discussion

4.3.1. The Design Strategy

OPVs have strong tendency for π-interaction with **CNTs**. Such π-interaction can be used to disperse **CNTs** in solvents for better processing. **MWNTs** of large diameter along with self-assembled **OPVs** having long hydrocarbon chains may provide nanohybrid surfaces with nano- as well as microscopic roughness. Coatings of such nanohybrids may lead to superhydrophobic surfaces similar to the lotus effect. However, the non-covalently attached **OPVs** over a period of time may leach out from the **CNT** surface thereby depleting the superhydrophobic properties. In order to avoid leaching, the self-assembled **OPVs** should be further modified to fix them around the **CNT** surface.

Based on the above-mentioned objectives, we synthesized **S-OPV1-3,** with hydrocarbon chains attached to their π-conjugated backbones and polymerizable end groups. The structures are shown in Figure 4.7. The rationale for the choice of these molecules is as follows: (i) they have a π-conjugated backbone for interaction with **MWNTs** surface through π-π stacking. (ii) The long hydrocarbon chains attached to the **OPV** provides better solution processability for the **MWNTs** via interaction with solvent molecules. (iii) Different lengths for the hydrocarbon chains at the central phenyl ring will help in optimizing their role in determining the superhydrophobic

properties. (iv) Polymerization of terminal groups followed by self-assembly process may help the **OPVs** to strongly bind to **CNTs** and hence provides better stability.

In addition, to use the superhydrophobic coatings in practical application, the cost for the preparation of the material should be affordable. Hence, we have designed an **OPV** molecule (**V-OPV**) with free terminal vinyl group that requires a lesser number of synthetic steps when compared to the multi-step synthesis of other **OPVs** (**S-OPV1-3**), thereby lowering the material cost for the formulation of the super-hydrophobic coatings.

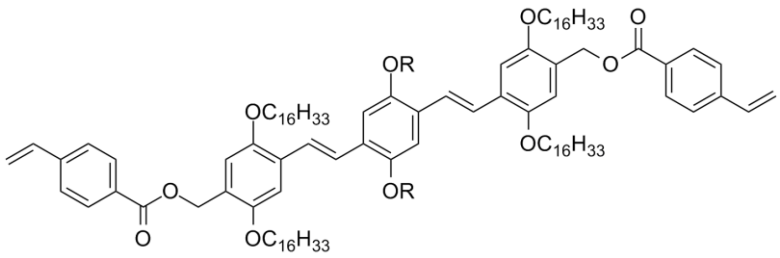

S-OPV1 : R = $C_{16}H_{33}$
S-OPV2 : R = C_4H_9
S-OPV3 : R = CH_3

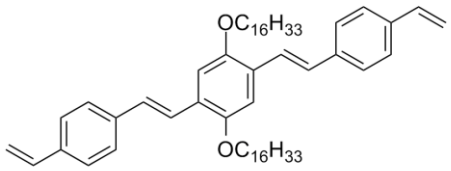

V-OPV

Figure 4.7. Chemical structure of **OPV** derivatives.

4.3.2. Synthesis of OPV Derivatives

Synthesis of **S-OPVs** was achieved as per our previous reports[40-43] (Scheme 4.1.). The bisalcohol derivatives **OPV1/4/5** were esterified with 4-vinylbenzoic acid (**9**) in dichloromethane in the presence of DCC and DMAP to yield the corresponding **S-OPVs**.[44]

Synthesis of **V-OPV** was accomplished by the Wittig-Horner reaction[41] involving the bisphosphonate ester (**10)** and 4-vinylbenzaldehyde (**11**) using *t*-BuOK

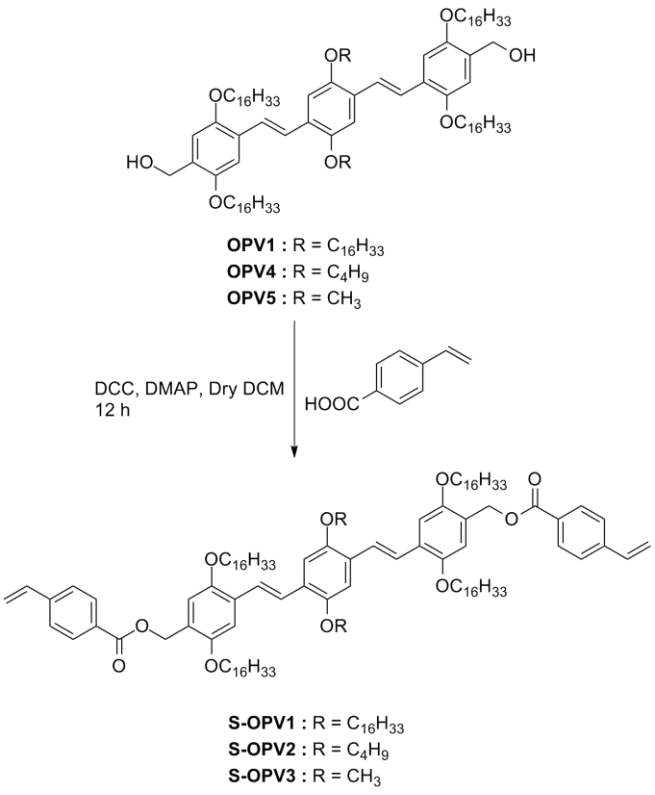

Scheme 4.1. Synthesis of **S-OPV1-3** derivatives.

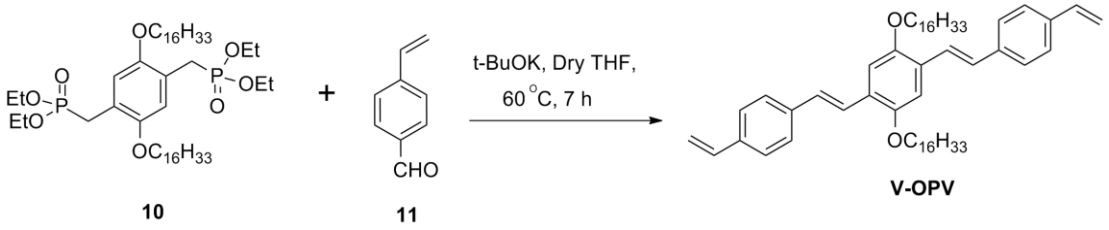

Scheme 4.2. Synthesis of **V-OPV** derivative.

in a 73% yield (Scheme 4.2). The corresponding bisphosphonate derivative (**10**) was prepared by the reaction of the bisbromomethyl derivative (**3)** (see Scheme 2.1 of the Chapter 2) with triethyl phosphite for 12 h at 100°C. The monoaldehyde (4-vinylbenzaldehyde) was synthesized using an already reported method.[45]

4.3.3. Preparation and Characterization of Polymer/MWNT Hybrids

The polymer/**MWNT** hybrid materials were prepared by acyclic diene metathesis polymerization (ADMET)[46] of the self-assembled styrene-appended **OPVs** (**S-OPV1-3**) on the surface of the **MWNTs** (Figure 4.8a and 4.8b). The polymerization was carried out in dry toluene using Grubb's catalyst (2nd generation) over 48 h. During the polymerization, the by-product (ethylene gas) was removed by vacuum treatment at liquid nitrogen temperature. After completion of the reaction, all the polymer/**MWNT** hybrids were precipitated in methanol, filtered and dried under ambient conditions. The dried samples were used for further studies.

The photophysical properties of polymer/**MWNT** hybrid materials and the individual components were studied by UV-Vis absorption and fluorescence spectroscopic techniques. **S-OPV1** showed three absorption peaks at 408, 320 and 268

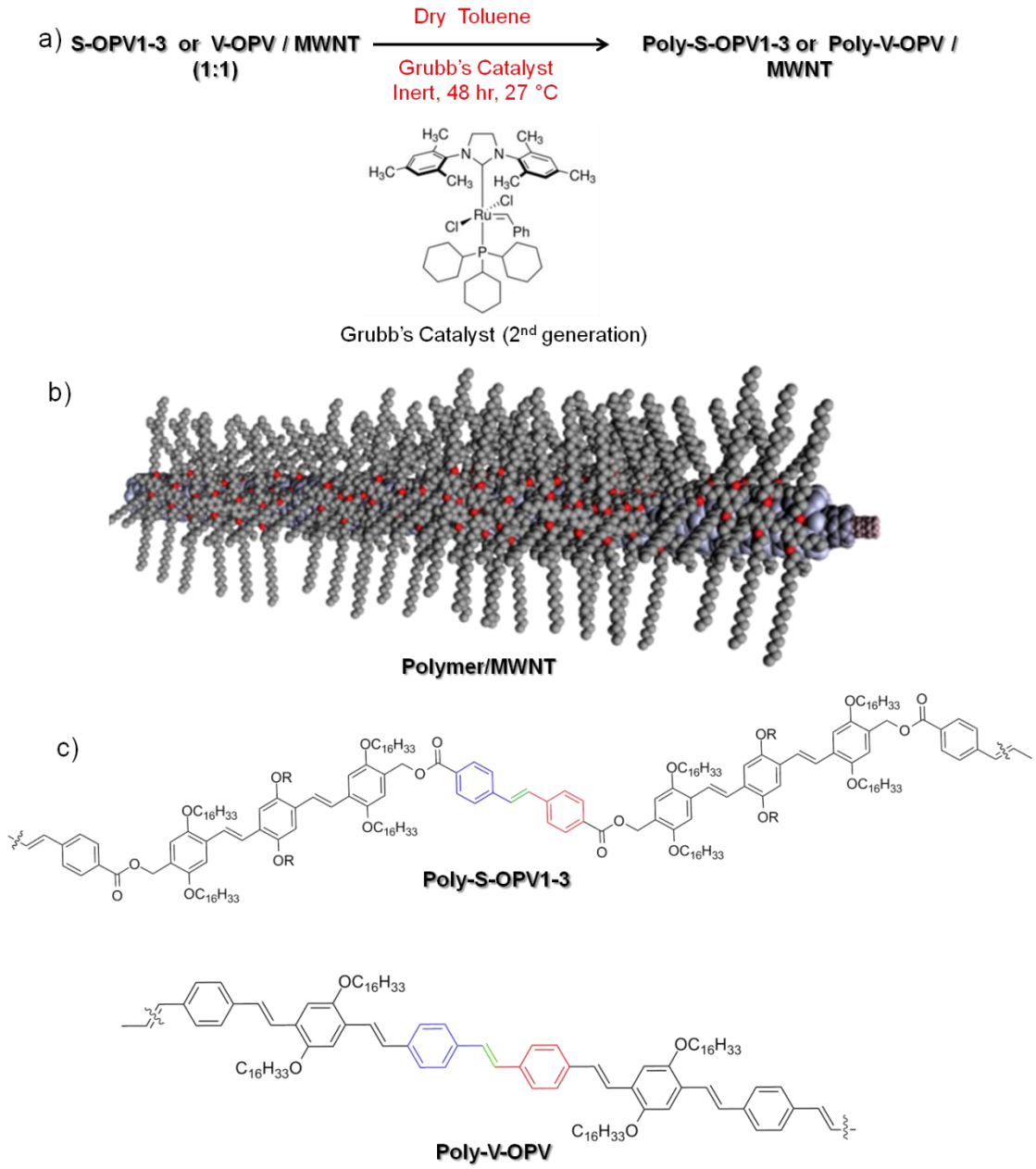

Figure 4.8. Schematic representations of a) the preparation of polymer/**MWNT** hybrids, b) the polymer coated **MWNTs** of polymer/**MWNT** hybrids. c) Chemical structures of **poly-S-OPV1-3** and **poly-V-OPV**.

nm (Figure 4.9a). Similarly, **poly-S-OPV1** also exhibited three absorption peaks at 409, 323 and 270 nm with slight shift in their absorption wavelength. The peak at 409

nm persisted with the least shift in the absorption spectra. On the other hand, the absorption peak at 323 nm corresponding to free styryl groups of **poly-S-OPV1**, showed a decrease in its absorption due to polymerization. A concomitant increase in the absorption peak at 323 nm was observed due to the newly formed stilbene groups in **poly-S-OPV1** (Figure 4.8c). Similar changes were also observed in the case of **poly-S-OPV1/MWNT** hybrid, confirming the presence of polymerized **S-OPV1** molecules in the hybrid material. It also showed a baseline shift due to Rayleigh scattering of dispersed **MWNTs** in solution. **S-OPV1** exhibited an emission maximum at 466 nm, with two shoulder peaks at 493 and 530 nm (Figure 4.9b). **Poly-S-OPV1** and **poly-S-OPV1/MWNT** exhibited emission peaks at 467, 494, 532 nm and 467, 494, 531 nm, respectively. A decrease in the emission intensity corresponding to **poly-S-OPV1** in the hybrid was observed due to quenching of its fluorescence by dispersed **MWNTs**. Unlike **S-OPV1**, **V-OPV** exhibited an absorption maximum at 407 nm and a shoulder band at 340 nm (Figure 4.9c), and **poly-V-OPV** at 430 nm (with a red shift of 23 nm). A visual color change was observed from light greenish yellow to bright yellow (Inset of Figure 4.9c). The red shifted absorption and hence the visible color change occurred due to the increase in conjugation during polymerization. **Poly-V-OPV/MWNT** showed an absorption maximum at 434 nm and also baseline shift due to Rayleigh scattering of the dispersed **MWNTs** in solution. **V-OPV** showed emission peaks at 464 and 491 nm with a shoulder band at 528 nm, whereas **poly-V-OPV** exhibited an emission maximum at 498 nm, with a shoulder band at 523 nm (Figure-

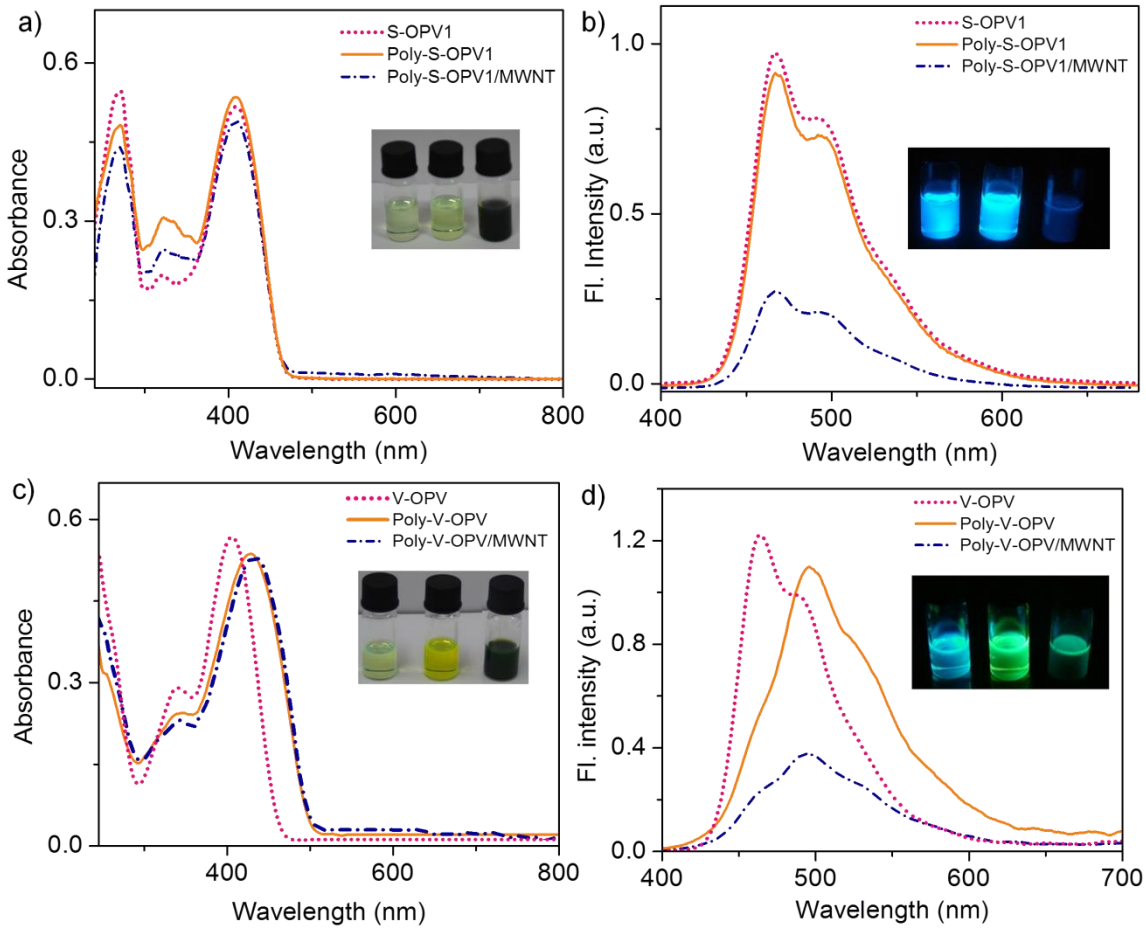

Figure 4.9. a), c) Absorption and b), d) fluorescence spectra of **S-OPV1** (c = 1 × 10^{-4} M), **poly-S-OPV1**, **poly-S-OPV1/MWNT** and **V-OPV** (c = 1 × 10^{-4} M), **poly-V-OPV**, **poly-V-OPV/MWNT,** respectively (Inset of Figure 4.9a and 4.9b: Photographs of **S-OPV1**, **poly-S-OPV1**, **poly-S-OPV1/MWNT** hybrid in chloroform (left to right) (4.9a) under ambient light and (4.9b) under UV light. Inset of Figure 4.9c and 4.9d: Photographs of **V-OPV**, **poly-V-OPV**, **poly-V-OPV/MWNT** hybrid in chloroform (left to right) (4.9c) under ambient light and (4.9d) under UV light).

4.9d). Similarly, **poly-V-OPV/MWNT** also exhibited emission peaks at 497 and 524 nm. The emission color change from cyan to green was observed due to the increase in conjugation of **poly-V-OPV** and **poly-V-OPV/MWNT** (Inset of Figure 4.9d). The **poly-V-OPV/MWNT** showed the emission peaks with lesser intensity when

compared to that of **poly-V-OPV** due to the quenching of fluorescence by dispersed **MWNT**s in the solution.

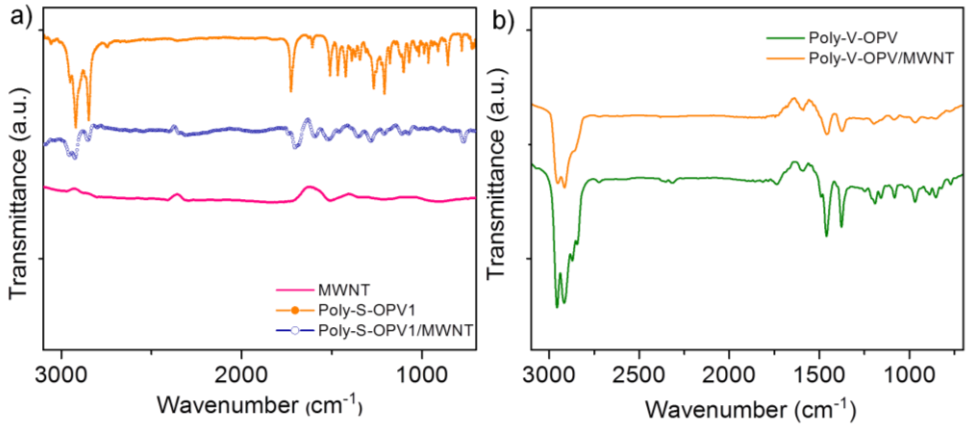

Figure 4.10. FT-IR spectra of a) **MWNT**, **poly-S-OPV1**, and **poly-S-OPV1/MWNT** and b) **poly-V-OPV**, and **poly-V-OPV/MWNT**.

The interaction between polymer and **MWNT** were studied by IR and Raman spectroscopic techniques as well as by XRD measurements. IR spectrum of **poly-S-OPV1** exhibited the aliphatic H-C-H stretching and carbonyl stretching vibrations in the range of 2985-2783 and 1729 cm^{-1}, respectively (Figure 4.10a). The H-C-H and C=C-H bending vibrations were present in the range of 1320-1536 and 800-900 cm^{-1}. IR spectrum of **MWNT** did not show any predominant peaks except broad peaks of the aromatic C-H stretching and C=C-H bending vibrations around 3000 and 1500 cm^{-1}. **Poly-S-OPV1/MWNT** showed the characteristic peaks of **poly-S-OPV1** that explains the presence of polymer in **poly-S-OPV1/MWNT** hybrid. In addition to that, the peaks corresponding to C=C-H bending (out of plane) vibration became broad and less intense due to the strong π-π interactions between **poly-S-OPV1** and **MWNT**.

Similarly, IR spectrum of **poly-V-OPV** showed the characteristic peaks corresponding to aliphatic H-C-H stretching, bending and C=C-H bending (out of plane) vibrations in the range of 2800-3000, 1300-1500 and 800-900 cm^{-1}, respectively (Figure 4.10b). The bending vibration peaks of C=C-H in the range 800-900 cm^{-1} became broad and less intense in the case of the hybrid due to the strong π-π interaction between polymer backbone and **MWNT**. The interaction between the polymer and **MWNT** was confirmed by Raman spectroscopy. Raman spectrum of the pristine **MWNT** exhibited a G-band at 1560 cm^{-1}, whereas **poly-S-OPV1/MWNT** showed the G-band at 1568 cm^{-1} with an upshift of 8 cm^{-1} when compared to that of **MWNT** (Figure 4.11a). Similarly, Raman spectrum of **poly-V-OPV** exhibited the G-band at 1565 cm^{-1}, with an upshift of 5 cm^{-1} (Figure 4.11b). The upshift of the G-band gave an evidence for the strong interaction between polymer and **MWNT** in the hybrid. XRD measurements

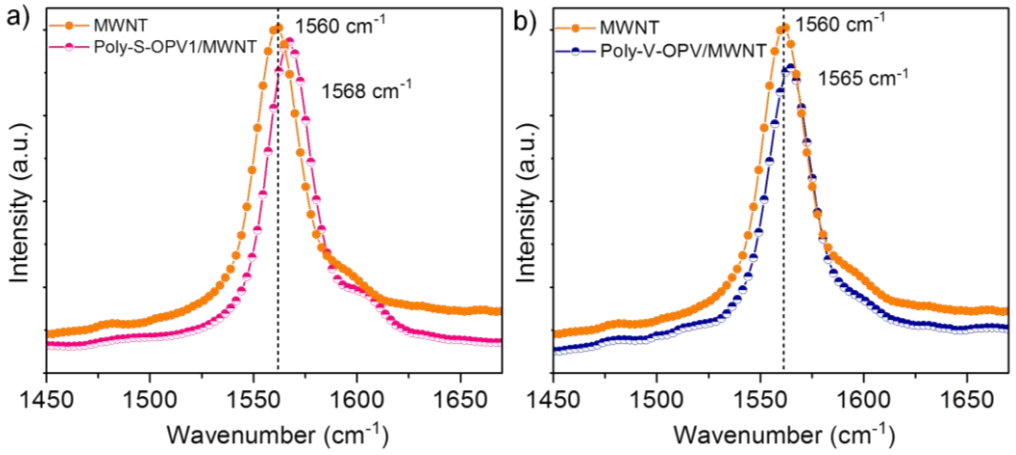

Figure 4.11. Raman spectra of a) **MWNT**, **poly-S-OPV1/MWNT** and b) **MWNT**, **poly-V-OPV/MWNT**.

were carried out to understand the molecular level interaction between the polymer and **MWNT**. The XRD profile of **MWNT** showed a strong peak at 2θ = 26.4° corresponding to the tubular distance for individual tubes in a single multi-walled nanotubes, which are concentric tubes with varying diameters. **Poly-S-OPV1/MWNT** showed three broad peaks at 2θ = 18.1°, 20.0°, and 23.4° corresponding to the d-spacing of 0.48, 0.44, and 0.38 nm, respectively in addition to a strong peak from **MWNT** at 2θ = 26.4 and peaks from **poly-S-OPV** (Figure 4.12a). The peaks at d = 0.48, 0.44, and 0.38 nm correspond to the various π-π stacking distances between polymer and **MWNTs**. Like **poly-S-OPV1/MWNT**, **poly-V-OPV/MWNT** also exhibited broad peaks at 2θ = 19.1° (d-spacing = 0.42 nm) and 23.6° (d-spacing = 0.37 nm) along with the sharp peak corresponding to **MWNT** and the peaks from **poly-V-**

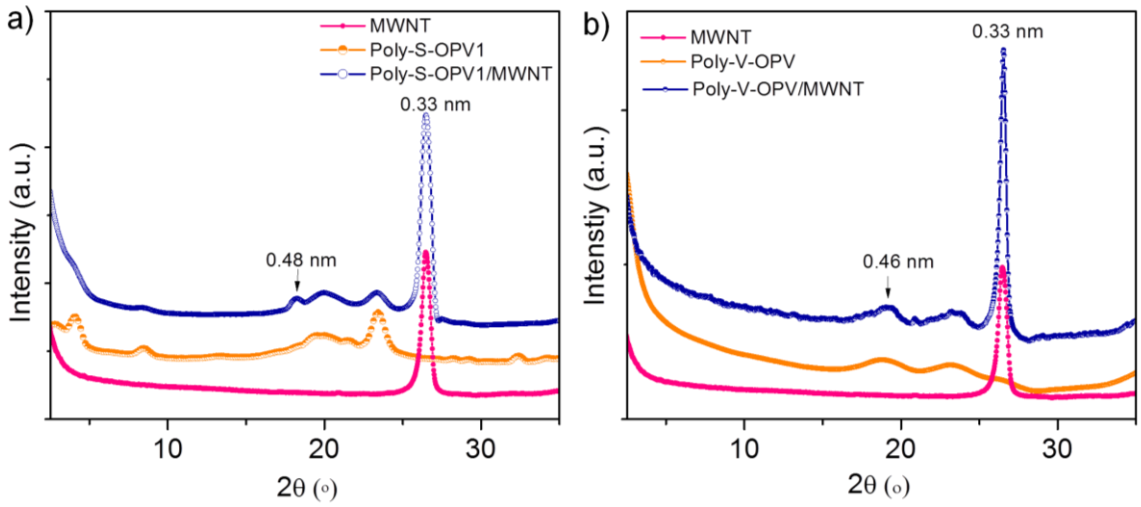

Figure 4.12. XRD profiles of a) **MWNT**, **poly-S-OPV1** and **poly-S-OPV1/MWNT** and b) **MWNT**, **poly-V-OPV** and **poly-V-OPV/MWNT**.

OPV (Figure 4.12b). Thermal stability of the hybrid materials was studied by thermogravimetric analysis (TGA). TGA revealed that the pyrolysis temperatures of **poly-S-OPV1/MWNT** and **poly-V-OPV/MWNT** hybrids were different from that of **poly-S-OPV, poly-V-OPV** and **MWNT** (Figure 4.13). The onset of the pyrolysis of **poly-S-OPV** and **poly-V-OPV** in the hybrids starts at a higher temperature when compared to that of **poly-S-OPV** and **poly-V-OPV** in the absence of **MWNT**, indicating that the polymers start to decompose at a higher temperature in the hybrids.

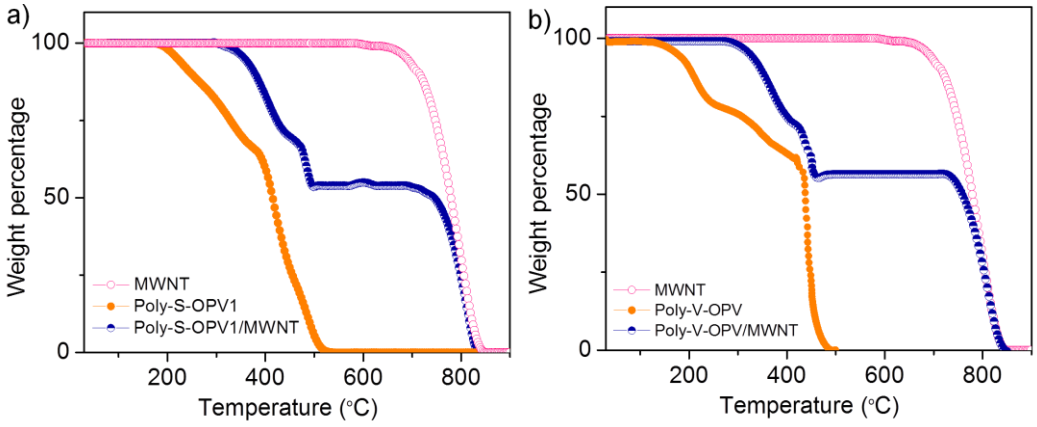

Figure 4.13. TGA curves of a) **MWNT**, **poly-S-OPV1**, and **poly-S-OPV1/MWNT** and b) **MWNT**, **poly-V-OPV**, and **poly-V-OPV/MWNT**. The measurements were carried out under nitrogen atmosphere with the heating rate of 10 °C min^{-1}.

Morphological analyses such as AFM, SEM and TEM gave insights on the nano- and microscopic structures of these hybrids. AFM and SEM images (Figure 4.14a and 4.14b) of **poly-S-OPV1/MWNT** revealed network structures composed of the polymer and **MWNT**. In these structures, the polymer chains are adsorbed on the surface of **MWNTs**, leading to nano- as well as microscopic roughness. The high

resolution TEM images of the hybrids indicated that the surface of **MWNT** was covered with polymer (Figure 4.14c-e). On the other hand, bare **MWNT** exhibited nanotubes with a smooth surface (Figure 4.14f).

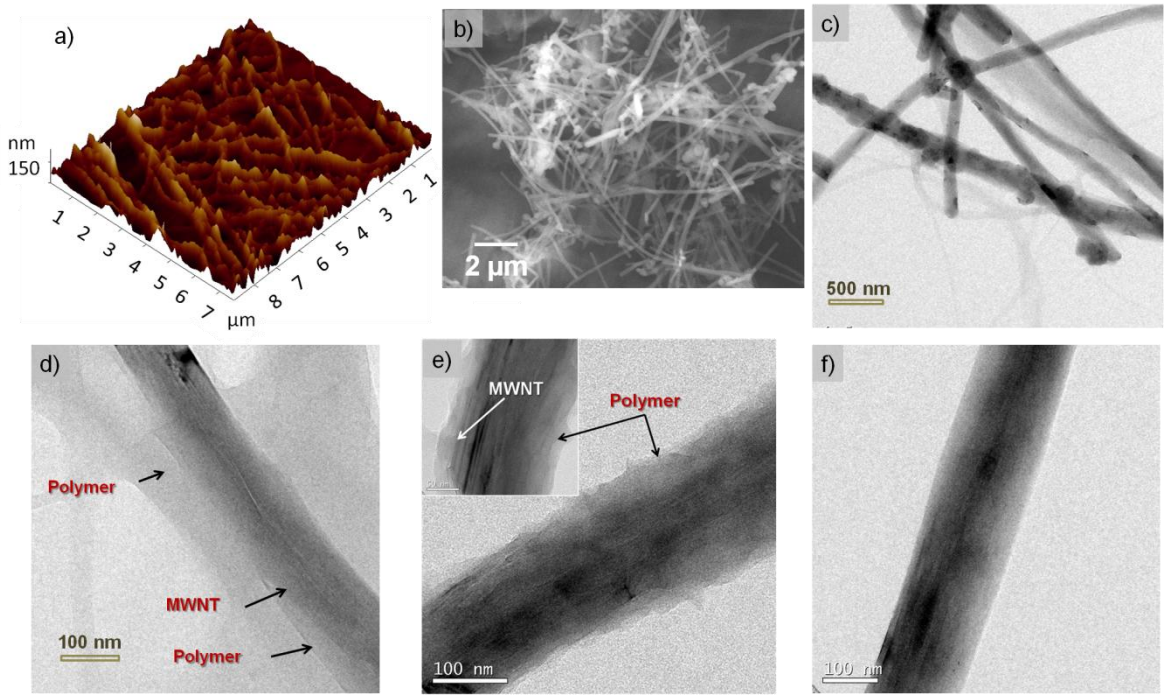

Figure 4.14. a) AFM, b) SEM, and TEM images of c), d) **poly-S-OPV1/MWNT**, e) **poly-V-OPV/MWNT**, and f) pristine **MWNT**.

Anti-wetting properties of the coatings made from polymer/**MWNT** hybrids were studied by water contact angle (WCA) measurements. A chloroform solution of polymer/**MWNT** hybrid was spray coated on a freshly cleaned glass plate, and dried under ambient conditions for WCA measurements. The bare **MWNT**, **poly-S-OPV1** and **poly-S-OPV1/MWNT** showed WCAs of 127, 112 and 169°, respectively (Figure

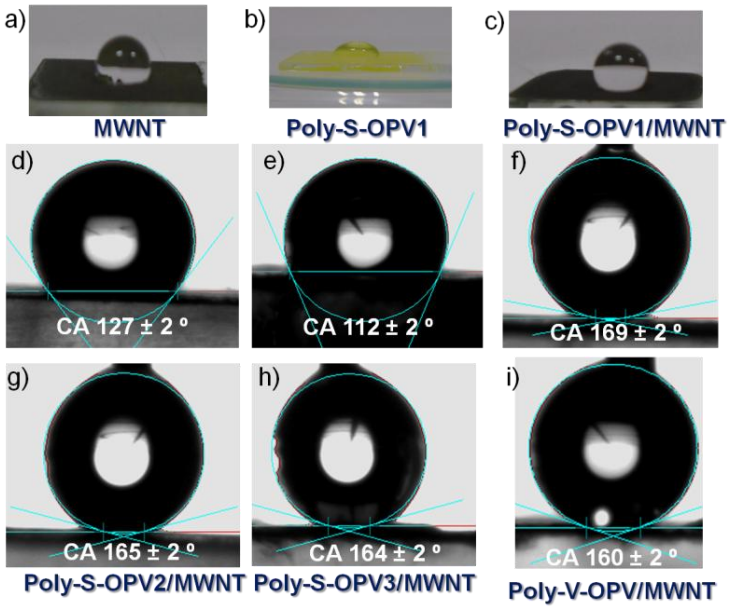

Figure 4.15. Photographs of water droplet on a) **MWNT**, b) **poly-S-OPV1**, and c) **poly-S-OPV1** coated glass substrates. Water contact angle measurements of d) **MWNT**, e) **poly-S-OPV1**, f-h) **poly-S-OPV1-3/MWNT** and i) **poly-V-OPV/MWNT** hybrids on glass substrate.

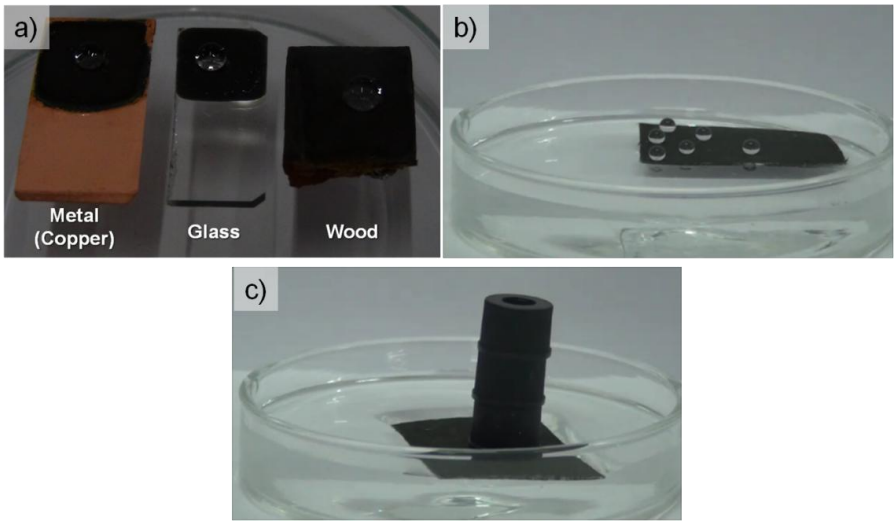

Figure 4.16. a) Superhydrophobic coatings of **poly-S-OPV1/MWNT** on various substrates. Photographs of b) a normal cotton fabric coated with **poly-S-OPV1/MWNT** placed on a water surface having water droplets on top (spherical shape), and c) a superhydrophobic cotton floats on the water surface carrying a weight of 1.4 g without sinking.

4.15a-f). Other hybrids **poly-S-OPV2/MWNT**, **poly-S-OPV3/MWNT**, and **poly-V-OPV/MWNT** exhibited WCAs of 165, 164, and 160 ± 2°, respectively (Figure 4.15g-i). The polymer/**MWNT** hybrids showed superhydrophobic property on multiple substrates such as metal, wood, cotton fabric, etc., in addition to glass (Figure 4.16a and 4.16b). A cotton fabric coated with **poly-S-OPV1/MWNT** exhibited an excellent water-repellent property and even with an added cargo of 1.4 g, it did not sink in a water tub (Figure 4.16c). The role of the weight percentage of **MWNT** in the hybrid on the superhydrophobicity was studied by measuring the WCA of coatings with various **MWNT** weight percentages. Results confirmed that the **poly-S-OPV1/MWNT** having 50 wt % of **MWNT** had a high WCA of 169 ± 2°, whereas **poly-V-OPV/MWNT** having 50-55 wt % of **MWNT** exhibited a WCA of 160 ± 2° (Figure 4.17a). The lower WCA of **poly-S-OPV2-3/MWNT** and **poly-V-OPV/ MWNT** hybrids were mainly due to the lower number and length of hydrocarbon chains when compared to that of **poly-S-OPV1/MWNT**. The dynamic WCA measurements were carried out to study the superhydrophobic behavior of the coatings. The measurement of advancing and receding contact angles showed a very small contact angle hysteresis, which is an important criterion for an efficient superhydrophobic surface (Figure 4.17b). On the other hand, **MWNT** and **poly-S-OPV1** exhibited a larger contact angle hysteresis (Figure 4.17c). The stability of the coating in terms of WCA with respect to strong acidic and basic conditions was monitored. Negligible variations in the WCA values of the superhydrophobic coating

at varying pH of aqueous solution, confirmed the enhanced stability under strong acidic and basic conditions (Figure 4.17d).

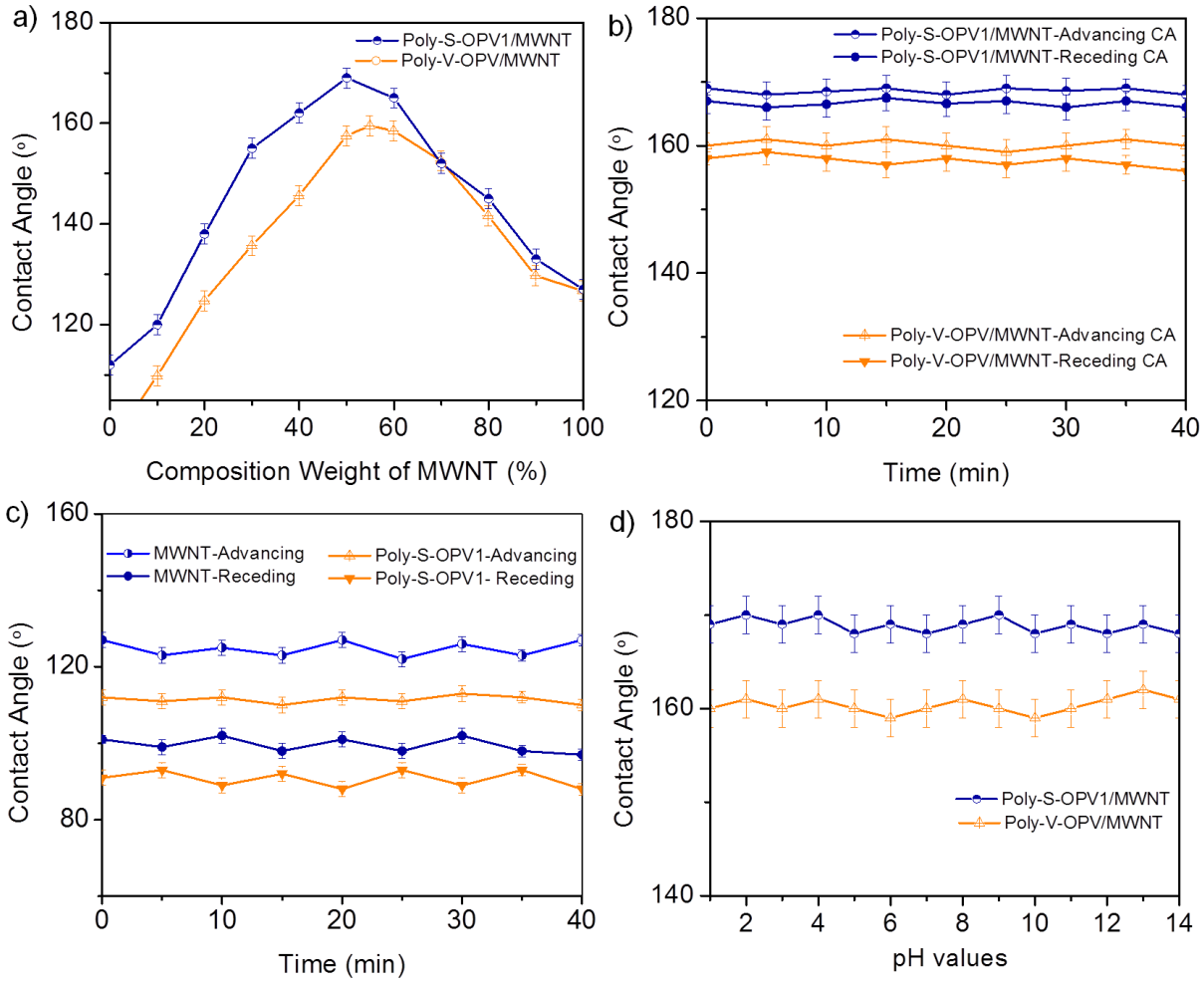

Figure 4.17. a) Variations in water contact angle of **poly-S-OPV1/MWNT** and **poly-V-OPV/MWNT** hybrids with respect to the weight percentage of **MWNT**. Plots of contact angle hysteresis of b) **poly-S-OPV1/MWNT** and **poly-V-OPV/ MWNT**, c) **MWNT** and **poly-S-OPV1**. d) Plot of effect of pH on WCA of **poly-S-OPV1/MWNT** and **poly-V-OPV/ MWNT** coatings.

4.3.4. Preparation of Superhydrophobic Paint Formulation and Its Applications

A superhydrophobic paint formulation was prepared by mixing **poly-V-OPV/MWNT** hybrid (200 mg) and polystyrene (M. wt. = 2000, 20 mg) as binder in chloroform (25 mL). The mixture was sonicated in a low power sonic bath for 15-20 min. The resultant viscous suspension was used to spray coat any pre-cleaned surface using a spray gun operating at 40-45 psi air pressure. The spray coated samples were dried under ambient conditions and were further used in estimating the drag force, drag coefficient, and buoyant force of water moving bodies.

Drag force is an important parameter acing at the interface of a solid surface and a fluid, which decides the energy efficiency of any moving object. Nature has its own mechanism of reducing the drag, thereby lowering the energy required to maintain the momentum of migrating objects.[47] Reduced skin friction of a shark in ocean, self-cleaning property of lotus leaves, etc., are examples for such phenomenon.[48-49] The nano- and microscopic surface morphologies play a key role during naturally occurring drag reduction processes. In the case of aquatic vehicles such as boats, ships, etc., drag reduction allows for lower fuel consumption, thereby reducing environmental pollution. Basically, ships use a large portion of fossil fuels to keep them moving by rendering the required propulsive power. The fictional drag is a major resistance experienced during water transport that accounts for ~80% of total

drag. By reducing the frictional drag, velocity of water vehicles could be increased thereby lowering the fuel consumption. Among several techniques adopted to decrease frictional drag, application of superhydrophobic coatings is considered as an effective and viable method.[19,50-51] The drag reducing effect of superhydrophobic coating comprised of **Poly-V-OPV/MWNT** hybrid for water transport vehicles was demonstrated using a model boat (mass of boat = 36 g) with a metallic (copper) hull. The cleaned boat hull was coated with the superhydrophobic formulation and dried at room temperature. The snapshots of bottom of the model boat before and after coating are shown in Figure 4.18a and 4.18b, respectively. The experimental set-up used to estimate the drag force and the drag coefficient calculation is described in the experimental section of this chapter. The drag force experienced by the model boat before (boat-1) and after (boat-2) coating with the superhydrophobic hybrid was measured by moving the boat with known propulsive force (F_P). The drag force (F_D) realized by the boat would be equal to the propulsive force (F_P), when the boat moves at a constant velocity (net acceleration, $a = 0$). It can be explained mathematically as follows:

$$F_P - F_D = m \times a = m \times 0 = 0 \qquad \text{(Eq. 4)}$$

where m is the mass of the boat.

$$F_P = F_D \text{ (for a boat travelling with a constant velocity)} \qquad \text{(Eq. 5)}$$

The measured drag forces (F_D) were used to calculate the drag coefficients for the boat-1and boat-2 using the following equation.

$$F_D = \frac{1}{2} \rho \, v^2 \, C_D \, A \qquad \text{(Eq. 6)}$$

where F_D is a drag Force (N), ρ is the density of water (kg m^{-3}), v is the velocity of the boat (m s^{-1}), A is the total wetted area (m^2), and C_D is the drag coefficient (dimensionless).

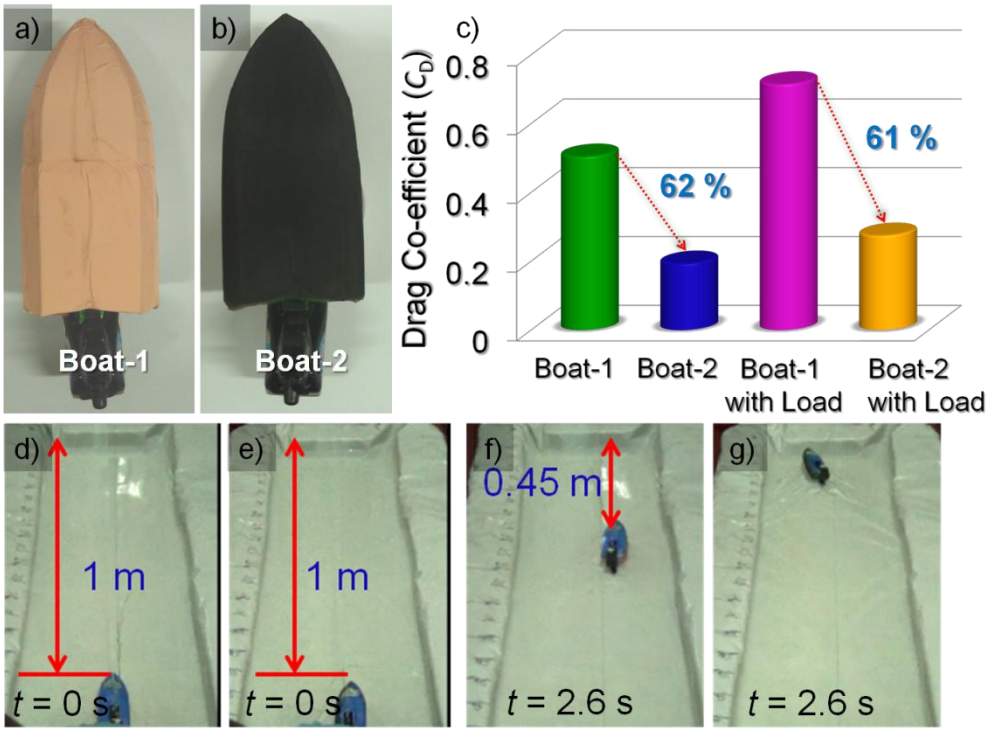

Figure 4.18. Snapshots of a boat (mass of 36 g) a) before (boat-1) and b) after (boat-2) coating with superhydrophobic formulation composed of **poly-V-OPV/MWNT**. c) 3D plot showing comparison of drag coefficients of boat-1, boat-2 and boat-2 with load of 22 g. Snapshots of boat-1and boat-2 at time of d), e) *t* = 0 s and f), g) *t* = 2.6 s, respectively.

The calculated drag coefficients of the boat-1 and boat-2 were 0.504 and 0.193, respectively. The boat-2 showed 62% of reduction in the drag coefficient when compared to that of the boat-1 on application of identical propulsive force (Figure

4.18c). Because of the reduced drag between the boat hull and the water surface, the velocity of the boat-2 (0.354 m s^{-1}) was higher than that of the boat-1 (0.219 m s^{-1}). The boat-2 exhibited 61% of reduction in drag even with a cargo of 22 g when compared to that of the boat-1 under identical conditions (mass of boat-2 was ~36 g and boat-2 had a cargo of 60% of its mass). The distance covered by the boat-1 and the boat-2 were 0.55 m and 1 m, respectively, after a given travel time of 2.6 s (Figure 4.18d-g). The difference in the distance travelled was ~0.45 m (45%). Therefore, the boat-2 covered almost twice the distance as the boat-1 during the same travel time (t = 2.6 s), which in turn is due to the enhanced velocity of boat-2. This enhancement in the velocity clearly shows the effect of superhydrophobic coating on the boat hull. Buoyant forces (F_B) of boat-1 and boat-2 were also calculated by using the following equation.

$$F_B = \rho V g \qquad \text{(Eq. 7)}$$

where F_B is a buoyant force (N), ρ is the density of water (kg m^{-3}), V is the volume of floating boat submerged (m^{-3}), and g is the gravitational acceleration (m s^{-2}).

The volume of boat hull submerged in water were calculated as 36.3 and 15 mL for boat-1 and boat-2, respectively by measuring the volume of water displaced by them (Figure 4.19a and 4.19b). The boat-1 with the mass of 36.3 g and area of 80.63 cm^2 had a buoyant force of 0.35 N, which is equal to the downward force due to gravitational acceleration (0.35 N). At the same time, boat-2 with the same mass and area of boat-1 exhibited a buoyant force of 0.56 N which is 1.6 times higher than that

of boat-1 (Figure 4.19e). The buoyant force of boat-2 was calculated by adding the amount of force corresponding to the difference in the submerged volumes between the boat-1 and the boat-2 to the buoyant force of the boat-1. The increased buoyant force of boat-2 is mainly due to the presence of the air (Figure 4.19d) trapped between the boat hull and the water surface, which generates an air pressure operating against the gravitational force. Because of the larger buoyant force, the volume of boat-2 submerged in water is lower when compared to that of boat-1 (Figure 4.19a and 4.19-

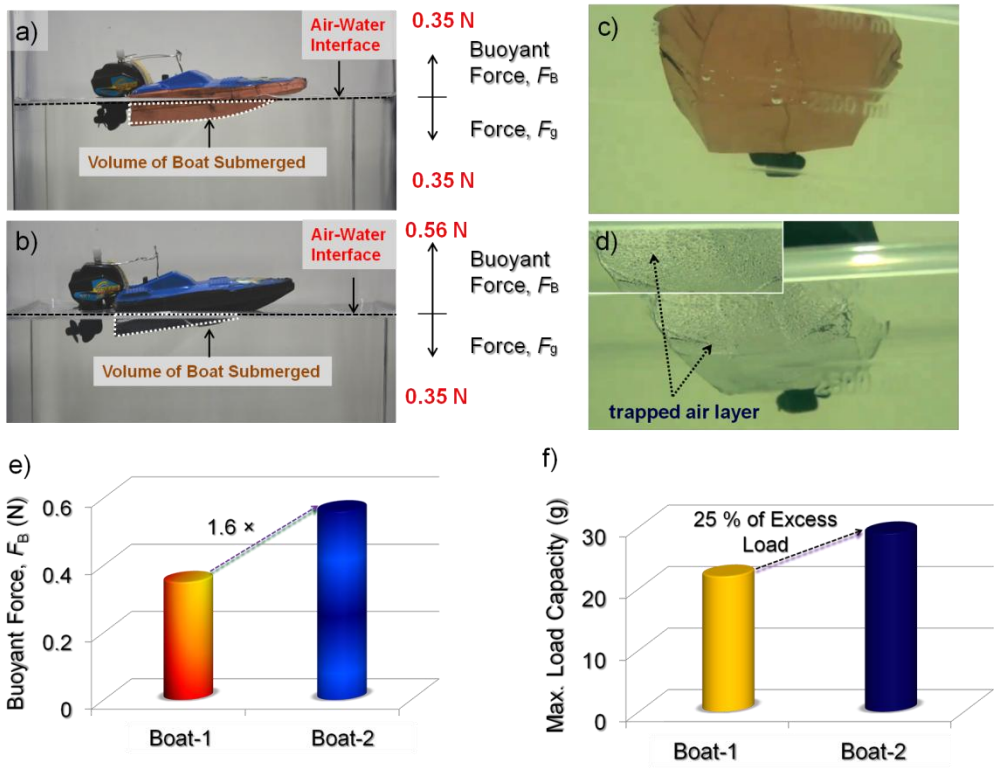

Figure 4.19. Snapshots of a) boat-1 and b) boat-2 floating on the water surface with different submerged volumes. Figures 4.19c and 4.19d show the presence and absence of air layer between the hull of boat-1/boat-2 and water, respectively. Plots showing e) comparison of buoyant forces of boat-1 and boat-2, f) difference in the maximum load capacity between boat-1 and boat-2.

b). By taking advantage of the increased buoyant force, the boat-2 could carry 25% more cargo, than the boat-1 could, under similar conditions (Figure 4.19f). The reduction in drag force and the increased buoyancy of the boat coated with the superhydrophobic formulation are directly reflected in fuel consumption and energy saving. A large quantity of fuel or energy can be saved if the hulls of boats and ships are coated with such superhydrophobic formulations, leading to real world applications.

4.4. Conclusions

Superhydrophobic hybrid materials were prepared by the polymerization of **OPV** derivatives having polymerizable end functional groups, on **MWNTs**. These hybrid materials were used in the preparation of superhydrophobic paint formulation by mixing with an appropriate amount of binder (polystyrene) in a non-polar solvent (chloroform/toluene). The coating of **poly-S-OPV1/MWNT** on various substrates exhibited water contact angle of 169 ± 2 °. The water contact angle is unaffected by highly acidic or basic conditions (pH=1 – 14). Spray coating on the hull of water moving vehicles by the superhydrophobic paint formulation of **poly-V-OPV/MWNT** reduced the drag force by ~62% and improved the buoyancy, thereby allowing faster transport as well as of additional cargo on board. In short, coating of the hulls of boats and ships with these materials would impart water repellency to their surfaces, thereby reducing the drag resistance for friction-minimized faster transportation. This increase in velocity could be translated into additional cargo on board or lesser transportation

time, leading to cost-effective marine transportation. While minimizing the costs associated with shipping, this strategy is envisioned to have a huge impact in terms of energy efficiency, via considerable decrease in fuel consumption due to shorter time of transportation or larger transportation capacity.

4.5. Experimental Section

4.5.1. General

MWNT was purchased from Sigma Aldrich. **OPVs** were synthesized and characterized according to reported methods.[52-53] ^{1}H and ^{13}C NMR spectra were recorded on a 500 MHz Bruker Advance DPX spectrometer using TMS as internal standard. FT-IR spectra were recorded on a Shimadzu IR Prestige-21 Fourier Transform Infrared Spectrophotometer. Matrix-assisted laser desorption ionization time-of-flight (MALDI-TOF) mass spectra were obtained on a Shimadzu AXIMA-CFR PLUS spectrometer using α-cyano-4-hydroxycinnamic acid as the matrix.

4.5.2. Synthesis and Characterization

Preparation of S-OPV1-3. The required **OPV** bisalcohol (**OPV1/4/5**, 1 mmol), prepared as per literature procedure,[40-43] was dissolved in dry CH_2Cl_2 (40 mL) by stirring under an argon atmosphere. 4-Vinylbenzoic acid (2.1 mmol) and DMAP (2.1 mmol) were added to this solution and the reaction mixture was cooled to 0 °C by using an ice-salt bath. DCC (2.5 mmol) was added to the reaction mixture and stirred for 4 h at room temperature. The reaction mixture was then filtered and the product

was precipitated by the addition of methanol. The crude product was then purified by column chromatography (100-200 mesh) using 1:3 $CHCl_3$-hexane mixture as an eluent.

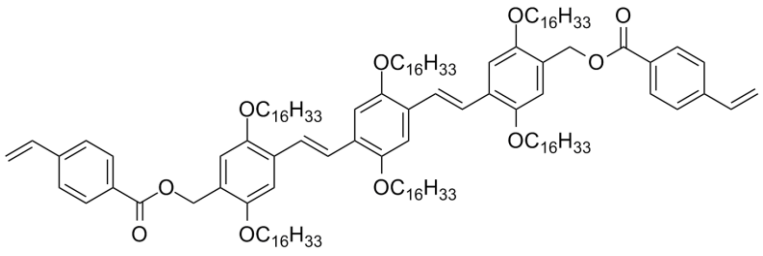

S-OPV1

Yield: 80%, **m. p.:** 102-103 °C; **FT-IR** (KBr) ν_{max}: 2913, 2851, 1726, 1520, 1467, 1426, 1386, 1346, 1260, 1207, 1111, 1028, 974, 921, 854, 781, 725 cm^{-1}; **^{1}H NMR** (500 MHz, $CDCl_3$) δ : 8.01-8.05 (m, 4*H*, terminal phenyl-*H*), 7.48-7.52 (m, 4H, terminal phenyl-*H*), 7.45 (m, 4H, vinyl-*H*), 7.15-7.16 (m, 4H, phenyl-*H*), 6.97-6.99 (m, 2H, phenyl-*H*), 6.71-6.76 (m, 2H, styryl–C*H*=C), 5.82-5.88 (m, 2H, =CH_2), 5.35 (s, 4H, –CH_2-O-CO), 4.9-5.01 (m, 2H, =CH_2), 3.96-4.06 (m, 12H, –OCH_2–), 1.20-1.87 (m, 168 H, –CH_2–), 0.84-0.90 (m, 18H, –CH_3) ppm; **^{13}C NMR** (125 MHz, $CDCl_3$) δ : 166.3, 151.614.0, 150.6, 142.0, 130.1, 136.1, 129.6, 128.0, 127.1, 126.1, 124.7, 123.7, 123.5, 116.4, 115.2, 109.8, 109.6, 76.7, 69.7, 69.2, 62.4, 31.9, 29.8, 29.7, 29.6, 29.5, 29.4, 29.1, 26.3, 26.2, 22.7, 19.6, 14.1 ppm; **MALDI-TOF-MS**: calculated *m/z* for $C_{138}H_{226}O_{10}$: 2043.72, found: 2043.07.

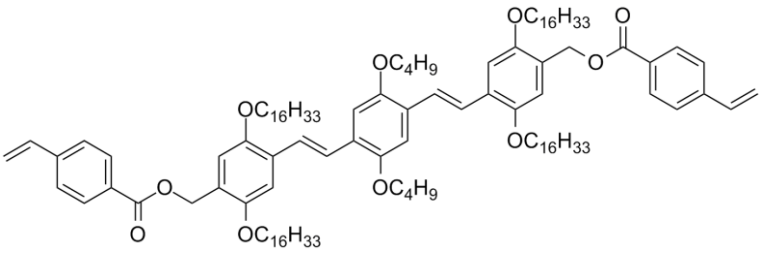

S-OPV2

Yield: 76%, **m. p.:** 116-117 °C; **FT-IR** (KBr) ν_{max}: 2914, 2852, 1726, 1521, 1468, 1425, 1386, 1347, 1260, 1208, 1113, 1029, 976, 920, 855, 782, 726 cm^{-1}; **^{1}H NMR** (500 MHz, $CDCl_3$) δ : 8.02-8.05 (m, 4*H*, terminal phenyl-*H*), 7.47-7.51 (m, 4H, terminal phenyl-*H*), 7.45 (m, 4H, vinyl-*H*), 7.15-7.16 (m, 4H, phenyl-*H*), 6.99-7.01 (m, 2H, phenyl-*H*), 6.71-6.79(m, 2H, styryl–C*H*=C), 5.82-5.88 (m, 2H, =CH_2), 5.36 (s, 4H, –CH_2-O-CO), 4.9-5.01 (m, 2H, =CH_2), 3.97-4.08 (m, 12H, –OCH_2–), 1.21-1.87 (m, 120 H, –CH_2–), 0.85-0.89 (m, 18H, –CH_3) ppm; **^{13}C NMR** (125 MHz, $CDCl_3$) δ : 166.3, 151.6, 150.6, 142.0, 136.1, 130.1, 129.6, 128.0, 127.1, 126.1, 124.7, 123.7, 123.5, 116.4, 115.2, 109.8, 109.6, 76.7, 69.7, 69.2, 62.4, 31.9, 29.8, 29.8, 29.7, 29.6, 29.5, 29.4, 26.3, 26.2, 22.7, 19.6, 14.1, 14.0 ppm; **MALDI-TOF-MS**: calculated *m/z* for $C_{114}H_{178}O_{10}$: 1707.34, found: 1707.76.

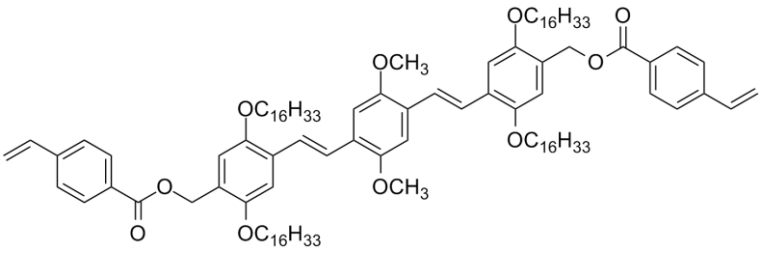

S-OPV3

Yield: 79%, **m. p.:** 121-122 °C; **FT-IR** (KBr) ν_{max}: 2914, 2853, 1726, 1521, 1469, 1427, 1385, 1347, 1260, 1206, 1112, 1029, 974, 920, 856, 782, 725 cm^{-1}; **^{1}H NMR** (500 MHz, $CDCl_3$) δ : 8.02-8.05 (m, 4*H*, terminal phenyl-*H*), 7.47-7.51 (m, 4H, terminal phenyl-*H*), 7.44 (m, 4H, vinyl-*H*), 7.15-7.17 (m, 4H, phenyl-*H*), 6.99-7.01 (m, 2H, phenyl-*H*), 6.71-6.79 (m, 2H, styryl–C*H*=C), 5.84-5.89 (m, 2H, =CH_2), 5.37 (s, 4H, –CH_2-O-CO), 4.9-5.01 (m, 2H, =CH_2), 3.97-4.05 (m, 8H, –OCH_2–), 3.92 (s, 6H, –OCH_3), 1.21-1.86 (m, 112 H, –CH_2–), 0.85-0.90 (m, 12H, –CH_3) ppm; **^{13}C NMR** (125 MHz, $CDCl_3$) δ : 166.3, 151.6, 151.5, 150.6, 141.9, 136.1, 130.0, 129.6, 127.9, 127.1, 126.1, 124.7, 123.7, 123.5, 116.4, 115.1, 109.8, 109.2, 76.8, 69.7, 69.1, 62.4, 56.3, 31.9, 29.9. 29.8, 29.7, 29.6, 29.5, 29.4, 29.3, 26.2, 26.1, 22.6, 14.3 ppm; **MALDI-TOF-MS**: calculated *m/z* for $C_{108}H_{166}O_{10}$: 1623.25, found: 1623.98.

Preparation of V-OPV. 4-Vinylbenzaldehyde (1 mmol) was dissolved in dry THF (15 mL) under argon atmosphere. A suspension of *t*-BuOK (4.5 mmol) and the phosphonate ester (**10**) (2.1 mmol) dissolved in dry THF (15 mL) was added drop wise using a pressure equalizer. The reaction mixture was heated at 60 °C for 7 h. The solution was then concentrated, extracted with chloroform and evaporated to dryness. It was then purified by column chromatography on silica gel (100-200 mesh) using 1:3 $CHCl_3$-hexane mixture as an eluent.

Yield: 73%; **m. p.:** 92-94 ºC; **FT-IR** (KBr) ν_{max}: 2958, 2916, 2858, 1486, 1458, 1375, 1199, 983, 959, 895, 848, 819, 760 cm^{-1}; **^{1}H NMR** (500 MHz, $CDCl_3$) δ: 7.48-

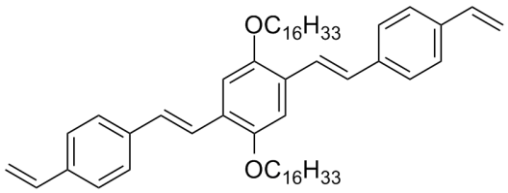

V-OPV

7.51 (m, 4H, terminal phenyl-*H*), 7.46 (s, 2H, vinyl-*H*), 7.39-7.42 (s, 2H, phenyl-*H*), 7.11-7.14 (m, 2H, phenyl-*H*), 7.10 (s, 2H, vinyl-*H*), 6.69-6.75 (m, 2H, styryl–C*H*=), 5.74-5.79 (m, 2H, =CH_2), 5.23-5.26 (m, 2H, =CH_2), 4.04-4.07 (m, 4H, –OCH_2–), 0.85-1.90 (m, 62H, –CH_2– and –CH_3) ppm; **^{13}C NMR** (125 MHz, $CDCl_3$) δ : 146.0, 137.5, 136.5, 128.3, 126.6, 126.5, 123.4, 116.2, 114.5, 69.1, 31.9, 29.9, 29.8, 29.7, 29.6, 29.5, 29.3, 26.3, 22.6, 14.1 ppm; **MALDI-TOF-MS**: calculated *m/z* for $C_{58}H_{86}O_2$: 814.66, found: 814.34.

Preparation of Polymer/MWNT Hybrids. S-OPV1-3/V-OPV (100 mg) and **MWNT** (102 mg) were added to chloroform (25 mL) in a round bottom flask. The mixture was sonicated for 20-30 minutes in a low power bath sonicator. The resultant suspension was centrifuged at 3000 rpm for 10 minutes at 25 °C and the supernatant was decanted to get **S-OPV1-3/V-OPV/MWNT** hybrid. The hybrid materials were obtained by slow evaporation of solvent under vacuum. The dried **S-OPV1-3/V-OPV/MWNT** hybrid (100 mg) and dry toluene (10 mL) were added to a schlenk tube and sealed. The mixture was sonicated for 3-5 minutes in a bath sonicator to achieve a homogeneous suspension. To this suspension, a dry toluene solution of Grubb's catalyst ([monomer] / [catalyst] ≈ 60) was added and stirred for 48 h. The by-product of the reaction (ethylene gas) was removed by freezing the reaction mixture followed

by vacuum treatment for 2 minutes. The removal of ethylene gas was carried out every hour for initial 10 h of the reaction. The reaction was then quenched by adding methanol (10 mL) to the reaction mixture and stirring for 30 minutes. The solvent was removed under reduced pressure and the resultant solid was washed with excess of methanol to remove the catalyst and by-products. The **poly-S-OPV1-3/V-OPV /MWNT** hybrid material was re-dispersed in toluene and precipitated using methanol to remove any trace of the catalyst. The resultant suspension was filtered and dried at 60 °C. Preparation of polymers (**poly-S-OPV1-3** and **poly-V-OPV**) without **MWNTs** was also carried out by using the above mentioned procedure.

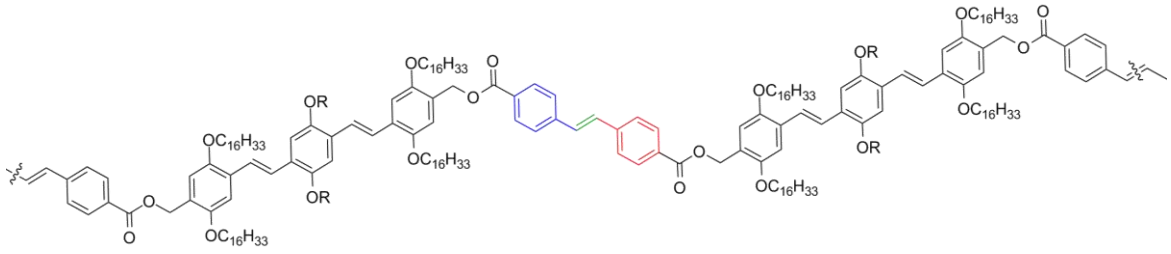

Poly-S-OPV1 : R = $C_{16}H_{33}$
Poly-S-OPV2 : R = C_4H_9
Poly-S-OPV3 : R = CH_3

Poly-S-OPV1. Yield: 70%; **FT-IR** (KBr) ν_{max}: 2924, 2845, 1726, 1508, 1465, 1423, 1387, 1344, 1273, 1208, 1101, 1073, 1023, 965, 858, 780 cm^{-1}; **^{1}H NMR** (500 MHz, $CDCl_3$) δ : 8.02-8.06 (m, terminal phenyl-*H*), 7.49-7.51 (m, terminal phenyl-*H*), 7.46 (m, vinyl-*H*), 7.16-7.18 (m, phenyl-*H*), 6.96-6.98 (m, phenyl-*H*), 6.70-6.75 (broad, styryl–C*H*=C), 5.83-5.89 (broad, trace, =CH_2), 5.36 (s, –CH_2-O-CO), 4.90-5.02

(broad, trace, =CH_2), 3.97-4.05 (broad, –OCH_2–), 1.21-1.88 (broad, –CH_2–), 0.85-0.91 (broad, –CH_3) ppm; M_n = 32050, M_w / M_n = 1.2 by GPC (Solvent -THF, Standard - Polystyrene).

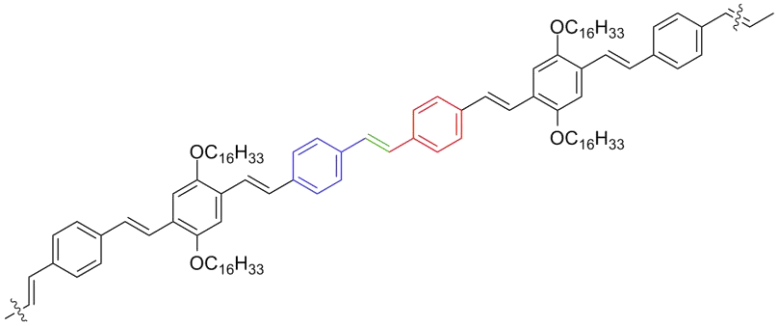

Poly-V-OPV

Poly-V-OPV. Yield: 67%; **FT-IR** (KBr) ν_{max}: 2962, 2919, 2869, 2847, 1592, 1461, 1377, 1194, 1159, 1081, 969, 894 cm^{-1}; **^{1}H NMR** (500 MHz, $CDCl_3$) δ: 7.47-7.50 (m, 4H, terminal phenyl-*H*), 7.44 (s, vinyl-*H*), 7.37-7.41 (s, phenyl-*H*), 7.12-7.15 (m, phenyl-*H*), 7.11 (s, vinyl-*H*), 6.68-6.74 (m, styryl–C*H*=), 5.74-5.78 (broad, trace, =CH_2), 5.24-5.26 (broad, trace, =CH_2), 4.05- 4.08 (broad, –OCH_2–), 0.87-1.92 (broad, –CH_2– and –CH_3) ppm; M_n = 12700, M_w / M_n = 1.4 by GPC (Solvent -THF, Standard - Polystyrene).

Preparation of Superhydrophobic Paint Formulation. The mixture of **poly-S-OPV1-3/V-OPV/MWNT** hybrid (200 mg) and polystyrene (20 mg) (M_w = 2000) as binder was sonicated in $CHCl_3$ (25 mL) for 3-5 minutes to get a homogeneous viscous

solution. The resultant solution was spray coated on cleaned glass/metal surfaces using spray gun operating at 40-45 psi pressure of air. The coating was dried at room temperature to obtain the corresponding superhydrophobic surface.

4.5.3. Description on Experimental Techniques

Measurements

The details of UV-Vis absorption spectrophotometer, spectrofluorimeter, Raman spectrometer, scanning electron microscope, atomic force microscope and transmission electron microscope are described in the section 2.5.3 of Chapter 2. Samples for the SEM, AFM and TEM studies were prepared by drop casting a chloroform solution of the polymer/**MWNT** hybrids on aluminium grid, freshly cleaved mica substrate and carbon coated TEM grids, respectively and the samples were dried at ambient conditions. Gel permeation chromatography (GPC) was conducted on WATERS. GPC was conducted in THF at 35 °C with a flow rate of 1.0 mL min^{-1}. The polymer samples were calibrated with polystyrene standards purchased from Sigma Aldrich.

Experiment of Drag Force and Drag Coefficient Calculation

Calculation of the drag force was carried out by measuring the propulsive force as shown below:

$$\text{Propulsive Force, } F_P = m \times g \text{ (Newton)} \qquad \text{(Eq. 8)}$$

where m is mass used to pull the boat (kg), g is gravitational acceleration (m s^{-2}).

The drag force (F_D) experienced by the boat would be equal to the propulsive force (F_P) when boat moves at a constant velocity (net acceleration, $a = 0$). It can be explained mathematically as follows:

$$F_P - F_D = m \times a = m \times 0 = 0 \quad \text{(Eq. 4)}$$

where m is the mass of the boat.

$$F_P = F_D \text{ (for a boat travelling with a constant velocity)} \quad \text{(Eq. 5)}$$

The measured drag forces (F_D) were used to calculate the drag coefficients of boat-1 and boat-2 by using the following equation.

$$F_D = \frac{1}{2} \rho \, v^2 \, C_D \, A \quad \text{(Eq. 6)}$$

where F_D is a drag force (N), ρ is the density of water (kg m^{-3}), v is the velocity of the boat (m s^{-1}), A is the wetted area (m^2), and C_D is the drag coefficient (dimensionless).

Procedure: A model boat with a metallic (copper) hull (mass of 36 g and area of 80 cm^2) was used for the experiment. The uncoated boat (boat-1) was connected to a known mass (0.01 kg) through a frictionless string via a two set pulley system as shown in Figure 4.20. Then, the boat-1 was kept at one end of a water channel (length x width x height: 1 m x 0.3 m x 0.1 m) and allowed to move to another end. The time taken to travel 1 m of distance was measured by recording the movement of the boat-1 using digital camera. The velocity of the boat-1 was calculated from the time taken to travel 1 m of distance. The same procedure was repeated with the boat coated by

superhydrophobic paint formulation (boat-2). From the measured velocities and drag forces, the drag coefficients were calculated by using Equation 6.

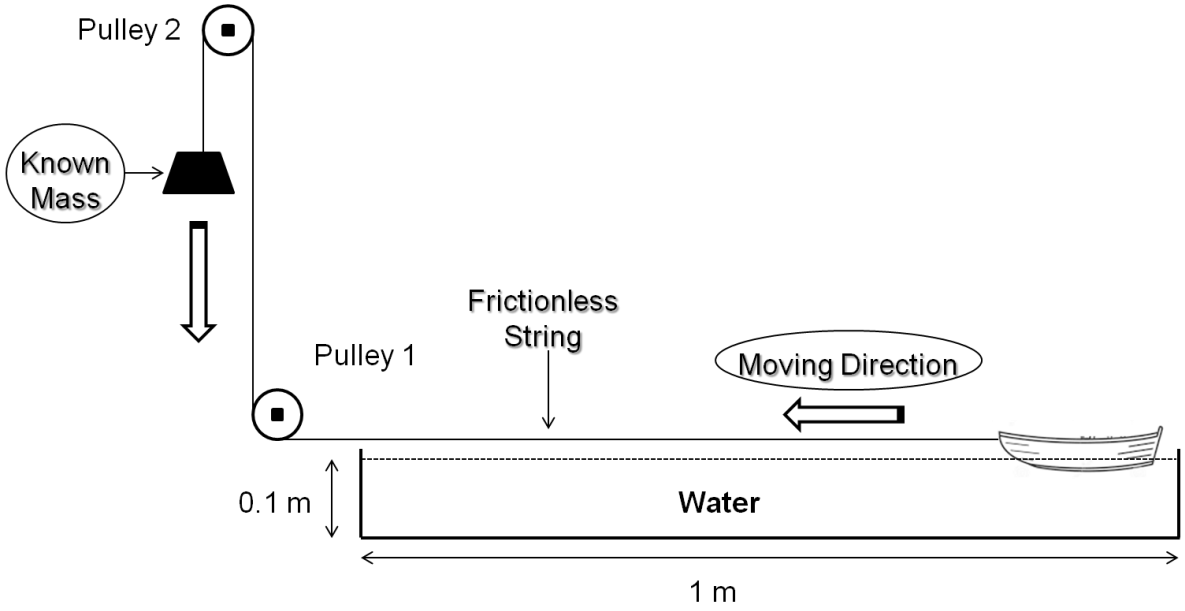

Figure 4.20. Schematic representation of the experimental set-up used for the calculation of drag force and drag coefficient.

Experiment of Buoyant Force Calculation

Boat-1 and boat-2 were used for the calculation of buoyant force using the following equation.

$$F_B = \rho V g \qquad \text{(Eq. 7)}$$

where F_B is a buoyant force (N), ρ is the density of water (kg m^{-3}), V is the volume of boat submerged (m^{-3}), and g is the gravitational acceleration (m s^{-2}).

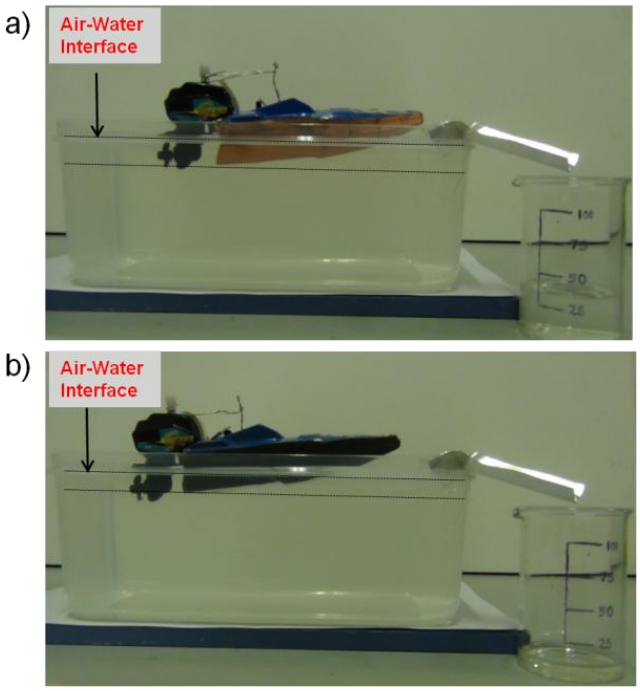

Figure 4.21. Photographs of the experimental set-up used for the calculation of buoyant forces of a) boat-1 and b) boat-2.

Procedure: Boat-1/boat-2 was kept in a tub (length x width x height: 0.24 m x 0.15 m x 0.10 m) already filled with water up to a mark as shown in the Figure 4.21. The volume of the boat-1 and boat-2 submerged was calculated by measuring the volume of water displaced. From the volume of boat submerged, the buoyant force of the boat-1 was calculated. The buoyant force of the boat-2 was calculated by adding the amount of force corresponding to the difference in the submerged volumes between boat-1 and boat-2 to the buoyant force of the boat-1.

4.6. References

(1) Ollivier, H. *Ann. Chim. Phys.* **1907**, *10*, 229.

(2) Barthlott, W.; Neinhuis, C. *Planta* **1997**, *202*, 1-8.

(3) Nosonovsky, M.; Bhushan, B. *Green Tribology: Biomimetics, Energy Conservation and Sustainability*; Springer: Berlin, Germany, 2012.

(4) Feng, L.; Li, S.; Li, Y.; Li, H.; Zhang, L.; Zhai, J.; Song, Y.; Liu, B.; Jiang, L.; Zhu, D. *Adv. Mater.* **2002**, *14*, 1857-1860.

(5) Parker, A. R.; Lawrence, C. R. *Nature* **2001**, *414*, 33-34.

(6) Gao, X.; Jiang, L. *Nature* **2004**, *432*, 36-36.

(7) Zheng, Y.; Bai, H.; Huang, Z.; Tian, X.; Nie, F.-Q.; Zhao, Y.; Zhai, J.; Jiang, L. *Nature* **2010**, *463*, 640-643.

(8) Liu, M.; Wang, S.; Wei, Z.; Song, Y.; Jiang, L. *Adv. Mater.* **2009**, *21*, 665-669.

(9) Chu, Z.; Seeger, S. *Chem. Soc. Rev.* **2014**, *43*, 2784-2798.

(10) Wen, L.; Tian, Y.; Jiang, L. *Angew. Chem. Int. Ed.* **2015**, *54*, 3387-3399.

(11) Cassie, A. B. D.; Baxter, S. *Trans. Faraday Soc.* **1944**, *40*, 546-551.

(12) Wenzel, R. N. *Ind. Eng. Chem.* **1936**, *28*, 988-994.

(13) Zhang, X.; Shi, F.; Niu, J.; Jiang, Y.; Wang, Z. *J. Mater. Chem.* **2008**, *18*, 621-633.

(14) Öner, D.; McCarthy, T. J. *Langmuir* **2000**, *16*, 7777-7782.

(15) Nakanishi, T.; Michinobu, T.; Yoshida, K.; Shirahata, N.; Ariga, K.; Möhwald, H.; Kurth, D. G. *Adv. Mater.* **2008**, *20*, 443-446.

(16) Jiang, Y.; Wan, P.; Smet, M.; Wang, Z.; Zhang, X. *Adv. Mater.* **2008**, *20*, 1972-1977.

(17) Zhang, X.; Shi, F.; Yu, X.; Liu, H.; Fu, Y.; Wang, Z.; Jiang, L.; Li, X. *J. Am. Chem. Soc.* **2004**, *126*, 3064-3065.

(18) Han, J. T.; Lee, D. H.; Ryu, C. Y.; Cho, K. *J. Am. Chem. Soc.* **2004**, *126*, 4796-4797.

(19) Dong, H.; Cheng, M.; Zhang, Y.; Wei, H.; Shi, F. *J. Mater. Chem. A* **2013**, *1*, 5886-5891.

(20) Chu, Z.; Feng, Y.; Seeger, S. *Angew. Chem. Int. Ed.* **2015**, *54*, 2328-2338.

(21) Han, Z.; Tay, B.; Tan, C.; Shakerzadeh, M.; Ostrikov, K. *ACS Nano* **2009**, *3*, 3031-3036.

(22) Tan, S. C.; Yan, F.; Crouch, L. I.; Robertson, J.; Jones, M. R.; Welland, M. E. *Adv. Funct. Mater.* **2013**, *23*, 5556-5563.

(23) Lin, Y.; Ehlert, G. J.; Bukowsky, C.; Sodano, H. A. *ACS Appl. Mater. Interfaces* **2011**, *3*, 2200-2203.

(24) Zhang, J.; Huang, W.; Han, Y. *Macromol. Rapid Commun.* **2006**, *27*, 804-808.

(25) Tu, C.-W.; Tsai, C.-H.; Wang, C.-F.; Kuo, S.-W.; Chang, F.-C. *Macromol. Rapid Commun.* **2007**, *28*, 2262-2266.

(26) Wang, Z.; Ci, L.; Chen, L.; Nayak, S.; Ajayan, P. M.; Koratkar, N. *Nano Lett.* **2007**, *7*, 697-702.

(27) Wang, J.-l.; Ren, K.-f.; Chang, H.; Zhang, S.-m.; Jin, L.-j.; Ji, J. *Phys. Chem. Chem. Phys.* **2014**, *16*, 2936-2943.

(28) Men, X.-H.; Zhang, Z.-Z.; Yang, J.; Wang, K.; Jiang, W. *Appl. Phys. A* **2009**, *98*, 275.

(29) Kota, A. K.; Kwon, G.; Choi, W.; Mabry, J. M.; Tuteja, A. *Nat. Commun.* **2012**, *3*, 1025.

(30) Hu, L.; Gao, S.; Ding, X.; Wang, D.; Jiang, J.; Jin, J.; Jiang, L. *ACS Nano* **2015**, *9*, 4835-4842.

(31) Li, S.; Li, H.; Wang, X.; Song, Y.; Liu, Y.; Jiang, L.; Zhu, D. *J. Phy. Chem. B* **2002**, *106*, 9274-9276.

(32) Aria, A. I.; Gharib, M. *Langmuir* **2014**, *30*, 6780-6790.

(33) Jeong, D.-W.; Shin, U.-H.; Kim, J. H.; Kim, S.-H.; Lee, H. W.; Kim, J.-M. *Carbon* **2014**, *79*, 442-449.

(34) Huang, T.-C.; Li, P.; Yao, H.; Sue, H.-J.; Kotaki, M.; Tsai, M.-H. *RSC Adv.* **2016**, *6*, 12431-12434.

(35) Srinivasan, S.; Praveen, V. K.; Philip, R.; Ajayaghosh, A. *Angew. Chem. Int. Ed.* **2008**, *47*, 5750-5754.

(36) Gu, J.; Xiao, P.; Huang, Y.; Zhang, J.; Chen, T. *J. Mater. Chem. A* **2015**, *3*, 4124-4128.

(37) Zheng, L.; Li, Z.; Bourdo, S.; Khedir, K. R.; Asar, M. P.; Ryerson, C. C.; Biris, A. S. *Langmuir* **2011**, *27*, 9936-9943.

(38) Chen, R. J.; Bangsaruntip, S.; Drouvalakis, K. A.; Wong Shi Kam, N.; Shim, M.; Li, Y.; Kim, W.; Utz, P. J.; Dai, H. *PNAS* **2003**, *100*, 4984-4989.

(39) Zhao, Y.-L.; Stoddart, J. F. *Acc. Chem. Res.* **2009**, *42*, 1161-1171.

(40) Ajayaghosh, A.; George, S. J. *J. Am. Chem. Soc.* **2001**, *123*, 5148-5149.

(41) George, S. J.; Ajayaghosh, A. *Chem. Eur. J.* **2005**, *11*, 3217-3227.

(42) Ajayaghosh, A.; Praveen, V. K. *Acc. Chem. Res.* **2007**, *40*, 644-656.

(43) Ajayaghosh, A.; Praveen, V. K.; Srinivasan, S.; Varghese, R. *Adv. Mater.* **2007**, *19*, 411-415.

(44) Ajayaghosh, A.; Vijayakumar, C.; Praveen, V. K.; Babu, S. S.; Varghese, R. *J. Am. Chem. Soc.* **2006**, *128*, 7174-7175.

(45) Jackson, A. W.; Stakes, C.; Fulton, D. A. *Polym. Chem.* **2011**, *2*, 2500-2511.

(46) Haque, T.; Nomura, K. *Catalysts* **2015**, *5*, 500-517.

(47) D. M. Bushnell, a. K. J. M. *Annu. Rev. Fluid Mech.* **1991**, *23*, 65-79.

(48) Dean, B.; Bhushan, B. *Phil. Trans. R. Soc. A* **2010**, *368*, 4775-4806.

(49) Bhushan, B. *Beilstein J. Nanotechnol.* **2011**, *2*, 66-84.

(50) Shirtcliffe, N. J.; McHale, G.; Newton, M. I.; Zhang, Y. *ACS Appl. Mater. Interfaces* **2009**, *1*, 1316-1323.

(51) Ahmadzadehtalatapeh, M.; Mousavi, M. *Int. J. Marit. Tech.* **2015**, *4*, 51-64.

(52) Srinivasan, S.; Babu, S. S.; Praveen, V. K.; Ajayaghosh, A. *Angew. Chem. Int. Ed.* **2008**, *47*, 5746-5749.

(53) Srinivasan, S.; Praveen, V. K.; Philip, R.; Ajayaghosh, A. *Angew. Chem. Int. Ed.* **2008**, *47*, 5750-5754.

List of Publications

1. Formation of Coaxial Nanocables with Amplified Supramolecular Chirality through an Interaction between Carbon Nanotubes and a Chiral π-Gelator, **B. Vedhanarayanan,** Vishnu S. Nair, Vijayakumar C. Nair, and A. Ajayaghosh, *Angew. Chem., Int. Ed.* **2016**, *55,* 10345–10349.

2. Exfoliation of Reduced Graphene Oxide with Self-assembled π-Gelators for Improved Electrochemical Performance, **B. Vedhanarayanan**, B. Babu, M. M. Shaijumon, and A. Ajayaghosh, *ACS Appl. Mater. Interfaces* **2016**, DOI: 10.1021/acsami.6b09418.

3. A Bio-Inspired Two-in-One Approach to Energy-Efficient Mechanical Motion using Chemically Engineered Superhydrophobic Surfaces. R. D. Mukhopadhyay, **B. Vedhanarayanan**, and A. Ajayaghosh, **2017**. (Under preparation)

4. Superhydrophobic Coatings of Carbon Nanotubes and Linear π-Systems with Polymerizable End Group for Various Applications. **B. Vedhanarayanan**, R. D. Mukhopadhyay, and A. Ajayaghosh **2017**. (To be submitted)

5. Development of Superhydrophobic Coatings for Energy Saving Mechanical Motion and Related Applications. A. Ajayaghosh, **B. Vedhanarayanan**, and R. D. Mukhopadhyay **2017**. (Patent- To be filed)

Papers Presented at Conferences (Posters)

1. Self-Assembled π-Gelator on Reduced Graphene Oxide. **B. Vedhanarayanan**, and A. Ajayaghosh. A poster presented at 4th International Conference on Nanoscience and Technology, Cochin Nano 2016 at CUSAT, Cochin, India, February 20-23, **2016**.
2. Self-Assembled Hybrids of π-Gelators and Reduced Graphene Oxide for Energy Storage Devices. **B. Vedhanarayanan**, and A. Ajayaghosh. A poster presented at International Workshop on Advanced Functional Materials and Devices, IWAFMD 2017 at MSU, Thirunelveli, India, 8-12 January **2017**.
3. Superhydrophobic Hybrid Materials of Carbon Nanotubes and Polymerizable Linear π-Systems. **B. Vedhanarayanan**, and A. Ajayaghosh. A poster presented at Short Course on Polymer Science and Indo-Japan Joint Symposium on Polymeric Materials at Thiruvananthapuram, India, 31st January – 1st February **2017**.